



**HAL**  
open science

# Phase-field modeling of dendritic solidification for an Al-4.5wt%Cu atomized droplet using an anisotropic adaptive mesh

Carole Sarkis

► **To cite this version:**

Carole Sarkis. Phase-field modeling of dendritic solidification for an Al-4.5wt%Cu atomized droplet using an anisotropic adaptive mesh. Material chemistry. Université Paris sciences et lettres, 2016. English. NNT : 2016PSLEM048 . tel-01649221

**HAL Id: tel-01649221**

**<https://pastel.hal.science/tel-01649221>**

Submitted on 27 Nov 2017

**HAL** is a multi-disciplinary open access archive for the deposit and dissemination of scientific research documents, whether they are published or not. The documents may come from teaching and research institutions in France or abroad, or from public or private research centers.

L'archive ouverte pluridisciplinaire **HAL**, est destinée au dépôt et à la diffusion de documents scientifiques de niveau recherche, publiés ou non, émanant des établissements d'enseignement et de recherche français ou étrangers, des laboratoires publics ou privés.

# THÈSE DE DOCTORAT

de l'Université de recherche Paris Sciences et Lettres

PSL Research University

Préparée à MINES ParisTech

Modélisation de la solidification dendritique d'un alliage Al-4.5% pdsCu atomisé avec  
une méthode de champs de phase anisotrope adaptative

~~~

Phase-field modeling of dendritic solidification for an Al-4.5wt%Cu atomized droplet  
using an anisotropic adaptive mesh

**École doctorale n° 364 :**

Sciences Fondamentales et Appliquées

**Spécialité** Mécanique numérique et matériaux

Soutenue par :

**Carole SARKIS**

**Le 01 Décembre 2016**

Dirigée par :

**Charles-André GANDIN**

**Luisa SILVA**



**COMPOSITION DU JURY :**

M. Patrice LAURE,  
Directeur de recherche CNRS, Université de Nice  
Sophia-Antipolis, Président

M. Julien BRUCHON, Maître Assistant, Ecole des  
Mines de Saint-Etienne, Rapporteur

M. Steven LE CORRE, Professeur, Université de  
Nantes, Rapporteur

M. Gregory LEGRAIN, Maître de Conférences,  
Ecole Centrale de Nantes, Examineur

M. Charles-André GANDIN, Directeur de recherche  
CNRS, MINES ParisTech, Examineur

Mme Luisa SILVA, Chargée de recherche, Ecole  
Centrale de Nantes, Examineur



# Acknowledgments

First of all, I would like to convey my deepest gratitude to the director of my Ph.D., Charles-André Gandin, for recruiting me. I appreciate all his contributions and remarks and also for his time and fruitful ideas and for guiding me through the important phases of this thesis. I would like also to thank my supervisor Luisa Silva for her help, support and indications. I appreciate all her contributions, ideas, and remarks. I thank her also for giving me the opportunity to achieve this work

I'd like to thank Mathis Plapp for all the help and guidance he offered during my three years of research. A special thank to Gildas Guillemot and Patrice Laure for their contributions in this work.

I thank also our colleagues, from France and Canada, in the MIMOSA project.

I'd like to thank Mr. Julien Bruchon and Mr. Steven Le Corre to accept being the reviewers of this thesis and for their comments. I'd like to thank Mr. Patrice Laure and Mr. Gregory Legrain for their participation for the jury members.

I would like to express my gratitude for all my friends in CEMEF, Nadine, Lionel, Rebecca, Fadi, Ghina, Ali, Jeff, Jose, Thi Thuy My, Valentine, Shijia... I can't forget my brothers and friends outside CEMEF who supported me and gave me good advices during these three years, Sophiadeo family.

A special "thanks" goes to the Ladies of CEMEF who make the working environment joyful, Marie-Françoise, Françoise, Geneviève, Florence, Carole, Murielle and the librarians Brigitte and Sylvie. I would like to thank also all the staff at CEMEF, Group EII and special mention to the director: Elisabeth Massoni.

I am very grateful to Patrick Coels for his advices, motivation, help, knowledge in life and managements and for the fruitful conversations we had.

Last but not least, I would like to thank my family and friends in Lebanon for their support.

The achievement of this thesis requires: Trust in God, Patience and Work.

Thank you God for giving me power and strength to complete this work.

To my family I dedicate my thesis.



# Contents

|                                                                        |    |
|------------------------------------------------------------------------|----|
| Chapter 1 .....                                                        | 1  |
| 1 Introduction.....                                                    | 1  |
| 1.1 Context of the thesis .....                                        | 1  |
| 1.2 Atomized droplets.....                                             | 2  |
| 1.3 Solidification .....                                               | 4  |
| 1.4 Dendrites .....                                                    | 6  |
| 1.5 Models used for the simulation of dendritic growth.....            | 8  |
| 1.5.1 Front tracking through level-set approaches .....                | 10 |
| 1.5.2 Phase-field approach .....                                       | 11 |
| 1.5.3 Cellular automaton approach .....                                | 12 |
| 1.5.4 Mesoscopic approach .....                                        | 12 |
| 1.5.5 Mean-field approach .....                                        | 14 |
| 1.6 Motivations and Objectives .....                                   | 14 |
| Chapter 2 .....                                                        | 17 |
| 2 Thermal model.....                                                   | 17 |
| 2.1 Model equations .....                                              | 17 |
| 2.2 Numerical resolution .....                                         | 24 |
| 2.2.1 Finite element solver .....                                      | 24 |
| 2.2.2 Mesh adaptation .....                                            | 28 |
| 2.2.3 Parallel computing.....                                          | 33 |
| 2.2.4 Validation on benchmark: temperature diffusion in a corner.....  | 35 |
| 2.3 Thermal dendritic growth .....                                     | 43 |
| 2.3.1 Timestep and number of elements adaptation.....                  | 46 |
| 2.3.2 Convergence of the tip velocity .....                            | 48 |
| 2.3.3 Computational time .....                                         | 49 |
| 2.3.4 Study of the capillary anisotropy .....                          | 52 |
| 2.3.5 3D thermal dendritic growth .....                                | 54 |
| 2.4 Conclusion.....                                                    | 59 |
| Chapter 3 .....                                                        | 61 |
| 3 Solutal model .....                                                  | 61 |
| 3.1 Model equations .....                                              | 61 |
| 3.1.1 Mass conservation equation .....                                 | 63 |
| 3.2 Numerical resolution .....                                         | 65 |
| 3.2.1 Finite element resolution of the mass conservation equation..... | 65 |
| 3.2.2 Mesh adaptation .....                                            | 67 |
| 3.2.3 1D validation .....                                              | 68 |
| 3.3 2D dendritic growth.....                                           | 74 |
| 3.3.1 Comparison with a model of direct growth.....                    | 74 |
| 3.3.2 Comparison with other models .....                               | 75 |

|            |                                                              |     |
|------------|--------------------------------------------------------------|-----|
| 3.3.3      | Parameter sensitivity study.....                             | 77  |
| 3.4        | Conclusion.....                                              | 81  |
| Chapter 4  | .....                                                        | 83  |
| 4          | Thermo-solutal model.....                                    | 83  |
| 4.1        | Model equations.....                                         | 83  |
| 4.2        | 1D thermo-solutal validation.....                            | 84  |
| 4.3        | Thermo-solutal dendritic growth.....                         | 88  |
| 4.3.1      | Mesh adaptation.....                                         | 88  |
| 4.3.2      | 2D thermo-solutal dendritic growth.....                      | 89  |
| 4.3.3      | 3D thermo-solutal dendritic growth.....                      | 94  |
| 4.4        | Conclusion.....                                              | 96  |
| Chapter 5  | .....                                                        | 99  |
| 5          | Physical simulations.....                                    | 99  |
| 5.1        | Modeling of equiaxed solidification in alloys.....           | 100 |
| 5.1.1      | Phase-field model (PF) description.....                      | 101 |
| 5.1.2      | Mean-field model (MF) description.....                       | 104 |
| 5.2        | PF and MF simulations and methodologies for comparisons..... | 110 |
| 5.2.1      | Studied configurations.....                                  | 110 |
| 5.2.2      | Phase-field simulation.....                                  | 113 |
| 5.2.3      | Grain envelope extration.....                                | 121 |
| 5.2.4      | Computation of average and representative quantities.....    | 123 |
| 5.2.5      | Mean-field simulation.....                                   | 125 |
| 5.3        | Parametric study.....                                        | 130 |
| 5.3.1      | Microstructure parameter.....                                | 131 |
| 5.3.2      | Droplet radius.....                                          | 134 |
| 5.3.3      | Initial droplet velocity.....                                | 135 |
| 5.3.4      | Nucleation temperature.....                                  | 136 |
| 5.3.5      | External temperature.....                                    | 137 |
| 5.3.6      | Atomisation gas.....                                         | 138 |
| 5.3.7      | Timestep and initial radius.....                             | 139 |
| 5.4        | Conclusion.....                                              | 140 |
| Chapter 6  | .....                                                        | 145 |
| 6          | Conclusions and perspectives.....                            | 145 |
| 6.1        | Conclusions.....                                             | 145 |
| 6.2        | Perspectives.....                                            | 146 |
| 6.2.1      | 3D PF simulations.....                                       | 146 |
| 6.2.2      | Kinetic anisotropy.....                                      | 147 |
| 6.2.3      | Growth with fluid flow.....                                  | 147 |
| Appendix A | Energy conservation equation.....                            | 149 |
| Appendix B | Analytical solution for corner test.....                     | 155 |
| Appendix C | 1D analytical solution.....                                  | 159 |
| References | .....                                                        | 161 |

## List of symbols

|                       |                                                                                 |                                |
|-----------------------|---------------------------------------------------------------------------------|--------------------------------|
| $\alpha$              | Averaged thermal diffusivity                                                    | $\text{m}^2\text{s}^{-1}$      |
| $\alpha^l / \alpha^s$ | Thermal diffusivity in the liquid/solid                                         | $\text{m}^2\text{s}^{-1}$      |
| $\beta$               | Latent to sensible heat ratio = $\frac{L}{c_s(T_F - T_W)}$                      | -                              |
| $\beta$               | Kinetic coefficient                                                             | $\text{m}^{-1}\text{s K}$      |
| $\Delta$              | Supercooling                                                                    | K                              |
| $\delta_c$            | Layer thickness                                                                 | m                              |
| $\delta_\phi$         | Dirac function                                                                  | -                              |
| $\varepsilon_\phi$    | Positive coefficient                                                            | -                              |
| $\varepsilon_4$       | Constant intensity of anisotropy                                                | -                              |
| $\phi$                | Signed function to determine the solid/liquid interface and vary between [-1;1] | -                              |
| $\phi_{LS}$           | Signed function for the LevelSet model                                          | -                              |
| $\Gamma$              | Gibbs-Thomson coefficient                                                       | m K                            |
| $\gamma$              | Excess free energy of the solid/liquid interface                                | $\text{J m}^{-2}$              |
| $\eta$                | Signed distance                                                                 | -                              |
| $\kappa$              | Averaged thermal conductivity                                                   | $\text{W m}^{-1}\text{K}^{-1}$ |
| $\kappa^l / \kappa^s$ | Thermal conductivity in the liquid / solid                                      | $\text{W m}^{-1}\text{K}^{-1}$ |
| $\kappa_r$            | Interface curvature term                                                        | $\text{m}^{-1}$                |
| $\kappa_{tip}$        | Tip curvature term                                                              | $\text{m}^{-1}$                |
| $\lambda$             | Dimensionless parameter related to the capillary length                         | -                              |
| $\lambda_c$           | Constant in one-dimensional solution- stationary interface position             | -                              |
| $\lambda_2$           | Secondary dendrite spacing                                                      | m                              |
| $\mu_E$               | Chemical potential                                                              | $\text{J mol}^{-1}$            |
| $\mu_f$               | Kinematic viscosity of the atomization gas.                                     | Pa.s                           |
| $\mu_k$               | Kinetic coefficient                                                             | $\text{m s}^{-1}\text{K}^{-1}$ |
| $\mu_p$               | Fluid viscosity on the surface of the droplet                                   | Pa.s                           |
| $\mu_\infty$          | Fluid viscosity far from the droplet                                            | Pa.s                           |
| $\Theta$              | Angle                                                                           | Degree $^\circ$                |
| $\Theta_0$            | Orientation angle                                                               | Degree $^\circ$                |
| $\theta$              | Non dimensional temperature                                                     | -                              |
| $\theta_0$            | Initial non dimensional temperature                                             | -                              |
| $\theta_{Anal}$       | Non dimensional analytic temperature                                            | -                              |
| $\theta_{ext}$        | Non dimensional external temperature                                            | -                              |
| $\theta_i$            | Interface temperature                                                           | -                              |
| $\theta_{imp}$        | Imposed non dimensional temperature                                             | -                              |
| $\theta_{nucl}$       | Non dimensional nucleus temperature                                             | -                              |
| $\rho$                | Density/Specific mass                                                           | $\text{kg/m}^3$                |
| $\rho_f$              | Gas density                                                                     | $\text{kg/m}^3$                |
| $\rho_0$              | Reference density at temperature $T_0$ and composition $C_{0,i}$                | $\text{kg/m}^3$                |
| $\rho_{tip}$          | Radius tip                                                                      | m                              |

|                    |                                                             |                      |
|--------------------|-------------------------------------------------------------|----------------------|
| $\sigma$           | Stress tensor                                               | Pa                   |
| $\tau$             | Non dimensional time                                        | -                    |
| $\tau_0$           | Characteristic time of attachment of atoms at the interface | s                    |
| $\Omega$           | Computational domain                                        | -                    |
| $\Omega_c$         | Supersaturation                                             | wt%                  |
| $\Omega^l$         | Liquid phase                                                | -                    |
| $\Omega^s$         | Solid phase                                                 | -                    |
| $\Omega^{s/l}$     | Interface between the solid and liquid phases               | -                    |
| $\xi$              | Vector used in the metric                                   | -                    |
| $A_{ext}$          | The exchange surface of heat with the exterior              | $m^2$                |
| $A^{\alpha/\beta}$ | Surface of the interface $\alpha/\beta$                     | $m^2$                |
| $Acc$              | Acceleration                                                | $m\ s^{-2}$          |
| $Arm$              | Number of dendritic arms                                    | -                    |
| $a_1$              | Positive constant deduced from the asymptotic analysis      | -                    |
| $a_2$              | Positive constant deduced from the asymptotic analysis      | -                    |
| $C$                | Constant in super hyperbola                                 | -                    |
| $C_0$              | Initial composition                                         | wt%                  |
| $c^l$              | Composition of the liquid phase                             | wt%                  |
| $c^s$              | Composition of the solid phase                              | wt%                  |
| $c^{l(intra)}$     | Composition of the liquid phase in the intradendritic zone  | wt%                  |
| $c^{l(extra)}$     | Composition of the liquid phase in the extradendritic zone  | wt%                  |
| $c^{s/l}$          | Composition of the solid phase at the $s/l$ interface       | wt%                  |
| $c^{l/s}$          | Composition of the liquid phase at the $s/l$ interface      | wt%                  |
| $c$                | Composition                                                 | wt%                  |
| $c_i$              | Interfaec composition                                       | wt%                  |
| $c_p$              | Specific heat at constant pressure                          | $J\ kg^{-1}\ K^{-1}$ |
| $c_\infty$         | Average concentration/Initial concentration                 | wt%                  |
| $D$                | Solute diffusion coefficient                                | $m^2\ s^{-1}$        |
| $D^l/D^s$          | Diffusion coefficient in the liquid/solid                   | $m^2\ s^{-1}$        |
| $D^i$              | Diffusion coefficient in phase $i$                          | $m^2\ s^{-1}$        |
| $D^j$              | Diffusion coefficient in phase $j$                          | $m^2\ s^{-1}$        |
| $d_0$              | Capillary length                                            | m                    |
| $E$                | Interface thickness                                         | -                    |
| $E_i$              | Internal energy                                             | J                    |
| $E_k$              | Kinetic energy                                              | J                    |
| $e_{ij}$           | Edge error                                                  | -                    |
| $e_{min}$          | Minimum edge error                                          | -                    |
| $F_v$              | Volumetric force                                            | $N\ m^{-3}$          |
| $F$                | Free energy                                                 | J                    |
| $FR$               | Remesh frequency                                            | -                    |
| $F_H$              | Ginzburg-Laudau free energy                                 | J                    |
| $f$                | Interface position in $x^*, y^*$ domain                     | -                    |

|                            |                                                               |                                                |
|----------------------------|---------------------------------------------------------------|------------------------------------------------|
| $f_\alpha$                 | Volumetric fraction of the phase $\alpha$                     | -                                              |
| $f_\beta$                  | Volumetric fraction of the phase $\beta$                      | -                                              |
| $f_H$                      | Helmholtz free energy                                         | J                                              |
| $g^l/g^s$                  | Liquid/Solid volume fraction                                  | -                                              |
| $H$                        | Specific enthalpy of phase                                    | J kg <sup>-1</sup>                             |
| $h_{ext}$                  | Heat extraction coefficient                                   | W m <sup>-2</sup> K <sup>-1</sup>              |
| $h_{min}$                  | Minimum mesh size                                             | -                                              |
| $i,j$                      | Notations used for solid and liquid phases                    | -                                              |
| $\mathbf{j}$               | The diffusion flow in species                                 | W m <sup>-2</sup>                              |
| $\mathbf{j}_t$             | Heat flux                                                     | W m <sup>-2</sup>                              |
| $\mathbf{j}_{at}$          | Antitrapping term                                             | W m <sup>-2</sup>                              |
| $K$                        | Curvature                                                     | m <sup>-1</sup>                                |
| $K_c$                      | Stiffness matrix from the convective term                     | -                                              |
| $K_d$                      | Stiffness matrix from the diffusive term                      | -                                              |
| $K$                        | Distribution/Partition coefficient                            | -                                              |
| $L$                        | Latent heat of fusion                                         | J kg <sup>-1</sup>                             |
| $Le$                       | Number of Lewis                                               | -                                              |
| $l^{\alpha\beta}$          | Diffusion length in $\alpha$ at the interface $\alpha/\beta$  | -                                              |
| $M$                        | Non dimensional liquidus slope                                | -                                              |
| $M_\phi$                   | Positive mobility of the phase-field function                 | m <sup>4</sup> J <sup>-1</sup> s <sup>-1</sup> |
| $M_c$                      | Positive mobility related to the composition                  | m <sup>4</sup> J <sup>-1</sup> s <sup>-1</sup> |
| $M_i$                      | Metric                                                        | -                                              |
| $M_m$                      | Mass matrix                                                   | -                                              |
| $m$                        | Exponent in super hyperbola                                   | -                                              |
| $m$                        | Liquidus slope                                                | K wt% <sup>-1</sup>                            |
| $NE$                       | Number of element                                             | -                                              |
| $NE_M$                     | Number of edges                                               | -                                              |
| $Nu$                       | Nusselt number                                                | -                                              |
| $Nb\_Proc$                 | Number of processors                                          | -                                              |
| $N_1$                      | Number of element to represent the interface                  | -                                              |
| $N_2$                      | Number of element to represent outside the interface          | -                                              |
| $\mathbf{n}$               | Unit normal vector to the interface                           | -                                              |
| $\mathbf{n}^{\alpha\beta}$ | Normal pointing to the exterior of the domain $\Omega^\alpha$ | -                                              |
| $Pe$                       | Peclet number                                                 | -                                              |
| $Pr$                       | Prandtl number                                                | -                                              |
| $P_{cal}$                  | Caloric power                                                 | W                                              |
| $P_{mech}$                 | Mechanical power of the external forces                       | W                                              |
| $p$                        | Pressure                                                      | Pa                                             |
| $p$                        | Stretching exponent                                           | -                                              |
| $p$                        | Number of cores                                               | -                                              |
| $q$                        | Space dimension                                               | -                                              |
| $Re$                       | Reynolds number                                               | -                                              |
| $R_g$                      | Gas constant                                                  | JK <sup>-1</sup> mol <sup>-1</sup>             |

|                             |                                                       |                |
|-----------------------------|-------------------------------------------------------|----------------|
| $R$                         | Radius at time $t$                                    | m              |
| $R_0$                       | Nucleus Radius                                        | m              |
| $S$                         | Solid region quantity                                 | -              |
| $S^{\alpha/\beta}$          | $\alpha/\beta$ interface density                      | $m^{-1}$       |
| $s_{ij}$                    | Edge stretching factor                                | -              |
| $\mathbf{T}$                | Stress vector                                         | Pa             |
| $T$                         | Temperature                                           | K              |
| $T_0$                       | Initial temperature                                   | K              |
| $T_{ext}$                   | External temperature                                  | K              |
| $T_F$                       | Fusion temperature                                    | K              |
| $T_i$                       | Interface temperature                                 | K              |
| $T_{imp}$                   | Imposed temperature                                   | K              |
| $T_L$                       | Liquidus temperature                                  | K              |
| $T^l / T^s$                 | Temperature in the liquid/solid                       | K              |
| $T_M$                       | Melting temperature                                   | K              |
| $T_{nucl}$                  | Nucleus temperature                                   | K              |
| $T_S$                       | Solidus temperature                                   | K              |
| $T_W$                       | Wall temperature                                      | K              |
| $t$                         | Time                                                  | s              |
| $t_{CPU}$                   | CPU time                                              | S              |
| $U$                         | Non dimensional composition                           | -              |
| $U_0$                       | Non dimensional initial composition                   | -              |
| $U_{Anal}$                  | Non dimensional analytic composition                  | -              |
| $U^L / U^S$                 | Non dimensional composition in the liquid/solid       | -              |
| $V$                         | Steady state growth velocity                          | $m s^{-1}$     |
| $V_0$                       | Initial droplet velocity                              | $m s^{-1}$     |
| $V_{interface}$             | Volume of the interface                               | -              |
| $V_{tip}^{GF}$              | Velocity tip computed with Green function             | -              |
| $\mathbf{V}$                | Velocity                                              | $m s^{-1}$     |
| $v_0$                       | Molar volume                                          | $m^3 mol^{-1}$ |
| $\mathbf{v}^{\alpha/\beta}$ | Local velocity of the interface                       | -              |
| $v_{LS}$                    | Velocity defined by the gibbs-Thomson equation        | $m s^{-1}$     |
| $v_n$                       | Normal velocity                                       | -              |
| $v_n^{st}$                  | Stationary normal velocity                            | -              |
| $v_{tip}$                   | Velocity tip                                          | -              |
| $V_{max}$                   | Maximum velocity                                      | $m s^{-1}$     |
| $W_{PF}$                    | Interface thickness for the phase-field model         | m              |
| $W_0$                       | Initial interface thickness                           | m              |
| $X_{ij}$                    | Edge between node $i$ and $j$                         | -              |
| $X$                         | Coordinate                                            | m              |
| $\alpha^*$                  | Non dimensional thermal diffusivity                   | -              |
| $\beta'$                    | Chosen constant to verify CFL condition for time step | -              |

|                                                  |                                                                             |                                   |
|--------------------------------------------------|-----------------------------------------------------------------------------|-----------------------------------|
| $\sigma^*$                                       | Tip selection parameter/Constant marginal stability                         | -                                 |
| $\tau_0^*$                                       | Non dimensional characteristic time of attachment of atoms at the interface | -                                 |
| $D^*$                                            | Non dimensional solute diffusion coefficient                                | -                                 |
| $d_0^*$                                          | Non dimensional capillary length                                            | -                                 |
| $h_{ext}^*$                                      | Non dimensional heat extraction coefficient                                 | -                                 |
| $W_0^*$                                          | Non dimensional interface thickness                                         | -                                 |
| $x^*$                                            | Non dimensional coordinate                                                  | -                                 |
| $x_0^*$                                          | Intersection of line $x^* = y^*$ and interface curve $x^*, y^*$ domain      | -                                 |
| $\Delta\tau$                                     | Non dimensional time step                                                   | -                                 |
| $\Delta H$                                       | Enthalpy                                                                    | J kg <sup>-1</sup>                |
| $\Delta H_f$                                     | Latent heat of fusion                                                       | J kg <sup>-1</sup>                |
| $\Delta t$                                       | Time step                                                                   | s                                 |
| $\Delta V^\alpha$                                | Volume of the subdomain defined by $\Omega^\alpha \cap \Delta V$            | m <sup>3</sup>                    |
| $\rho c_p$                                       | Heat capacity                                                               | J m <sup>-3</sup> K <sup>-1</sup> |
| $\rho H$                                         | Volume specific enthalpy                                                    | J m <sup>-3</sup>                 |
| $\rho L$                                         | Latent heat                                                                 | J m <sup>-3</sup>                 |
| $\partial\Omega$                                 | Surface of the domain/Domain boundary                                       | -                                 |
| $\dot{\varepsilon}$                              | Strain rate tensor                                                          | s <sup>-1</sup>                   |
| $\dot{Q}_T$                                      | Volumetric heat production term                                             | W m <sup>-3</sup>                 |
| $\Gamma(i)$                                      | Set of nodes connected to the node $i$                                      | -                                 |
| $q(\phi)$                                        | Dimensionless function                                                      | -                                 |
| $W(\mathbf{n})$                                  | Capillary anisotropy                                                        | -                                 |
| $\delta(\mathbf{x} - \mathbf{x}^{\alpha/\beta})$ | Dirac function centered at the point $\mathbf{x}^{\alpha/\beta}$            | -                                 |
| $d(x^*, \tau)$                                   | Real distance of $x^*$ from the interface at time $\tau$                    | -                                 |
| $\text{erf } x$                                  | Error function                                                              | -                                 |
| $\text{erfc } x$                                 | Complementary error function                                                | -                                 |



# Chapter 1

## 1 Introduction

---

|       |                                                         |    |
|-------|---------------------------------------------------------|----|
| 1.1   | Context of the thesis .....                             | 1  |
| 1.2   | Atomized droplets.....                                  | 2  |
| 1.3   | Solidification .....                                    | 4  |
| 1.4   | Dendrites .....                                         | 6  |
| 1.5   | Models used for the simulation of dendritic growth..... | 8  |
| 1.5.1 | Front tracking through level-set approaches .....       | 10 |
| 1.5.2 | Phase-field approach .....                              | 11 |
| 1.5.3 | Cellular automaton approach .....                       | 12 |
| 1.5.4 | Mean-field approach .....                               | 14 |
| 1.6   | Motivations and Objectives .....                        | 14 |

---

### 1.1 Context of the thesis

The development of aluminum alloys with increased strength and ductility is an ongoing challenge for automotive and aerospace applications, as those illustrated in Figure 1.1. Improved properties are achievable through increased refinement of the microstructure, i.e. higher cooling rates (rapid solidification), as well as through alloying additions. The combination of using alloying additions and rapid solidification often results in a solidified primary phase that is supersaturated in alloying elements. This has been shown to occur in a number of aluminum alloys [HEN2010][ROY2005].



Figure 1.1 Examples of products with an aluminum alloy body for automotive and aerospace applications.

An undercooled melt corresponds to a non-equilibrium state of the liquid. Upon undercooling, driving forces are present in the melt. The number of possible solidification modes increases with undercooling, making accessible a broad range of metastable microstructures and structurally different phases. Crystal and dendrite growth velocities vary significantly with undercooling. Hence, models of the solidifying microstructure are tools to help in developing structure-property relationships for aluminum alloys under a range of high cooling rate

conditions. These models provide valuable insight into the relationship between process and material performance for the development of the next generation of aluminum alloys.

This study has been performed in the framework of MIMOSA (Microstructural Modelling of Rapidly Solidified Droplets and Spray Formed Strips of Aluminum-Copper-Scandium Alloys), a project funded by the French National Research Agency (ANR, France) in collaboration with the Natural Sciences and Engineering Research Council of Canada (NSERC, Canada).

The 3-year project is a collaborative effort between Canada and France involving three teams of researchers. Powder and spray formed samples were generated using Impulse Atomization, a rapid solidification technique of Al-Cu alloy was used.

The solidified samples were characterized using Scanning Electron Microscopy (SEM), X-Ray diffraction, differential scanning calorimetry and microhardness at **AMPL (UofA, Edmonton, Canada)**. In addition, advanced characterizations were carried out, such as neutron diffraction and 3D-micro tomography together with automatic indexing of electron backscatter diffraction patterns (EBSD) at **AMPL (UofA)** and **IM2NP (Univ d'Aix Marseille, Marseille, France)**. The characterization data collected were also intended to be used for comparison with the models. Finally, Direct modelling of the dendritic microstructure for an Al-Cu binary alloy processed by atomization was developed at **ARMINES CEMEF (MinesParisTech, Sophia Antipolis, France)** using the phase-field method. This is the goal of the present work

## 1.2 Atomized droplets

Impulse Atomization (IA) is a single fluid atomization process. This technique has been extensively used for making metal powders, spray deposits, metal-matrix composites and spray refining of pig iron [DIN1997], [ELL2004], [HER2007], [PRA2006], [PRA2009]. It consists of a 0.5 m diameter and 4 m height cylindrical chamber, as schematized in Figure 1.2. This chamber is atmospherically sealed and can be filled with the gas of choice. In the case of atomization, an inert gas (such as He, N<sub>2</sub> or Ar) is used. The top portion of the chamber consists of an impulse unit where the material is melted at a controlled temperature and subsequently pushed through small orifices. The ensuing discontinuous melt streams break down into small droplets that fall through the gas in the chamber. The droplets attain a free-fall situation in the initial stages and therefore there is no gravity induced convection in these droplets. Droplets completely solidify as they fall through 3.5 m of the gas filled chamber and are collected in glass beakers filled with oil. It has been shown that IA produces rapidly solidified droplets and it is a useful technique for studying rapidly cooled systems, but also for varying alloy composition as it is more important to the fraction of phase distribution than cooling rate [PRA2009]. Successful pilot scale tests have been carried out with IA for the atomization of zinc through up to 400 orifices operating for 3 continuous hours, showing its potential as in the total process.

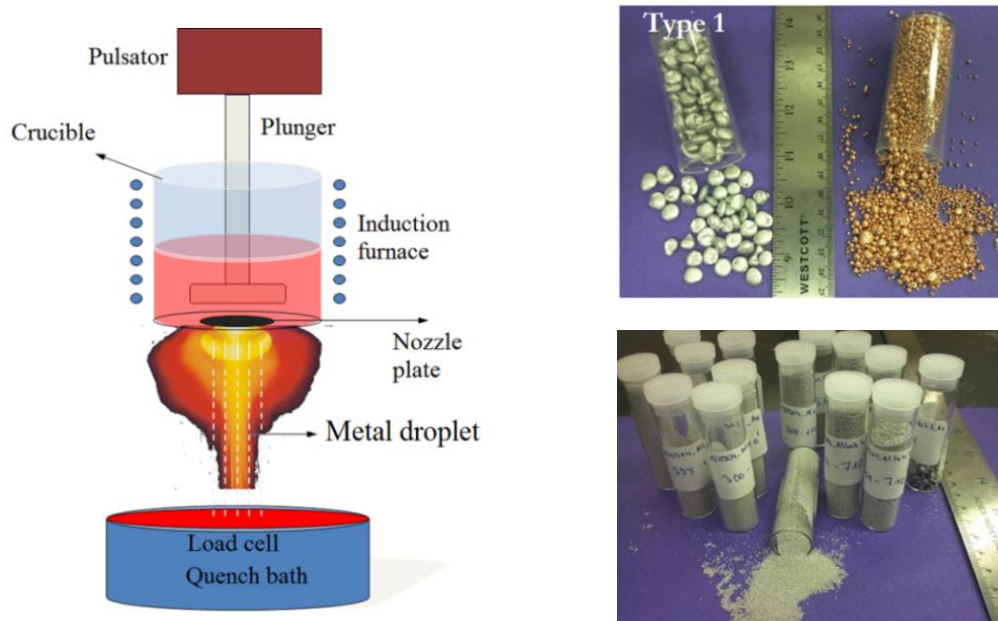


Figure 1.2 Schematic representation of an Impulse Atomization Unit and the atomized material before and after being melted [ELL2004].

Since the atomization temperature of an Al-Cu system is above 1 000 K, the liquid droplets may lose heat by radiation. However, since the droplets cool rapidly, the radiation heat loss component decreases, and therefore, has a small effect on the total heat loss [PRA2009]. The gas being stagnant, its primary function is to withdraw the heat from the liquid droplets, although the surface tension between the gas and liquid metal does play a part in breaking the liquid stream into droplets. Wiskel *et al.* [WIS2002] have shown that the cooling rate of Al-4.5wt%Cu atomized in He varies from 325 to 2 400 Ks<sup>-1</sup> for droplets of diameter 950 to 275 μm, respectively. On the other hand, the same range of droplets sizes atomized under N<sub>2</sub> shows cooling rates from 150 to 800Ks<sup>-1</sup>. Because of the better conductivity of He gas compared to N<sub>2</sub>, the cooling rate is higher. Thus, a droplet of a given size in He shows a finer structure compared to the same droplet size atomized in N<sub>2</sub>. The data also shows that the microstructure length scale decreases as the droplet size decreases, since smaller droplets cool at a faster rate. These cooling rate values show that IA can produce rapidly solidified powders.

To provide a better description of the microstructures, let us present shortly the experimental results obtained by Mimosa's project partners [BED2015]. Firstly, IA leads to a size distribution of the droplets with diameter from less than 200 μm to more than 1 mm in the same batch. The droplets are thus sieved into several size classes by the technique described in [FED2012].

The microstructure morphologies were then investigated for different size ranges and for the two cooling gases, He and Ar. For this purpose, synchrotron X-ray micro-tomography was used post-mortem [NGU2012]. This technique provides a three-dimensional reconstruction of the droplets microstructure as the grey level depends on the X-ray transmission of the phase. The primary Al phase being less absorbing than the eutectic (mixture of the Al phase + the Al<sub>2</sub>Cu intermetallic), the latter appears in lighter grey in the tomography reconstructions. The resolution used was of 0.56 μm/pixel (field of view of 1146.88 μm), which enables to study several small droplets at once. The statistical analysis of the droplet morphology has been carried out using the ImageJ

software [ABR2004]. The final droplet microstructure is the result of a complex three dimensional competition between dendrite arms, interdendritic intermetallic, as well as porosity. Therefore, only the cross-sections showing characteristic morphologies are shown in Figure 1.3, where four distinct morphologies were observed in the more than hundred studied droplets.

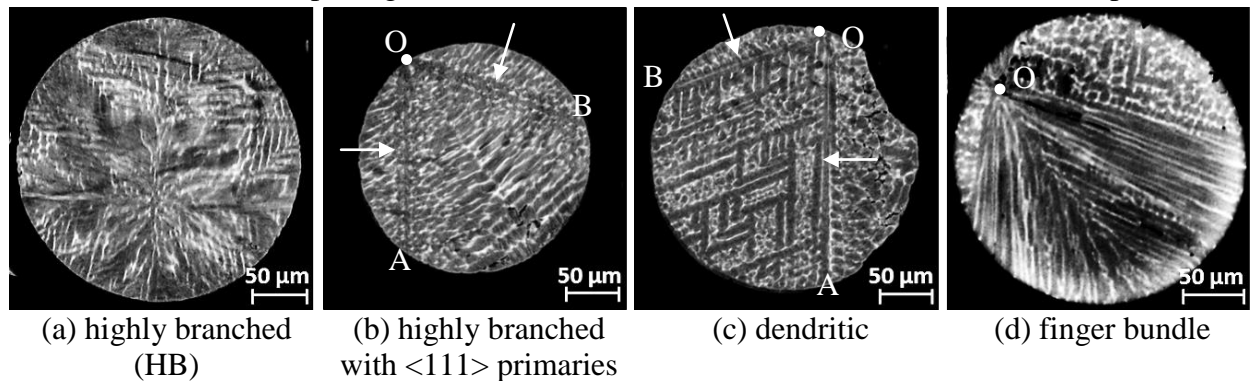


Figure 1.3 Examples of the four morphologies identified in the Al-4.5wt.%Cu droplets, of diameter between 250 and 300  $\mu\text{m}$ : (a) highly branched morphology, (b) highly branched morphology with primary arms oriented along  $\langle 111 \rangle$  directions, (c) dendritic morphology and (d) finger bundle morphology. The nucleation position noted O is shown by a white dot and the primary arms noted OA and OB by white arrows [BED2015]. Grey level has been inverted, the dendritic structure appearing darker than the eutectic region.

A major result of the synchrotron X-ray micro-tomography analysis was the variety of dendrite morphologies for Al-Cu droplets solidifying under the same process conditions, as shown in Figure 1.3. These morphologies were described in [BED2015] so only their main characteristics are here reminded. Some of the droplets grow in the usual  $\langle 100 \rangle$  directions and present a highly branched microstructure, as illustrated in Figure 1.3(a). A structure growing first in  $\langle 111 \rangle$  directions and then in  $\langle 100 \rangle$  directions can also be observed as in Figure 1.3(b). The two other types of morphologies are fully growing along  $\langle 111 \rangle$  directions, with a dendritic (Figure 1.3(c)) or a finger-bundle (Figure 1.3(d)) morphology. The growth orientations for this microstructure were validated by EBSD analyses [BED2015].

Interpretation given was that the first solid grow along the  $\langle 111 \rangle$  direction if its growth velocity reaches values beyond a growth orientation transition. Eventually, its growth velocity decreases and the last part of the droplet would grow in the  $\langle 100 \rangle$  direction, as observed in Figure 1.3(b). At lower velocity, the usual  $\langle 100 \rangle$  is observed, as in standard foundry technologies.

### 1.3 Solidification

Solidification is the phase transformation studied here. It is involved in at least one of the manufacturing stages of almost every man-made object [KUR1998], [LUD2004]. Some important processes which involve solidification are

- casting: continuous, ingot, form, precision, die;
- welding: arc, resistance, plasma, electron beam, laser, friction;
- soldering/brazing;

- rapid solidification processing: melt spinning, planar flow casting, atomization, bulk undercooling, remelting surface and atomization;
- directional solidification: Bridgman, liquid metal cooling, Czochralski, electroslag remelting.

In the forming of aluminum alloys, solidification is a transformation step during which the metal, initially liquid, gradually becomes solid upon cooling. The typical stages are: nucleation, primary growth dendritic structure, and secondary and further growth (peritectic or eutectic) [LUD2004]. Once a nucleus is formed, it is limited by capillarity and transport of heat and mass, leading to a morphological instability of the  $s/l$  interface and dendritic growth.

Figure 1.4 shows a temperature history measured of an Al-4wt%Cu melt. It reveals (I) heat transfer until the undercooling state appears and the nucleus is created, (II) recalescence due to dendritic growth, (III) another cooling, (IV) secondary nucleation of an eutectic structure and its associated reference and (V) cooling of the fully solid structure.

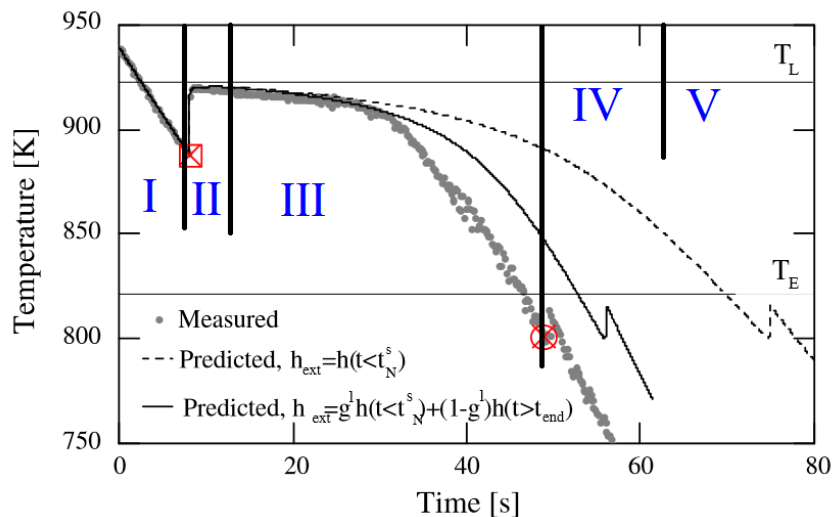


Figure 1.4 Temperature profile during solidification of an Al-4wt%Cu alloy [GAN2008].

The energy of the system is changed by heat extraction in several ways: firstly, there is a decrease in the enthalpy of the liquid and solid phases due to cooling; second, the transformation from liquid to solid releases the latent heat of fusion. But the transformation from the liquid to the solid also creates a curved and mobile solid/liquid interface, defined as an intermediate zone between the solid and the liquid, the thickness which is composed of a few atoms [MEC2010]. The curvature introduces capillary effects and microscopic heat and mass flows and the solid/liquid interface area is associated with an excess of interfacial energy. Therefore, systems that have a large interface have a higher energy.

In the case of an alloy, both heat and solute are rejected at the solid/liquid interface. Solute is released not only into the interdendritic liquid but also accumulates in a boundary layer outside the mushy zone or grain envelope. This is demonstrated by post mortem analysis of the average composition of Cu, as shown in Figure 1.5, revealing a non uniform distribution.

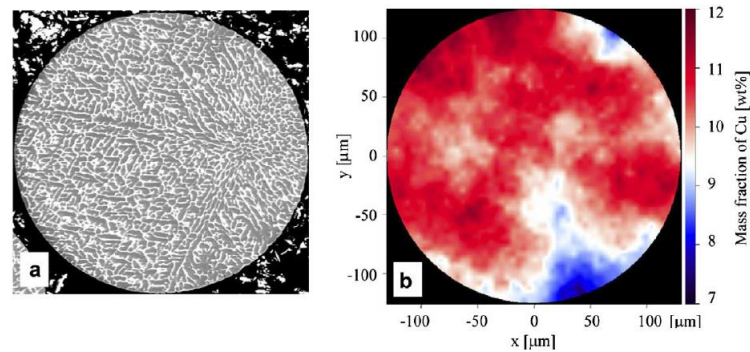


Figure 1.5 Cross-section through the center of a 250 μm diameter Al–10 wt.%Cu droplet, produced by atomization in nitrogen showing, (a) dendritic microstructure as observed with scanning electron microscope and (b) corresponding average composition map (%Cu) deduced from microprobe analysis [HER2006].

Figure 1.5 shows, on the left, a dendrite structure in grey surrounded with the interdendritic structure in white. On the right, the distribution map of Cu, with the presence of 10wt% of Cu in the alloy. Finally, diffusion flux is present at the very large scale of the dendritic arm.

## 1.4 Dendrites

The most frequently observed primary solidified microstructure is the dendrite. The descriptive term “dendrite” derives from the greck “ $\delta\varepsilon\nu\delta\rho\nu$ ”, a tree, with highly branched, arborescent appearance. It consists generally of a primary branch or trunk, secondary arms, eventually with tertiary branches growing from the secondaries and so on. This growth morphology is characterized by its paraboloid-like tip. There are different types of dendrites: the equiaxed dendrites that freely grow and are governed by solute and thermal diffusion, and the columnar alloy dendrites constrained by a temperature gradient and controlled by solute diffusion. In undercooled solidification processing, the highest nucleation temperature and the highest growth rate control the final appearance of microstructures and phases.

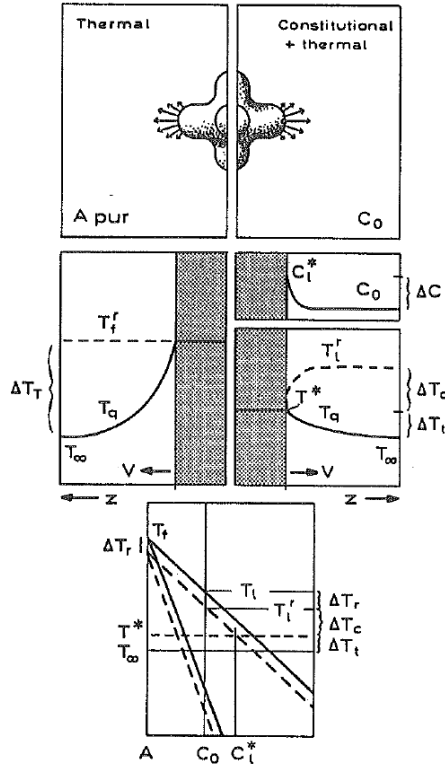


Figure 1.6 Equiaxed dendritic growth of a pure metal and an alloy showing the evolution of the temperature and composition in the liquid [KUR1998].

The growth of equiaxed dendrites of pure metals occurs under conditions where only heat flows from the interface to the surrounding liquid. The temperature gradient is negative at the interface and a thermal undercooling  $\Delta T_T$  exists. In the case of equiaxed alloy growth, there exists a negative temperature gradient and solute accumulation ahead of the dendrite tip leading to thermal and solutal undercooling, respectively  $\Delta T_c$  and  $\Delta T_t$ , as shown in Figure 1.6.

In the solidification of binary alloy system, physical phenomena are usually described by stating the conservation for energy and the conservation for the solute species in each phase and using the Gibbs-Thomson relation to establish the normal velocity of propagation of the  $s/l$  interface [BOE2002], [TAN2006], [ZAR2009]. The mathematical description of these phenomena is given here after, while its approximation will be detailed later, in chapters 2-4.

$$\left\{ \begin{array}{ll} \frac{\partial c^s}{\partial t} = D^s \Delta c^s & \text{Species composition conservation in the solid} \quad (1.1) \\ \frac{\partial c^l}{\partial t} = D^l \Delta c^l & \text{Species composition conservation in the liquid} \quad (1.2) \\ \frac{\partial T^s}{\partial t} = \alpha^s \Delta T^s & \text{Energy conservation in the solid} \quad (1.3) \\ \frac{\partial T^l}{\partial t} = \alpha^l \Delta T^l & \text{Energy conservation in the liquid} \quad (1.4) \\ (c^l - c^s)v_n = (D^s \nabla c^s - D^l \nabla c^l) \cdot \mathbf{n} & \text{Composition conservation at the } s/l \text{ interface} \quad (1.5) \\ \rho L v_n = (\kappa^s \nabla T^s - \kappa^l \nabla T^l) \cdot \mathbf{n} & \text{Energy conservation at the } s/l \text{ interface} \quad (1.6) \\ T_i = T_M + m c_i^l - \Gamma \kappa_r - v_n / \mu_\kappa & \text{Gibbs-Thomson equation at the } s/l \text{ interface} \quad (1.7) \end{array} \right.$$

Here,  $T$  is the temperature and  $c$  the alloy composition,  $s$  and  $l$  are the solid and liquid phases,  $t$  is the time,  $D^s$  and  $D^l$  are the solute diffusion in the solid and in the liquid,  $\alpha^s$  and  $\alpha^l$  are the thermal diffusion in the solid and liquid,  $\rho L$  is the latent heat,  $v_n$  is the normal velocity to the  $s/l$  interface ( $v_n = \mathbf{v} \cdot \mathbf{n}$ ),  $\kappa^s$  and  $\kappa^l$  are the thermal conductivity in the solid and liquid,  $\mu_k$  is the kinetic coefficient,  $\mathbf{n}$  is the unit normal vector to the interface,  $\Gamma$  is the Gibbs-Thomson coefficient related to the surface energy  $\gamma$  by the relation  $\Gamma = \frac{\gamma T_M}{\rho L}$ ,  $\kappa_r$  is the interface curvature term,  $m$  is the slope of the liquidus curve of the phase diagram for the alloy.  $T_i$  is the interface temperature,  $T_M$  is the melting temperature of the pure solvent and  $c_i^l$  is the concentration on the liquid side of the interface. This system of equations provides the sharp interface formulation of our solidification problem. In a diffuse interface context, instead of solving the equations for each phase with the given interface conditions, we may obtain a set of equations valid in the whole domain [KAR1998].

A few measurements have been reported for alloy dendrites. A number of researchers have performed experiments to measure the dendrite tip velocity and radius for transparent alloy systems [AST2009], [BOU1989], [CHA1987], [CHO1988], [DOU1988], [GLI1988], [KAH1970]. Only the succinonitrile-acetone (SCN-acetone) experiments of Chopra et al. [CHO1988] resulted in data over a sufficiently large range of undercoolings and solute concentrations to allow a detailed comparison with theory.

Macroscopic conditions (such as undercooling upon equiaxed growth) affect the solidification but microscopic internal characteristics play also an important role. The most important factors of internal characteristics are the anisotropy of the properties at the  $s/l$  interface, key parameters affecting the evolution of crystal morphology [HOU2008]. Anisotropy at the  $s/l$  interface includes the energy,  $\gamma$ , and the kinetic coefficient,  $\mu_k$  [MUL1964].

## 1.5 Models used for the simulation of dendritic growth

Modeling of dendritic growth in solidification of pure metals and alloys remains a significant challenge in materials science and applied physics. Successful modelling of dendritic solidification requires both the solution of a complex free-boundary problem and an accurate account of the interface energy and kinetic anisotropy. The first task is difficult because of the difference in orders of length scale between the thickness of the diffusion boundary layer of heat/solute that surrounds the dendrite tip and grain envelope, and the microscopic capillary scale, while the second task is complicated by the need to compute the curvature of the interface [ZAB2006]. Figure 1.7 shows different scales for the  $s/l$  interface, experimental view and numerical modeling. The various scales are illustrative and not directly comparable, because all these quantities vary with the material, especially between metals and organic alloys. The smallest scale is for the atomic interface that can be simulated using molecular dynamics models, the dendritic scale is at the micrometer size, simulated often using phase-field methods, the grain structure which can be simulated using the CAFE (cellular automaton-finite element) model and the process scale of many meters simulated with finite volume or finite element methods.

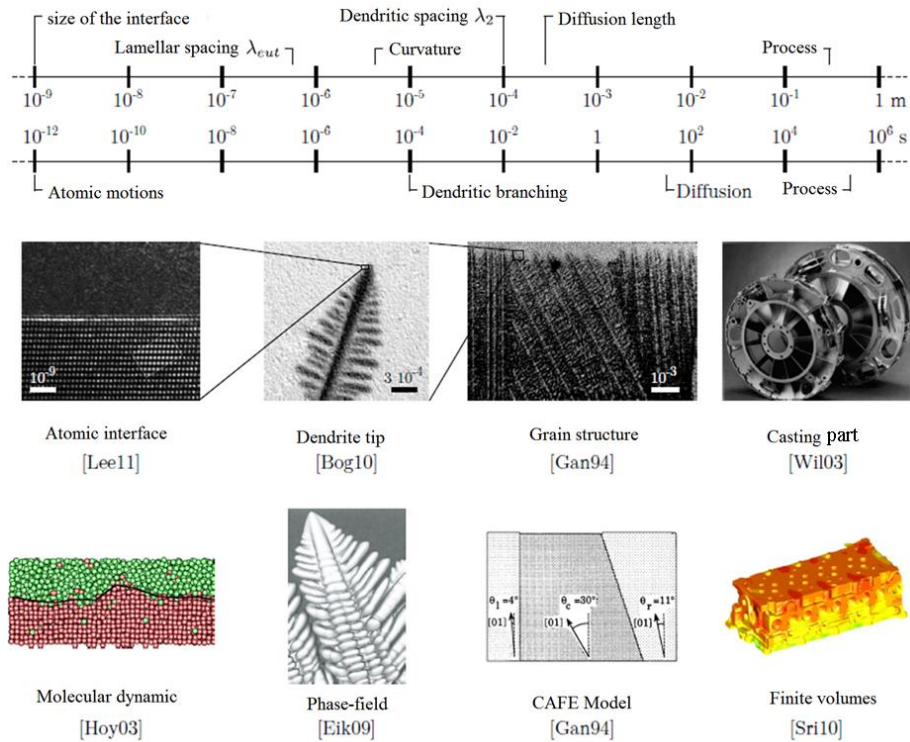


Figure 1.7 Different scales for the  $s/l$  interface (top), and corresponding description of the microstructure with illustrations from experimental observations (middle) and numerical simulations (bottom) [CAR2012].

In the last years, special attention has been given to the development of modeling techniques at various length scales for deeper understanding of microstructure formation. In the literature, at least four different approaches applied to dendritic growth can be identified. Firstly, sharp interface models [BAN1994], [NAK2006], [SAI1988], [UDA1999] are used to precisely reproduce the surface between solid and liquid by a dynamically refined mesh of the  $s/l$  interface. Secondly, phase-field (PF) models deal with the solid-liquid interface by introducing a continuous transitional layer of finite thickness using an additional quantity, thus eliminating the problem of explicitly tracking the interface and avoiding direct computations of the curvature. Several reviews on the methodology and capabilities of the PF models are available [AST2009], [BOE2002], [FRI2009], [HEC2004]. Thirdly, microscopic cellular automata (CA) were also employed for simulation of dendritic growth. When coupled with finite element modelling, this technique is referred to as CA-FE modeling [GAN1999], [RAP1993] and is then used to predict the development of the grain envelope, not directly simulating dendritic morphology. Fourthly, coarser-grained models have been developed at the mesoscale to predict the unsteady growth of dendritic grains and their internal solid fraction [STE1999], [STE2005], [ZAL2013], in 2D and 3D. These models track the evolution of the envelope of the dendritic grain, defined as an imaginary surface that passes through the tips of primary branches. However, they do not resolve exactly interactions between individual branches. Fifthly, the mean-field approach, which cannot follow dendrite morphologies, but may give us an equivalent grain envelope, and repartition of phase fractions inside/outside the envelope as well as average solution fields, studied in 1D dimension by [TOU2009]. Other authors developed a virtual front tracking (VFT) method of the solid-liquid interface [BEL2003], [BEL2004]. Discretization methods most often used are the

finite element method (FEM), the finite volume method (FVM), the finite difference method (FDM) and the average volume method (AVM). One finds, in the literature, computations using structured isotropic meshes, structured anisotropic meshes (squares divided in smaller squares or triangles) as illustrated in Figure 1.8 (a), in 2D and 3D [BAN1994], [TON1998a], [XIE2013] and unstructured anisotropic meshes [NAR2007] as illustrated in Figure 1.8 (b).

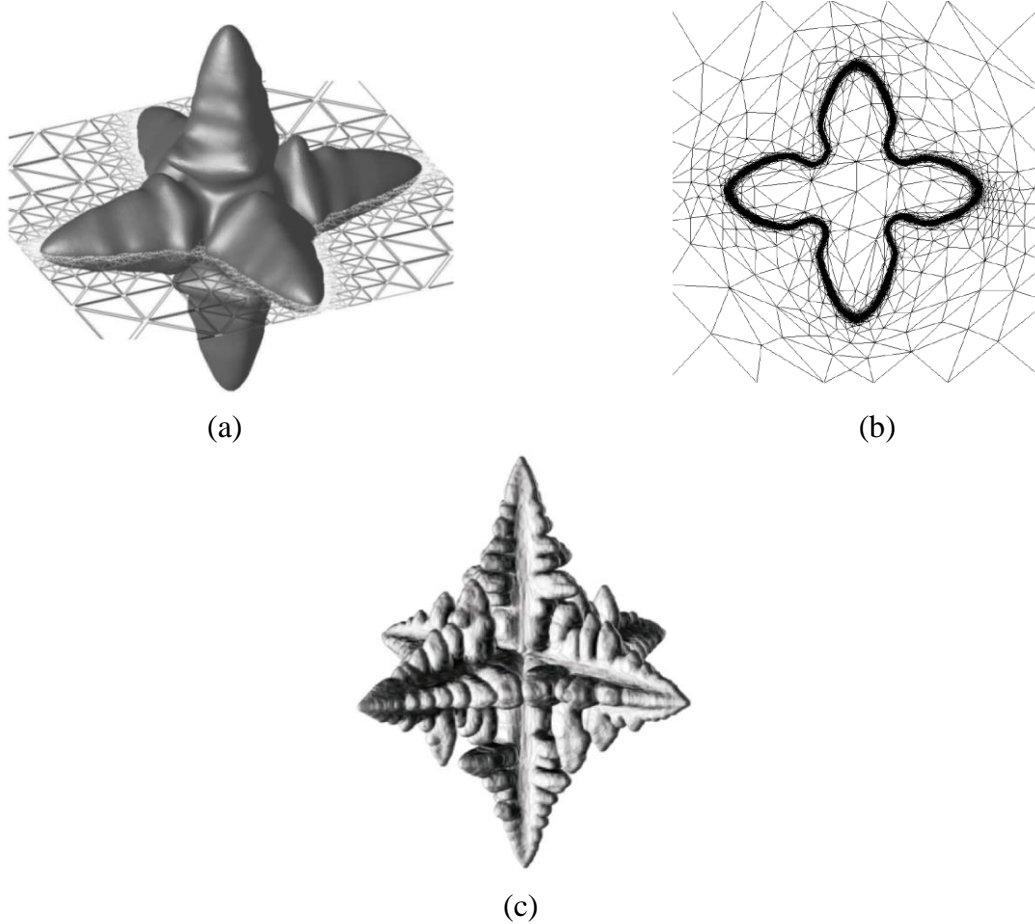


Figure 1.8 Examples of dendritic growth using: (a) the front tracking approach with an anisotropic structured mesh [BAN1994], (b) the phase-field approach with unstructured anisotropic adaptive mesh [NAR2007], (c) a microscopic cellular automaton method [CHO2012].

### 1.5.1 Front tracking through level-set approaches

These models are mainly based on the use of the level-set functions, classically employed in many areas where it is necessary to follow an interface [BAN1994]. A level-set function,  $\phi_{LS}$ , is a signed function that varies continuously from a positive value inside a phase, to a negative value outside. The interface is defined by the isovalue  $\phi_{LS} = 0$ . Most often,  $\phi_{LS}$  is the signed distance to the interface. Interface is displaced by the resolution of the level-set equation:

$$\frac{\partial \phi_{LS}}{\partial t} + v_{LS} |\nabla \phi_{LS}| = 0$$

where  $v_{LS}$  is the velocity field, determined from the Gibbs-Thomson condition for solidification problems. After the position of the front is calculated, the energy and solute conservation equations are solved. The main advantage of the level-set method is its ability to represent

complex topological changes. This method can be used to simulate growth with fluid flow [ZAB2006].

Among its claimed advantages, fairly easy implementation and fast computation time can be mentioned. However, the error associated with the estimation of curvature from the divergence of the normalized gradient of  $\phi$  is large (10-30%). Since preferred growth directions and dendrite tip kinetics are governed by the small anisotropy of the interfacial energy (1-10% in metallic alloys), such methods can only give qualitative results, unless mesh sizes around the interface become very small in the perpendicular direction to it. The later condition may then become incompatible with the fast computation time advantage.

## 1.5.2 Phase-field approach

This method introduces a function  $\phi$  which continuously varies from a constant value in a phase (eg. solid) to another constant in the other phase (eg. liquid). Most generally, the phase-field variable,  $\phi$ , varies smoothly from -1 to 1 between the two phases over the diffused-interface region, which has a small but numerically resolvable thickness,  $W_{PF}$ . The phase-field method derives its attractiveness from the fact that explicit tracking of the interface and satisfaction of the interfacial boundary conditions are avoided. Furthermore, computation of interface normal and curvature is also avoided by solving an evolution equation for the phase-field variable which may be derived from the free energy or entropy formulation and coupled to the evolution of heat and solute. The fundamental difference with a classical level-set method is that a thickness  $W_{PF}$  is thus given to the interface itself, which becomes diffuse. The principle is to minimize the free energy of the system by stating:

$$\frac{\partial \phi}{\partial t} = -M_{\phi} \frac{\partial F_H(\phi)}{\partial t} \quad (1.8)$$

where  $M_{\phi}$  is the mobility of the phase-field,  $F_H$  is the Ginzburg-Landau free energy and is defined by a Ginzburg-Landau type of integration in the domain:

$$F_H = \int_{\Omega} \left( f_H(\phi) + \frac{W(\mathbf{n})^2}{2} |\nabla \phi|^2 \right) d\Omega \quad (1.9)$$

$f_H(\phi)$  is the Helmholtz free energy and  $W(\mathbf{n})$  represents the anisotropy at the interface. The gradient term is introduced because of the representation of the diffuse interface. The derivation of these equations allows to move the interface and to minimize the energy,  $F_H$ . The results are poor when using a large interface: it should be less than the capillary length to converge to a sharp interface solution [XIE2013], which may be problematic in problems with fluid flow, in particular without remeshing or grid adaptation [PRO1999].

Karma and Rappel [KAR1996] improved asymptotic coefficients for the thin-interface limit of the phase-field equations, which ameliorate the convergence of the method for a coarser grid density. It lowers the range of undercooling and allows the use of a larger width of the diffuse interface region (compared with the capillary length), and gives the possibility to choose the model parameters in a way to make interface kinetics vanishing. Other recent changes have been added to these methods such as the use of an adaptive FEM formulation that refines the zone near the diffuse interface [PRO1998] or the use of a stochastic Monte Carlo treatment of the large scale diffusion field [PLA2000b]. This method was implemented by adding fluid flow

effects [TON1998a], [TON1998b], as well as used to represent eutectic solidification [ELD1994], [KAR1994], [WHE1996] and the peritectic reaction [LO2001], i.e. including multiple solid phases. Yet, phase-field simulations are limited to represent growth at a grain scale, especially for concentrated alloys that need a large solidification range and have a low supersaturation.

For a classical problem of dendritic crystal growth, several multi-grid [BRA1997] or adaptive meshing algorithms [SCH1996] have been proposed in recent years. One particularly cited method proposed by Provatas et al. [PRO1998] uses the phase-field model on a regular grid to compute the dendrite, whereas the temperature diffusion field is integrated on an adaptive mesh using finite element techniques. While this method appears to be promising, it has yet to be implemented in three dimensions, where the difficulty of adaptive meshing becomes significantly enhanced.

### 1.5.3 Cellular automaton approach

The cellular automaton microscopic methods have been applied to the prediction of dendritic structures during solidification [CAR2012]. By the fact that global fields throughout the area (temperature, composition) indirectly influence the local state of the cells, these models were baptized Modified Cellular Automata, MCA. Several versions have been developed, but the most common models are based on the same principle as the phase-field. The difference is that the interface thickness is simply equal to a row of cells, that may have different sizes [KRA2009], [NAS1999], and they have been developed for their computational speed and their ability to be used on larger areas than the phase-field. Their main disadvantage is the anisotropy induced by a regular grid of cells (square or cubic), not obvious to erase. However, these methods were shown to achieve quantitative results [CHO2012], [YIN2011], [ZHU2007]. Finally, we note the existence of cellular automata models where the kinetics of the interface is calculated from analytical equations, such as the KGT method [ZHU2001].

### 1.5.4 Mesoscopic approach

The mesoscopic modeling technique consists on coupling numerical calculation of the temperature field at the macroscopic scale with an analytical model of dendrite tip growth. A Representative Elementary Volume (REV) is used and is large enough to include a representative sampling of the microscopic structures and, at the same time, small enough to enable a continuum description of the variables averaged over the REV on the macroscopic scale. This model can predict the evolution of the grain shapes, the growth interactions between multiple grains, and the nature of the thermal field in the melt between the dendrites. With this method, the computational power requirements are reduced compared to a direct microstructure simulation on a microscopic scale. A schematic illustration of the various length scales present, at the mesoscopic modeling scale, in equiaxed dendritic growth, is shown in Figure 1.9 (a).

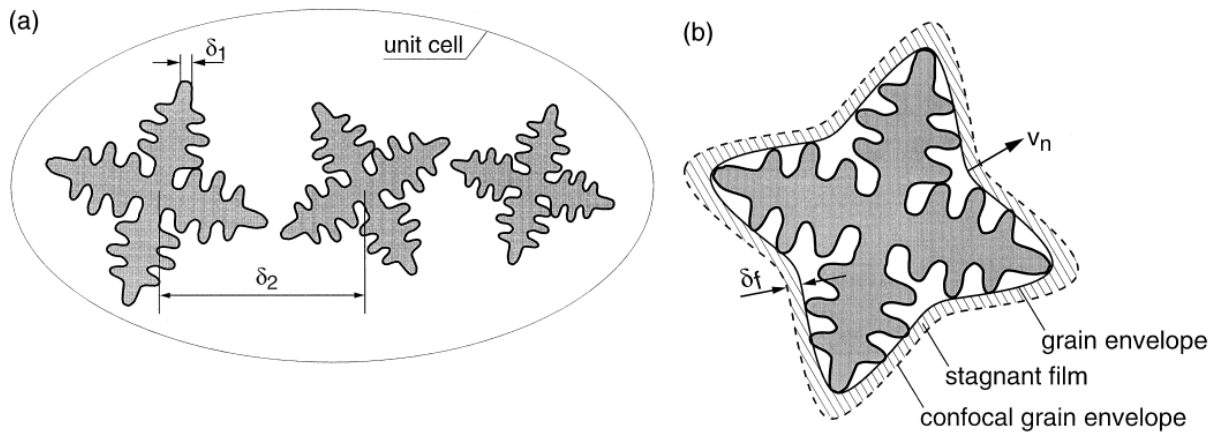


Figure 1.9 Schematic illustration of equiaxed dendritic growth: (a) unit cell, where  $\delta_1$  is the microscopic scale and  $\delta_2$  is the mesoscopic scale; (b) grain envelope and stagnant film [STE1999].

The prediction of the tip growth speeds and radii requires the resolution of the thermal field at the scale  $\delta_1$ , accomplished using a local analytical solution. The growth velocities of the grain envelope can be obtained from dendrite tip speeds. The Ivantsov solution is used. The supercooling is applied at a confocal isothermal paraboloid located at a finite distance  $\delta_f$  away from the dendrite tip and moving with the same speed as the tip. The tip speeds are calculated for every point on the envelope. Solid fraction can be deduced from the temperature gradient at the envelope.

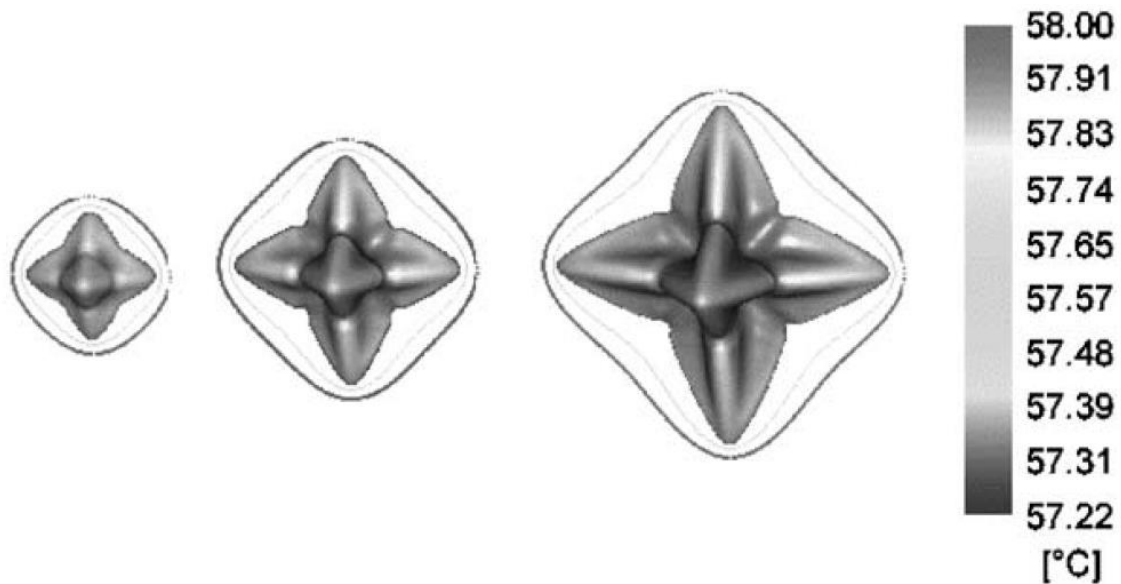


Figure 1.10 Example of the evolution of the dendrite envelope for a single equiaxed dendrite [STE2005].

The model was later used for two-phase representation with a volume-averaged Euler-Euler method that consists of two parts: a macroscopic part with momentum, mass, heat, solute mass, and grain population conservation equations, and a microscopic part that describes the nucleation and growth of grains.

### 1.5.5 Mean-field approach

This model tracks the evolution of the envelope of the dendritic grain, defined as an imaginary surface that passes through the tips of primary branches. However, interactions between individual branches are not exactly solved. Moreover, conservation equations are solved by projecting the dendrite in 1D and are based on the average volume method. This model and its combination with finite element or finite difference methods may also be used to study microstructural selection mechanisms, such as the dendritic spacing selection and its history dependence, but do not approximate the microstructure selection within a grain under non-steady-state growth conditions. It requires dendrite arms spacings as an input, which have an influence on microsegregation [TOU2011a][TOU2011b] and macrosegregation [BEC2002]. This model is detailed in Chapter 5.

## 1.6 Motivations and Objectives

An adaptive phase-field model is developed and presented in this thesis.

The aims of this present work are thus

- to describe the finite element implementation and programming of the proposed phase-field model with different homogenization schemes in a finite element code;
- to use parallel computing and automatic adaptive anisotropic unstructured meshes available with a C++ library developed at CEMEF, MINESParisTech, and their importance on the computational cost (time and memory);
- to obtain quantitative results using this model;
- to simulate dendritic growth for Al-Cu droplets;
- to start comparisons with a mean-field approach, and justify the differences, i) of macroscopic integration (Thesis of Thi-Thuy-My NGUYEN [NGU2015]), ii) of computational time. This is based on the phase-field methodology, known to be quantitative.
- to show that we have a difficulty to do a computation for an Al-4.5wt%Cu system of big size.
- to justify the advanced numerical methods (parallel computation, mesh adaptation, timestep adaptation, number of elements adaptation).

This manuscript is organized as follows, to model dendritic growth in a solidifying droplet as discussed in this chapter. Chapter 2 describes the phase-field model, for the solidification of a pure substance, by detailing the numerical resolution used for the diffusion, including mesh adaptation and parallel computation. Validation in 2D is presented, as well as capillary anisotropy implementation. Some symmetry assumptions are assumed for 3D simulations. Chapter 3 extends the phase-field model to represent the isothermal solidification of a binary alloy, explaining the difference from the previous one, in the numerical resolution and in the construction of the adapted mesh. Validations in 1D and 2D and sensitivity studies of the numerical parameters are presented. Chapter 4 couples thermal and solutal diffusion for a binary alloy. Finally, chapter 5 applies the model to the solidification of Al-Cu droplets and shows comparisons with a macroscopic mean-field model.

A general conclusion summarizes the study and opens perspectives.

**Résumé**

Dans cette introduction, le cadre des travaux de thèse, ainsi que différentes définitions, sont introduits. Nous présentons le procédé d'atomisation de gouttes pendant lequel la solidification a lieu. La morphologie dendritique est alors décrite, aussi bien que les méthodes numériques utilisées dans la littérature pour sa simulation. Nous terminons par définir les objectifs et les motivations de ces travaux: simulation de la croissance dendritique d'une goutte d'Al-Cu en utilisant le modèle de champs de phase et la méthode des éléments finis avec remaillage et calcul parallèle ainsi que d'autres optimisations pour diminuer le temps de calcul.



## Chapter 2

### 2 Thermal model

---

|       |                                                         |    |
|-------|---------------------------------------------------------|----|
| 2.1   | Model equations .....                                   | 17 |
| 2.2   | Numerical resolution .....                              | 24 |
| 2.2.1 | Finite element solver .....                             | 24 |
| 2.2.2 | Mesh adaptation.....                                    | 28 |
| 2.2.3 | Parallel computation .....                              | 33 |
| 2.2.4 | Test: temperature diffusion on a corner.....            | 35 |
| 2.3   | Thermal dendritic growth.....                           | 43 |
| 2.3.1 | Time adaptation of timestep and number of element ..... | 46 |
| 2.3.2 | Convergence of the tip velocity.....                    | 48 |
| 2.3.3 | Computational time .....                                | 49 |
| 2.3.4 | Study of the capillary anisotropy .....                 | 52 |
| 2.3.5 | 3D Thermal dendritic growth .....                       | 54 |
| 2.4   | Conclusion.....                                         | 59 |

---

In this chapter, we present the mathematical model used for solidification of a pure substance under anisothermal conditions. The model is based mainly on a continuous formulation of the phase-field method, given in [KAR1998]. It is developed for solidification, assuming local thermal equilibrium. We use the equations in a dimensionless form, and show its numerical solution. Thermal dendritic growth is illustrated with a validation in 2D, including sensitivity studies for the computational time and capillary anisotropy magnitude, and also through 3D simulations.

#### 2.1 Model equations

Let us consider conservation equations written for the sharp interface problem and limited to a pure substance, with a solid,  $s$ , growing in the liquid,  $l$ . In the absence of phase motion, they lead to:

$$\frac{\partial T^s}{\partial t} = \alpha^s \Delta T^s \quad (2.1)$$

$$\frac{\partial T^l}{\partial t} = \alpha^l \Delta T^l \quad (2.2)$$

$$\rho L v_n = (\kappa^s \nabla T^s - \kappa^l \nabla T^l) \cdot \mathbf{n} \quad (2.3)$$

$$T_i = T_M - \Gamma \kappa_r - v_n / \mu_k \quad (2.4)$$

We have supposed that the pure substance has constant and equal density,  $\rho$  [ $\text{kg} \cdot \text{m}^{-3}$ ], thermal conductivity,  $\kappa$  [ $\text{Wm}^{-1}\text{K}^{-1}$ ], and specific heat at constant pressure,  $c_p$  [ $\text{J} \cdot \text{K}^{-1}\text{kg}^{-1}$ ], in both solid and liquid phases and thus constant, as well as an equal thermal diffusivity,  $\alpha = \kappa / \rho c_p$  [ $\text{m}^2\text{s}^{-1}$ ].

Here,  $\kappa_r = \nabla \cdot \mathbf{n}$  [ $\text{m}^{-1}$ ] is the curvature term,  $\mu_k$  [ $\text{m} \cdot \text{s}^{-1} \text{K}^{-1}$ ] the kinetic coefficient,  $\Gamma$  the Gibbs-Thomson coefficient related to the surface energy  $\gamma$  [ $\text{Jm}^{-2}$ ] by the relation  $\Gamma = \frac{\gamma T_M}{\rho L}$  [ $\text{mK}$ ],  $T_M$  [ $\text{K}$ ] the melting temperature of the pure solvent,  $T_i$  [ $\text{K}$ ] the interface temperature,  $T$  [ $\text{K}$ ] the temperature,  $t$  [ $\text{s}$ ] the time,  $\rho L$  [ $\text{J} \cdot \text{m}^{-3}$ ] the latent heat and  $v_n = \mathbf{v} \cdot \mathbf{n}$  [ $\text{m} \cdot \text{s}^{-1}$ ] the normal velocity to the  $s/l$  interface.

It is convenient to define the dimensionless variable  $\theta$ , measure of the undercooling,  $T_M - T$ , as:

$$\theta = \frac{T - T_M}{L/c_p} \quad (2.5)$$

To use non-dimensional coordinates, in space and time, for the simulation, we define  $x^*$  as

$$x^* = x/W_0 \quad (2.6)$$

and  $\tau$  as a dimensionless time:

$$\tau = \frac{t}{\tau_0} \quad (2.7)$$

where  $\tau_0$  is the phase-field relaxation time, in [ $\text{s}$ ].

The free-boundary problem described above becomes (Appendix A):

$$\begin{aligned} \frac{\partial \theta^s}{\partial \tau} &= \alpha^{s*} \Delta \theta^s \\ \frac{\partial \theta^l}{\partial \tau} &= \alpha^{l*} \Delta \theta^l \end{aligned} \quad (2.8)$$

$$v_n = \alpha^* (\nabla \theta^s - \nabla \theta^l) \quad (2.9)$$

$$\theta_i = -d_0 \kappa_r - \beta v_n \quad (2.10)$$

where  $\alpha^*$  is the thermal diffusivity:

$$\alpha^* = \frac{\alpha \tau_0}{W_0^2} \quad (2.11)$$

The thermal capillarity length  $d_0$  [ $\text{m}$ ] is defined as:

$$d_0 = \frac{\Gamma}{\rho L / \rho c_p} = \frac{\gamma T_M \rho c_p}{\rho L^2} \quad (2.12)$$

and  $\gamma$  [ $\text{J} \cdot \text{m}^{-2}$ ] is the excess free energy of the solid/liquid interface. The kinetic coefficient  $\beta$  [ $\text{m}^{-1} \text{s}$ ] is defined as:

$$\beta = \frac{c_p}{\mu_k L} \quad (2.13)$$

In this approach,  $W_0$ , the thickness of the interface, is assumed small compared to the scale of the microstructure pattern, but not smaller than  $d_0$ , the capillarity length.

The phase-field equation presented was derived for the anisothermal case, but has to be coupled to the energy equation. Let us consider equal diffusivities in the solid and in the

liquid, so  $\langle \alpha \rangle = \alpha^s = \alpha^l = \text{cte}$ , as well as equal heat capacities  $\langle \rho c_p \rangle = \rho c_p^s = \rho c_p^l = \text{cte}$ . The average equation of energy, developed in Appendix A, becomes:

$$\frac{\partial T}{\partial t} - \alpha \Delta T = -\frac{1}{2} \frac{(\rho L)^{s/l}}{\rho c_p} \frac{\partial \phi}{\partial t} \quad (2.14)$$

Where  $(\rho L)^{s/l}$  is the latent heat associated with the transformation  $s \rightarrow l$ . As defined before, the dimensionless temperature  $\theta$  is used and the equation to solve becomes:

$$\frac{\partial \theta}{\partial \tau} - \alpha^* \Delta \theta = -\frac{1}{2} \frac{\partial \phi}{\partial \tau} \quad (2.15)$$

Let us define  $\phi$  as a function which describes the presence of the liquid and the solid phases in the computational domain  $\Omega$ , made by the two subdomains,  $\Omega^s$  in the solid and  $\Omega^l$  in the liquid. An interface  $\Omega^{s/l}$  is defined between  $\Omega^s$  and  $\Omega^l$ . The  $\phi$  function varies between  $-1$  and  $1$  as illustrated by Figure 2.1, and is defined as:

$$\phi = -\tanh\left(\frac{\eta}{W_0^* \sqrt{2}}\right) \quad (2.16)$$

In this expression,  $W_0^*$  is a non dimensional interface thickness ( $W_0^* = W/W_0$ ), where  $W_0$ , as previously introduced, measures a physical width and  $W$  represent the variable of this physical width. It is convenient to consider that it characterizes the diffuse solid/liquid interface, where  $x$  is the physical coordinate system and  $W_0$  is a physical arbitrarily chosen length.

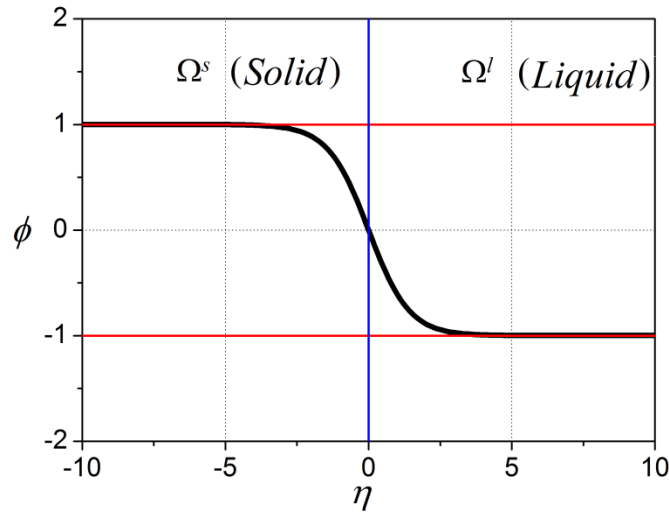


Figure 2.1 Variation of the phase function  $\phi$  with the signed distance  $\eta$  to a stationary flat liquid-solid interface, with  $W = W_0$ .

The variable  $\eta$  used in expression (2.16) is the signed distance to the solid/liquid interface. It is defined as

$$\eta = \begin{cases} d(x^*, \tau) & \text{if } x^* \in \Omega^s \\ 0 & \text{if } x \in \Omega^{s/l} \\ -d(x^*, \tau) & \text{if } x^* \in \Omega^l \end{cases} \quad (2.17)$$

where  $d(x^*, \tau)$  is the distance of  $x^*$  to the interface  $\Omega^{s/l}$  at time  $\tau$ .

Let us define the free energy functional  $F(\phi, \theta)$ , which must decrease during any thermodynamic process, as [KAR1998]

$$F(\phi, \theta) = \int_{\Omega} F^{int} dV \quad (2.18)$$

with  $F^{int} = f(\phi, \theta) + \frac{W(\mathbf{n})^2}{2} |\nabla \phi|^2$ .  $F^{int}$  is the sum of the volumetric energy given by the free energy density,  $f(\phi, \theta)$ , and the interfacial energy, respectively.  $W(\mathbf{n})$  is a measure of the anisotropy in the surface energy and  $\mathbf{n} = -\frac{\nabla \phi}{|\nabla \phi|}$ , the normal vector, and may be defined as follows [KAR1998]:

$$W(\mathbf{n}) = W_0^* (1 - 3\varepsilon_4) \left[ 1 + \frac{4\varepsilon_4}{1 - 3\varepsilon_4} \frac{(\partial_{x^*} \phi)^4 + (\partial_{y^*} \phi)^4}{|\nabla \phi|^4} \right] \text{ in 2D} \quad (2.19)$$

or

$$W(\mathbf{n}) = W_0^* (1 - 3\varepsilon_4) \left[ 1 + \frac{4\varepsilon_4}{1 - 3\varepsilon_4} \frac{(\partial_{x^*} \phi)^4 + (\partial_{y^*} \phi)^4 + (\partial_{z^*} \phi)^4}{|\nabla \phi|^4} \right] \text{ in 3D} \quad (2.20)$$

The instability of the solid/liquid interface that forms the dendrites is influenced by the anisotropy of the solid/liquid interfacial energy presented by the parameter  $\varepsilon_4$

Allen-Cahn equation [CAH1979] may be used to guarantee that the total free energy decreases with time due to an excess in the interfacial energy:

$$\frac{\partial F(\phi, \theta)}{\partial \tau} \leq 0 \quad \forall \tau > 0 \quad (2.21)$$

The Allen-Cahn equation is written by deriving the free energy to obtain, finally, the phase-field equation:

$$\frac{\partial \phi}{\partial \tau} = -M_{\phi} \frac{\delta F}{\delta \phi} = -M_{\phi} \left( \frac{\partial F^{int}}{\partial \phi} - \nabla \cdot \frac{\partial F^{int}}{\partial \nabla \phi} \right) \quad (2.22)$$

where  $M_{\phi}$  is a positive mobility parameter. The free energy density,  $f(\phi, \theta)$ , for a pure material, can be given by:

$$f(\phi, \theta) = g(\phi) + \lambda \theta p(\phi) \quad (2.23)$$

$\lambda$  is a dimensionless parameter that controls the strength of the coupling between the phase and diffusion fields. It is typically of the order of unity. This term can correct the contribution of the heat added and ensure that the relation  $([15/8(\lambda p(+1)) - 15/8(\lambda p(-1))]/2 = 1)$  is verified, whatever  $p(\phi)$  is chosen. In this expression of the free energy density of a pure element,  $p(\phi)$  is a function of  $\phi$  that guarantees  $\partial f / \partial \phi = 0$  for  $\phi = -1$  and for  $\phi = 1$  and for all temperatures. Furthermore,  $g(\phi)$  must provide the energy hump between the solid and liquid phases, with a maximum value at the interface and a minima at  $\phi = \pm 1$ . Hence, the following functions have been suggested by Karma and will be used in our model [KAR1998]:

$$g(\phi) = -\frac{\phi^2}{2} + \frac{\phi^4}{4} \quad (2.24)$$

$$p(\phi) = \phi - \frac{2\phi^3}{3} + \frac{\phi^5}{5} \quad (2.25)$$

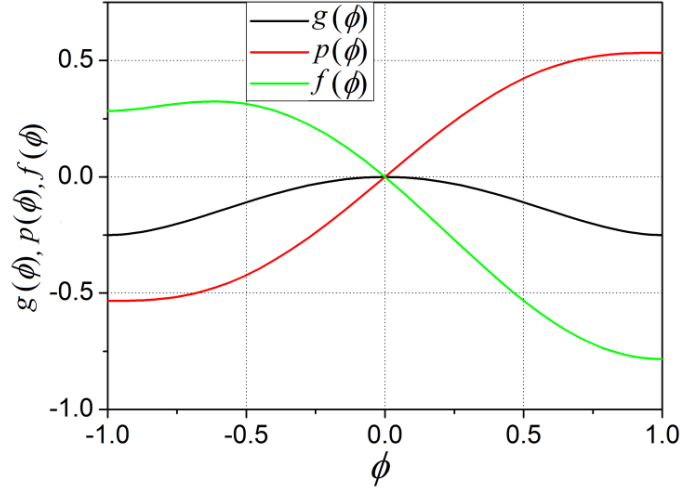


Figure 2.2 Illustration of the variations of  $f(\phi, \theta)$ ,  $g(\phi)$  and  $p(\phi)$  with  $\lambda = 2$  and  $\theta = -0.5$ .

From Eq.(2.22), the evolution equation for variable  $\phi$ , defining the position of the interface [EIK2010], is:

$$\begin{aligned} \frac{\partial \phi}{\partial \tau} = -M_\phi \frac{\delta F}{\delta \phi} = -M_\phi \left[ \frac{\partial F^{int}}{\partial \phi} - \nabla \left( \frac{\partial F^{int}}{\partial \nabla \phi} \right) \right] = \\ -M_\phi \left[ \frac{\partial f}{\partial \phi} - \frac{\partial}{\partial x^*} \left( \frac{\partial F^{int}}{\partial_{x^*} \phi} \right) - \frac{\partial}{\partial y^*} \left( \frac{\partial F^{int}}{\partial_{y^*} \phi} \right) - \frac{\partial}{\partial z^*} \left( \frac{\partial F^{int}}{\partial_{z^*} \phi} \right) \right] \end{aligned} \quad (2.26)$$

$$\text{Since } \frac{\partial F^{int}}{\partial \phi} = \frac{\partial}{\partial \phi} \left( f(\phi, \theta) + \frac{W(\mathbf{n})^2}{2} |\nabla \phi|^2 \right) = \frac{\partial f}{\partial \phi} + 0 = \frac{\partial f}{\partial \phi}, \text{ then } \frac{\partial f}{\partial \phi} = \frac{\partial g(\phi)}{\partial \phi} + \lambda \theta \frac{\partial p(\phi)}{\partial \phi} \quad (2.27)$$

This derivation is equal to

$$\frac{\partial f}{\partial \phi} = -\phi + \phi^3 + \lambda \theta (1 - 2\phi^2 + \phi^4) \quad (2.28)$$

and a factorization is used to obtain the simple form

$$\frac{\partial f}{\partial \phi} = \phi(\phi^2 - 1) + \lambda \theta (1 - \phi^2)^2 = (1 - \phi^2)(\lambda \theta (1 - \phi^2) - \phi) \quad (2.29)$$

Replacing in equation (2.26), one obtains:

$$\begin{aligned} \tau(\mathbf{n}) \frac{\partial \phi}{\partial \tau} - \nabla \cdot (W^2(\mathbf{n}) \nabla \phi) = [\phi - \lambda \theta (1 - \phi^2)](1 - \phi^2) + \frac{\partial}{\partial x^*} \left( |\nabla \phi|^2 W(\mathbf{n}) \frac{\partial W(\mathbf{n})}{\partial (\partial_{x^*} \phi)} \right) \\ + \frac{\partial}{\partial y^*} \left( |\nabla \phi|^2 W(\mathbf{n}) \frac{\partial W(\mathbf{n})}{\partial (\partial_{y^*} \phi)} \right) + \frac{\partial}{\partial z^*} \left( |\nabla \phi|^2 W(\mathbf{n}) \frac{\partial W(\mathbf{n})}{\partial (\partial_{z^*} \phi)} \right) \end{aligned} \quad (2.30)$$

where  $\tau(\mathbf{n}) = \frac{1}{M_\phi}$ .

Our attention is focused on the growth in the limit of vanishing interface kinetics. This limit is obtained by setting  $\tau(\mathbf{n})$  and  $\lambda$  equal to the values [KAR1998]:

$$\tau(\mathbf{n}) = \tau_0^* \left[ (1 - 3\varepsilon_4) \left[ 1 + \frac{4\varepsilon_4}{1 - 3\varepsilon_4} \frac{(\partial_{x^*} \phi)^4 + (\partial_{y^*} \phi)^4 + (\partial_{z^*} \phi)^4}{\nabla \phi^4} \right] \right]^2 \quad (2.31)$$

$$\lambda = \frac{\alpha \tau_0}{W_0^2 a_2} = \frac{\alpha^*}{a_2} \quad (2.32)$$

This second expression is related with the fact that one may redefine the coefficient  $\beta$  to include the variation of  $\theta$  across the interface using the asymptotic analysis:

$$\beta = a_1 \left[ \frac{\tau_0}{\lambda W_0} - \frac{a_2 W_0}{\alpha} \right] \quad (2.33)$$

which vanishes when kinetic effects are eliminated. Langer [LAN1986] and then Caginalp [CAG1989] have derived:

$$d_0 = a_1 \frac{W_0}{\lambda} \quad (2.34)$$

In these expressions,  $\tau_0$  is the characteristic time of attachment of atoms at the interface ( $10^{-13}$  s for metallic systems),  $a_1$  is a positive constant of order unity that depends on the details of the assumed form of free energy computed from the asymptotic analysis,  $a_2$  is a positive constant of order unity that depends on the details of the functional forms chosen for  $f(\phi)$ ,  $g(\phi)$  and  $p(\phi)$ . Karma and Rappel [KAR1998] deduced from the asymptotic analyses that  $a_1 = 0.8839$  and  $a_2 = 0.6267$ .

To do the simulation of the dendritic growth, one needs to compute the value of  $\nabla W(\mathbf{n})$ ,  $\frac{\partial}{\partial x^*} \left( |\nabla \phi|^2 W(\mathbf{n}) \frac{\partial W(\mathbf{n})}{\partial (\partial_{x^*} \phi)} \right)$ ,  $\frac{\partial}{\partial y^*} \left( |\nabla \phi|^2 W(\mathbf{n}) \frac{\partial W(\mathbf{n})}{\partial (\partial_{y^*} \phi)} \right)$  and  $\frac{\partial}{\partial z^*} \left( |\nabla \phi|^2 W(\mathbf{n}) \frac{\partial W(\mathbf{n})}{\partial (\partial_{z^*} \phi)} \right)$ , derived from the anisotropy form of the interface,  $W(\mathbf{n})$ . We can write  $W(\mathbf{n})$  in different forms as defined in eq.(2.70) and eq(2.71) for 2D, eq(2.72) and eq(2.73) for 3D where  $\varepsilon_1$  and  $\varepsilon_2$  define the intensity of the anisotropy like  $\varepsilon_4$ . We compute  $\nabla W(\mathbf{n})$  numerically and for the others we have implemented their analytical derivation in our code to use it directly. The derivation forms are shown below in Table 2.1:

|                                          |                                                                                                                                                                                                                                                                                                                                                                                                                                                                                                                                                                                                                                                                                                             |
|------------------------------------------|-------------------------------------------------------------------------------------------------------------------------------------------------------------------------------------------------------------------------------------------------------------------------------------------------------------------------------------------------------------------------------------------------------------------------------------------------------------------------------------------------------------------------------------------------------------------------------------------------------------------------------------------------------------------------------------------------------------|
| Anisotropy<br>Expression $W(\mathbf{n})$ | Derivation terms $\frac{\partial}{\partial x^*} \left(  \nabla \phi ^2 W(\mathbf{n}) \frac{\partial W(\mathbf{n})}{\partial (\partial_{x^*} \phi)} \right)$                                                                                                                                                                                                                                                                                                                                                                                                                                                                                                                                                 |
| (2.70)                                   | $-\frac{\partial}{\partial x^*} (W(\mathbf{n}) (W(\mathbf{n}))' \partial_{y^*} \phi)$                                                                                                                                                                                                                                                                                                                                                                                                                                                                                                                                                                                                                       |
| (2.71)                                   | $\frac{\partial}{\partial x^*} \left( W(\mathbf{n}) W_0^* 4\varepsilon_4 \left[ \frac{4(\partial_{x^*} \phi)^3}{ \nabla \phi ^2} - \frac{(4\partial_{x^*} \phi) ((\partial_{x^*} \phi)^4 + (\partial_{y^*} \phi)^4)}{ \nabla \phi ^4} \right] \right)$                                                                                                                                                                                                                                                                                                                                                                                                                                                      |
| (2.72)                                   | $\frac{\partial}{\partial x^*} \left( W(\mathbf{n}) W_0^* 4\varepsilon_4 \left[ \frac{4(\partial_{x^*} \phi)^3}{ \nabla \phi ^2} - \frac{(4\partial_{x^*} \phi) ((\partial_{x^*} \phi)^4 + (\partial_{y^*} \phi)^4 + (\partial_{z^*} \phi)^4)}{ \nabla \phi ^4} \right] \right)$                                                                                                                                                                                                                                                                                                                                                                                                                            |
| (2.73)                                   | $W_0^* W(\mathbf{n}) \left[ 4\varepsilon_1 \left( \frac{\partial_{x^*} \phi^3}{ \nabla \phi ^2} - \frac{\partial_{x^*} \phi (\partial_{x^*} \phi^4 + \partial_{y^*} \phi^4 + \partial_{z^*} \phi^4)}{ \nabla \phi ^4} \right) \right] +$<br>$W_0^* W(\mathbf{n}) \left[ 12\varepsilon_2 \left( \frac{\partial_{x^*} \phi^3}{ \nabla \phi ^2} - \frac{\partial_{x^*} \phi (\partial_{x^*} \phi^4 + \partial_{y^*} \phi^4 + \partial_{z^*} \phi^4)}{ \nabla \phi ^4} \right) + 132\varepsilon_2 \left( \frac{\partial_{x^*} \phi \partial_{y^*} \phi^2 \partial_{z^*} \phi^2}{ \nabla \phi ^4} - \frac{3 \partial_{x^*} \phi^3 \partial_{y^*} \phi^2 \partial_{z^*} \phi^2}{ \nabla \phi ^6} \right) \right]$ |
| Anisotropy<br>expression $W(\mathbf{n})$ | Derivation terms $\frac{\partial}{\partial y^*} \left(  \nabla \phi ^2 W(\mathbf{n}) \frac{\partial W(\mathbf{n})}{\partial (\partial_{y^*} \phi)} \right)$                                                                                                                                                                                                                                                                                                                                                                                                                                                                                                                                                 |
| (2.70)                                   | $\frac{\partial}{\partial y^*} (W(\mathbf{n}) (W(\mathbf{n}))' \partial_{x^*} \phi)$                                                                                                                                                                                                                                                                                                                                                                                                                                                                                                                                                                                                                        |
| (2.71)                                   | $\frac{\partial}{\partial y^*} \left( W(\mathbf{n}) W_0^* 4\varepsilon_4 \left[ \frac{4(\partial_{y^*} \phi)^3}{ \nabla \phi ^2} - \frac{(4\partial_{y^*} \phi) ((\partial_{x^*} \phi)^4 + (\partial_{y^*} \phi)^4)}{ \nabla \phi ^4} \right] \right)$                                                                                                                                                                                                                                                                                                                                                                                                                                                      |
| (2.72)                                   | $\frac{\partial}{\partial y^*} \left( W(\mathbf{n}) W_0^* 4\varepsilon_4 \left[ \frac{4(\partial_{y^*} \phi)^3}{ \nabla \phi ^2} - \frac{(4\partial_{y^*} \phi) ((\partial_{x^*} \phi)^4 + (\partial_{y^*} \phi)^4 + (\partial_{z^*} \phi)^4)}{ \nabla \phi ^4} \right] \right)$                                                                                                                                                                                                                                                                                                                                                                                                                            |
| (2.73)                                   | $W_0^* W(\mathbf{n}) \left[ 4\varepsilon_1 \left( \frac{\partial_{y^*} \phi^3}{ \nabla \phi ^2} - \frac{\partial_{y^*} \phi (\partial_{x^*} \phi^4 + \partial_{y^*} \phi^4 + \partial_{z^*} \phi^4)}{ \nabla \phi ^4} \right) \right] +$<br>$W_0^* W(\mathbf{n}) \left[ 12\varepsilon_2 \left( \frac{\partial_{y^*} \phi^3}{ \nabla \phi ^2} - \frac{\partial_{y^*} \phi (\partial_{x^*} \phi^4 + \partial_{y^*} \phi^4 + \partial_{z^*} \phi^4)}{ \nabla \phi ^4} \right) + 132\varepsilon_2 \left( \frac{\partial_{x^*} \phi^2 \partial_{y^*} \phi \partial_{z^*} \phi^2}{ \nabla \phi ^4} - \frac{3 \partial_{x^*} \phi^2 \partial_{y^*} \phi^3 \partial_{z^*} \phi^2}{ \nabla \phi ^6} \right) \right]$ |
| Anisotropy<br>expression $W(\mathbf{n})$ | Derivation terms $\frac{\partial}{\partial z^*} \left(  \nabla \phi ^2 W(\mathbf{n}) \frac{\partial W(\mathbf{n})}{\partial (\partial_{z^*} \phi)} \right)$                                                                                                                                                                                                                                                                                                                                                                                                                                                                                                                                                 |
| (2.70)                                   | -                                                                                                                                                                                                                                                                                                                                                                                                                                                                                                                                                                                                                                                                                                           |
| (2.71)                                   | -                                                                                                                                                                                                                                                                                                                                                                                                                                                                                                                                                                                                                                                                                                           |
| (2.72)                                   | $\frac{\partial}{\partial z^*} \left( W(\mathbf{n}) W_0^* 4\varepsilon_4 \left[ \frac{4(\partial_{z^*} \phi)^3}{ \nabla \phi ^2} - \frac{(4\partial_{z^*} \phi) ((\partial_{x^*} \phi)^4 + (\partial_{y^*} \phi)^4 + (\partial_{z^*} \phi)^4)}{ \nabla \phi ^4} \right] \right)$                                                                                                                                                                                                                                                                                                                                                                                                                            |
| (2.73)                                   | $W_0^* W(\mathbf{n}) \left[ 4\varepsilon_1 \left( \frac{\partial_{z^*} \phi^3}{ \nabla \phi ^2} - \frac{\partial_{z^*} \phi (\partial_{x^*} \phi^4 + \partial_{y^*} \phi^4 + \partial_{z^*} \phi^4)}{ \nabla \phi ^4} \right) \right] +$<br>$W_0^* W(\mathbf{n}) \left[ 12\varepsilon_2 \left( \frac{\partial_{z^*} \phi^3}{ \nabla \phi ^2} - \frac{\partial_{z^*} \phi (\partial_{x^*} \phi^4 + \partial_{y^*} \phi^4 + \partial_{z^*} \phi^4)}{ \nabla \phi ^4} \right) + 132\varepsilon_2 \left( \frac{\partial_{x^*} \phi^2 \partial_{y^*} \phi^2 \partial_{z^*} \phi}{ \nabla \phi ^4} - \frac{3 \partial_{x^*} \phi^2 \partial_{y^*} \phi^2 \partial_{z^*} \phi^3}{ \nabla \phi ^6} \right) \right]$ |

Table 2.1 Analytical derivation for the anisotropy expression needed for the phase-field simulations

## 2.2 Numerical resolution

We present here the numerical methods used to solve the phase-field equation and the energy conservation equation. The finite element method (FEM) is used for the spatial discretization and the Galerkin method for the approximation, with SUPG stabilization techniques. First order simplex elements are used (triangles P1) and we compute a metric defined to obtain an unstructured anisotropic adaptive mesh. Parallel computations reduce the computational time and time step adaptation and a variation of the number of elements used in the mesh during computation, improve simulations. The numerical methods are implemented in the C++ based library, CimLib, developed at CEMEF.

### 2.2.1 Finite element solver

#### Galerkin classical formulation

The weak formulation of the problem is presented here [HAC2009].

The FEM is distinguished from other methods because it is more capable of dealing with complex geometries, and it allows the use of non structured grids and more natural imposition of the boundary conditions. The principle of the FEM consists first in decomposing the spatial domain under consideration into a set of elements of arbitrary shape and size. This decomposition is commonly called a grid or a mesh, as shown in Figure 2.3.

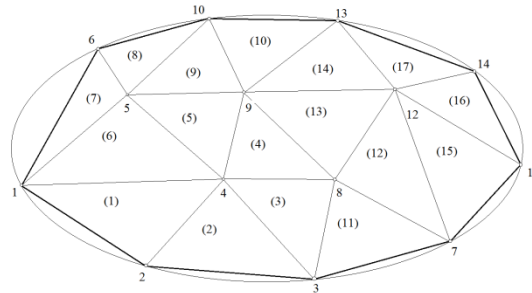


Figure 2.3 Schematic example of a two dimensional mesh composed of triangles with different sizes [RAP2003].

In the phase-field equation, eq(2.30),  $W^2(\mathbf{n})$  depends on  $\phi$  through eq (2.19) or (2.20). Equation (2.30) is developed as follows:

$$\begin{aligned} \tau(\mathbf{n}) \frac{\partial \phi}{\partial \tau} - W^2(\mathbf{n}) \Delta \phi - 2 W(\mathbf{n}) \nabla W(\mathbf{n}) \nabla \phi = [\phi - \lambda \theta (1 - \phi^2)] (1 - \phi^2) + \frac{\partial}{\partial x^*} \left( |\nabla \phi|^2 W(\mathbf{n}) \frac{\partial W(\mathbf{n})}{\partial (\partial_{x^*} \phi)} \right) \\ + \frac{\partial}{\partial y^*} \left( |\nabla \phi|^2 W(\mathbf{n}) \frac{\partial W(\mathbf{n})}{\partial (\partial_{y^*} \phi)} \right) + \frac{\partial}{\partial z^*} \left( |\nabla \phi|^2 W(\mathbf{n}) \frac{\partial W(\mathbf{n})}{\partial (\partial_{z^*} \phi)} \right) \end{aligned} \quad (2.35)$$

For a matter of simplicity, we note  $C = -2 W(\mathbf{n}) \nabla W(\mathbf{n}) / \tau(\mathbf{n})$ ,  $D = W^2(\mathbf{n}) / \tau(\mathbf{n})$ , and  $f =$  ‘‘Source term’’ the right hand side of the equation (2.35). The strong formulation for our problem can be generally written as:

$$\begin{aligned} \frac{\partial \phi}{\partial \tau} + C \cdot \nabla \phi - \nabla \cdot (D \cdot \nabla \phi) = f \quad \text{in } \Omega \times (0, T) \\ \phi(x^*, 0) = \phi_0 \quad \text{in } \Omega \end{aligned} \quad (2.36)$$

The same solver is used for the energy equation (2.15), since one may show that we have the same type of equation, the only difference being that  $C = 0$  in this last case. In order to solve the equations using the FEM, we may define: the Sobolev space,  $H^1(\Omega)$ , of functions with square integrable derivatives; the Lebesgue space,  $L^2(\Omega)$ ;  $H_0^1(\Omega)$ , the space of functions in  $H^1(\Omega)$  with vanishing values on the boundary  $\partial\Omega$ ;  $L^\infty(\Omega)$ , a space that contains measurable bounded functions. Hence,

$$\begin{aligned} H^1(\Omega) &= \{ \psi \in L^2(\Omega), \nabla \psi \in L^2(\Omega) \} \\ L^2(\Omega) &= \{ \psi, \int_{\Omega} \psi^2 d\Omega < \infty \} \\ H_0^1(\Omega) &= \{ \psi \in H^1(\Omega), \psi = 0 \text{ on } \partial\Omega \} \\ L^\infty(\Omega) &= \{ \psi, \psi(x^*) \leq \text{cte } \forall x^* \} \end{aligned} \quad (2.37)$$

The weak formulation can be written as: find  $\phi \in V := H_0^1(\Omega) / \forall \psi \in V$  such that:

$$\frac{\partial \phi}{\partial \tau} \psi + C \cdot \nabla \phi \psi - D \Delta \phi \psi = f \psi \quad (2.38)$$

Integrating over  $\Omega$  leads to.

$$\int_{\Omega} \frac{\partial \phi}{\partial \tau} \psi dV + \int_{\Omega} C \cdot \nabla \phi \psi dV - \int_{\Omega} D \Delta \phi \psi dV = \int_{\Omega} f \psi dV \quad (2.39)$$

We know that using the Green formula, we have:

$$- \int_{\Omega} \Delta \phi D \psi dV = \int_{\Omega} \nabla \phi \nabla (D \psi) dV - \int_{\partial\Omega} \frac{\partial \phi}{\partial \mathbf{n}} \cdot D \psi dS = \int_{\Omega} \nabla \phi \nabla (D \psi) dV \quad (2.40)$$

Since  $\frac{\partial \phi}{\partial \mathbf{n}} = \langle \nabla \phi, \mathbf{n} \rangle = 0$  on  $\partial\Omega$ , the integration becomes:

$$\int_{\Omega} \frac{\partial \phi}{\partial \tau} \psi dV + \int_{\Omega} C \cdot \nabla \phi \psi dV + \int_{\Omega} D \nabla \phi \nabla \psi dV = \int_{\Omega} f \psi dV \quad (2.41)$$

The weak formulation can be written clearly as: for a given  $f \in H^{-1}(\Omega)$  and  $C, D \in L^\infty(\Omega)$ , find  $\phi \in V := H_0^1(\Omega)$ , such that

$$\left( \frac{\partial \phi}{\partial \tau}, \psi \right) + (C \cdot \nabla \phi, \psi) + (D \nabla \phi, \nabla \psi) = (f, \psi)_{H_0^1(\Omega)} \quad (2.42)$$

For the spatial discretization, let us consider the finite element mesh  $\mathcal{T}_h$ , triangulating  $\Omega$  into a set of  $N_{el}$  elements  $K$ , such that they cover the domain and are either disjointed or share a complete edge. Using this partition, the above defined functional space  $V$  can be approached by a finite dimensional space  $V_h$ , spanned by continuous piecewise polynomials. Thus,

$$V_h = \{ \psi^h \in H_0^1(\Omega), \psi^h \text{ is linear for } \forall K \in \mathcal{T}_h \} \quad (2.43)$$

The Galerkin discrete problem consists now in finding  $\phi^h \in V_h$  such that:

$$\left( \frac{\partial \phi^h}{\partial \tau}, \psi^h \right) + (C \cdot \nabla \phi^h, \psi^h) + (D \nabla \phi^h, \nabla \psi^h) = (f, \psi^h) \quad (2.44)$$

Rewriting it in the integral form:

$$\int_{\Omega} \frac{\partial \phi^h}{\partial \tau} \psi^h dV_h + \int_{\Omega} C \cdot \nabla \phi^h \psi^h dV_h + \int_{\Omega} D \nabla \phi^h \nabla \psi^h dV_h = \int_{\Omega} f \psi^h dV_h \quad (2.45)$$

Each integral is the sum over the element of  $\Omega$ . The equation can be written as:

$$\begin{aligned} \sum_{e=1}^{N_{el}} \int_{\Omega_e} \frac{\partial \phi^h}{\partial \tau} \psi^h dV_h + \sum_{e=1}^{N_{el}} \int_{\Omega_e} C \cdot \nabla \phi^h \psi^h dV_h + \sum_{e=1}^{N_{el}} \int_{\Omega_e} D \nabla \phi^h \nabla \psi^h dV_h = \\ \sum_{e=1}^{N_{el}} \int_{\Omega_e} f \psi^h dV_h \end{aligned} \quad (2.46)$$

Since we are using the first order linear triangle element, we can replace  $\phi^h = \sum_{i=1}^N \phi_i^h N_i$  and

$\nabla \phi^h = \sum_i \phi_i^h \nabla N_i$ . Taking  $(N_i)_{i=1, \dots, N}$ , the finite element vector space basis,  $\phi_i^h$ , are computed

locally in each node of the triangle element.

$$\begin{aligned} \sum_{e=1}^{N_{el}} \int_{\Omega_e} \sum_{i=1}^N \frac{\partial \phi_i^h}{\partial \tau} N_i N_j dV_h + \sum_{e=1}^{N_{el}} \int_{\Omega_e} \sum_{i=1}^N C \cdot \phi_i^h \nabla N_i N_j dV_h + \sum_{e=1}^{N_{el}} \int_{\Omega_e} \sum_{i=1}^N D \phi_i^h \nabla N_i \nabla N_j dV_h \\ = \sum_{e=1}^{N_{el}} \int_{\Omega_e} f N_j dV_h \end{aligned} \quad (2.47)$$

We write this last equation as:

$$\begin{aligned} \sum_{e=1}^{N_{el}} \int_{\Omega_e} N_i N_j dV_h \sum_{i=1}^N \frac{\partial \phi_i^h}{\partial \tau} + \sum_{e=1}^{N_{el}} \int_{\Omega_e} C \cdot \nabla N_i N_j dV_h \sum_{i=1}^N \phi_i^h + \sum_{e=1}^{N_{el}} \int_{\Omega_e} D \nabla N_i \nabla N_j dV_h \sum_{i=1}^N \phi_i^h \\ = \sum_{e=1}^{N_{el}} \int_{\Omega_e} f N_j dV_h \end{aligned} \quad (2.48)$$

By simplifying the sum we obtain:

$$\begin{aligned} \sum_{e=1}^{N_{el}} \int_{\Omega_e} N_i N_j dV_h \frac{\partial \phi^h}{\partial \tau} + \sum_{e=1}^{N_{el}} \int_{\Omega_e} C \cdot \nabla N_i N_j dV_h \phi^h + \sum_{e=1}^{N_{el}} \int_{\Omega_e} D \nabla N_i \nabla N_j dV_h \phi^h \\ = \sum_{e=1}^{N_{el}} \int_{\Omega_e} f N_j dV_h \end{aligned} \quad (2.49)$$

The linear matrix system reads, after assembly of the element matrices, a system of first order differential equations:

$$M_m \dot{\Phi} + K_c \Phi + K_d \Phi = F \quad (2.50)$$

where  $\Phi$  is the vector of nodal unknowns,  $M_m$  is the mass matrix,  $K_c$  is the stiffness matrix issued from the conductive term,  $K_d$  is the stiffness matrix generated from the diffusive term and  $F$  is the term load vector. The finite element matrix equations must be solved with an

appropriate set of boundary conditions. The coefficient matrices and load vector are defined as follows:

$$M_m = \mathbf{A} \int_{K_e}^{N_{el}} N_i N_j dK$$

$$K_c = \mathbf{A} \int_{K_e}^{N_{el}} C \nabla N_i N_j dK$$

$$K_d = \mathbf{A} \int_{K_e}^{N_{el}} D \nabla N_i \nabla N_j dK$$

$$F = \mathbf{A} \int_{K_e}^{N_{el}} f N_j dK$$

$\mathbf{A}$  is the matrix assembly operator defined such that one has:  $K = \mathbf{A} \int_{K_e}^{N_{el}} K_e$ , where  $K$  is an element and  $K_e$  is a sub-element.

### SUPG stabilization method

The original SUPG method was first designed for the steady version as a method to avoid the numerical oscillations found using the Galerkin approach when the diffusion term is small (mainly in convection dominated problems).

Let us apply the backward implicit Euler method to equation (2.44): given  $\phi^n$ , find  $\phi^{n+1}$  satisfying the boundary conditions and  $\forall \psi^h \in V_h$  such that

$$\left( \frac{\phi_h^{n+1}}{\Delta \tau}, \psi^h \right) + (C \cdot \nabla \phi_h^{n+1}, \psi^h) + (D \nabla \phi_h^{n+1}, \nabla \psi^h) = \left( \frac{\phi_h^n}{\Delta t}, \psi^h \right) + \langle f, \psi^h \rangle \quad (2.51)$$

One may add a streamline upwind perturbation, acting in the flow direction, to the test function:

$$\tilde{\psi}^h = \psi^h + C \cdot \tau_K \nabla \psi^h \quad (2.52)$$

Where the parameter  $\tau_K$ , is often called ‘intrinsic time’ which can determine and calibrate the amount of upwinding weighting locally in each element.

Inserting it in equation (2.51), its stabilized form becomes:

$$\begin{aligned} \left( \frac{\phi_h^{n+1}}{\Delta \tau}, \psi^h \right) + (C \cdot \nabla \phi_h^{n+1}, \psi^h) + (D \nabla \phi_h^{n+1}, \nabla \psi^h) + \sum_K (\mathcal{R}(\phi^h), \tau_K C \cdot \nabla \psi^h) \\ = \left( \frac{\phi_h^n}{\Delta t}, \psi^h \right) + \langle f, \psi^h \rangle \end{aligned} \quad (2.53)$$

In this equation,  $\mathcal{R}(\phi^h)$  is the appropriate residual of the finite element components  $\phi^h$ . We can see that this method is consistent in the sense that the additional stabilizing term is zero if  $u^h$  is the solution of the continuous equation.

$$S^{\text{SUPG}} = \sum_K (\mathcal{R}(\phi^h), \tau_K C \nabla \psi^h) = \sum_K \tau_K \left( \frac{\phi_h^{n+1}}{\Delta \tau} + C \cdot \nabla \phi_h^{n+1} - D \Delta \phi_h^{n+1} - \frac{\phi_h^n}{\Delta t} - f, C \nabla \psi^h \right)_K \quad (2.54)$$

This method has been used in convection dominated problems by introducing the streamline diffusion in the context of weighted residual methods. The added stabilizing terms are indicated by a subscript  $K$  which denotes integration over the element. Note that the third term vanishes in (2.54) when using linear interpolations. We still have to define how to compute the parameter  $\tau_K$ .

A computation of  $\tau_K$  is often proposed on the basis of the convergence and error analysis of the method. The definition of the stabilization parameters directly implemented in our finite element code is [HAC2009]:

$$\tau_K = \frac{h}{2 \|C\|} \xi(Pe) \quad (2.55)$$

where  $\xi(Pe)$ , a function of the Péclet number  $Pe = \|C\| h / 2 \alpha^*$ , is derived from nodal exactness as:

$$\xi(Pe) = \max \left( \frac{1}{\tanh(Pe)} - \frac{1}{Pe}; 1 \right) \quad (2.56)$$

$h$  is defined for each element as:

$$h = \left( \sum_j^{N_j} \frac{C_i}{\|C\|} \frac{\partial N_j}{\partial x_i} \right)^{-1} \quad \text{with} \quad \|C\| = \sqrt{\sum_{i=1}^2 C_i^2} \quad (2.57)$$

$C_i$  is the  $i$  coordinate of the vector  $C$ .  $N_j$  is the basis function associated with the local node  $j$ . The linear system of equations issuing from the discretization is solved implicitly using the conjugate bi gradient-least squares method (BCGSL). There is also preconditioning to the resolution using the Jacobi method with incomplete factorization LU per block of size 2. For that, the PETSC library [BAL2015] has been interfaced with Cimlib.

### 2.2.2 Mesh adaptation

The mesh is initially (and throughout time) adapted using a topological mesher [COU2011], [COU2014] based on a metric field and given at the nodes of the mesh.  $M$  is a unit metric field associated with any unstructured mesh, built using the affine transformation to a reference element in a Riemanian space which has to be equilateral of edge length equal to unity. It provides both the size and the stretching of the elements. In our case, this field can be computed using the edge vectors of the mesh,  $X_{ij} = X_j - X_i$ ,  $i$  and  $j$  being the extreme nodes of the edge. Starting from an existing mesh, the new nodal metrics field  $M_i$ , computed and given to the mesher, is:

$$M_i = \left( \frac{1}{q} \sum_j^{\Gamma(i)} s_{ij}^2 X_{ij} \otimes X_{ij} \right)^{-1} \quad (2.58)$$

$q$  being the space dimension,  $\Gamma(i)$  being the set of nodes connected to node  $i$ .  $s_{ij}$  is the stretching factor applied to obtain the new edge size. The edge stretching factor,  $s_{ij}$ , is obtained from the *a posteriori* estimated error, and is given by

$$s_{ij} = (\mathcal{A}/e_{ij})^{1/p} \quad (2.59)$$

where  $e$  represents the committed edge error and  $p$  a stretching exponent,  $1 < p < q$ . A constraint is applied here for the choice of  $s_{ij}$  based on  $h_{min}$ , the minimal mesh size,  $s_{ij} = \min\left(s_{ij}; \frac{\sqrt{h_{ij}}}{h_{min}}\right)$  with  $h_{ij} = \frac{\|\mathbf{X}_{ij}\|}{(i,j)}$ . Starting from a given element, we examine what information we can construct from the set of edges. Since more than only two edges can be encountered for a node, it is necessary then to find an approximation or an averaging process of the information. For this reason, they first state that the length size of the edges sharing a given node is exactly the interpolation of the continuous length distribution function defined in the space at the considered point. Using this,  $\Lambda$  is given by the error along and in the direction of each edge  $e_{ij}$ ,

$$\Lambda = \left( \sum_i \sum_j^{\Gamma(i)} e_{ij}^{\frac{p}{p+2}} / NE_M \right)^{\frac{p+2}{p}} \quad (2.60)$$

$NE$  is the number of elements,  $NE_M$  is the number of edges and it is defined as  $NE_M = NE \times 3 \times 2$  in 2D and  $NE_M = NE \times 4 \times 3$  in 3D. The error is computed using the recovered gradient of the solution on which we wish to adapt (phase field, temperature, composition, or all). In the case of temperature and phase-field computation, we construct a solution vector ( $\xi = (\phi, \theta)$ ) which contains the fields to adapt with and we compute its gradient.

In fact,  $e_{ij} = \max(|\nabla \xi \cdot \mathbf{X}_{ij}|; e_{min} |\mathbf{X}_{ij}|^2)$  and  $\nabla \xi = (\mathbf{X}_i)^{-1} \cdot \xi_i$ , where  $\mathbf{X}_i = \frac{1}{|\Gamma(i)|} \sum_j^{\Gamma(i)} \mathbf{X}_{ij} \otimes \mathbf{X}_{ij}$  is the

edge length distribution tensor and  $\xi_i = \sum_j^{\Gamma(i)} \xi_{ij} \mathbf{X}_{ij}$ .  $e_{min}$  is a chosen constant.

Figure 2.4 illustrates this metric field construction through an example on adaptation on a phase-field function defining a circle. One may observe that mesh sizes are smaller at the interface and larger outside. In this figure, the red color represents the solid, the blue one represents the liquid, the green one is the thickness of the interface and the black one represents the  $s/l$  interface.

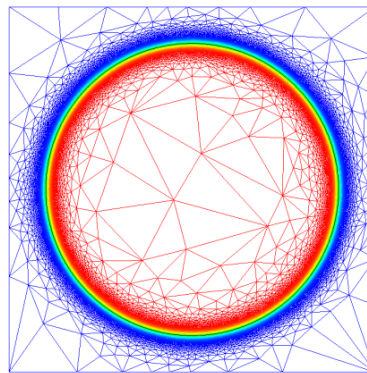


Figure 2.4 Example of mesh adaptation on a circle shape of radius 0.4, using only  $\phi$  (which defines the circle inner and outer parts) as the field for error estimation. In this example, the domain size is  $[0;1] \times [0;1]$ ,  $e_{min} = 10^{-9}$ ,  $h_{min} = 0.001$ ,  $NE = 50\,000$ ,  $W_0^* = 0.005$  and  $R_0 = 0.4$ .

In this adaptation loop, the thickness  $W_0^*$  will be important, because it provides the measure of the recovered gradient. To control the adaptation and the value of the metric field, other

parameters are provided:  $h_{min}$ , the minimum mesh size;  $e_{min}$  for computing the error  $e_{ij}$  by imposing a minimum error so that one controls the background mesh size; the number of elements  $NE$ , because error minimization is performed under this constraint.

To see the influence of the thickness  $W_0^*$ , let us consider a domain size of  $[0;1] \times [0;1]$ , with an initial seed of  $R_0 = 0.05$ , Figure 2.5 shows the difference between the mesh for three different values, showing that it follows well this parameter. When  $W_0^*$  increases, the interface thickness also increases and so does the green zone (varying one between maximum and minimum values).

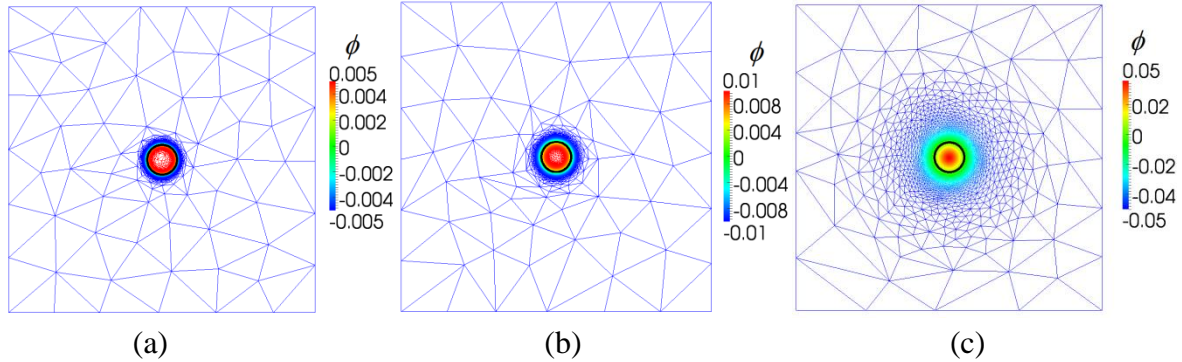


Figure 2.5 Adapted mesh with  $NE = 20\,000$ ,  $e_{min} = 10^{-4}$ ,  $h_{min} = 0.001$  for different interface thicknesses, (a)  $W_0^* = 0.005$ , (b)  $W_0^* = 0.01$ , (c)  $W_0^* = 0.05$ .

In what concerns the other referred numerical parameters, when the total number of elements is increased, the mesh is enriched around the interface as well as outside the circle, as illustrated in Figure 2.6. If we continue increasing the number of elements, the mesh size outside the interface thickness will continue decreasing. Adaptation thus begins enriching there because the computed error around the interface has reached its objective.

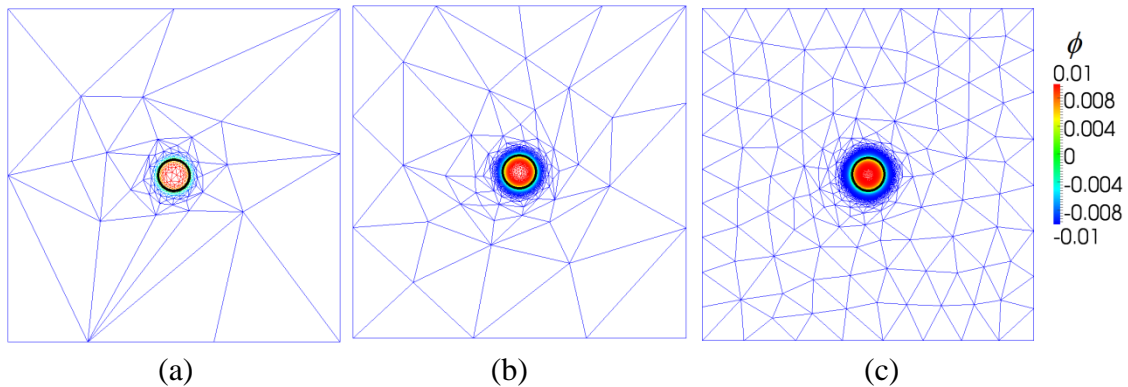


Figure 2.6 Adapted mesh with  $e_{min} = 10^{-4}$ ,  $h_{min} = 0.001$ ,  $W_0^* = 0.01$  for different number of elements, (a)  $NE = 1000$ , (b)  $NE = 10\,000$ , (c)  $NE = 40\,000$

In Figure 2.7, the influence of the value of  $e_{min}$ , which controls the background mesh size is illustrated, showing that the mesh size outside the interface thickness increases when this parameter decreases.

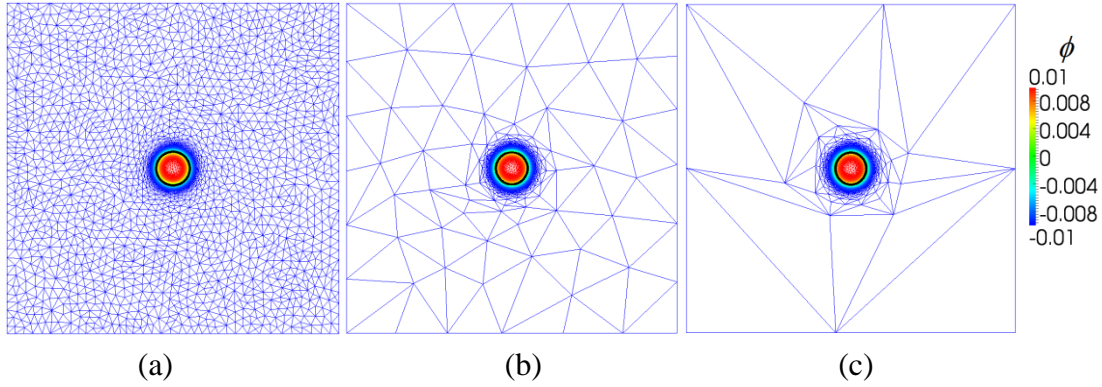


Figure 2.7 Adapted mesh with  $NE = 20\,000$ ,  $h_{min} = 0.001$ ,  $W_0^* = 0.01$  for different background errors, a)  $e_{min} = 10^{-1}$ , b)  $e_{min} = 10^{-4}$ , c)  $e_{min} = 10^{-9}$

In Figure 2.8, the influence of the value of  $h_{min}$ , which controls the mesh size at the interface is illustrated, showing that when  $h_{min}$  is smaller or equal to  $W_0^*$ , the circle is well represented and when it decreases, more elements are added at the interface. When  $h_{min}$  is bigger than  $W_0^*$  some big elements are at the interface which are not sufficient to represent the circle. Instead we have a square, which is a bad representation.

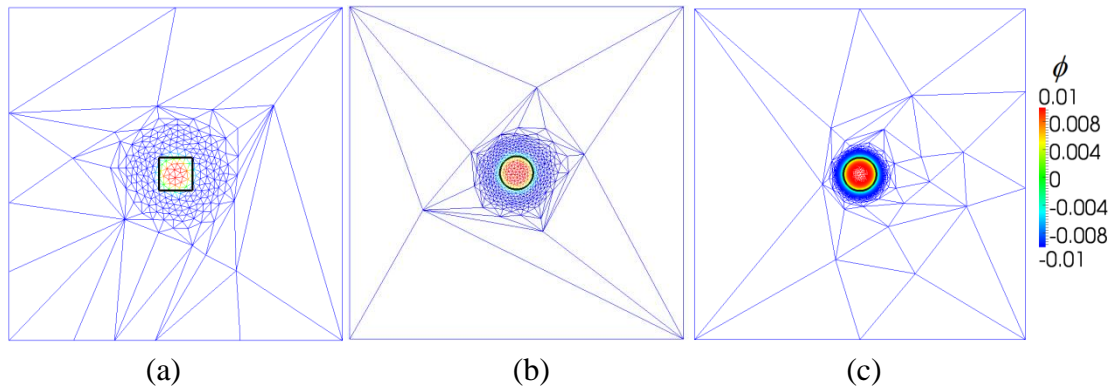


Figure 2.8 Adapted mesh with  $NE = 20\,000$ ,  $e_{min} = 10^{-9}$ ,  $W_0^* = 0.01$  for different minimal mesh size, a)  $h_{min} = 0.02$ , b)  $h_{min} = 0.01$ , c)  $h_{min} = 0.001$ .

We have studied the influence of  $h_{min}$  by using an example of a growing circle under a constant radial velocity, equal to 0.02. We have considered a computational domain of size of  $[0;1] \times [0;1]$ , with a geometry of the circle defining the interface;  $\text{Circle}(O, R_0)$ , with  $O(0.5;0.5)$ ,  $e_{min} = 10^{-4}$  and  $R_0 = 0.05$ . The relative error between the analytical radius and the numerical one was computed while growing and compared (Figure 2.9).

Here, we plot the relative error evolution with time, computed as:

$$\text{Relative error} = \frac{|\text{Analytical radius} - \text{Numerical radius}|}{\text{Analytical radius}} \quad (2.61)$$

Initially, an anisotropic mesh has been built, which consists of triangular elements with different sizes, Figure 2.7.b.

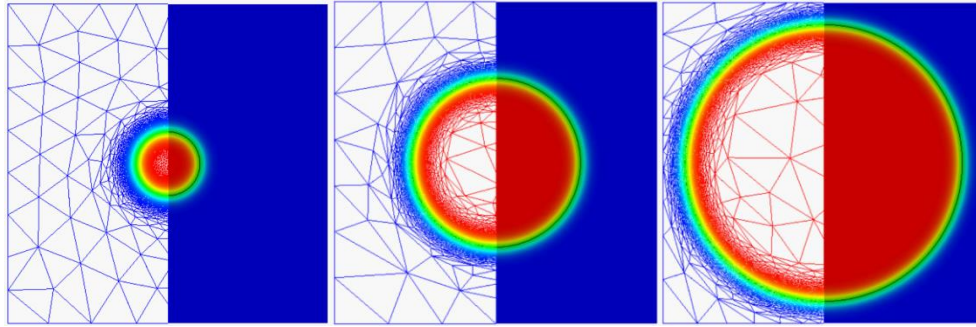


Figure 2.9 Growth of a circular seed with a constant radial velocity equal to 0.02, with mesh adaptation on the circle position, given by a phase-field function  $\phi$  at  $\tau = 0$ ,  $\tau = 0.2$ ,  $\tau = 0.45$ , with  $NE = 20\ 000$ ,  $h_{min} = 0.001$ ,  $W_0^* = 0.01$  and  $\Delta\tau = 0.01$ .

One may observe that the error on the position capture decreases when increasing the number of nodes, as shown in Figure 2.10, where the error converges with  $NE = 20\ 000$  and  $40\ 000$ . To see the influence of  $h_{min}$ , we trace the blue line, the case of  $NE = 20\ 000$  and we start from the same case with  $W_0^* = 0.01$ ,  $h_{min} = 0.001$ , as seen in Figure 2.10.(a). When decreasing the value of  $h_{min}$  the error decreases, as seen in Figure 2.10.(b). If we take a small  $h_{min}$  and we increase  $W_0^*$ , we will have more elements to represent the interface and the error decreases more, because it is well represented, as seen in Figure 2.11 Figure 2.10.(c).

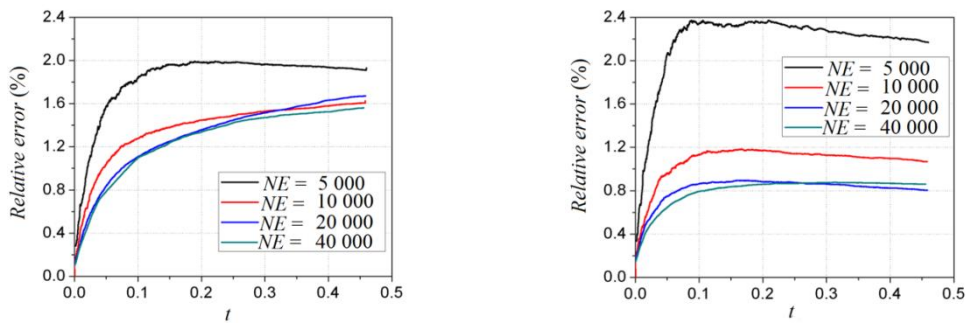


Figure 2.10 Error evolution on the position capture during the growth of a circle, with  $W_0^* = 0.01$ ,  $h_{min} = 0.001$  and with different number of required elements, error measured using the radius (a) in the direction of a  $0^\circ$  angle, (b) in the direction of a  $45^\circ$  angle.

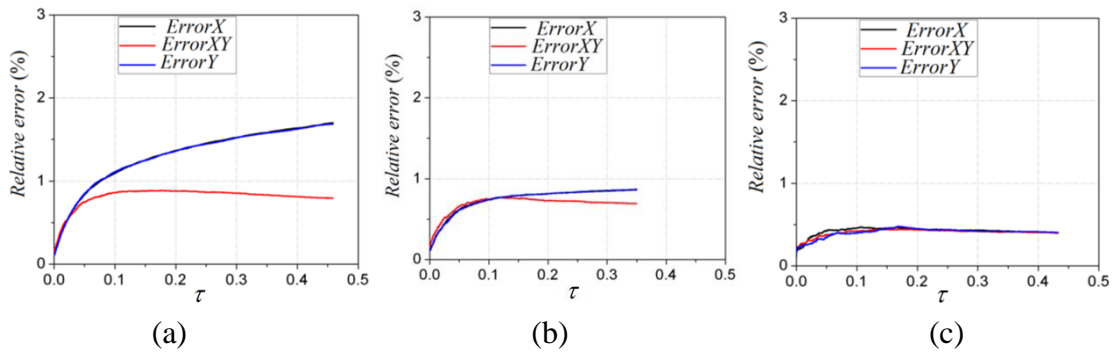


Figure 2.11 Error evolution measured in the directions of  $0^\circ$  (*ErrorX*),  $45^\circ$  (*ErrorXY*) and  $90^\circ$  (*ErrorY*) with  $NE = 20\ 000$ , (a)  $W_0^* = 0.01$  and  $h_{min} = 0.001$ , (b)  $W_0^* = 0.01$  and  $h_{min} = 0.0005$ , (c)  $W_0^* = 0.05$  and  $h_{min} = 0.0005$ .

For a matter of CPU time optimization, we have defined a remeshing frequency, which introduces one other numerical parameter,  $FR$ . To compute it in an appropriate way, we use the estimated velocity, inspired from the Gibbs-Thomson velocity, neglecting  $\beta$ , over the entire domain as:

$$v_{tip} = \max(-\theta - d_0 K) \quad (2.62)$$

with  $d_0 = \frac{a_1 W(\mathbf{n})}{\lambda}$ , where  $K = \nabla_T \cdot \mathbf{n}$  is the curvature,  $\nabla_T$  is the tangential divergence and  $\mathbf{n}$  the outward unit normal to the interface,  $\mathbf{n} = -\frac{\nabla \phi}{\|\nabla \phi\|}$ .

One may also compute the velocity at the interface directly in the computation, as

$$v_{tip} = \max\left(\delta_\phi \frac{\partial \phi / \partial t}{\partial \phi / \partial x}\right) \quad (2.63)$$

where  $\delta_\phi$  is a dirac function, given by  $\delta_\phi = \begin{cases} 0 & \text{if } \phi > \varepsilon_\phi \\ \frac{1}{2\varepsilon_\phi} & \text{if } \phi \in [-\varepsilon_\phi; \varepsilon_\phi] \\ 0 & \text{if } \phi < -\varepsilon_\phi \end{cases}$

Comparison of these two velocities showed that the estimation was bigger than the directly computed velocity.

To obtain  $FR$ , the displacement  $v_{tip} \cdot \Delta t$  is computed and added to the displacements of the previous time steps. When the sum of the displacements exceeds  $3W_0^*/2$  (half the green zone at the interface, that is equal to  $3W_0^*$ ), mesh adaptation is activated.

### 2.2.3 Parallel computing

We use parallel computation to do our simulations and reduce the computational time. We explain here how we use the memory in parallel to subdivide the job between many cores. There are two methods to perform parrallelization:

- a shared memory model, using OpenMP;
- a distributed memory model, the two standards being PVM (Parallel Virtual Machine) and MPI (Message Passing Interface).

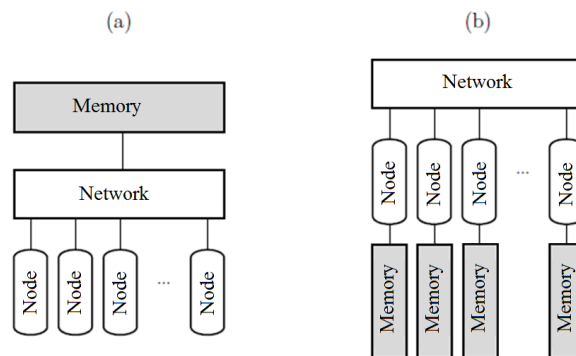


Figure 2.12 Two management models for Parallel use of memory: (a) shared, where memory is in common for all compute nodes and (b) distributed, where memory is managed independently by each node, according to [DIG2001].

Shared memory management, presented in Figure 2.12(a), allows a unique space addressing: each computing unit, or "core", can access a common centralized memory. Cores are physically grouped into nodes. The nodes are similar to conventional servers linked to the network, and typically contain a few tens of cores. Modifications of a core in the memory are directly visible by all other units. This is a simple way to parallelize a calculation code, but is restricted to shared memory machines. These are usually limited to less than 32 cores. Note also that the calculation code is parallelized semi-automatically by the compiler, which can do so on pieces of relatively simple codes. The management of the so-called distributed memory, presented in Figure 2.12(b) separates the contrary memory between compute nodes. The addressing space is multiple, that means each computing unit will have its own memory that may change independently. PVM and MPI standards are based on the one-time exchange of messages between the computing units, which must be explicitly specified by the programmer. This leaves a lot of flexibility in the design of code that can be optimized to perfection. This is the best approach today to better performance and massively parallel computing. It is more complex to implement because the programmer itself must manage and optimize communications between the cores.

Here, we will use the MPI based implementation developed by [DIG2001], [DIG2003] to solve our equations and for the representation of the dendritic growth. CIMLib contains a mesh partitioning/ repartitioning algorithm called MeshMigration, that allows to balance well the number of mesh entities (vertices or elements) per processor [MES2009].

It is important to notice that in the script files used there is no reference to any parallel instruction. The user has only to specify over how much processors he wants to run using the traditional "mpirun" command.

In what concerns meshing, we use a sequential mesher MTC [COU2000a] and it is partitioned in several sub-domains. The chosen parallelization procedure uses the sequential mesher in a massive parallel context, by following an iterative two successive steps procedure [COU2000b]: independent adaptive meshing of each subdomain with blocked interfaces; constrained repartitioning and interface displacement. When a good quality mesh is obtained, a finite element load-balancing repartitioning step is performed. All fields defined on the initial mesh may then be mapped on the new one.

For linear system resolution, parallelization has been performed by interfacing the parallel partitionner with the PETSc library [BAL2015] and also by applying a multi-grid preconditionner. Figure 2.14 shows this strategy applied to a simple square with 4 processors.

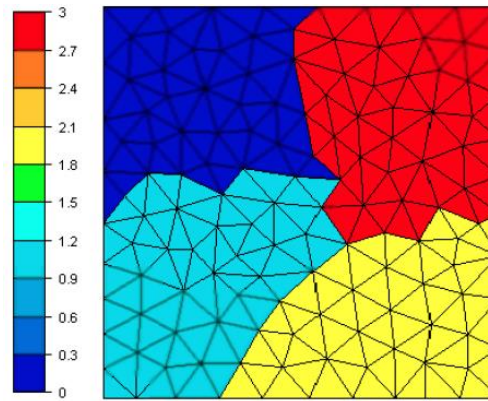


Figure 2.13 Illustration of the strategy used to parallelize the mesher. We have here the partition of the domain [DIG2003] H.Digonnet, T. Coupez, «Object-oriented programming for "fast and easy" development of parallel applications in forming processes simulation», *2nd MIT Conference on Computational Fluid and Solid Mechanics*, pp.1922-1924, 2003 [DIG2007].

For complex 3D geometries and complex physical laws, parallel computation remains essential. It allows us to run complete simulations with a reasonable precision, inaccessible (for memory and time limits) with sequential runs. It also makes possible to speed up the simulation run such that the global computation time will still be acceptable. In the last years, processor's performance has not increased by improving the clock rate but by multiplying the number of cores in a CPU. Most of the computation time is spent on remeshing and on the resolution of several large linear systems.

#### 2.2.4 Validation on benchmark: temperature diffusion in a corner

To validate the coupled phase-field and energy solvers, let us consider the example of the temperature diffusion in a corner [RAT1971], as shown in Figure 2.14. We study in this example a Stephan problem (which is a free boundary problem) for controlled heat flow.

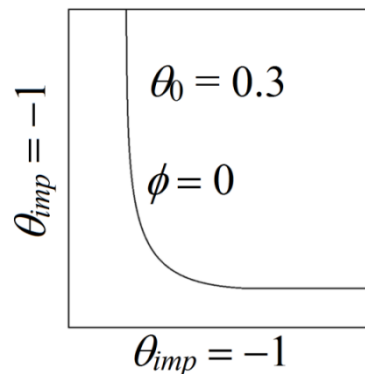


Figure 2.14 Representation of a square domain with an initial temperature  $\theta_0 = 0.3$  cooled from its left corner with an imposed temperature  $\theta_{imp} = -1$  at its left and bottom boundaries.

The square domain  $[0;1] \times [0;1]$  is defined and composed of a mesh with 20 000 elements. Mesh adaptation depends on  $\phi$  and  $\theta$  and the phase-field function used here,

$\phi = E \tanh\left(\frac{\eta}{W_0^*}\right)$ . Remeshing parameters are  $h_{min}$ , the interface thickness introduced here as  $E = 0.01$ ,  $e_{min} = 10^{-5}$ ,  $\Delta\tau = 10^{-6}$ . The corner is the intersection of two planes placed at the point (0.1;0.1). We use the thermal diffusivity  $\alpha^* = 1$ .

We solve the phase-field equation, with a modified source term and without anisotropy; being  $W_0^* = 1$ .

$$\frac{\partial\phi}{\partial\tau} - W_0^* \Delta\phi = 2 \frac{\phi}{E^2} \left(1 - \left(\frac{\phi}{E}\right)^2\right) - \frac{3}{4E} (-\theta) \left(1 - \left(\frac{\phi}{E}\right)^2\right) \quad (2.64)$$

In this expression  $\phi$  is built in a slightly different way from the classical phase-field formulation, leading to a different source term in equation (2.64). The energy equation is the same as previously:

$$\frac{\partial\theta}{\partial\tau} - \alpha^* \Delta\theta = -\frac{1}{2} \frac{\partial\phi}{\partial\tau} \quad \text{and} \quad \theta = \frac{T - T_M}{T_M - T_{imp}} \quad \text{with} \quad T_M = 0 \text{ K} \quad (2.65)$$

Boundary conditions are imposed on the left and on the bottom sides ( $\theta_{imp} = -1$ ), and the initial temperature in the domain is  $\theta_0 = 0.3$ .

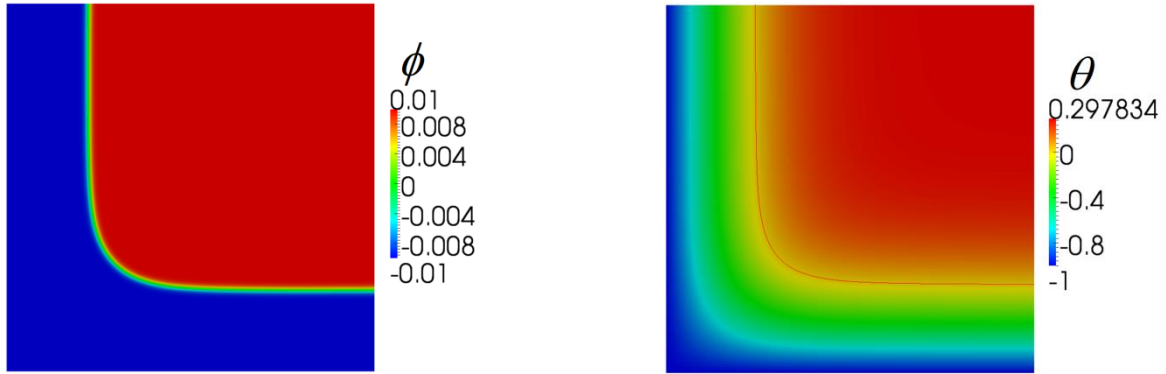


Figure 2.15 Phase field and temperature field with interface position for  $E = 0.01$ ,  $W_0^* = 1$ ,  $h_{min} = 0.001$ ,  $e_{min} = 10^{-5}$ ,  $\Delta\tau = 10^{-7}$  at  $\tau = 0.018$ .

Starting from the initial conditions, interface evolves from the corner, as illustrated in Figure 2.15. Numerical results obtained may be compared with the analytical solutions developed in Appendix B in the  $x$ - $y$  direction.

The error between the numerical and analytical temperature profiles is computed as follows:

$$Error\theta = \frac{|\theta_{Analytic} - \theta_{Numeric}|}{|\theta_{Analytic}|} \quad (2.66)$$

In the first case, the influence of  $h_{min}$  and  $NE$  on the thermal solver is studied by considering only the energy equation and not solving the phase-field one. The comparison is done for different cases as presented in Table 2.2. Results are shown at  $\tau = 0.0192$  in Figure 2.16 and Figure 2.17.

| Parameter                     | Symbol       | (a)       | (b)         | (c)         | (d)         | Unit |
|-------------------------------|--------------|-----------|-------------|-------------|-------------|------|
| Type of mesh                  | -            | Isotropic | Anisotropic | Anisotropic | Anisotropic | -    |
| Number of elements            | $NE$         | 5 000     | 5 000       | 5 000       | 20 000      | -    |
| Mesh size                     | $h_{min}$    | 0.02      | 0.02        | 0.001       | 0.001       | -    |
| Interface thickness           | $E$          | 0.01      | 0.01        | 0.01        | 0.01        | -    |
| Domain                        | $R_D^*$      | 1         | 1           | 1           | 1           | -    |
| Numerical initial temperature | $\theta_0$   | 0.3       | 0.3         | 0.3         | 0.3         | -    |
| Numerical thermal diffusivity | $\alpha^*$   | 1         | 1           | 1           | 1           | -    |
| Minimal error                 | $e_{min}$    | $10^{-5}$ | $10^{-5}$   | $10^{-5}$   | $10^{-5}$   | -    |
| Time step                     | $\Delta\tau$ | $10^{-6}$ | $10^{-6}$   | $10^{-6}$   | $10^{-6}$   | -    |

Table 2.2 Parameters for temperature diffusion in a corner for the different cases presented in Figure 2.16 and Figure 2.17.

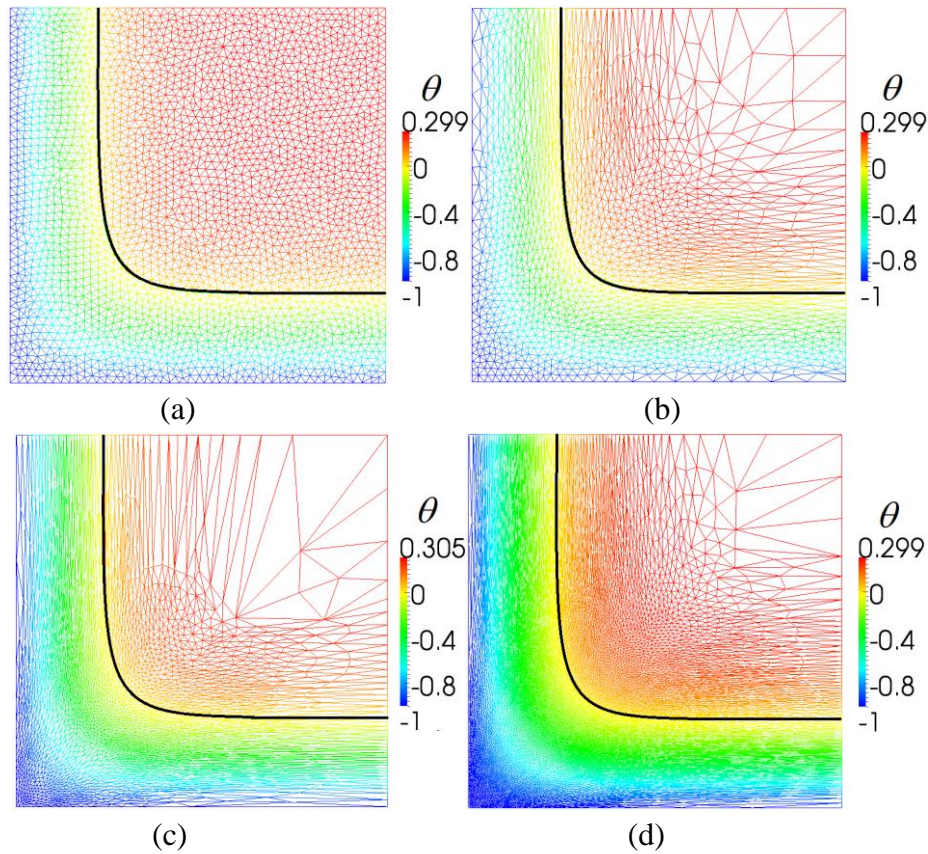


Figure 2.16 Temperature distribution and interface position added at  $\tau = 0.0192$  for different numerical parameters, a) Isotropic mesh with  $h = 0.02$  and  $NE = 5\,000$ , b) Anisotropic mesh with  $h_{min} = 0.02$  and  $NE = 5\,000$ , c) Anisotropic mesh with  $h_{min} = 0.001$  and  $NE = 5\,000$ , d) Anisotropic mesh with  $h_{min} = 0.001$  and  $NE = 20\,000$ .

By a comparison of the temperature fields, one may observe that both isotropic as well as anisotropic meshes may be used, as confirmed by drawing the  $\theta$  profile along the  $x$ - $y$  direction in Figure 2.17. Similar results are obtained using these two different types of meshes.

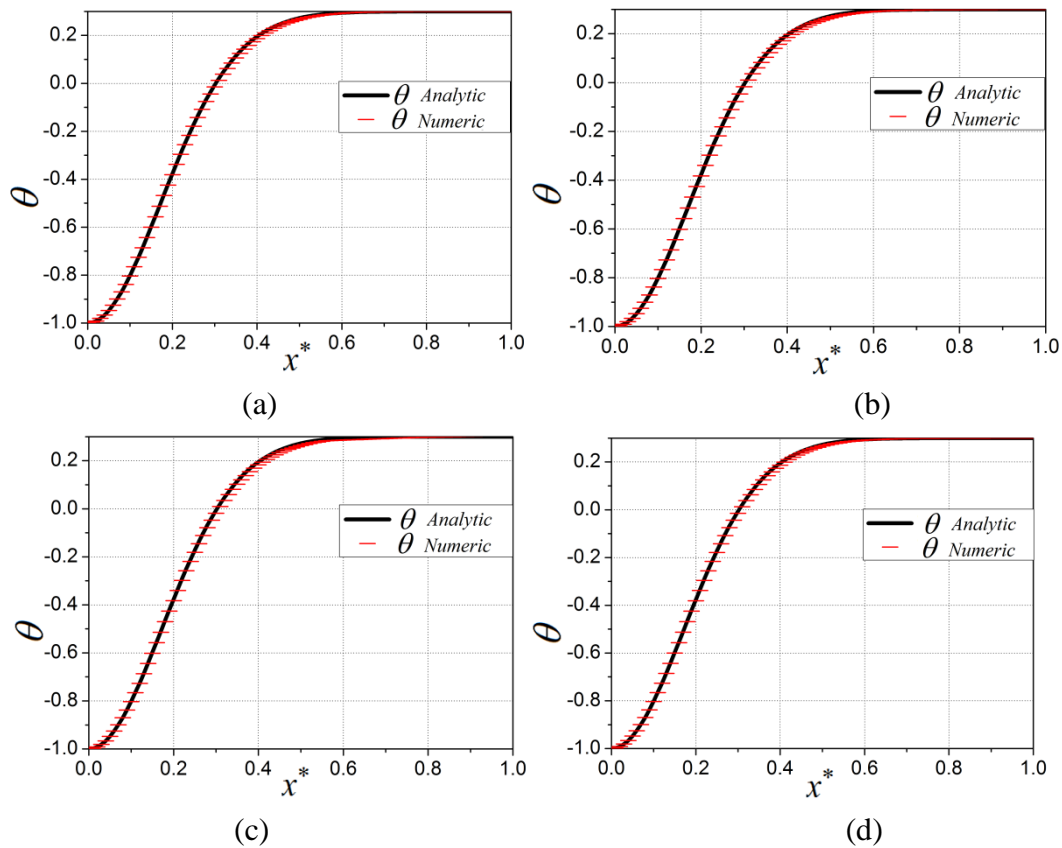


Figure 2.17 Numerical and analytical temperature profiles in the direction of the diagonal of the square with a) isotropic mesh with  $h = 0.02$  and  $NE = 5\,000$ , b) anisotropic mesh with  $h_{min} = 0.02$  and  $NE = 5\,000$ , c) anisotropic mesh with  $h_{min} = 0.001$  and  $NE = 5\,000$ , d) anisotropic mesh with  $h_{min} = 0.001$  and  $NE = 20\,000$ .

As observed in Figure 2.18, by comparing the red and green curves, the error increases when decreasing  $h_{min}$ , because we are asking for smaller mesh sizes without adding more elements to capture the good temperature profile. When increasing the number of elements while decreasing  $h_{min}$ , the error decreases (blue curve). The same error exists between isotropic and anisotropic meshes when  $h_{min}$  is small and a sufficient number of elements  $NE$  is used.

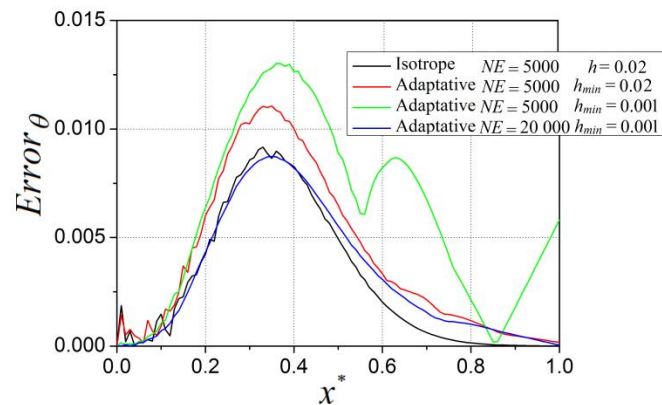


Figure 2.18 Error profiles between the numerical and analytical profiles, using different meshes, as illustrated in Figure 2.16 and Figure 2.17.

Both phase-field and energy equations are now solved, and interface position is thus dynamically tracked. Sensivity to the different numerical parameters was also studied. Firstly, we consider three different cases, as presented in Table 2.3, to see the influence of  $h_{min}$  value as illustrated in Figure 2.19 for  $\tau = 0.05$ . The mesh is adapted on both  $\theta$  and  $\phi$ .

| Parameter                     | Symbol       | (a)         | (b)         | (c)         | Unit |
|-------------------------------|--------------|-------------|-------------|-------------|------|
| Type of mesh                  | -            | Anisotropic | Anisotropic | Anisotropic | -    |
| Number of elements            | $NE$         | 20 000      | 20 000      | 20 000      | -    |
| Mesh size                     | $h_{min}$    | 0.01        | 0.001       | 0.00025     | -    |
| Interface thickness           | $E$          | 0.01        | 0.01        | 0.01        | -    |
| Domain                        | $R_D^*$      | 1           | 1           | 1           | -    |
| Numerical initial temperature | $\theta_0$   | 0.3         | 0.3         | 0.3         | -    |
| Numerical thermal diffusivity | $\alpha^*$   | 1           | 1           | 1           | -    |
| Minimal error                 | $e_{min}$    | $10^{-5}$   | $10^{-5}$   | $10^{-5}$   | -    |
| Time step                     | $\Delta\tau$ | $10^{-6}$   | $10^{-6}$   | $10^{-6}$   | -    |

Table 2.3 Parameters for temperature diffusion in a corner for the different cases presented in Figure 2.19, Figure 2.20 and Figure 2.21.

One may notice that larger values of  $h_{min}$  provide poorer results, but when decreasing this value, analytical and numerical profiles become similar. Error on temperature computation decreases from 14% to 5% when decreasing the minimal mesh size (Figure 2.20), at different instants of the computation.

The interface position is plotted in Figure 2.21, for different times and for the prescribed  $h_{min}$  values. Numerically obtained profiles are far from analytical ones in term of temperature, and become coincident only at the lowest given  $h_{min}$ . For large  $h_{min}$  value, we will have big elements at the interface and not a sufficient number of meshes to represent the interface thickness. The numerical and analytical results do not match.

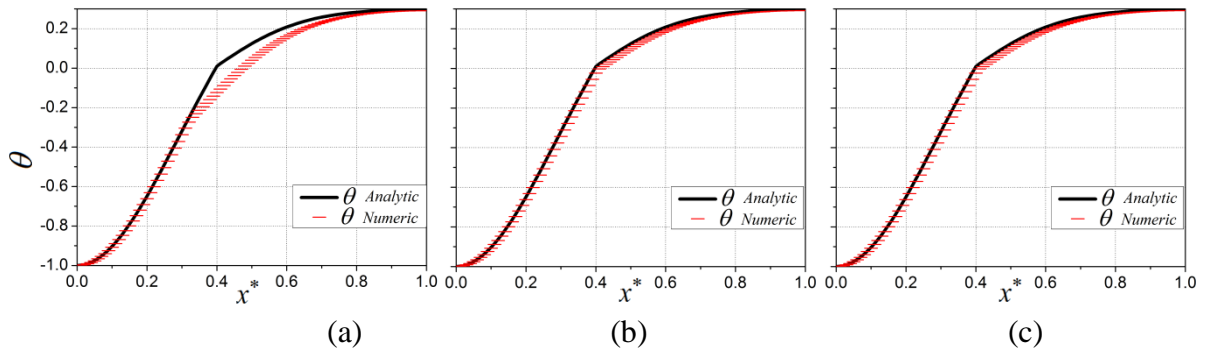


Figure 2.19 Numerical and analytical temperature profiles in the direction of the diagonal of the square for  $\tau = 0.05$  with, a)  $h_{min} = 0.01$ , b)  $h_{min} = 0.001$ , c)  $h_{min} = 0.00025$ .

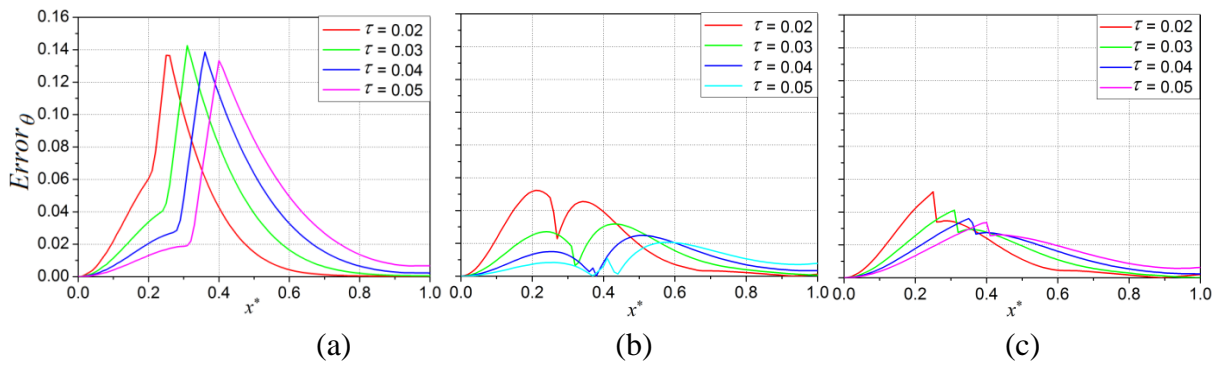


Figure 2.20 Temperature error profiles for a)  $h_{min} = 0.01$ , b)  $h_{min} = 0.001$ , c)  $h_{min} = 0.00025$ , plotted at different instant ( $\tau$ ) values.

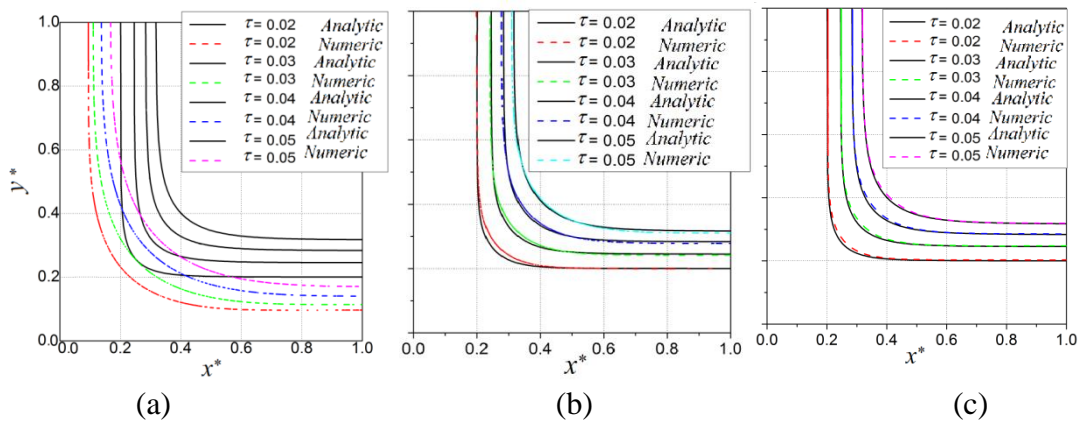


Figure 2.21 Numerical and analytical interface position for a)  $h_{min} = 0.01$ , b)  $h_{min} = 0.001$ , c)  $h_{min} = 0.00025$ .

Looking at the sensitivity of the results to the mesh adaptation type (isotropic, anisotropic adapting on  $\phi$  and  $\theta$  or anisotropic adapting on  $\phi$  only), Figure 2.22, shows that for  $\Delta\tau = 10^{-6}$  and for the parameters taken from Table 2.4.

- for the same  $h_{min}$ , isotropic and anisotropic adaptation does not influence the result;
- computing  $\theta$  and  $\phi$  in two different meshes (one adapted on  $\phi$  and the other isotropic) provide similar results.

This shows that anisotropic adaptation may be used to do the simulation with the same results as using an isotropic mesh.

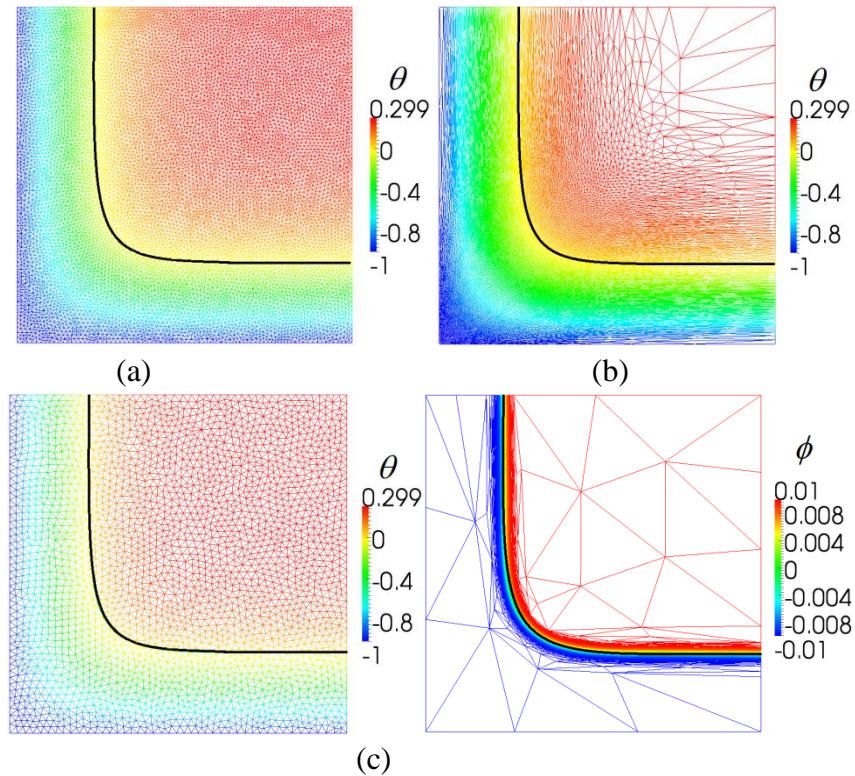


Figure 2.22 Phase field and temperature field with interface position at  $\tau = 0.05$  with a) isotropic mesh with  $h = 0.0002$  and  $NE = 20\,000$ , b) anisotropic mesh with  $h_{min} = 0.00025$  and  $NE = 20\,000$ , c) anisotropic mesh for  $\phi$  with  $h_{min} = 0.001$  and  $NE = 20\,000$  and an isotropic mesh for  $\theta$  with  $h = 0.02$  and  $NE = 5\,000$ .

| Parameter                     | Symbol       | (a)       | (b)         | (c)                   | Unit |
|-------------------------------|--------------|-----------|-------------|-----------------------|------|
| Type of mesh                  | -            | Isotropic | Anisotropic | Anisotropic+Isotropic | -    |
| Number of elements            | $NE$         | 20 000    | 20 000      | 20 000                | -    |
| Mesh size                     | $h_{min}$    | 0.0002    | 0.00025     | 0.001                 | -    |
| Interface thickness           | $E$          | 0.01      | 0.01        | 0.01                  | -    |
| Domain                        | $R_D^*$      | 1         | 1           | 1                     | -    |
| Numerical initial temperature | $\theta_0$   | 0.3       | 0.3         | 0.3                   | -    |
| Numerical thermal diffusivity | $\alpha^*$   | 1         | 1           | 1                     | -    |
| Minimal error                 | $e_{min}$    | $10^{-5}$ | $10^{-5}$   | $10^{-5}$             | -    |
| Time step                     | $\Delta\tau$ | $10^{-6}$ | $10^{-6}$   | $10^{-6}$             | -    |

Table 2.4 Parameters for temperature diffusion in a corner for the different cases presented in Figure 2.22, Figure 2.23, Figure 2.24 and Figure 2.25.

We can conclude from Figure 2.23 and Figure 2.24, that we have the same profiles using an isotropic mesh or two meshes for the different fields with the same maximum error, so no need to have two meshes. And using an anisotropic mesh for the two fields gives a similar result as using the isotropic mesh but with a bigger maximum error of 5 %. We can still use

the mesh adaptation having results needed with a small error. Using an isotropic mesh the computational time is equal to 210 h, but for the anisotropic mesh used the computational time is equal to 179h. If we use a smaller  $e_{min}$  it should decrease the number of elements and the computational time, because we will have bigger elements outside the interface.

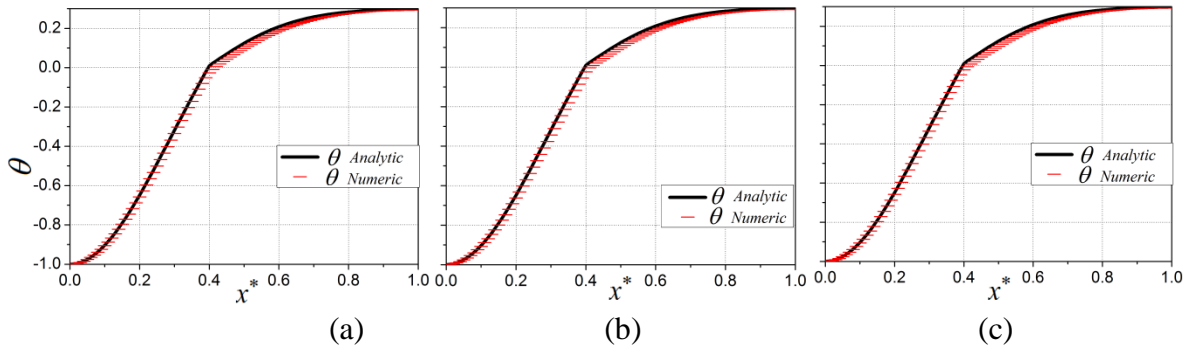


Figure 2.23 Temperature profile at  $\tau = 0.05$ , in the direction of the diagonal of the square, using a) an isotropic mesh with  $h = 0.0002$  and  $NE = 20\,000$ , b) an anisotropic mesh with  $h_{min} = 0.00025$  and  $NE = 20\,000$ , c) an anisotropic mesh for  $\phi$  with  $h_{min} = 0.001$  and  $NE = 20\,000$  and an isotropic mesh for  $\theta$  with  $h = 0.02$  and  $NE = 5\,000$ .

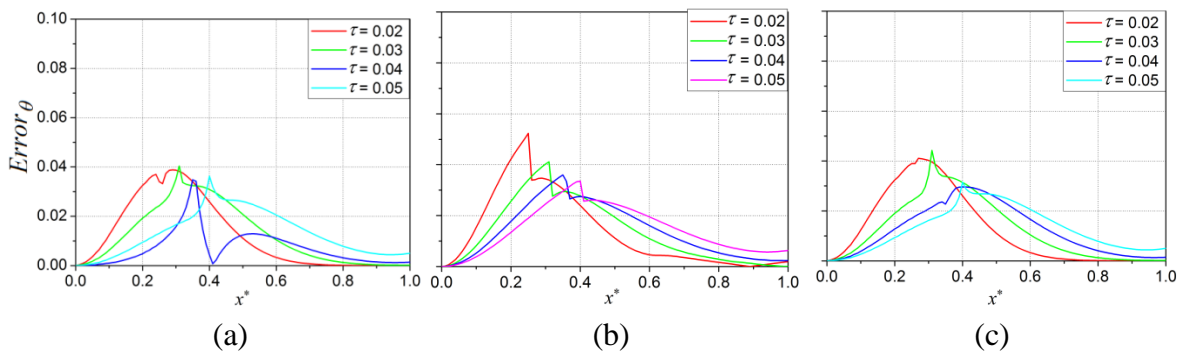


Figure 2.24 Error on temperature profile between the analytical and the numerical solution at  $\tau = 0.05$  using a) an isotropic mesh with  $h = 0.0002$  and  $NE = 20\,000$ , b) an anisotropic mesh with  $h_{min} = 0.00025$  and  $NE = 20\,000$ , c) an anisotropic mesh for  $\phi$  with  $h_{min} = 0.001$  and  $NE = 20\,000$  and an isotropic mesh for  $\theta$  with  $h = 0.02$  and  $NE = 5\,000$ .

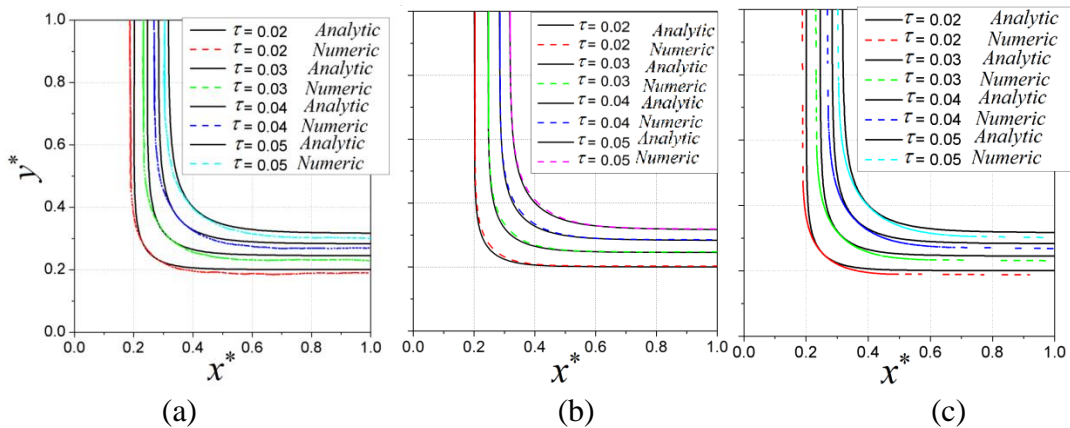


Figure 2.25 Numerical and analytical comparison for the interface positions at  $\tau = 0.02$ ,  $\tau = 0.03$ ,  $\tau = 0.04$  and  $\tau = 0.05$  using a) an isotropic mesh with  $h = 0.0002$  and  $NE = 20\,000$ , b) an anisotropic mesh with  $h_{min} = 0.00025$  and  $NE = 20\,000$ , c) an anisotropic mesh for  $\phi$  with  $h_{min} = 0.001$  and  $NE = 20\,000$  and an isotropic mesh for  $\theta$  with  $h = 0.02$  and  $NE = 5\,000$ .

Even if the error is slightly higher in the anisotropic case (5% against 4%), interface using an anisotropic mesh are better followed, as shown in Figure 2.25. No sensitivity study to  $e_{min}$  has been performed here (it will be given for a different test case in the next section). But one may already conclude that dynamic anisotropic adaptation, on both  $\phi$  and  $\theta$ , is accurately performed for the Stephan problem. This anisotropic method may not give us the best results but it can be used in problems where the isotropic method can not be used. Is it better to use anisotropic mesh for various problems with a 5% error or is it better to use isotropic mesh for some problems.

### 2.3 Thermal dendritic growth

A first example has been simulated to show how a dendrite pattern can develop, starting from a small nucleus (Figure 2.26), which grows in an undercooled melt. The material property is chosen with an interface anisotropy term to develop a four arms dendrite.

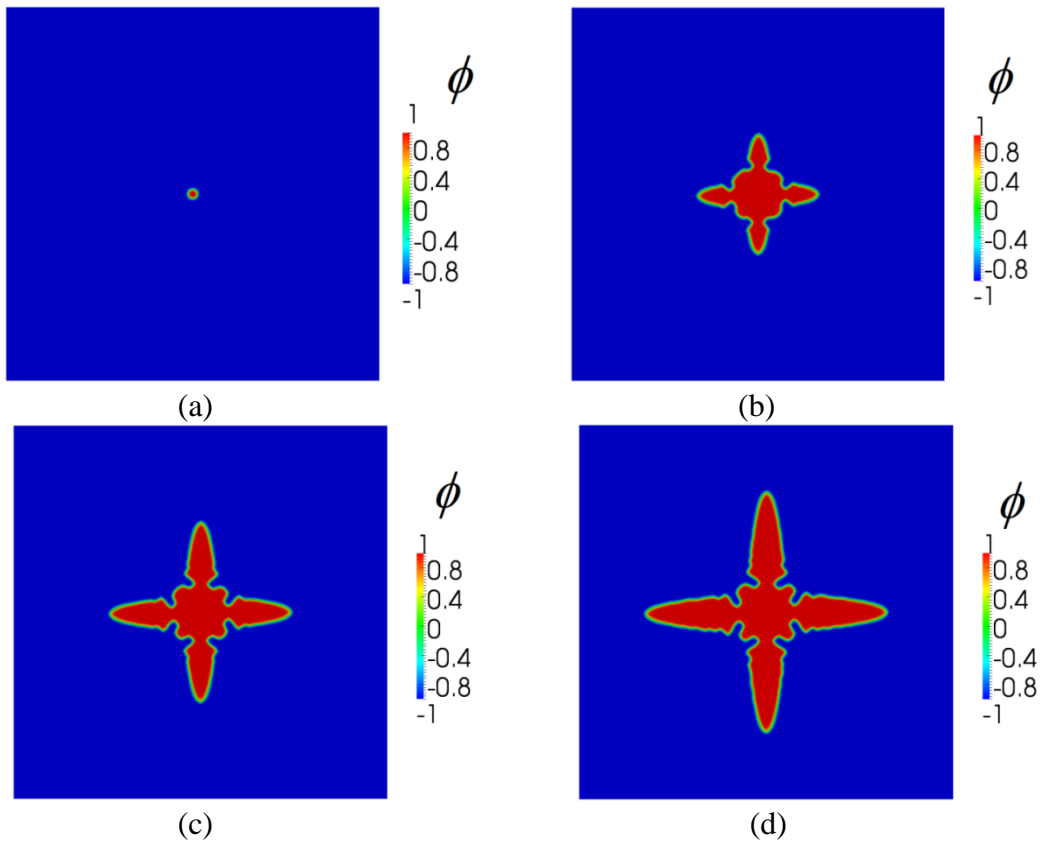


Figure 2.26 Example of simulation of dendritic growth using the parameters defined in Table 2.5 at, a)  $\tau = 0$ , b)  $\tau = 64$ , c)  $\tau = 96$ , d)  $\tau = 128$ .

Simulations were performed in a  $[-200,200] \times [-200,200]$  domain. Parameters taken here are presented in Table 2.5 with the anisotropy form:  $W(\mathbf{n}) = W_0^* \left( 1 + \varepsilon_4 \cos \left( 4 \arctan \frac{\partial_y^* \phi}{\partial_x^* \phi} \right) \right)$ . This simulation is done with 25 cores with a computational time equal to 25 h 30 min.

| Parameter                     | Symbol          | value    | Unit |
|-------------------------------|-----------------|----------|------|
| Number of elements            | $NE$            | 150 000  | -    |
| Mesh size                     | $h_{min}$       | 0.4      | -    |
| Interface thickness           | $W_0^*$         | 1        | -    |
| Unit time                     | $\tau_0^*$      | 1        | -    |
| Domain                        | $R_D^*$         | 400      | -    |
| Nucleus radius                | $R_0^*$         | 5        | -    |
| Numerical initial temperature | $\theta_0$      | -0.55    | -    |
| Numerical thermal diffusivity | $\alpha^*$      | 4        | -    |
| Anisotropy frequency          | $\varepsilon_4$ | 0.02     | -    |
| Time step                     | $\Delta\tau$    | 0.008    | -    |
| Cores number                  | -               | 25       | -    |
| CPU time                      | $t_{CPU}$       | 25h30min | -    |

Table 2.5 Parameters for thermal dendritic growth shown in Figure 2.26.

Thermal dendritic growth has been studied by comparing results obtained using the finite difference method with an isotropic structured grid (model developed in Matlab) and the finite element method with parallel computation and an isotropic unstructured mesh and an anisotropic unstructured adaptive mesh (CimLib) in terms of CPU time and dendritic morphology, as illustrated in

Figure 2.27. Simulations were performed in a  $[-200,200] \times [-200,200]$  domain and parameters are shown in Table 2.6.

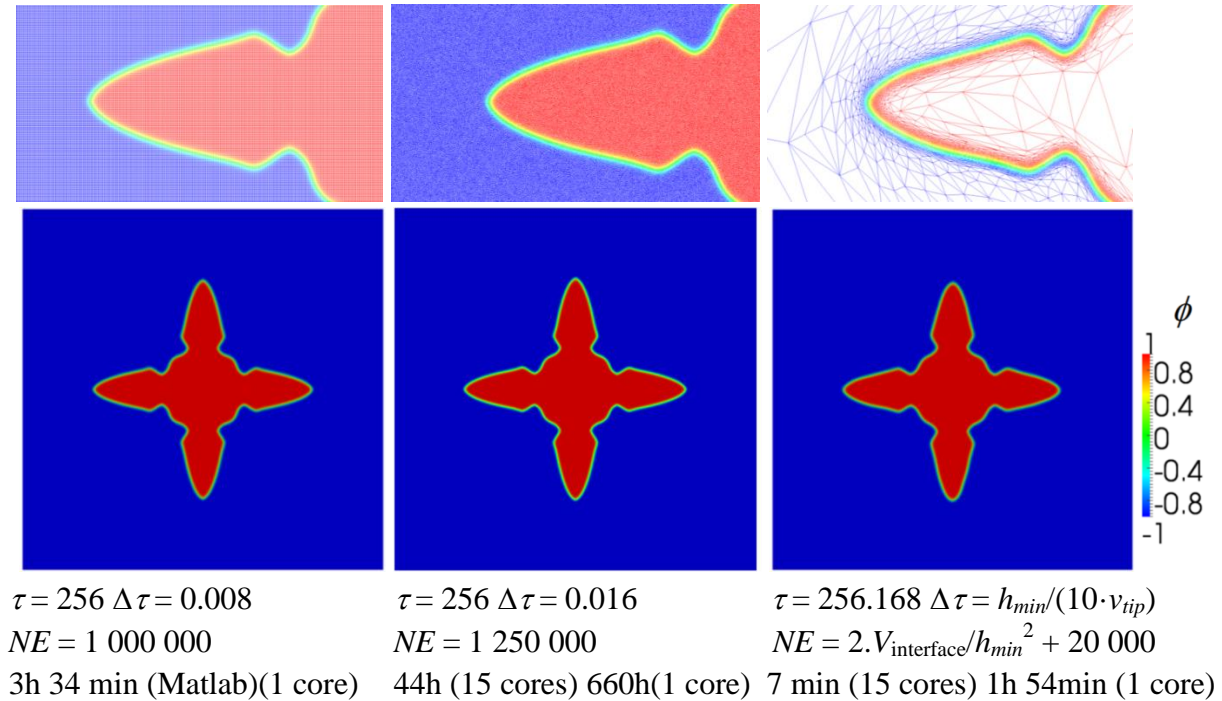


Figure 2.27 Simulations using the finite difference and the finite element method with isotropic and anisotropic meshes, illustration at one growth instant.  $\tau = 256$  and the parameters used are shown in Table 2.6.

| Parameter                     | Symbol           | Matlab    | Isotrope  | Anisotrope                                            | Unit |
|-------------------------------|------------------|-----------|-----------|-------------------------------------------------------|------|
| Number of elements            | $NE$             | 1 000 000 | 1 250 000 | $2 \cdot V_{\text{interface}}/h_{\text{min}}^2 + N_2$ | -    |
| Constant number of element    | $N_2$            | -         | -         | 20 000                                                | -    |
| Mesh size                     | $h_{\text{min}}$ | 0.4       | 0.4       | 0.4                                                   | -    |
| Interface thickness           | $W_0^*$          | 1         | 1         | 1                                                     | -    |
| Unit time                     | $\tau_0^*$       | 1         | 1         | 1                                                     | -    |
| Domain                        | $R_D^*$          | 400       | 400       | 400                                                   | -    |
| Nucleus radius                | $R_0^*$          | 5         | 5         | 5                                                     | -    |
| Numerical initial temperature | $\theta_0$       | -0.55     | -0.55     | -0.55                                                 | -    |
| Numerical thermal diffusivity | $\alpha^*$       | 4         | 4         | 4                                                     | -    |
| Minimal error                 | $e_{\text{min}}$ | -         | -         | $10^{-9}$                                             | -    |
| Anisotropy frequency          | $\varepsilon_4$  | 0.05      | 0.05      | 0.05                                                  | -    |
| Time step                     | $\Delta\tau$     | 0.008     | 0.016     | $h_{\text{min}}/(10 \cdot v_{\text{tip}})$            | -    |
| Cores number                  | -                | 1         | 15; 1     | 15 ; 1                                                | -    |
| CPU time                      | $t_{\text{CPU}}$ | 3h34min   | 44h; 660h | 7min ; 1h54min                                        | -    |

Table 2.6 Parameters for thermal dendritic growth shown in Figure 2.27 and Figure 2.28.

Firstly, one can observe that using an isotropic unstructured mesh and the finite element method takes more time than the simulation done with the finite difference method, for almost the same number of degrees of freedom.

Using adaptive meshing, one has 16 201 nodes instead of 1 million for the isotropic case, so we have reduced the space needed in the memory to store the results and the computational time decreases from 3h 34 min to 7 min when using 15 cores.

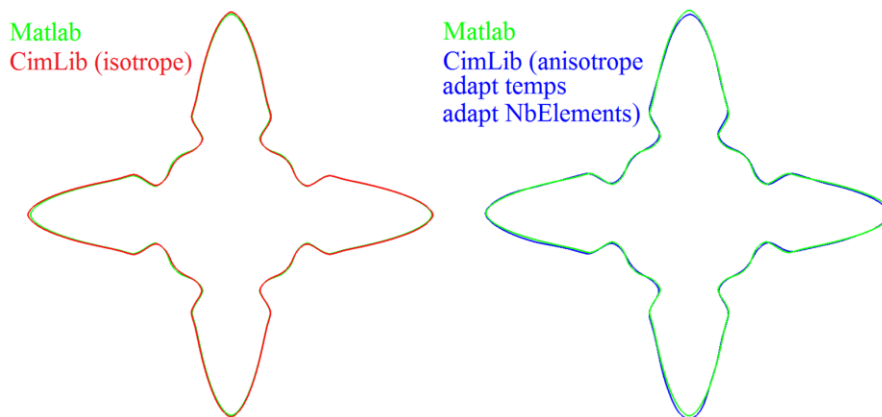


Figure 2.28 Solid/liquid interface position using the finite difference method and the finite element method, with isotropic and anisotropic meshes, as well as further optimisations, at  $\tau = 256$

Figure 2.28 shows that the two interface positions, using the finite difference method and the finite element method provide the same results.

### 2.3.1 Timestep and number of elements adaptation

Improvements on CPU time have been obtained by automatic adjustment of the time step  $\Delta\tau$  to the interface velocity evolution, by:

$$\Delta\tau = h_{min}/(\beta' \cdot v_{tip}) \quad (2.67)$$

$h_{min}$  is the minimal mesh size and  $\beta'$  is a chosen constant to ensure that this equation verifies the CFL (Courant-Friedrichs-Lewy) condition, that is  $\Delta\tau$  must satisfy the relation:

$$\Delta\tau < h_{min}/v_{tip} \quad (2.68)$$

At the beginning of growth, a small time step is needed. Then growth velocity decreases, and larger time steps are authorized.

This optimization was put in place because, during dendritic growth, the number of elements should increase since the surface of the interface increases, more elements are needed to represent it. An estimation of the “interface volume”, defined as the volume occupied by the “interface thickness” of the phase field function,  $V_{interface}$  (a surface in 2D) can be obtained as follows:

$$V_{Interface} = \int_{-\infty}^{\infty} \delta_{\phi} dV, \text{ with } \delta_{\phi} = \begin{cases} 0 & \text{for } \phi < -W_0^* \\ \frac{1}{2W_0^*} + \frac{1}{2W_0^*} \cos\left(\frac{\pi\phi}{W_0^*}\right) & \text{for } -W_0^* < \phi < W_0^* \\ 0 & \text{for } \phi > W_0^* \end{cases} \quad (2.69)$$

In our computations,  $W_0^* = 1$ . The number of elements needed within this volume may be computed as:

$$N_1 = S_{Interface}/S_{element} = 2 \cdot S_{interface}/h_{min}^2 \quad \text{in 2D}$$

or

$$N_1 = V_{Interface}/V_{element} = 6 \cdot V_{interface}/h_{min}^3 \quad \text{in 3D}$$

One may then estimate the total number of elements needed as  $NE = N_1 + N_2$ , with  $N_2$  a constant to add a certain number of elements outside the interface thickness. Using this expression,  $NE$  may be variable throughout computation, and given at each mesh adaptation step.

Assuming symmetrical growth only  $1/4$  of the domain is used, reducing the computational time and the memory used. Figure 2.29 illustrates mesh adaptation following the solid/liquid interface and the temperature profile. The number of element is increasing during the computation to capture these profiles. Parameters used in this simulation are shown in Table 2.10.

| Parameter                     | Symbol           | value                                                   | Unit |
|-------------------------------|------------------|---------------------------------------------------------|------|
| Number of elements            | $NE$             | $2 \cdot V_{\text{interface}} / h_{\text{min}}^2 + N_2$ | -    |
| Constant number of element    | $N_2$            | 50 000                                                  | -    |
| Mesh size                     | $h_{\text{min}}$ | 0.4                                                     | -    |
| Interface thickness           | $W_0^*$          | 1                                                       | -    |
| Unit time                     | $\tau_0^*$       | 1                                                       | -    |
| Domain                        | $R_D^*$          | 120                                                     | -    |
| Nucleus radius                | $R_0^*$          | 5                                                       | -    |
| Numerical initial temperature | $\theta_0$       | -0.55                                                   | -    |
| Numerical thermal diffusivity | $\alpha^*$       | 4                                                       | -    |
| Minimal error                 | $e_{\text{min}}$ | $10^{-9}$                                               | -    |
| Anisotropy frequency          | $\varepsilon_4$  | 0.05                                                    | -    |
| Time step                     | $\Delta\tau$     | $h_{\text{min}} / (10 \cdot v_{\text{tip}})$            | -    |
| Cores number                  | -                | 8                                                       | -    |
| CPU time                      | $t_{\text{CPU}}$ | 10 min                                                  | -    |

Table 2.7 Parameters for thermal dendritic growth shown in Figure 2.29 and Figure 2.30.

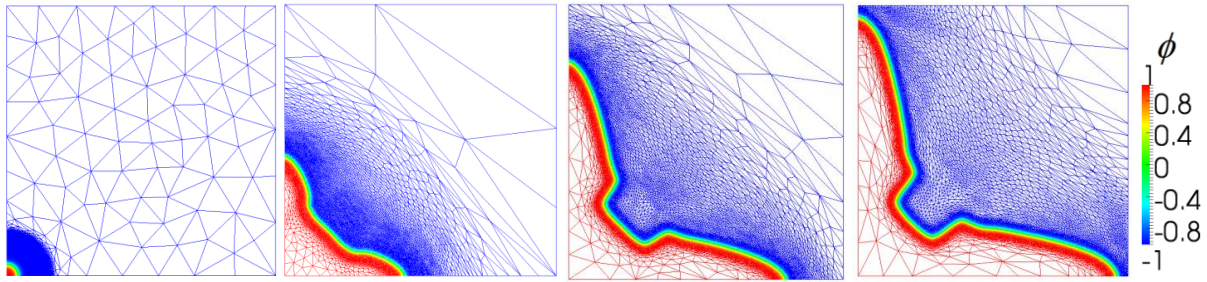


Figure 2.29 Dendritic mesh at  $\tau = 0$ ,  $\tau = 56$ ,  $\tau = 132$ ,  $\tau = 200$ , for an evolving  $NE$ . Parameters are shown in Table 2.10.

Figure 2.30 shows the variation of the time step and the number of elements with time during thermal dendritic growth. We can see clearly that the time step and the number of element are increasing with growth. The time step will stagnates when we reach the stationary velocity and the number of elements is increasing linearly with time.

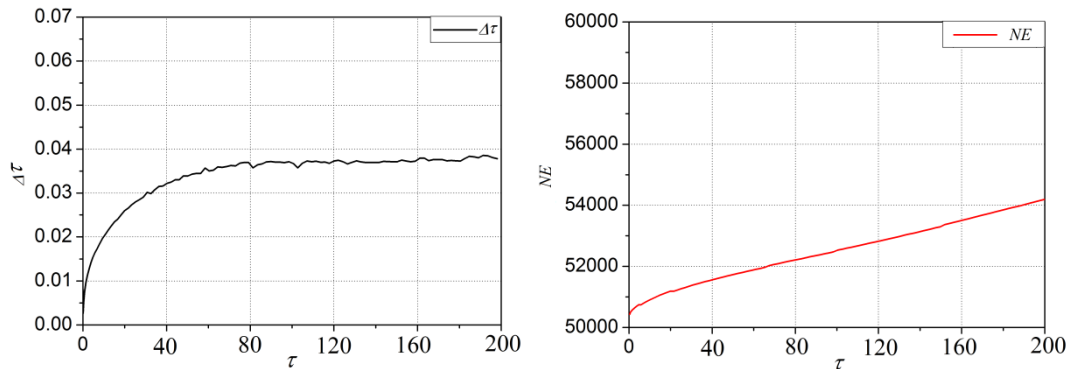


Figure 2.30 Variation of  $\Delta\tau$  and  $NE$  with time during thermal dendritic growth with  $\alpha^* = 4$  and  $N_2 = 50\,000$ . Parameters are shown in Table 2.10.

### 2.3.2 Convergence of the tip velocity

We now compare our results with the results presented in [KAR1998], where an analytical solution in 2D for thermal dendritic growth has been computed with the Green function method.

Let us consider a rectangular domain of size  $[0;1000] \times [0;300]$  on which an initial nucleus of size 5 is placed in the left bottom corner, a rectangle is chosen instead of a square of  $[0;1000] \times [0;1000]$  to follow the dendrite velocity until it stabilizes with a small computational time and a smaller  $NE$ . To check the convergence toward a steady state regime, the tip velocity in the  $x$  direction is computed. The simulation parameters are given in Table 2.8.

| Parameter                     | Symbol           | value                                                   | Unit |
|-------------------------------|------------------|---------------------------------------------------------|------|
| Number of elements            | $NE$             | $2 \cdot V_{\text{interface}} / h_{\text{min}}^2 + N_2$ | -    |
| Constant number of element    | $N_2$            | 25 000                                                  | -    |
| Unit time                     | $\tau_0^*$       | 1                                                       | -    |
| Nucleus radius                | $R_0^*$          | 5                                                       | -    |
| Numerical initial temperature | $\theta_0$       | -0.65                                                   | -    |
| Numerical thermal diffusivity | $\alpha^*$       | 1                                                       | -    |
| Minimal error                 | $e_{\text{min}}$ | $10^{-9}$                                               | -    |
| Anisotropy frequency          | $\varepsilon_4$  | 0.05                                                    | -    |
| Time step                     | $\Delta \tau$    | $h_{\text{min}} / (10 \cdot v_{\text{tip}})$            | -    |
| Capillarity length            | $d_0^*$          | 0.554                                                   | -    |

Table 2.8 Parameters for thermal dendritic growth shown in Figure 2.31 and Figure 2.32.

We will study the influence of varying  $W_0^*$  and  $h_{\text{min}}$ . In the following, we compare the solution for different values of the minimal mesh size  $h_{\text{min}}$ .

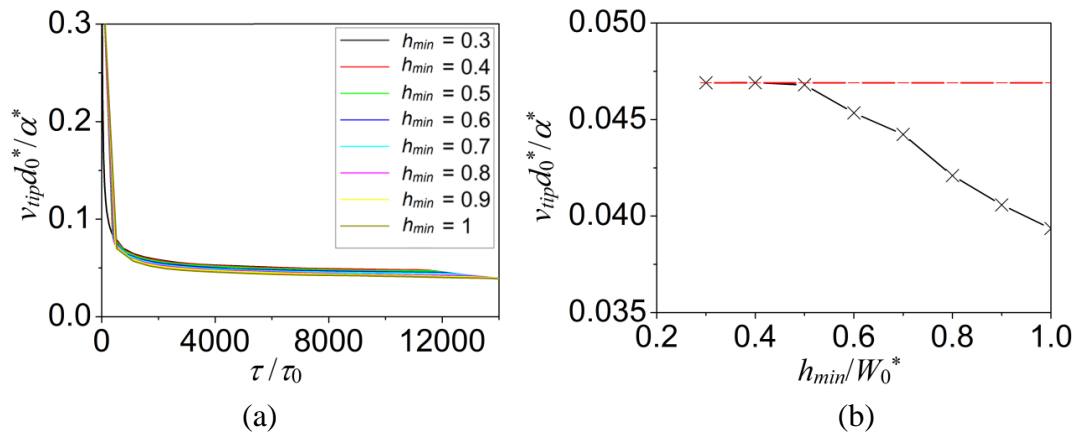


Figure 2.31 a) Evolution of dimensionless tip velocity as a function of time for different  $h_{\text{min}}$ , b) dimensionless tip velocity, when it stabilizes, as a function of grid spacing. The red line corresponds to the value obtained from the Green function calculation [KAR1998].

Parameters of the simulations are given in Table 2.8.

In Figure 2.31 (a), we observe that the tip velocity decreases with time to a constant value, named the steady-state velocity. When the tip reaches the border of the domain this value changes, meaning that the computation no longer fits the hypothesis behind the analytical solution. In Figure 2.31 (a), the sensitivity of the solution to the mesh's minimal size is represented. In Figure 2.31 (b), the steady-state velocity computed value is compared with the value obtained using the Green function calculation. One observes that when decreasing the minimal mesh size in the interface, the velocity converges to the analytical solution in red.

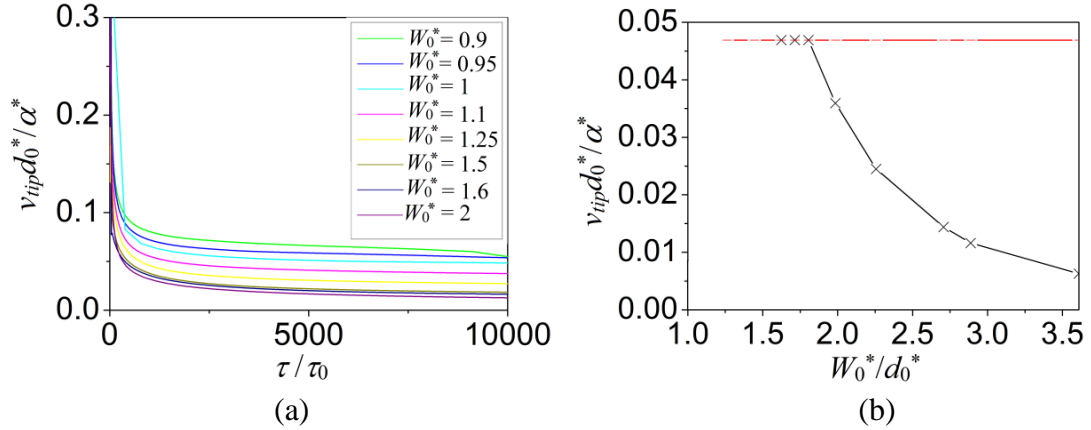


Figure 2.32 a) Evolution of dimensionless tip velocity as a function of time for different  $W_0^*$ , b) dimensionless tip velocity, when it stabilizes, as a function of interface thickness. The red line corresponds to the value obtained from the Green function calculation [KAR1998].

Parameters of the simulations are given in Table 2.8.

The same type of study is done, but by varying  $W_0^*$  as illustrated in Figure 2.32. When  $W_0^*$  decreases, the velocity tip converges towards the analytical one, drawn in red. This convergence can be established using a small  $W_0^* / d_0^*$ . Decreasing  $\alpha^*$  is equivalent to decreasing simultaneously  $W_0^* / d_0^*$  showing that our results are independent of interface thickness. This shows that our phase-field model can quantitatively predict results for the thermal dendritic growth velocity.

### 2.3.3 Computational time

To reduce the CPU time, numerical methods and different optimization previously described are used, such as parallel computation, time step adaptation, number of mesh elements variation and adaptive meshing itself. We check the influence on the CPU time of these different optimizations in thermal dendritic growth, in 2D, and using 15 cores.

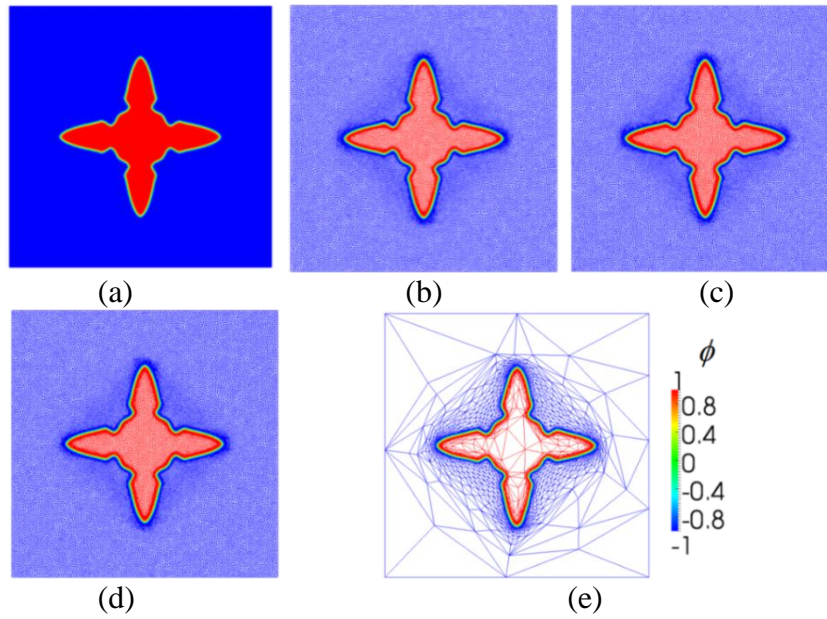


Figure 2.33 Thermal dendritic growth on a  $[-200,200]$  square, supposing the initial nucleus in the middle of the square and using different optimizations, for  $h_{min} = 0.4$ , a) isotropic mesh, b) anisotropic adaptive meshing (each  $\Delta\tau$ ) with  $\Delta\tau = 0.016$ ,  $NE = 100\,000$  and  $e_{min} = 10^{-4}$ , c) anisotropic adaptive meshing with  $FR$ ,  $\Delta\tau = 0.016$ ,  $NE = 100\,000$  and  $e_{min} = 10^{-4}$ , d) anisotropic adaptive meshing with  $FR$ ,  $\Delta\tau = h_{min}/(10 \cdot v_{tip})$ ,  $NE = 100\,000$  and  $e_{min} = 10^{-4}$ , e) anisotropic adaptive meshing with  $FR$ ,  $\Delta\tau = h_{min}/(10 \cdot v_{tip})$ ,  $NE = 2 \cdot V_{interface}/h_{min}^2 + 25\,000$  and  $e_{min} = 10^{-9}$ .

| Parameter                     | Symbol          | (a)       | (b)         | (c)         | (d)                          | (e)                          |
|-------------------------------|-----------------|-----------|-------------|-------------|------------------------------|------------------------------|
| Number of elements            | $NE$            | 1 000 000 | $N_1 + N_2$ | $N_1 + N_2$ | $N_1 + N_2$                  | $N_1 + N_2$                  |
| Constant number of element    | $N_2$           | -         | 100 000     | 100 000     | 100 000                      | 20 000                       |
| Mesh size                     | $h_{min}$       | 0.4       | 0.4         | 0.4         | 0.4                          | 0.4                          |
| Interface thickness           | $W_0^*$         | 1         | 1           | 1           | 1                            | 1                            |
| Unit time                     | $\tau_0^*$      | 1         | 1           | 1           | 1                            | 1                            |
| Nucleus radius                | $R_0^*$         | 5         | 5           | 5           | 5                            | 5                            |
| Numerical initial temperature | $\theta_0$      | -0.65     | -0.65       | -0.65       | -0.65                        | -0.65                        |
| Numerical thermal diffusivity | $\alpha^*$      | 1         | 1           | 1           | 1                            | 1                            |
| Minimal error                 | $e_{min}$       | -         | $10^{-4}$   | $10^{-4}$   | $10^{-4}$                    | $10^{-9}$                    |
| Anisotropy frequency          | $\varepsilon_4$ | 0.05      | 0.05        | 0.05        | 0.05                         | 0.05                         |
| Time step                     | $\Delta\tau$    | 0.016     | 0.016       | 0.016       | $h_{min}/(10 \cdot v_{tip})$ | $h_{min}/(10 \cdot v_{tip})$ |
| Capillarity length            | $d_0^*$         | 0.554     | 0.554       | 0.554       | 0.554                        | 0.554                        |
| Cores number                  | -               | 16        | 16          | 16          | 16                           | 16                           |
| CPU time                      | $t_{CPU}$       | 44h       | 15h30min    | 1h55min     | 32min                        | 7min                         |

Table 2.9 Parameters for thermal dendritic growth shown in Figure 2.33, Figure 2.34 and Figure 2.35.

Figure 2.34 schematically provides the CPU time decrease obtained for all the conditions.

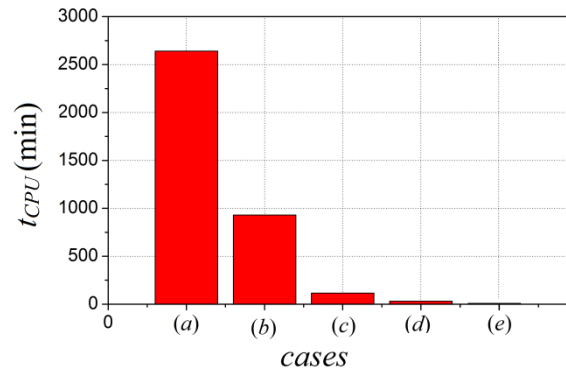


Figure 2.34 Variation of the CPU time for the examples shown in Figure 2.33, illustrating the influence of the different optimizations.

To further extend this analysis, differences on the computational time for different numerical parameters are shown for a rectangular domain [1000;300] with the same parameters of Table 2.9.

| <i>Case</i> | $V_{Tip}$ | $NE$      | $h_{min}$ | $Nb\_Proc$ | $Fr$ | <b>Adapt Time</b> | <b>Adapt NE</b>      | $T_{CPU}$ |
|-------------|-----------|-----------|-----------|------------|------|-------------------|----------------------|-----------|
| 1           | 0.0469    | 4 638 842 | 0.4       | 1          | No   | No                | No                   | 36 000 h* |
| 2           | 0.0469    | 4 638 842 | 0.4       | 4          | No   | No                | No                   | 13 000 h* |
| 3           | 0.0469    | 4 638 842 | 0.4       | 16         | No   | No                | No                   | 3 480 h   |
| 4           | 0.0485    | 100 000   | 0.4       | 16         | 1    | No                | No                   | 504h      |
| 5           | 0.051     | 80 000    | 0.4       | 16         | Yes  | No                | No                   | 80h       |
| 6           | 0.05      | 80 000    | 0.4       | 16         | Yes  | Yes               | No                   | 13h       |
| 7           | 0.0469    | 46 000    | 0.4       | 16         | Yes  | Yes               | Yes( $N_2 = 25000$ ) | 10h       |

\* Predicted time

Table 2.10 Computational times for different test conditions using the parameters of Table 2.9.

The predicted time is computed as follows: for case 1 the simulation is done arriving to  $(1000/12.5 = 80)$  of the domain taking 2880h; prediction time is equal to  $2880 \cdot (1000/12.5)$  using cross multiplication to reach the domain. The same prediction is done for cases 2 and 3. Parallel computing gain is observed on the CPU time on the first three cases, using 1, 4 or 16 processors. From case 3 and case 4, we show CPU time decrease due to mesh adaptation. From case 4 to case 5, we show the influence of the mesh adaptation with the frequency computed above depending on the velocity. In cases 6 and 7 we have added the time adaptation and the number of element evolution. Results obtained are plotted in Figure 2.35.

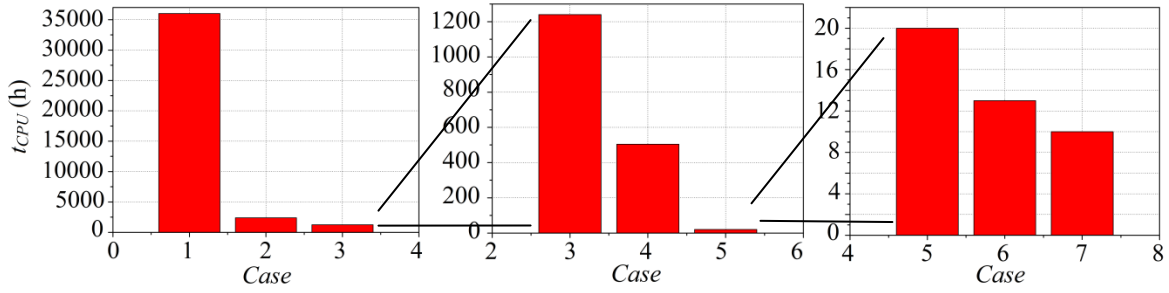


Figure 2.35 CPU times obtained for the different conditions (Table 2.10) taken which simulate the same dendritic growth.

Table 2.11 presents a study when varying,  $\theta_0$  or material parameters  $\alpha^*$  or  $\varepsilon_4$ . It reveals that, one may obtain exactly the same tip velocity  $V_{tip}$ , as computed using the Green function  $V_{tip}^{GF}$ . We can obtain a negligible error for the velocity tip in each case by choosing the right number of elements (the right  $N_2$  to represent the mesh outside the interface). When we have small thermal diffusion or small initial undercooling or a small anisotropy, we need to do the simulation with a larger domain and the computation takes more time to reach a steady state regime.

| $\theta_0$ | $\varepsilon_4$ | $\alpha^*$ | $d_0^*/W_0^*$ | $V_{Tip}$ | $V_{Tip}^{GF}$ | % error | Domain     | NE     | $T_{CPU}$ |
|------------|-----------------|------------|---------------|-----------|----------------|---------|------------|--------|-----------|
| 0.65       | 0.05            | 1          | 0.554         | 0.0469    | 0.0469         | 0       | [1000;300] | 46 000 | 10h       |
| 0.55       | 0.05            | 2          | 0.277         | 0.017     | 0.017          | 0       | [1000;300] | 44 000 | 6h 30min  |
| 0.55       | 0.05            | 4          | 0.139         | 0.017     | 0.017          | 0       | [500;150]  | 34 000 | 2h 30 min |
| 0.45       | 0.05            | 4          | 0.139         | 0.00545   | 0.00545        | 0       | [1000;300] | 50 000 | 5h 50 min |
| 0.55       | 0.02            | 2          | 0.277         | 0.00685   | 0.00685        | 0       | [1000;300] | 30 000 | 7h 30 min |

Table 2.11 Ccomparison on the tip velocity value for different physical parameters.

### 2.3.4 Study of the capillary anisotropy

Patterns forming in solidification are linked to the solid/liquid interface. Perturbations are done on the equilibrium structure due to the additional free energy of the solid/liquid interface. If this excess in energy is isotropic, the area of the interface will be minimized. Since the solid is crystalline,  $\gamma$  is anisotropic depending on the growth orientation. The instability of the solid/liquid interface that forms the dendrites is influenced by the anisotropy of the solid/liquid interfacial energy presented by the parameter  $\varepsilon_4$ .

Several expressions for the capillary anisotropy,  $W(\mathbf{n})$ , may be defined. They can be written [KAR1998], [FRI2009]:

$$W(\mathbf{n}) = W_0^* \left( 1 + \varepsilon_4 \cos \left( \text{Arm} \arctan \frac{\partial_{y^*} \phi}{\partial_{x^*} \phi} \right) \right) \text{ In 2D} \quad (2.70)$$

$$W(\mathbf{n}) = W_0^* (1 - 3\varepsilon_4) \left[ 1 + \frac{4\varepsilon_4}{1 - 3\varepsilon_4} \frac{(\partial_{x^*} \phi)^4 + (\partial_{y^*} \phi)^4}{|\nabla \phi|^4} \right] \text{ In 2D} \quad (2.71)$$

$$W(\mathbf{n}) = W_0^* (1 - 3\varepsilon_4) \left[ 1 + \frac{4\varepsilon_4}{1 - 3\varepsilon_4} \frac{(\partial_{x^*} \phi)^4 + (\partial_{y^*} \phi)^4 + (\partial_{z^*} \phi)^4}{|\nabla \phi|^4} \right] \text{ In 3D} \quad (2.72)$$

$$W(\mathbf{n}) = W_0^* \left[ 1 + \varepsilon_1 \left( Q - \frac{3}{5} \right) + \varepsilon_2 \left( 3Q + 66S - \frac{17}{7} \right) \right] \text{ In 3D} \quad (2.73)$$

$$\text{with } Q = n_x^4 + n_y^4 + n_z^4 = \frac{\partial_{x^*} \phi^4 + \partial_{y^*} \phi^4 + \partial_{z^*} \phi^4}{|\nabla \phi|^4} \text{ and } S = n_x^2 n_y^2 n_z^2 = \frac{\partial_{x^*} \phi^2 \partial_{y^*} \phi^2 \partial_{z^*} \phi^2}{|\nabla \phi|^6}$$

$\varepsilon_4$  represents the intensity of the anisotropy,  $Arm$  is the number of primary branches or arms and  $W_0^*$  is the initial thickness of the interface. When  $\varepsilon_4$  increases, the anisotropy increases, as illustrated in Figure 2.36. The number of arms changes with the value of  $Arm$  (Figure 2.37).

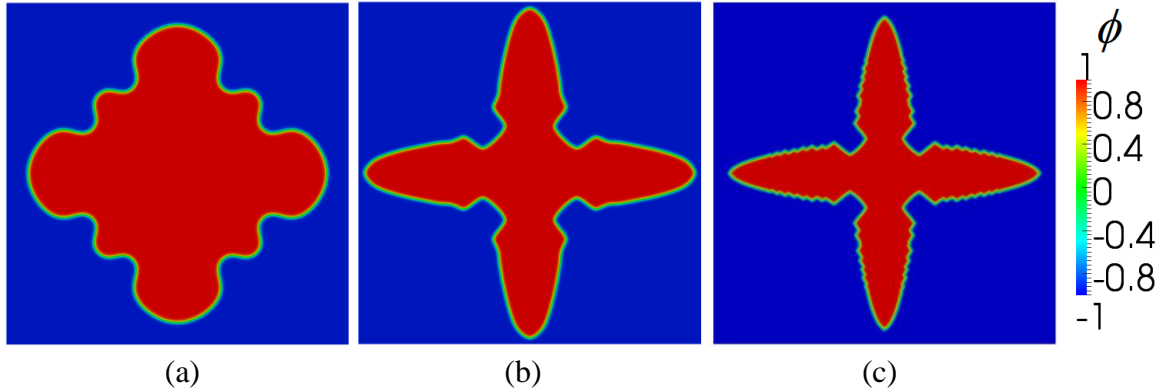


Figure 2.36 Thermal dendritic growth morphology for different values of  $\varepsilon_4$ , for  $Arm = 4$ :  
a)  $\varepsilon_4 = 0.01$ , b)  $\varepsilon_4 = 0.05$ , c)  $\varepsilon_4 = 0.1$ .

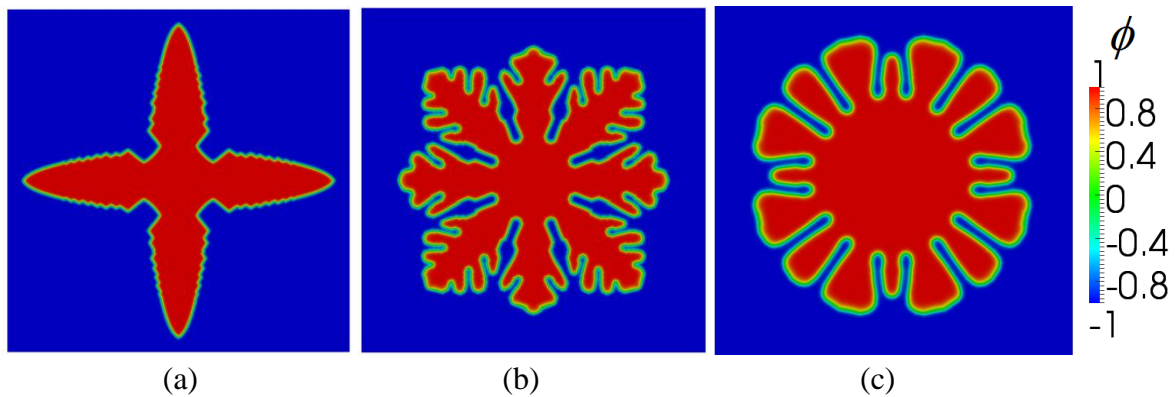


Figure 2.37 Thermal dendritic growth morphomogy obtained for different number of arms for  $\varepsilon_4 = 0.1$ : a)  $Arm = 4$ , b)  $Arm = 8$ , c)  $Arm = 16$ .

In 2D, the principle growth direction may be imposed by adding an angle of rotation to equation (2.70), and the expression of the capillary anisotropy may be written as:

$$W(\mathbf{n}) = W_0^* (1 + \varepsilon_4 \cos (4(\Theta - \Theta_0))) \quad (2.74)$$

Where  $\Theta = \arctan \frac{\partial \phi_{y^*}}{\partial \phi_{x^*}}$  and  $\Theta_0$  is the prescribed angle which provides the growth direction.

Figure 2.38 illustrates the effect of this rotation and also certifies that the result is not depending on it. In fact mesh evolves with adaptation during growth and follows the interface in all directions, unlike classical phase-field approaches, for which results may be grid dependent.

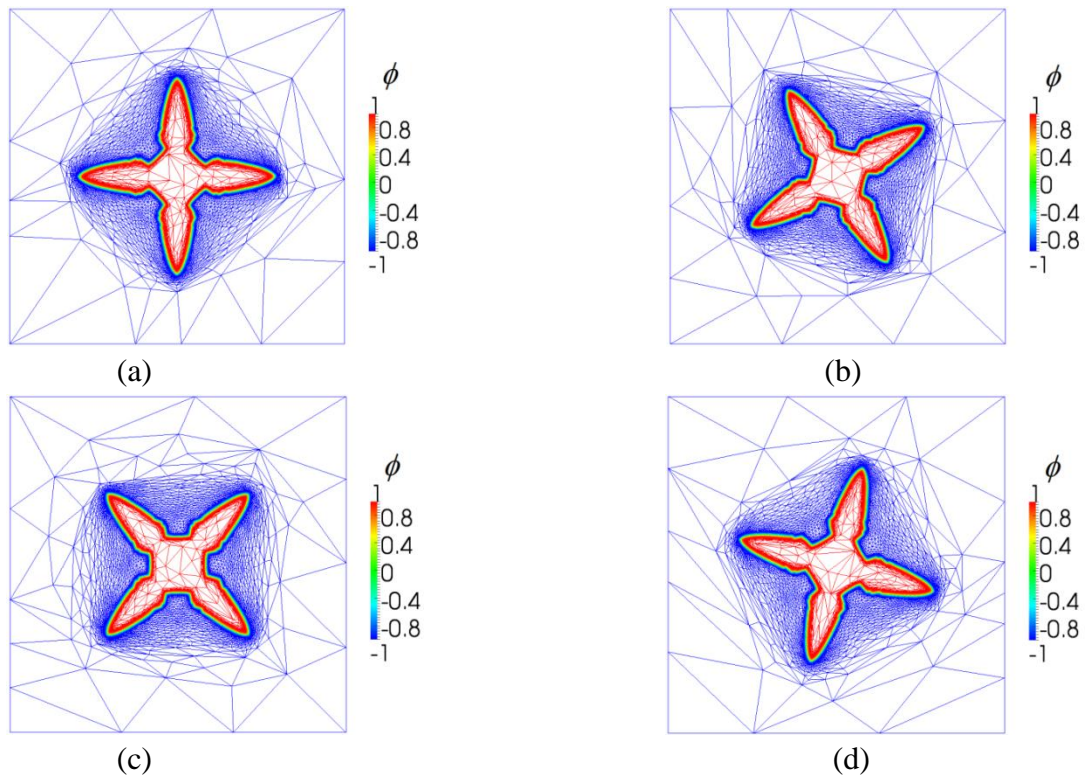


Figure 2.38 Four cases of dendritic growth, in 2D, with initial growth direction that has an angle with the horizontal axis of a)  $0^\circ$ , b)  $30^\circ$ , c)  $45^\circ$ , d)  $75^\circ$ .

Solid/liquid interfaces for the different growth prescribed directions are superposed in Figure 2.39. For each direction growth we take the interface and we rotate it to obtain a  $0^\circ$  oriented dendrite then we superpose the different interfaces and we see that they are the same.

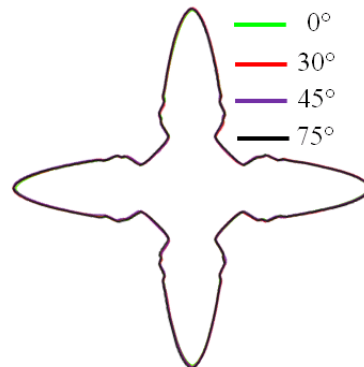


Figure 2.39 Superposed solid/liquid interfaces for the different growth directions.

### 2.3.5 3D thermal dendritic growth

We now solve the equations of the model in 3D using the anisotropy expression for the 3D case. We have a growing dendrite with arms in the  $\langle 100 \rangle$  directions corresponding to the main XYZ axes. We can have dendrite growing from the center of the domain or at the border of the domain. Computational time is higher in 3D than in 2D and the adaptive mesh is more complicated.

Because of the cubic symmetry case for the directions  $\langle 100 \rangle$ , simulation can be performed on 1/8 of the cube or even on 1/48 of it in the  $zxy$  symmetry plane. When the computational domain is 1/8 of the overall one, it is a cubic subdomain of linear size equal to half the domain size and we suppose the initial nucleus in the corner of coordinates (0,0,0). When the simulation is finished, we reconstruct the whole cubic domain to represent the dendrite by doing a symmetry  $\%X = 0$  and  $\%Y = 0$  and  $\%Z = 0$ .

In the case of 1/48, one has a tetrahedral subdomain and the initial nucleus appears in the vertex of the tetrahedron of coordinates (0,0,0). Some rotations and symmetries operations (rotation  $45^\circ$   $\%X$  symmetry  $\%Y$  rotation  $-45^\circ$   $\%X$ , rotation  $-45^\circ$   $\%Y$  symmetry  $\%X$  rotation  $45^\circ$   $\%Y$ , rotation  $45^\circ$   $\%Z$  symmetry  $\%X$  rotation  $-45^\circ$   $\%Z$ ) are performed to obtain the 1/8 of the cube then we do the three symmetries described before to obtain the cube.

To check the influence of using these symmetry properties, thermal dendritic growth is simulated using the finite element method on an isotropic structured mesh and an anisotropic unstructured adaptive mesh corresponding to 1/8 of the domain and on an anisotropic unstructured adaptive mesh corresponding to 1/48 of the domain. We use a domain of size  $[0;100] \times [0;100] \times [0;100]$ . Parameters are present in Table 2.12. The computational time reduces from the first case (1/8, isotrope), to the last cited one (1/48, anisotrope) from 160 h to 27 min, as shown in Figure 2.40. The number of elements  $NE$  for the 1/8 and the 1/48 cases are linked as follows:  $NE(1/8) = 6 NE(1/48)$ .

| Parameter                     | Symbol           | (a)       | (b)                                                   | (c)                                                   |
|-------------------------------|------------------|-----------|-------------------------------------------------------|-------------------------------------------------------|
| Number of elements            | $NE$             | 2 000 000 | $2 \cdot V_{\text{interface}}/h_{\text{min}}^2 + N_2$ | $2 \cdot V_{\text{interface}}/h_{\text{min}}^2 + N_2$ |
| Constant number of element    | $N_2$            | -         | 600 000                                               | 100 000                                               |
| Mesh size                     | $h_{\text{min}}$ | 1         | 0.4                                                   | 0.4                                                   |
| Interface thickness           | $W_0^*$          | 1         | 1                                                     | 1                                                     |
| Unit time                     | $\tau_0^*$       | 1         | 1                                                     | 1                                                     |
| Nucleus radius                | $R_0^*$          | 5         | 5                                                     | 5                                                     |
| Numerical initial temperature | $\theta_0$       | -0.65     | -0.65                                                 | -0.65                                                 |
| Numerical thermal diffusivity | $\alpha^*$       | 1         | 1                                                     | 1                                                     |
| Minimal error                 | $e_{\text{min}}$ | -         | $10^{-9}$                                             | $10^{-9}$                                             |
| Anisotropy frequency          | $\varepsilon_4$  | 0.05      | 0.05                                                  | 0.05                                                  |
| Time step                     | $\Delta \tau$    | 0.016     | $h_{\text{min}}/(10 \cdot v_{\text{tip}})$            | $h_{\text{min}}/(10 \cdot v_{\text{tip}})$            |
| Cores number                  | -                | 20        | 20                                                    | 20                                                    |
| Number of iterations          | -                | 1 410     | 1 410                                                 | 1 410                                                 |
| CPU time                      | $t_{\text{CPU}}$ | 160h      | 7h43min                                               | 27min                                                 |

Table 2.12 Parameters for thermal dendritic growth shown in Figure 2.40 and Figure 2.41.

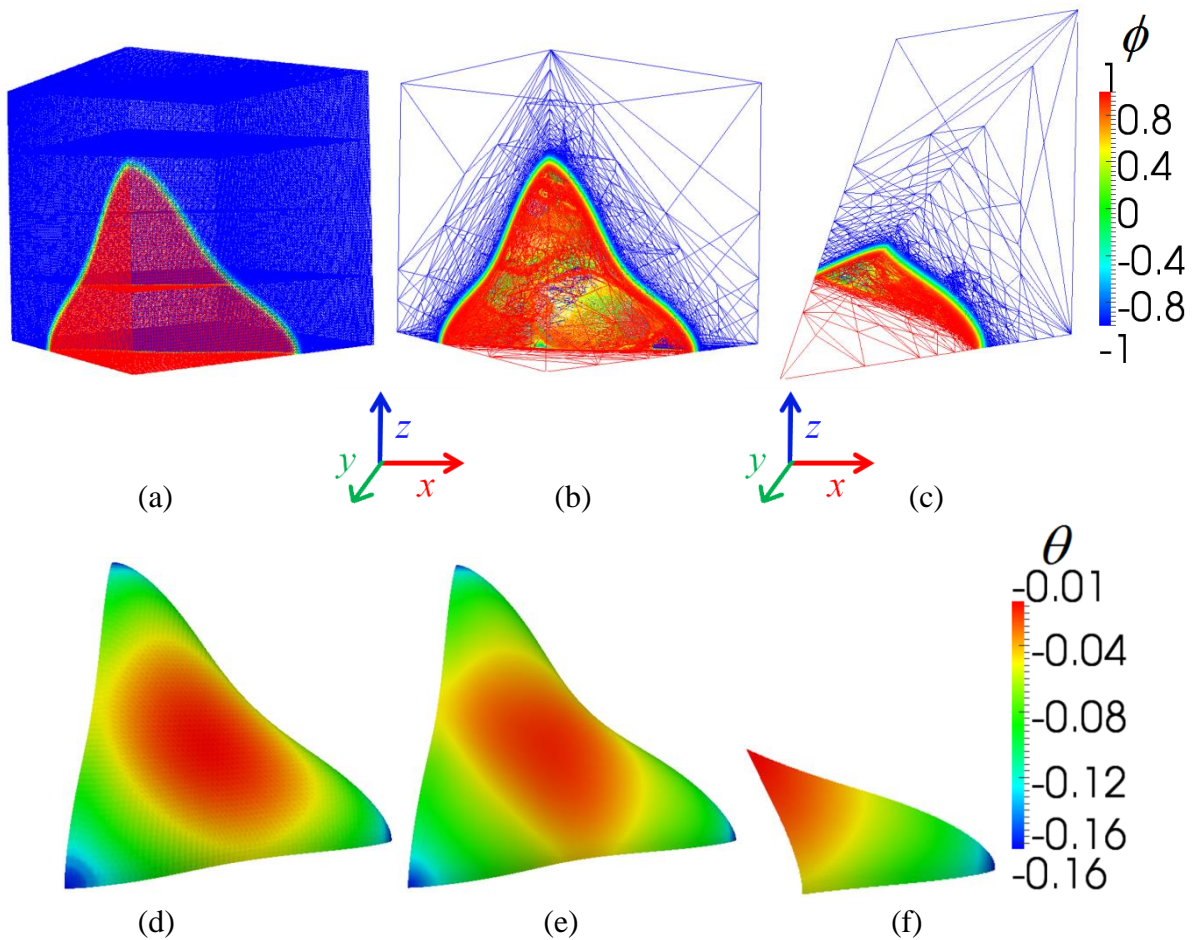


Figure 2.40 3D thermal dendritic growth computation using 20 cores, drawn at  $\tau = 256$  for a) a structured mesh for 1/8 of the domain with  $\Delta\tau = 0.016$  and  $h_{min} = 1$ ,  $NE = 2\,000\,000$ ,  $t_{CPU} = 160$  h, b) an unstructured anisotropic adaptive 1/8 mesh with  $\beta' = 10$ ,  $N_2 = 600\,000$ ,  $NE = 782\,000$ ,  $t_{CPU} = 7$  h 43 min c) an unstructured anisotropic adaptive 1/8 mesh with  $\beta' = 10$ ,  $N_2 = 100\,000$ ,  $NE = 132\,000$ ,  $t_{CPU} = 27$  min.

Figure 2.41 provides the comparison, for a developed state of the morphology of the solid/liquid interface in the  $\langle 100 \rangle$  direction growth. We have the same growth for 1/8 or 1/48 domain with a small difference at the dendrite tip. We can use 1/48 instead of 1/8 to reduce the CPU time and the memory in case of pure thermal dendritic growth.

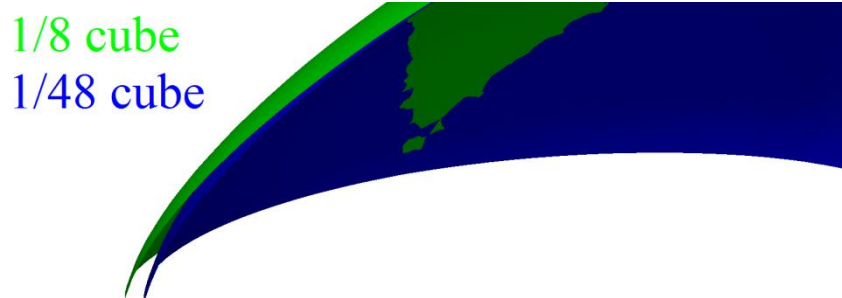


Figure 2.41 Zoom of the dendrite tip to show the difference between computations performed in 1/8 (anisotropic) and 1/48 (anisotropic) of the domain.

3D simulation for dendrite using 1/48 of a cube is further studied to benefit from this symmetry. A domain of size  $[0;1000] \times [0;1000] \times [0;1000]$  is used and parameters are present in Table 2.13. Mesh adaptation is based on  $(\phi, \theta)$ . Results are shown in Figure 2.42, after the reconstruction of the whole domain.

| Parameter                     | Symbol           | Value                                                   |
|-------------------------------|------------------|---------------------------------------------------------|
| Number of elements            | $NE$             | $2 \cdot V_{\text{interface}} / h_{\text{min}}^2 + N_2$ |
| Constant number of element    | $N_2$            | 2 000 000                                               |
| Mesh size                     | $h_{\text{min}}$ | 0.4                                                     |
| Interface thickness           | $W_0^*$          | 1                                                       |
| Unit time                     | $\tau_0^*$       | 1                                                       |
| Nucleus radius                | $R_0^*$          | 1                                                       |
| Numerical initial temperature | $\theta_0$       | -0.59                                                   |
| Numerical thermal diffusivity | $\alpha^*$       | 3.3897                                                  |
| Minimal error                 | $e_{\text{min}}$ | $10^{-9}$                                               |
| Anisotropy frequency          | $\varepsilon_4$  | 0.02                                                    |
| Time step                     | $\Delta \tau$    | $h_{\text{min}} / (10 \cdot v_{\text{tip}})$            |
| Cores number                  | -                | 30                                                      |
| Number of iterations          | -                | 2 000                                                   |
| CPU time                      | $t_{\text{CPU}}$ | 288h                                                    |

Table 2.13 Parameters for thermal dendritic growth shown in Figure 2.42.

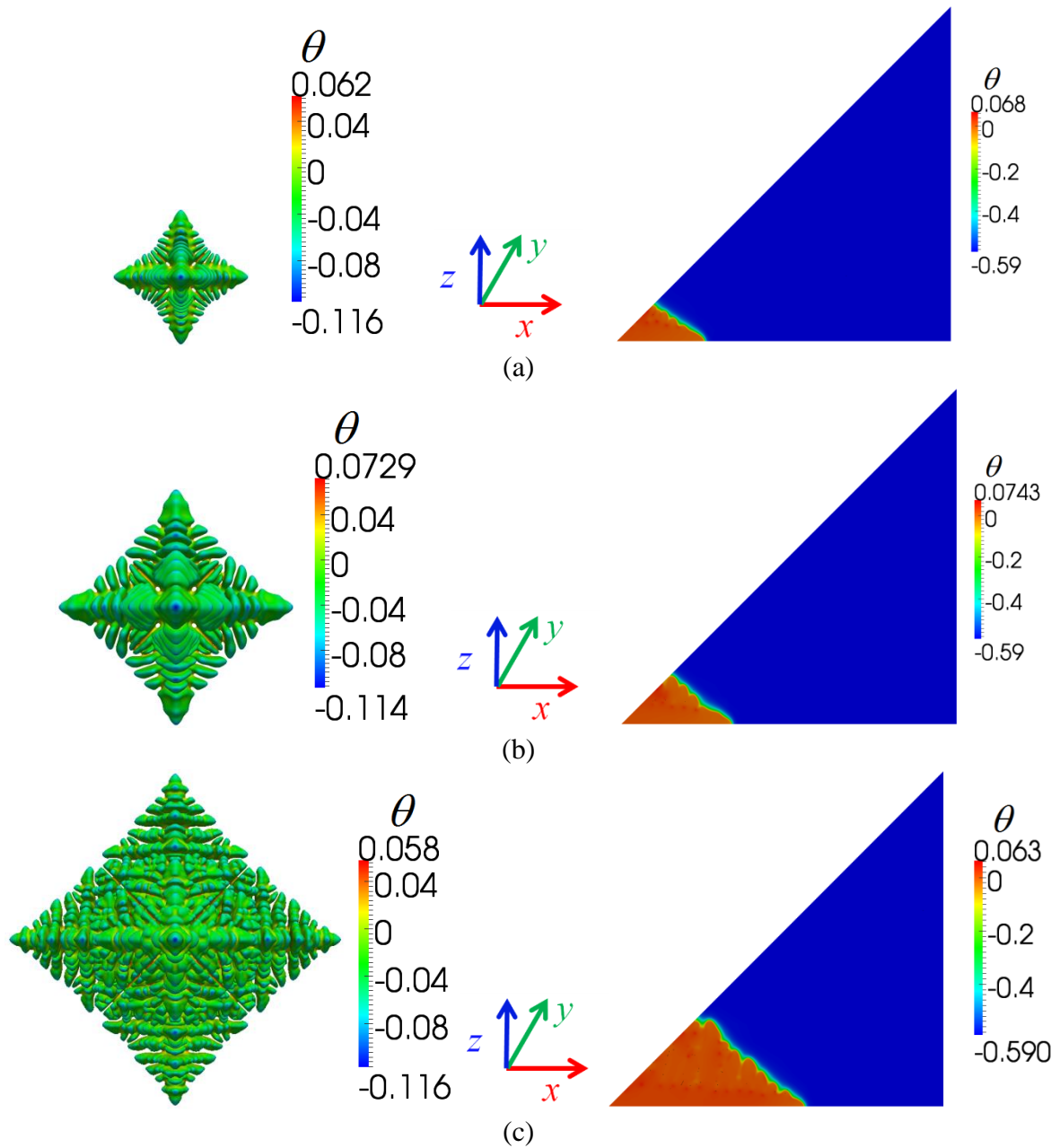


Figure 2.42 3D thermal dendritic growth showing: on the left, the solid/liquid interface and the computed temperature projected on this interface; on the right, the temperature distribution in the computational domain at a)  $\tau = 421.148$ , b)  $\tau = 526.361$ , c)  $\tau = 933.7$ .

## 2.4 Conclusion

Two equations are solved for the simulation of thermal dendritic growth: the phase-field equation and the energy conservation equation. These equations are solved after reformulating them with dimensionless variables:

$$\begin{aligned} \tau(\mathbf{n}) \frac{\partial \phi}{\partial \tau} - \nabla \cdot (W^2(\mathbf{n}) \nabla \phi) &= [\phi - \lambda \theta (1 - \phi^2)](1 - \phi^2) + \frac{\partial}{\partial x^*} \left( |\nabla \phi|^2 W(\mathbf{n}) \frac{\partial W(\mathbf{n})}{\partial (\partial_{x^*} \phi)} \right) \\ &+ \frac{\partial}{\partial y^*} \left( |\nabla \phi|^2 W(\mathbf{n}) \frac{\partial W(\mathbf{n})}{\partial (\partial_{y^*} \phi)} \right) + \frac{\partial}{\partial z^*} \left( |\nabla \phi|^2 W(\mathbf{n}) \frac{\partial W(\mathbf{n})}{\partial (\partial_{z^*} \phi)} \right) \end{aligned} \quad (2.75)$$

$$\frac{\partial \theta}{\partial \tau} - \alpha^* \Delta \theta = -\frac{1}{2} \frac{\partial \phi}{\partial \tau} \quad (2.76)$$

with

$$\theta = \frac{T - T_M}{L/c_p} \quad (2.77)$$

and

$$\phi = -\tanh \left( \frac{\eta}{W_0^* \sqrt{2}} \right) \quad (2.78)$$

We have used the finite element method with anisotropic unstructured adaptive meshing and parallel computing. The numerical methods used in our simulations, can reduce the CPU time compared with finite difference method using one core in Matlab by 1.8 times and using 16 cores about 30.5 times. Next chapter focuses on dendritic growth of metallic alloys mainly controlled by solutal exchanges.

## Résumé

Dans ce chapitre, nous avons présenté les équations utilisées dans le modèle développé, basé sur une approche champs de phase pour la croissance dendritique thermique. La représentation de l'interface solide/liquide utilise une fonction de tangente hyperbolique. Deux équations sont résolues : la conservation de l'énergie, pour obtenir la distribution de l'énergie ; l'équation de champs de phase, pour avoir l'évolution de l'interface solide/liquide. Plusieurs paramètres physiques influencent la morphologie obtenue. Nous avons, montré le rôle de la définition de l'anisotropie capillaire et de la diffusion thermique  $\alpha^*$  et le coefficient de capillarité  $d_0^*$ . La résolution numérique est présentée avec la méthode de remaillage utilisée et le calcul parallèle en utilisant différentes optimisations d'adaptation du pas de temps, du nombre de maille et des symétries du problème. A la fin une croissance dendritique est présentée en 2D avec une validation et une étude sur le temps de calcul. Une simulation en 3D est donnée.



## Chapter 3

### 3 Solutal model

|       |                                                                  |    |
|-------|------------------------------------------------------------------|----|
| 3.1   | Model equations .....                                            | 61 |
| 3.1.1 | Mass conservation equation .....                                 | 63 |
| 3.2   | Numerical resolution .....                                       | 65 |
| 3.2.1 | Finite element resolution of the mass conservation equation..... | 65 |
| 3.2.2 | Mesh adaptation .....                                            | 67 |
| 3.2.3 | 1D validation .....                                              | 68 |
| 3.3   | 2D dendritic growth.....                                         | 74 |
| 3.3.1 | Comparison with a model of direct growth.....                    | 74 |
| 3.3.2 | Comparison with other models .....                               | 75 |
| 3.3.3 | Parameter sensitivity study.....                                 | 77 |
| 3.4   | Conclusion.....                                                  | 81 |

#### 3.1 Model equations

Let us consider the phase diagram of a diluted binary alloy as schematized in Figure 3.1, where a single phase dominates the microstructure of the material. The system contains two components: the solvent (A) and the solute (B).

The Liquidus and Solidus transitions are approximated by straight lines of slope  $m$  and  $m/k$ , respectively, where  $k$  is the partition coefficient defined as the ratio of the concentrations at the interface and  $m$  is the Liquidus slope.

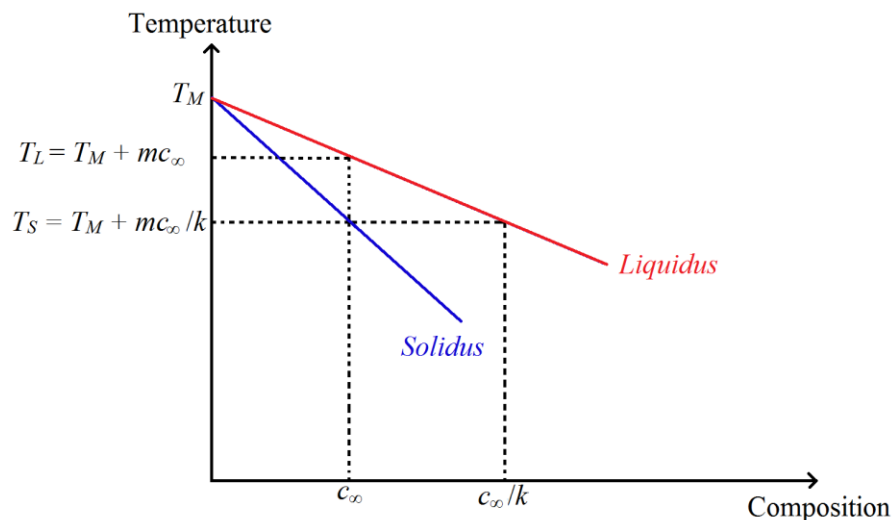


Figure 3.1 Phase diagram of a diluted binary alloy of average solute concentration  $c_\infty$ .  $T_M$  is the melting temperature of the pure body,  $T_L$  and  $T_S$ , are respectively, the Liquidus and solidus temperatures. For the considered alloy, the partition coefficient is  $k < 1$  and the Liquidus slope is  $m < 0$ .

Let us consider now the isothermal solute growth for the binary alloy. Supposing a zero solid-state solute diffusivity, the standard equations for the sharp interface model consists in:

$$\frac{\partial c}{\partial t} = D^l \Delta c \quad (3.1)$$

$$c_i (1 - k)v_n = -D^l \nabla c_i \quad (3.2)$$

$$T_i = T_M + m c_i - \Gamma \kappa_r - v_n / \mu_\kappa \quad (3.3)$$

where  $c$  is the phase composition,  $c_i$  is the composition at the interface, with  $c^l$  as  $c^s = kc^l$ .

One may then define again the dimensionless variables [RAM2004],  $U$  and  $\theta$ , as:

$$U = \left[ \frac{2c/c_\infty}{1 + k - (1 - k)\phi} - 1 \right] \left( \frac{1}{1 - k} \right) \quad (3.4)$$

$$\theta = \frac{T - T_M - mc_\infty}{L/c_p} \quad (3.5)$$

$c_\infty$  is the value of  $c$  far from the interface and is equal to the initial concentration of the alloy solute element. According to the above definitions,  $U$  is the dimensionless measure of the solute concentration.

The above free-boundary problem may be rewritten:

$$\frac{\partial U}{\partial \tau} = D^* \Delta U \quad (3.6)$$

$$[1 + (1 - k)U^l] v_n = -D^* \nabla U^l \quad (3.7)$$

$$\theta_i + Mc_\infty U_i = -d_0 \kappa_r - \beta v_n \quad (3.8)$$

In these equations, the dimensionless solute diffusivity is defined as:

$$D^* = \frac{D \tau_0}{W_0^2} \quad (3.9)$$

where the scaled magnitude of the liquidus slope is:

$$M = \frac{-m(1 - k)}{L/c_p} \quad (3.10)$$

As formulated previously, one may define the the free energy as a function of the non-dimensional composition  $U$ . Supposing a constant temperature, it may be given by:

$$F(\phi, T_M, c) = \int_{\Omega} \frac{W(\mathbf{n})^2}{2} |\nabla \phi|^2 + f(\phi, T_M, c) \, dV = \int_{\Omega} F^{int} \, dV \quad (3.11)$$

We use the same double-well potential  $g(\phi)$  as before to obtain the expression of  $f(\phi, T_M, c)$  as:

$$f(\phi, T_M, c) = g(\phi) + \frac{R_g T_M}{v_0} (c \ln c - c) + \bar{\varepsilon} c + \bar{g}(\phi) \frac{\Delta \varepsilon}{2} c \quad (3.12)$$

By applying the same reasoning as previously, one derives the Allen-Cahn equation for the phase-field function evolution, after performing the variable change of  $c$  in  $U$ :

$$\begin{aligned} \tau(\mathbf{n}) \frac{\partial \phi}{\partial \tau} - \nabla \cdot (W^2(\mathbf{n}) \nabla \phi) &= [\phi - \lambda(\theta + Mc_\infty U)(1 - \phi^2)](1 - \phi^2) + \frac{\partial}{\partial x^*} \left( |\nabla \phi|^2 W(\mathbf{n}) \frac{\partial W(\mathbf{n})}{\partial (\partial_{x^*} \phi)} \right) \\ &+ \frac{\partial}{\partial y^*} \left( |\nabla \phi|^2 W(\mathbf{n}) \frac{\partial W(\mathbf{n})}{\partial (\partial_{y^*} \phi)} \right) + \frac{\partial}{\partial z^*} \left( |\nabla \phi|^2 W(\mathbf{n}) \frac{\partial W(\mathbf{n})}{\partial (\partial_{z^*} \phi)} \right) \end{aligned} \quad (3.13)$$

Comparing the phase-field equation (2.75) for the thermal case and equation (3.13) for the isothermal solubal case, one observes the existence of a right-hand side expression, which is a function of  $U$  and  $\theta$ , even if  $\theta$  is a constant

### 3.1.1 Mass conservation equation

Determination of  $c$  is obtained by solving the mass conservation equation. The final form used in this work has been derived like in [RAM2004] and its resolution has been coupled to the one of the phase-field equation. In the following, an additional term for anti-trapping, reported by Ramirez [RAM2004], has also been considered.

We have previously shown how to obtain the phase-field equation from the free energy form using the Allen-Cahn equation [CAH1958]. The Cahn-Hilliard framework is also used to derive the mass conservation equation form considered here:

$$\frac{\partial c}{\partial t} = \nabla \cdot \left( M_c \nabla \frac{\delta F}{\delta c} - \mathbf{j}_{at} \right) = \nabla \cdot \left( M_c \nabla \left( \frac{\partial F^{int}}{\partial c} - \nabla \cdot \frac{\partial F^{int}}{\partial \nabla c} \right) - \mathbf{j}_{at} \right) = \nabla \cdot (M_c \nabla \mu_E - \mathbf{j}_{at}) \quad (3.14)$$

where  $M_c$  is the positive mobility related to the composition,  $\mathbf{j}_{at}$  the antitrapping term is used to recover local equilibrium at the interface and to eliminate interface stretching and surface diffusion effects that arise when the solubal diffusivities are unequal in the solid and liquid and  $\mu_E$  is the chemical potential. This equation may be also expressed as follows. This equation may be expressed as follows:

$$\frac{\partial c}{\partial t} = \nabla \cdot \left( M_c \nabla \left( \frac{R_g T_M}{v_0} \ln c + \bar{\varepsilon} + \bar{g}(\phi) \frac{\Delta \varepsilon}{2} \right) - \mathbf{j}_{at} \right) \quad (3.15)$$

Here,  $\bar{\varepsilon} = (\varepsilon_s + \varepsilon_l) / 2$ , being  $\varepsilon_s$  the energy density in the solid and  $\varepsilon_l$  the energy density in the liquid; and  $\bar{g}(\phi)$  is a function of  $\phi$  verifying that  $\bar{g}(\pm 1) = \pm 1$  when  $\phi = \pm 1$ , which corresponds to the solid and liquid phases. Using Fick's law of diffusion in the liquid, the form

$$M_c = \frac{v_0}{R_g T_M} D q(\phi) c \quad (3.16)$$

is chosen, where  $q(\phi)$  is the dimensionless function that dictates how the solute diffusivity varies through the diffuse interface. Equation (3.15) becomes:

$$\frac{\partial c}{\partial t} = \nabla \cdot \left( \frac{v_0}{R_g T_M} D q(\phi) c \nabla \left( \frac{R T_M}{v_0} \ln c + \bar{g}(\phi) \frac{\Delta \varepsilon}{2} \right) - \mathbf{j}_{at} \right) \quad (3.17)$$

This equation may be simplified to obtain:

$$\frac{\partial c}{\partial t} = \nabla \cdot \left( D q(\phi) c \nabla \left( \ln c + \bar{g}(\phi) \frac{v_0}{R_g T_M} \frac{\Delta \varepsilon}{2} \right) - \mathbf{j}_{at} \right) \quad (3.18)$$

From equation (3.14), it is known that:

$$\ln k = -\frac{\nu_0 \Delta \varepsilon}{R_g T_M} \quad (3.19)$$

It finally leads to:

$$\frac{\partial c}{\partial t} = \nabla \cdot \left( D q(\phi) c \nabla \left( \ln c - \bar{g}(\phi) \frac{\ln k}{2} \right) - \mathbf{j}_{at} \right) \quad (3.20)$$

From this latter, one other form for the mass conservation equation may be derived:

$$\frac{\partial c}{\partial t} = \nabla \cdot (D q(\phi) c \nabla u - \mathbf{j}_{at}) \quad (3.21)$$

Considering a first variable change, such that  $u = \ln \left( \frac{2c}{c_\infty (1+k - (1-k)\phi)} \right)$

The following expressions for  $q(\phi)$  and  $\mathbf{j}_{at}$  were chosen:

$$q(\phi) = \frac{1 - \phi}{1 + k - (1 - k)\phi} \quad (3.22)$$

$$\mathbf{j}_{at} = \frac{-c_\infty (1 - k) W_0}{2\sqrt{2}} \exp(u) \frac{\partial \phi}{\partial t} \frac{\nabla \phi}{|\nabla \phi|} \quad (3.23)$$

A second variable change brings us back to the dimensionless solute concentration chosen and given by equation (3.4),  $U$ , by computing:

$$U = \frac{\exp u - 1}{(1 - k)} \quad (3.24)$$

This means also that  $\Rightarrow u = \ln[(1 - k)U + 1]$  and  $\ln \left( \frac{2c}{c_\infty (1+k - (1-k)\phi)} \right) = \ln[(1 - k)U + 1]$

From this, one deduces that  $\frac{2c}{c_\infty (1+k - (1-k)\phi)} = (1 - k)U + 1$

and  $c = [(1 - k)U + 1] \frac{c_\infty}{2} (1 + k - (1 - k)\phi)$ . Derivation of  $c$  with respect to time provides:

$$\frac{\partial c}{\partial t} = \frac{c_\infty}{2} \left( (1 - k) (1 + k - (1 - k)\phi) \frac{\partial U}{\partial t} + \left( - (1 - k) [(1 - k)U + 1] \frac{\partial \phi}{\partial t} \right) \right) \quad (3.25)$$

This expression is then used in the mass conservation equation to obtain the evolution equation of the dimensionless solute concentration,  $U$ , as:

$$\begin{aligned} & \frac{c_\infty}{2} \left( (1 - k) (1 + k - (1 - k)\phi) \frac{\partial U}{\partial \tau} + \left( - (1 - k) [(1 - k)U + 1] \frac{\partial \phi}{\partial \tau} \right) \right) = \\ & \nabla \cdot \left( D^* \frac{1 - \phi}{1 + k - (1 - k)\phi} \frac{c_\infty}{2} [(1 - k)U + 1] (1 + k - (1 - k)\phi) \nabla U \frac{1 - k}{(1 - k)U + 1} \right) \\ & + \nabla \cdot \left( c_\infty \frac{W(\mathbf{n})}{2\sqrt{2}} (1 - k) [(1 - k)U + 1] \frac{\partial \phi}{\partial \tau} \frac{\nabla \phi}{|\nabla \phi|} \right) \end{aligned} \quad (3.26)$$

This equation can be simplified to obtain:

$$\begin{aligned} & \frac{1}{2} (1 + k - (1 - k)\phi) \frac{\partial U}{\partial \tau} - \nabla \cdot \left( D^* \frac{1 - \phi}{2} \nabla U \right) = \\ & \nabla \cdot \left( \frac{W(\mathbf{n})}{2\sqrt{2}} (1 + (1 - k)U) \frac{\partial \phi}{\partial \tau} \frac{\nabla \phi}{|\nabla \phi|} \right) + \frac{1}{2} (1 + (1 - k)U) \cdot \frac{\partial \phi}{\partial \tau} \end{aligned} \quad (3.27)$$

Which is the final chosen form, solved using our finite element library.

## 3.2 Numerical resolution

The phase-field equation is solved using the same methods as in the thermal case. The only difference is that the divergence term on the left hand-side of the solute equation is not further developed, since  $D^*(1 - \phi)/2$  does not depend on the unknown  $U$ . In the following, resolution of the mass conservation equation (3.27) is detailed, even if close to the resolution of the energy equation, since both are of the convection-diffusion-reaction type.

### 3.2.1 Finite element resolution of the mass conservation equation

For a sake of simplicity, we note  $D = D^*(1 - \phi)/2$ , and  $f$  as the source term, which represents the right hand side of equation (3.27). The strong formulation for our problem can be thus written as:

$$\begin{cases} \frac{\partial U}{\partial \tau} - \nabla \cdot (D \nabla U) = f & \text{in } \Omega \times (0, T) \\ U = 0 & \text{on } \partial \Omega \times (0, T) \\ U(\cdot, 0) = U_0 & \text{in } \Omega \end{cases} \quad (3.28)$$

The corresponding weak formulation is: find  $U \in \mathbf{V} := H_0^1(\Omega) / \forall \psi \in \mathbf{V}$ , such that

$$\frac{\partial U}{\partial \tau} \psi - \nabla \cdot (D \nabla U) \psi = f \psi \quad (3.29)$$

Integration over  $\Omega$  gives,

$$\int_{\Omega} \frac{\partial U}{\partial \tau} \psi \, dV - \int_{\Omega} \nabla \cdot (D \nabla U) \psi \, dV = \int_{\Omega} f \psi \, dV \quad (3.30)$$

Using the integration by parts, one obtains:

$$- \int_{\Omega} \nabla \cdot (D \nabla U) \psi \, dV = \int_{\Omega} D \nabla U \nabla \psi \, dV + \int_{\partial \Omega} D \nabla U \cdot \psi \, dS = \int_{\Omega} D \nabla U \nabla \psi \, dV \quad (3.31)$$

And since  $\psi = 0$  on  $\partial \Omega$ , integration becomes:

$$\int_{\Omega} \frac{\partial U}{\partial \tau} \psi \, dV + \int_{\Omega} D \nabla U \nabla \psi \, dV = \int_{\Omega} f \psi \, dV \quad (3.32)$$

The weak formulation can be written clearly as: for a given  $f \in H^{-1}(\Omega)$  and  $D \in L^\infty(\Omega)$ , find  $U \in \mathbf{V} := H_0^1(\Omega)$  such that

$$\left( \frac{\partial U}{\partial \tau}, \psi \right) + (D \nabla U, \nabla \psi) = (f, \psi)_{H_0^1(\Omega)} \quad (3.33)$$

As previously, we consider the discretization  $\mathcal{T}_h$  of  $\Omega$  into a set of elements  $N_{el}$  elements  $K$  and we approach the functional space  $\mathbf{V}$  by a finite dimensional one,  $\mathbf{V}_h$ , spanned by continuous piecewise polynomials:  $\mathbf{V}_h = \{ \psi^h \in H_0^1(\Omega), \psi^h \text{ is linear for } K \in \mathcal{T}_h \}$

The Galerkin discrete problem consists now in finding  $U^h \in \mathbf{V}_h$  such that:

$$\left( \frac{\partial U^h}{\partial \tau}, \psi^h \right) + (D \nabla U^h, \nabla \psi^h) = (f, \psi^h) \quad (3.34)$$

This may be rewritten in the integral form:

$$\int_{\Omega} \frac{\partial U^h}{\partial \tau} \psi^h dV_h + \int_{\Omega} D \nabla U^h \nabla \psi^h dV_h = \int_{\Omega} f \psi^h dV_h \quad (3.35)$$

Each integral is the sum over the element of  $\Omega$ , leading to:

$$\sum_{e=1}^{N_{el}} \int_{\Omega_e} \frac{\partial U^h}{\partial \tau} \psi^h dV_h + \sum_{e=1}^{N_{el}} \int_{\Omega_e} D \nabla U^h \nabla \psi^h dV_h = \sum_{e=1}^{N_{el}} \int_{\Omega_e} f \psi^h dV_h \quad (3.36)$$

Since we are using the first order linear interpolation for unknowns and test function, we can replace  $U^h = \sum_{i=1}^N U_i^h N_i$  and  $\nabla U^h = \sum_{i=1}^N U_i^h \nabla N_i$  taking  $(N_i)_{i=1, \dots, N}$  the finite element vector space basis,  $U_i^h$  are computed locally in each node.

$$\begin{aligned} \sum_{e=1}^{N_{el}} \int_{\Omega_e} \sum_{i=1}^N \frac{\partial U_i^h}{\partial \tau} N_i N_j dV_h + \sum_{e=1}^{N_{el}} \int_{\Omega_e} \sum_{i=1}^N D U_i^h \nabla N_i \nabla N_j dV_h \\ = \sum_{e=1}^{N_{el}} \int_{\Omega_e} f N_j dV_h \end{aligned} \quad (3.37)$$

Previous system is rewritten as:

$$\begin{aligned} \sum_{e=1}^{N_{el}} \int_{\Omega_e} N_i N_j dV_h \sum_{i=1}^N \frac{\partial U_i^h}{\partial \tau} + \sum_{e=1}^{N_{el}} \int_{\Omega_e} D \nabla N_i \nabla N_j dV_h \sum_{i=1}^N U_i^h \\ = \sum_{e=1}^{N_{el}} \int_{\Omega_e} f N_j dV_h \end{aligned} \quad (3.38)$$

After simplification, we obtain:

$$\sum_{e=1}^{N_{el}} \int_{\Omega_e} N_i N_j dV_h \frac{\partial U^h}{\partial \tau} + \sum_{e=1}^{N_{el}} \int_{\Omega_e} D \nabla N_i \nabla N_j dV_h U^h = \sum_{e=1}^{N_{el}} \int_{\Omega_e} f N_j dV_h \quad (3.39)$$

The final linear matrix system obtained reads;

$$M_m \dot{\mathcal{U}} + K_d \mathcal{U} = F \quad (3.40)$$

Where  $\mathcal{U}$  is the vector of nodal unknowns,  $M_m$  is the mass matrix,  $K_d$  is the stiffness matrix and  $F$  is the internal source vector. This system must be solved to obtain the numerical boundary conditions. The coefficient matrices and the load vector are defined as follows:

$$M_m = \mathbf{A}_{i=1}^{N_{el}} \int_{K_i} N_i N_j dK$$

$$K_d = \mathbf{A}_{i=1}^{N_{el}} \int_{K_i} D \nabla N_i \nabla N_j dK$$

$$F = \mathbf{A}_{i=1}^{N_{el}} \int_{K_i} f N_j dK$$

With  $N_i$  the linear interpolation function at node  $i$  and  $\mathbf{A}$  is the matrix assembly operator, defined in such a way that we have:  $K = \mathbf{A}_{i=1}^{N_{el}} K_i$ .

The linear system of equations issuing from the discretization is solved implicitly using the conjugate bi gradient-least squares method (BCGSL). There is also preconditioning to the resolution using the Jacobi method with incomplete factorization LU per block of size 2.

A small indication to explain why we are using the developed form of the divergence term for the phase-field equation and the non-developed form of the divergence for the solute equation.

Remark:

The diffusion term for the phase-field equation depends on  $\phi$ , so the equation is non linear. On the other hand, the diffusion term for the solute equation does not depend on  $U$ , so we have a linear equation. The same finite element solver has been used for both equations and is based on the construction of a linear system. To accelerate convergence, the divergence term in the left hand-side of the phase-field equation has been developed and rewritten allowing the elimination of the diffusion term inside it. Figure 3.2 recalls the results obtained for convergence during thermal growth when this development has not been considered, showing that the high non-linearity on the phase-field equation needs this special treatment (which avoids also the implementation of a particular non-linear scheme). The blue line represents the variation of the adapted number of element depending on the dendritic growth for each case. When we increase  $h_{min}/W_0^*$  the number of element  $N_1$  decreases because we have bigger elements, but when we increase  $W_0^*/d_0^*$ ,  $N_1$  increases because the interface thickness increase and we have more element inside with the size of  $h_{min}$ .

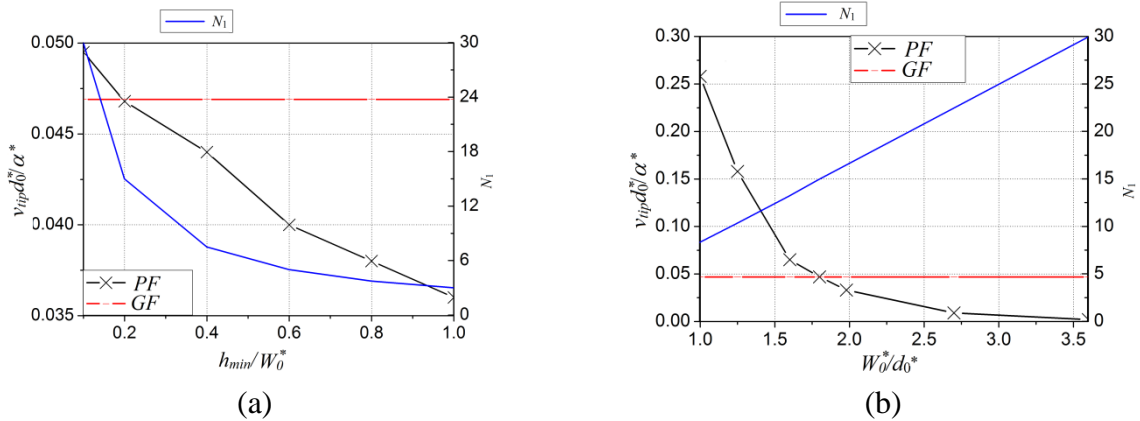


Figure 3.2 Dimensionless tip velocity as a function of the grid spacing  $h_{min}$  and interface thickness  $W_0^*$  for  $\Delta = 0.65$ ,  $d_0^*/W_0^* = 0.554$  and  $N_2 = 25\,000$ . The red line corresponds to the value obtained from the Green function calculation. a)  $W_0^* = 1$ , b)  $h_{min} = 0.4$ .

### 3.2.2 Mesh adaptation

The methodology developed to build the metric field, described in section 2.2.2, is used to minimize the error on  $\phi$  and  $U$ , by computing the error on the vector  $\zeta = (\phi, U)$ . Mesh sizes are

small at the solid/liquid interface, following the high gradient of  $\phi$ , but the mesh is also fine in the part of the domain where the solute composition gradient is high, as illustrated in Figure 3.3, where one may observe that the mesh size transition well follows the solute diffusion layer around the solid/liquid interface.

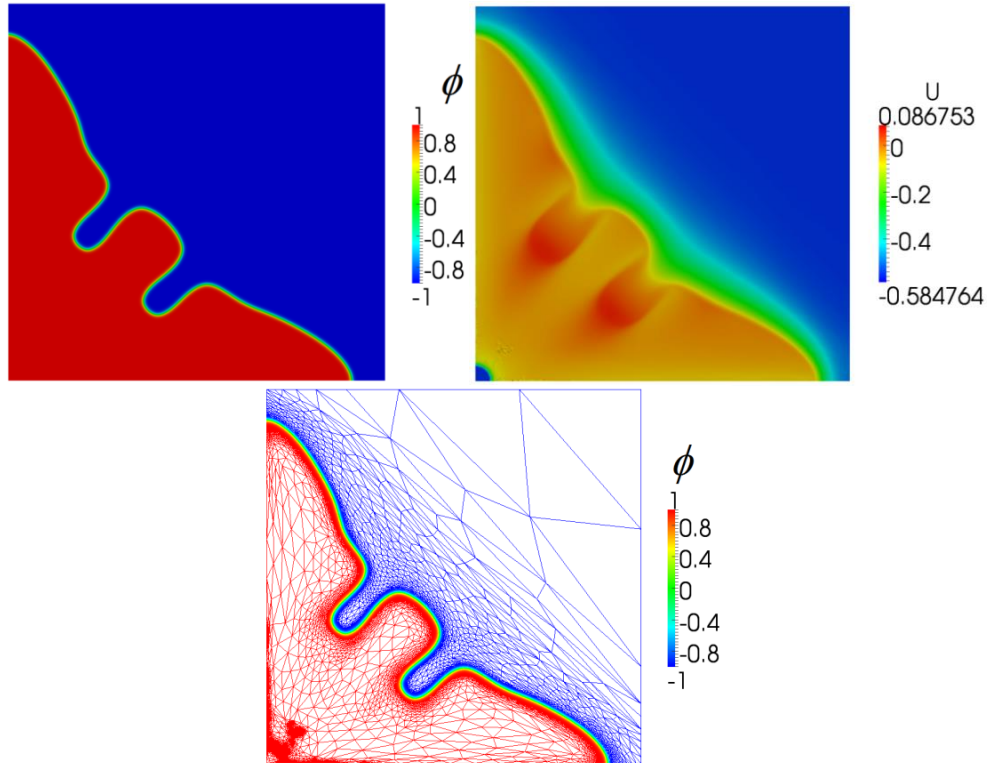


Figure 3.3 Illustration of the obtained adapted mesh, using  $\phi$  and  $U$  solutions of a solutal dendritic growth, drawn at a final stage of the growth simulation.

### 3.2.3 1D validation

To validate the developed solver and check the sensitivity of the methodology to certain numerical features, the proposed solutal model was applied to a 1D case. Numerical solutions for the composition profiles and the growth velocity are thus compared to the analytical ones, which have been developed in Appendix C. The analytical form for the steady-state solute composition, as a function of the interface position coordinate,  $x_0^*$ , is given by [AAR1970]:

$$c(x^*, \tau) = c_\infty + (c_{l/s} - c_\infty) \frac{\text{Erfc}\left(\frac{\lambda_c (x^* - x_0^*)}{2(x_{0t}^* - x_0^*)}\right)}{\text{Erfc}\left(\frac{\lambda_c}{2}\right)} \quad (3.41)$$

Here,  $x^*$  is the non-dimensional position,  $x_{0t}^*$  is the non-dimensional position at instant  $t$ ,  $\lambda_c$  is a constant in one-dimensional solution- stationary interface position and Erfc is the *erf* function, detailed in Appendix B. This analytical equation is true for the non-stationary velocity case and a planar precipitate. This means that solute compositions in the solid and in the liquid are different and that the growth velocity decreases with respect to the steady case,

where  $v = \frac{\lambda_c \sqrt{D^*}}{2\sqrt{\tau}}$ , and will tend towards zero. The solution obtained for the composition fields is schematically plotted in Figure 3.4.

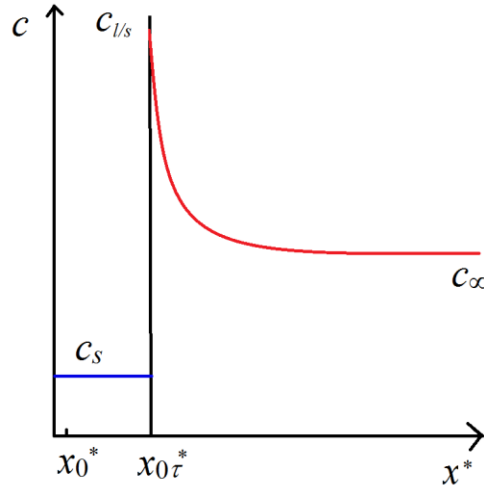


Figure 3.4 Composition profile at a certain time for a non-stationary velocity, when  $k < 1$  and  $\Omega_c < 1$ .

Simulation of solidification has been performed in a  $[-1600;1600]$  1D domain [ref], with  $\Delta x^* = 0.4$ . The function  $\phi = -\tanh\left(\frac{x^*}{W_0^* \sqrt{2}}\right)$  has been used to represent the solid, the liquid and their interface. We have considered  $\theta_0 = -0.340$ , 8 000 nodes,  $x_0^* = -1500$ ,  $k = 0.15$ ,  $M_{c_\infty} = 0.15$ ,  $D^* = 2$ ,  $\Delta\tau = 0.008$ ,  $\beta = 1.5$ ,  $U_0 = 2$  and  $\lambda = 1$ . The solid/liquid interface diffuses from the initial position  $x_0^*$  to the end of the domain, with the composition field. To study the analytical and numerical comparison when  $\Omega_c \rightarrow 1$  ( $c^s = c^l$ ), we have chosen different values for  $\Omega_c$ . For that, we compute, for a certain  $c_\infty$  (initial composition in the domain) and  $k$ , the composition in the solid  $c^s$  and the composition that we should have at the interface  $c^{l/s}$  for a constant temperature, using the equation for the supersaturation  $\Omega_c$ , given by:

$$\Omega_c = \frac{c_\infty - c^{l/s}}{c^s - c^{l/s}} \quad (3.42)$$

$$c^{l/s} = \frac{T_0 - T_M}{m} = \frac{\theta_0(1-k)}{-M} + c_\infty \quad \text{and} \quad c^s = kc^{l/s} \quad (3.43)$$

To start the simulation, we also need  $\theta_0$ , computed from the equations above, and  $U_0$  obtained from  $c_\infty$  using equation (3.4). Figure 3.5 shows the different composition profiles in the liquid for different  $\Omega_c$  at different adimensional instants ( $\tau_1 = 800$ ,  $\tau_2 = 4\,000$ ,  $\tau_3 = 8\,872$ ,  $\tau_4 = 19\,776$ ,  $\tau_5 = 34\,400$  and  $\tau_6 = 69\,256$ ).

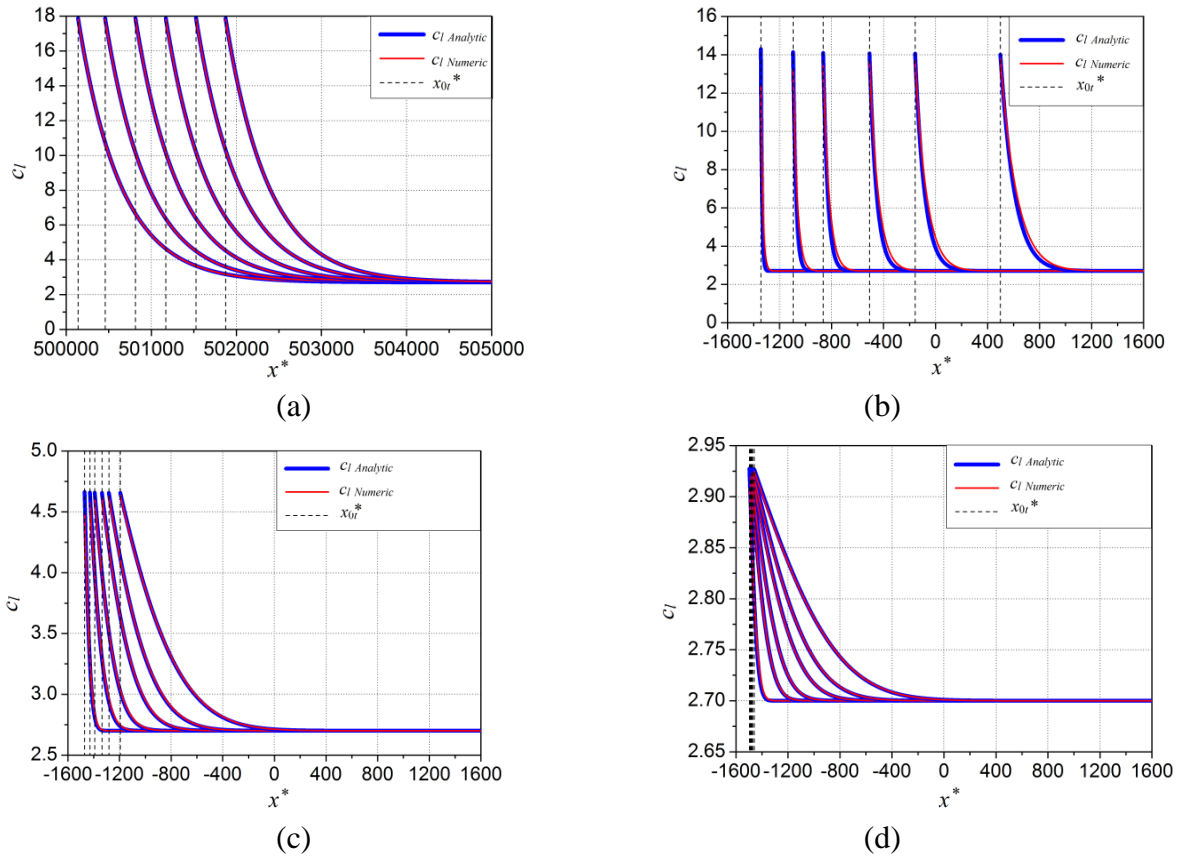


Figure 3.5 Analytical and numerical profiles of liquid composition around the interface for, a)  $c_\infty = 2.7$ ,  $c^s = 2.682$ ,  $c^{l/s} = 17.88$ ,  $\lambda_c = 44.654361$  and  $\Omega_c = 0.999$ , b)  $c_\infty = 2.7$ ,  $c^s = 2.105$ ,  $c^{l/s} = 14.033$ ,  $\lambda_c = 5.882473$  and  $\Omega_c = 0.950$ , c)  $c_\infty = 2.7$ ,  $c^s = 0.69825$ ,  $c^{l/s} = 4.655$ ,  $\lambda_c = 0.849279$  and  $\Omega_c = 0.494$ , d)  $c_\infty = 2.7$ ,  $c^s = 0.439$ ,  $c^{l/s} = 2.9268$ ,  $\lambda_c = 0.109295$  and  $\Omega_c = 0.091$ . The different curves on each plot represent different instants: ( $\tau_1 = 800$ ,  $\tau_2 = 4\,000$ ,  $\tau_3 = 8\,872$ ,  $\tau_4 = 19\,776$ ,  $\tau_5 = 34\,400$  and  $\tau_6 = 69\,256$ ). In the first case, a zoom at the interface region has been done.

Analytical (blue) and numerical (red) solutions are plotted in Figure 3.5. In the numerical profile, we observe that the value of  $c^{l/s}$  is not the same as the analytical computed one, but after some iteration, when the velocity decreases and small variations occur, the numerical composition at the interface converges to the analytical one. As we have a constant temperature, when we reach the analytical  $c^{l/s}$ , the composition profile cannot have higher values than this one, but its slope continues increasing. In addition, the growth velocity decreases when decreasing  $\Omega_c$ . Figure 3.6 shows the variation of the velocity for different  $\Omega_c$ . One observes that the analytical velocity is always the same. However, for  $\Omega_c \approx 1$ , we notice that this analytical velocity has not been reached for the assumed size of the computational domain. To overcome with this problem, the domain has been increased to obtain the same velocity in the numerical simulation as the analytical one, and the graph of the composition comparison has been drawn.

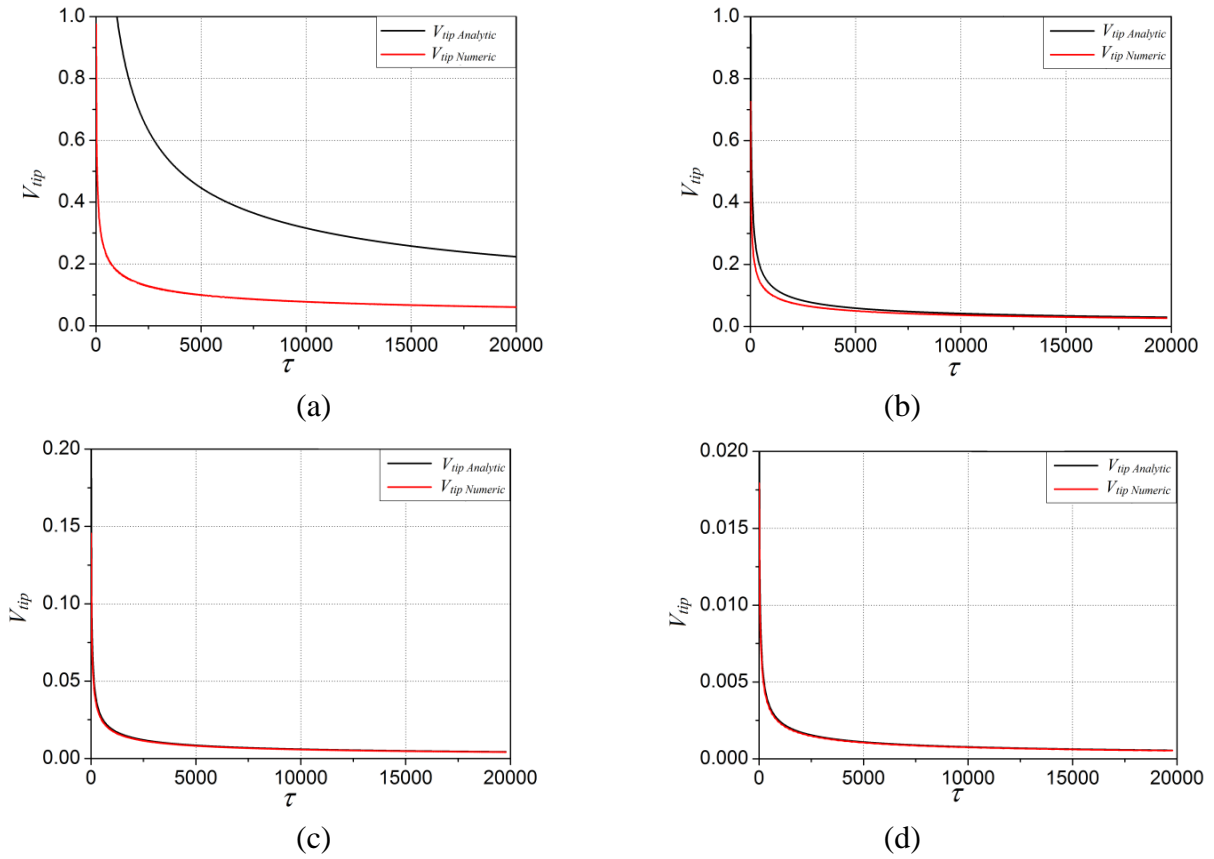


Figure 3.6 Evolution of the growth velocity as a function of time for, a)  $\Omega_c = 0.999$ , b)  $\Omega_c = 0.950$ , c)  $\Omega_c = 0.494$ , d)  $\Omega_c = 0.091$ .

After validating the numerical results concerning the growth velocity, one must compare the exponential analytical solution to the Erfc analytical one, for the composition profile, to see if we obtain the same profiles when  $\Omega_c \rightarrow 1$ . Figure 3.7 shows that the Erfc and the exponential profiles are not comparable when  $\Omega_c$  is far from 1. The more we approach from  $\Omega_c = 1$ , the more they become coincident.

To obtain an analytical expression for the dimensionless composition  $U$ , we must solve the following equation

$$v_n^{st} \frac{\partial U}{\partial x^*} + D^* \frac{\partial^2 U}{\partial x^{*2}} = 0 \quad (3.44)$$

with the interface condition:

$$[1 + (1 - k) U_i] v_n^{st} = -D^* \partial_{x^*} U|_l \quad (3.45)$$

and the far-field boundary condition:

$$\lim U(x^*) = U_0 \text{ when } x^* \rightarrow +\infty \quad (3.46)$$

The following 1D differential equation having  $U$  as variable is solved:

$$D^* U'' + v_n^{st} U' = 0 \quad (3.47)$$

The solution for this equation can be written as:

$$U = c_1 \exp(ax^*) + c_2 \exp(bx^*) \text{ with } a = 0 \text{ and } b = -v_n^{st}/D^* \quad (3.48)$$

$$\text{or } U = c_1 + c_2 \exp\left(\frac{-v_n^{st} x^*}{D^*}\right)$$

The boundary and interface conditions are used to find the constant values  $c_1 = U_0$  and  $c_2 = \frac{1 + U_0(1 - k)}{k}$ , leading thus the final form of the analytical solution for the dimensionless solute composition distribution:

$$U_{Anal} = U_0 + \frac{1 + U_0(1 - k)}{k} \exp\left(\frac{-v_n^{st} x^*}{D^*}\right) \quad (3.49)$$

One may demonstrate analytically that this exponential equation fits with the Erfc solution when  $\Omega_c \rightarrow 1$  (or  $\lambda_c \rightarrow \infty$ ) as obtained in the numerical results. Replacing in (C5) in Appendix C, we have:

$$\frac{\sqrt{\pi}}{2} \lambda_c \exp\left(\frac{\lambda_c^2}{4}\right) \text{Erfc}\left(\frac{\lambda_c}{2}\right) \approx 1 \quad (3.50)$$

Defining  $r = x^* - x_0^*$  and  $R = x_{0r}^* - x_0^*$ ,

$$\frac{\text{Erfc}\left(\frac{r}{2\sqrt{D^*}\tau}\right)}{\text{Erfc}\left(\frac{\lambda_c}{2}\right)} \approx \frac{\frac{2}{\sqrt{\pi}} \frac{\sqrt{D^*}\tau}{r} \exp\left(-\frac{r^2}{2\sqrt{D^*}\tau}\right)^2}{\frac{2}{\sqrt{\pi}} \lambda_c \exp\left(-\frac{\lambda_c^2}{4}\right)} \quad (3.51)$$

After simplification,

$$\frac{\text{Erfc}\left(\frac{r}{2\sqrt{D^*}\tau}\right)}{\text{Erfc}\left(\frac{\lambda_c}{2}\right)} \approx \frac{\lambda_c \sqrt{D^*}\tau}{r} \exp\left(\frac{1}{4}\left(\lambda_c^2 - \frac{r^2}{D^*\tau}\right)\right) \quad (3.52)$$

$$\frac{\text{Erfc}\left(\frac{r}{2\sqrt{D^*}\tau}\right)}{\text{Erfc}\left(\frac{\lambda_c}{2}\right)} \approx \frac{R}{r} \exp\left(\frac{1}{4}\left(\frac{R^2}{D^*\tau} - \frac{r^2}{D^*\tau}\right)\right) \quad (3.53)$$

$$\frac{\text{Erfc}\left(\frac{r}{2\sqrt{D^*}\tau}\right)}{\text{Erfc}\left(\frac{\lambda_c}{2}\right)} \approx \frac{R}{r} \exp\left(\frac{1}{4}\left(\frac{(R-r)(R+r)}{D^*\tau}\right)\right) \quad (3.54)$$

Near the interface  $r \sim R$  so we obtain:

$$\frac{\operatorname{Erfc}\left(\frac{r}{2\sqrt{D^* \tau}}\right)}{\operatorname{Erfc}\left(\frac{\lambda_c}{2}\right)} \approx \frac{R}{r} \exp\left(\frac{1}{4} \left(\frac{(R-r)(2R)}{D^* \tau}\right)\right) \quad (3.55)$$

$$\frac{\operatorname{Erfc}\left(\frac{r}{2\sqrt{D^* \tau}}\right)}{\operatorname{Erfc}\left(\frac{\lambda_c}{2}\right)} \approx \frac{R}{r} \exp\left(\left(\frac{(R-r)R}{D^* 2\tau}\right)\right) \quad (3.56)$$

Velocity can be expressed as:

$$v = \frac{\lambda_c \sqrt{D^*}}{2\sqrt{\tau}} = \frac{R}{2\tau} \quad (3.57)$$

Then equation (3.56) becomes:

$$\frac{\operatorname{Erfc}\left(\frac{r}{2\sqrt{D^* \tau}}\right)}{\operatorname{Erfc}\left(\frac{\lambda_c}{2}\right)} \approx \exp\left(\left(\frac{-(r-R)}{D^*} v\right)\right) \quad (3.58)$$

Replacing the value of Erfc by this exp equality in the analytical expression (C6) in Appendix C, we obtain the following analytical expression, valid for  $\Omega_c = 1$ :

$$U(1-k) + 1 = U_0(1-k) + 1 + \left(\frac{U_0(1-k) + 1}{k} - U_0(1-k) - 1\right) \exp\left(\frac{-(r-R)}{D^*} v\right) \quad (3.59)$$

Which may lead to:

$$U = U_0 + \left(\frac{U_0}{k} + \frac{1}{k(1-k)} - U_0 - \frac{1}{(1-k)}\right) \exp\left(\frac{-(r-R)}{D^*} v\right) \quad (3.60)$$

$$U = U_0 + \left(\frac{U_0(1-2k+k^2) + (1-k)}{k(1-k)}\right) \exp\left(\frac{-(r-R)}{D^*} v\right) \quad (3.61)$$

Finally,

$$U = U_0 + \left(\frac{1+U_0(1-k)}{k}\right) \exp\left(\frac{-(r-R)}{D^*} v\right) \quad (3.62)$$

This is equivalent to equation (3.49) when  $\lambda_c \rightarrow \infty$  or  $\Omega_c \rightarrow 1$ .

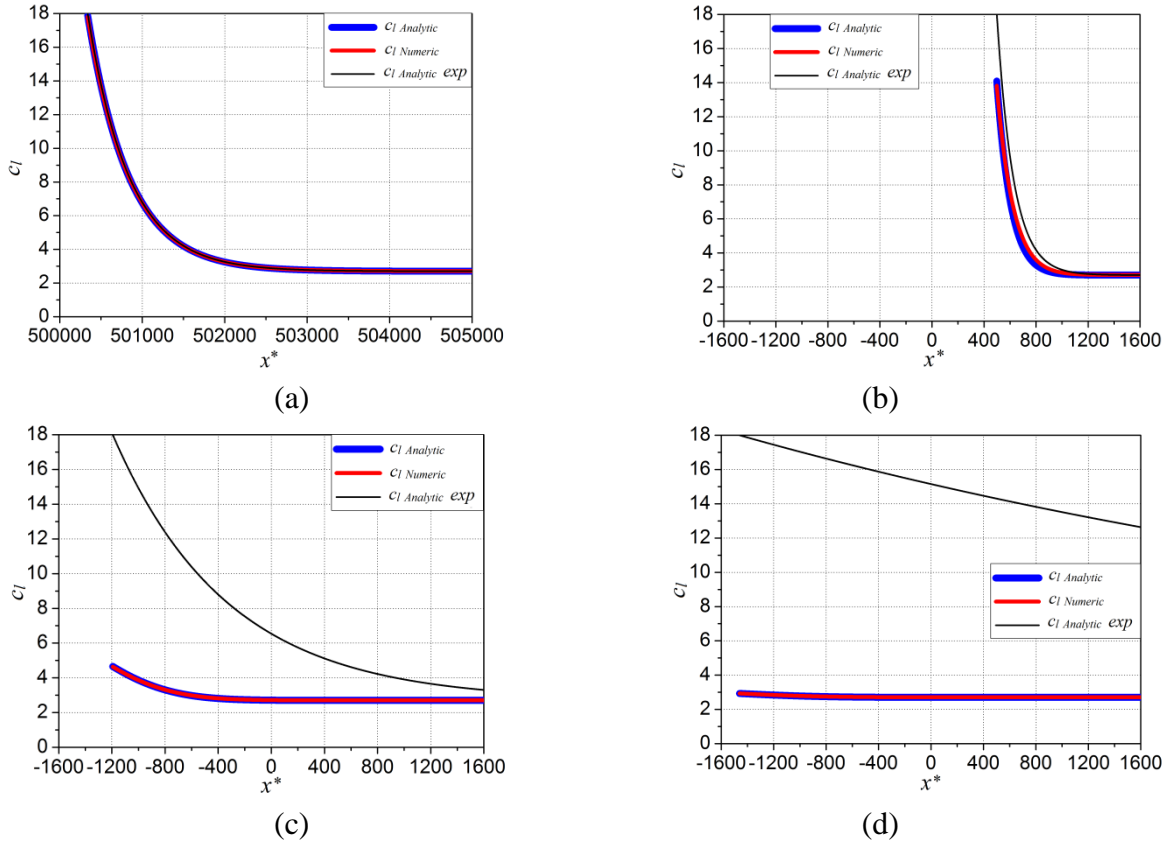


Figure 3.7 Liquid composition profiles around the interface: comparison between numerical and analytical (exp and Erfc values) for, a)  $\Omega_c = 0.999$ , b)  $\Omega_c = 0.950$ , c)  $\Omega_c = 0.494$ , d)  $\Omega_c = 0.091$ .

This shows that 1D numerical solution agree with analytical ones for 1D growth due to solutal exchange. Now, the same set of equations will be used to represent 2D solutal dendritic growth and will be validated by comparing the results obtained with other author's simulations.

### 3.3 2D dendritic growth

#### 3.3.1 Comparison with a model of direct growth

Let us consider a square domain  $[0;240] \times [0;240]$ , on which we place an initial circle seed of size  $22d_0^*$  where  $d_0^*$  represents the dimensionless capillarity. To study the convergence of our method, the tip velocity along the  $x$  direction has been extracted. The anisotropy function used for growth is  $W(\mathbf{n}) = W_0^* (1 - 3\varepsilon_4) \left[ 1 + \frac{4\varepsilon_4}{1 - 3\varepsilon_4} \frac{(\partial_{x^*}\phi)^4 + (\partial_{y^*}\phi)^4}{|\nabla\phi|^4} \right]$ , with  $\varepsilon_4 = 0.02$ . The other simulation parameters are:  $U_0 = -0.55$ ;  $k = 0.15$ ;  $\beta^* = 300$ ;  $\Delta\tau = h_{min}/(\beta^* \cdot v_{tip})$ ;  $\theta$  is taken equal to zero;  $Mc_\infty = 1$ . In the following, the variation of the tip velocity and composition profiles computed with CimLib are compared with the results obtained in [KAR2001] using a finite difference Eulerian method, with a structured mesh of  $\Delta x^* = 0.4$  and a constant timestep,  $\Delta\tau = 0.008$ .

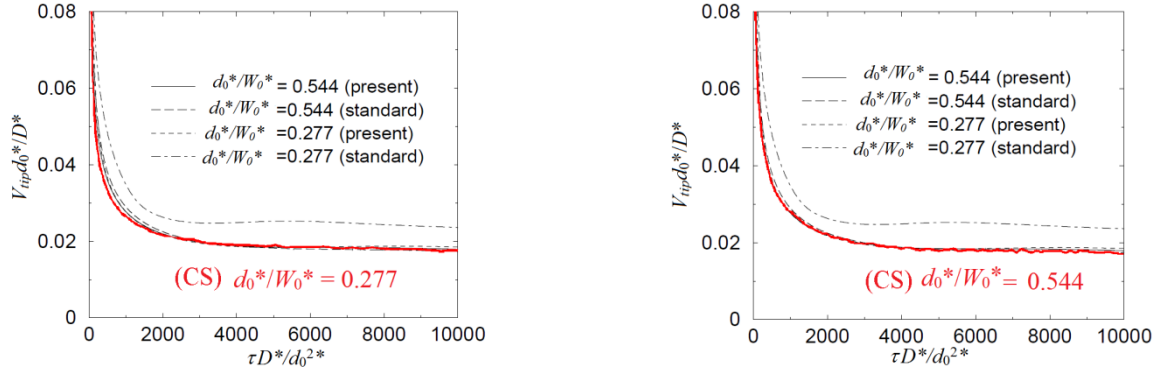


Figure 3.8 Compared plots of scaled dendrite tip velocity  $v_{tip}d_0^*/D^*$  vs scaled time  $\tau D^*/d_0^{*2}$  for different values of  $d_0^*$ .

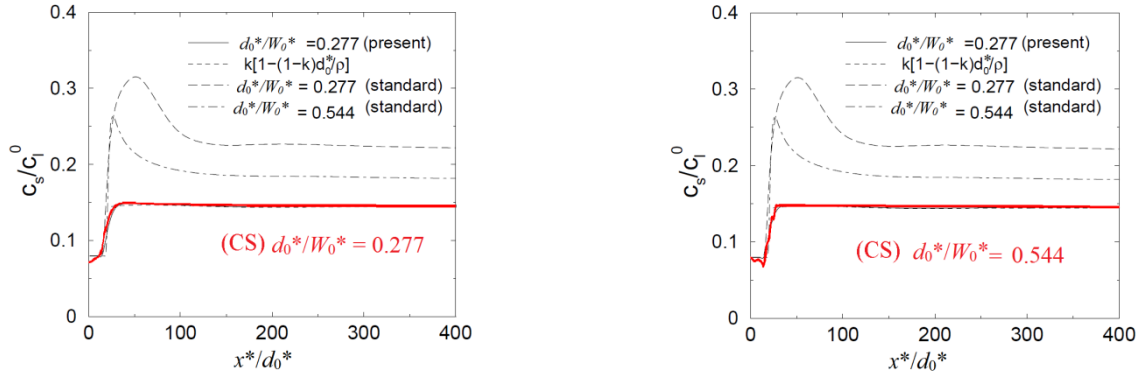


Figure 3.9 Compared plots of solute profiles in the solid along the central dendrite axis.

The dimensionless dendrite tip velocity  $V_{tip}d_0^*/D^*$  is plotted vs the dimensionless time  $\tau D^*/d_0^{*2}$  in Figure 3.8 for the two models and the scaled composition  $c^s/c_l^0$  in the solid vs the scaled position  $x^*/d_0^*$  in the  $x$  direction is plotted for the two types of numerical resolution in Figure 3.9, for different values of the solute diffusion, at  $\tau = 3010$  for  $D^* = 1$  and  $\tau = 400$  for  $D^* = 2$ . We know that  $D^* = a_1 a_2 / d_0^*$ , so for  $D^* = 1$  we have  $d_0^* = 0.544$  and for  $D^* = 2$  we have  $d_0^* = 0.277$ . The results of [KAR2001] concern the growth velocity and the composition, and present small oscillations in the beginning of the computation for the composition. Oscillations can be also seen in Figure 3.3, in the corner, where one observes a trace of adaptation and thus mesh size changes. These results show also that the solutions converges for the two values of  $d_0^*$ , especially when comparing the composition profile with the one arising from Gibbs-Thomson relation:  $c^s/c_l^0 = k [1 - (1 - k)d_0^*/\rho_{tip}]$  where  $\rho_{tip}$  is the dendrite tip radius. This will be further detailed in chapter 4.

### 3.3.2 Comparison with other models

We have done a comparison of the results using our model with grid and time adaptation (named here CS) and the results obtained in [KAR2001] (named here DT) with the anti-trapping term using the finite difference method based on [KAR2001], Karma's method is done without grid or time adaptation. The results present the same convergent evolution.

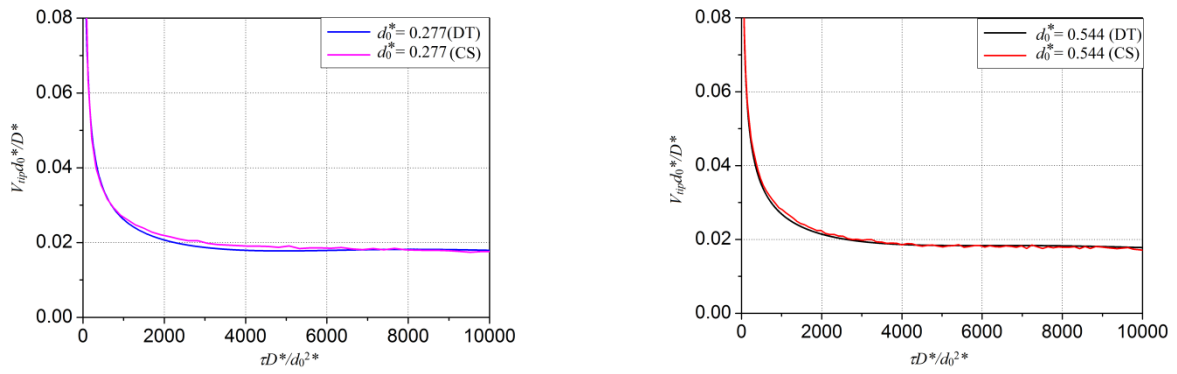


Figure 3.10 Compared plots of scaled dendrite tip velocity  $v_{tip}d_0^*/D^*$  vs scaled time  $\tau D^*/d_0^{*2}$  for different values of  $d_0^*$ .

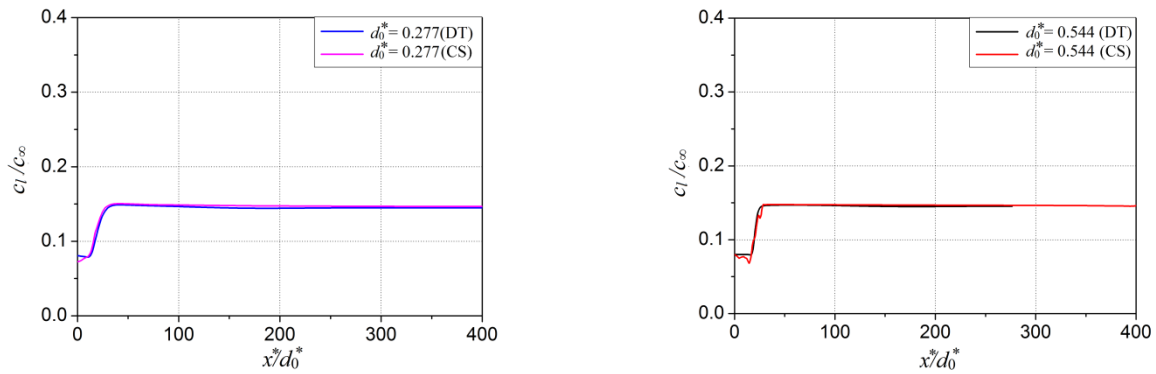


Figure 3.11 Compared plots of solute profiles in the solid along the central dendrite axis, as a function of  $x^*/d_0^*$ .

Parallel computations at CEMEF have been done on a Cluster equipped with bi-processors AMD Opteron Magny-Cours 2.3 Ghz with 8 cores and 32 Go of RAM ( $\rightarrow$ 2 Go /core) and a 146 Go disk local SAS.

[KAR2001] computations have also been done in parallel, but on GPUs, on a Cluster GeForge GTX 680 using 1536 cores and on a GTX TITAN using 2688 cores.

Computational times were longer in our case, but scalability should be further studied to check if times became closer if more CPU resources were available.

|                    | $d_0^*/W_0^*$ | Cores<br>(CPU or GPU) | $t_{CPU}$ or $t_{GPU}$ |
|--------------------|---------------|-----------------------|------------------------|
| CEMEF              | 0.544         | 32                    | 1h 15 min              |
| CEMEF              | 0.277         | 32                    | 34 min                 |
| Damien (GTX 680)   | 0.544         | 1536                  | 9 min 21 s             |
| Damien (GTX 680)   | 0.277         | 1536                  | 2 min 5 s              |
| Damien (GTX TITAN) | 0.544         | 2688                  | 8 min 11 s             |
| Damien (GTX TITAN) | 0.277         | 2688                  | 4 min 32 s             |

Table 3.1 Compared computational times using: our finite element code, parallelized using MPI and run on a CPU cluster; [KAR2001] code, parallelized and run on GPU clusters.

In our simulations, the time step has been increased while decreasing the velocity and increasing the number of elements needed to represent the interface, as shown in Figure 3.12.

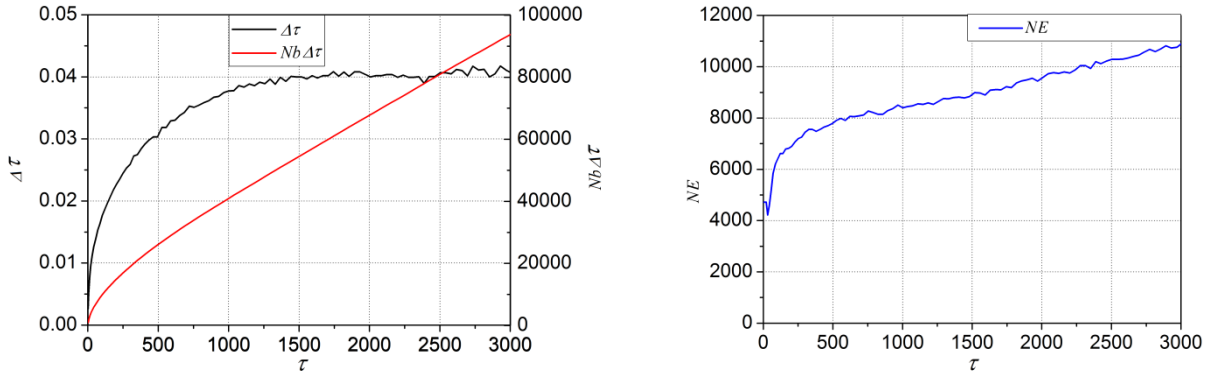


Figure 3.12 Number of elements and time step profiles during the simulation for  $d_0^* = 0.544$ .

### 3.3.3 Parameter sensitivity study

The influence of the different numerical parameters on the results has been studied. Firstly, the number of fixed elements has been changed by changing  $N_2$ ,  $e_{min}$ , and  $\beta^*$ . We deduce that we cannot greatly reduce  $N_2$  because there will not be enough elements to represent the dendrite's shape (as observed in Figure 3.13 (f)). The same happens for  $\beta^*$ : it cannot be decreased because the time step will increase in such a way that computation diverges and dendrite morphology is not attained. For  $e_{min}$ , it will not influence the result; it will only affect the mesh size outside the solid liquid interface and the solute diffusion layer.

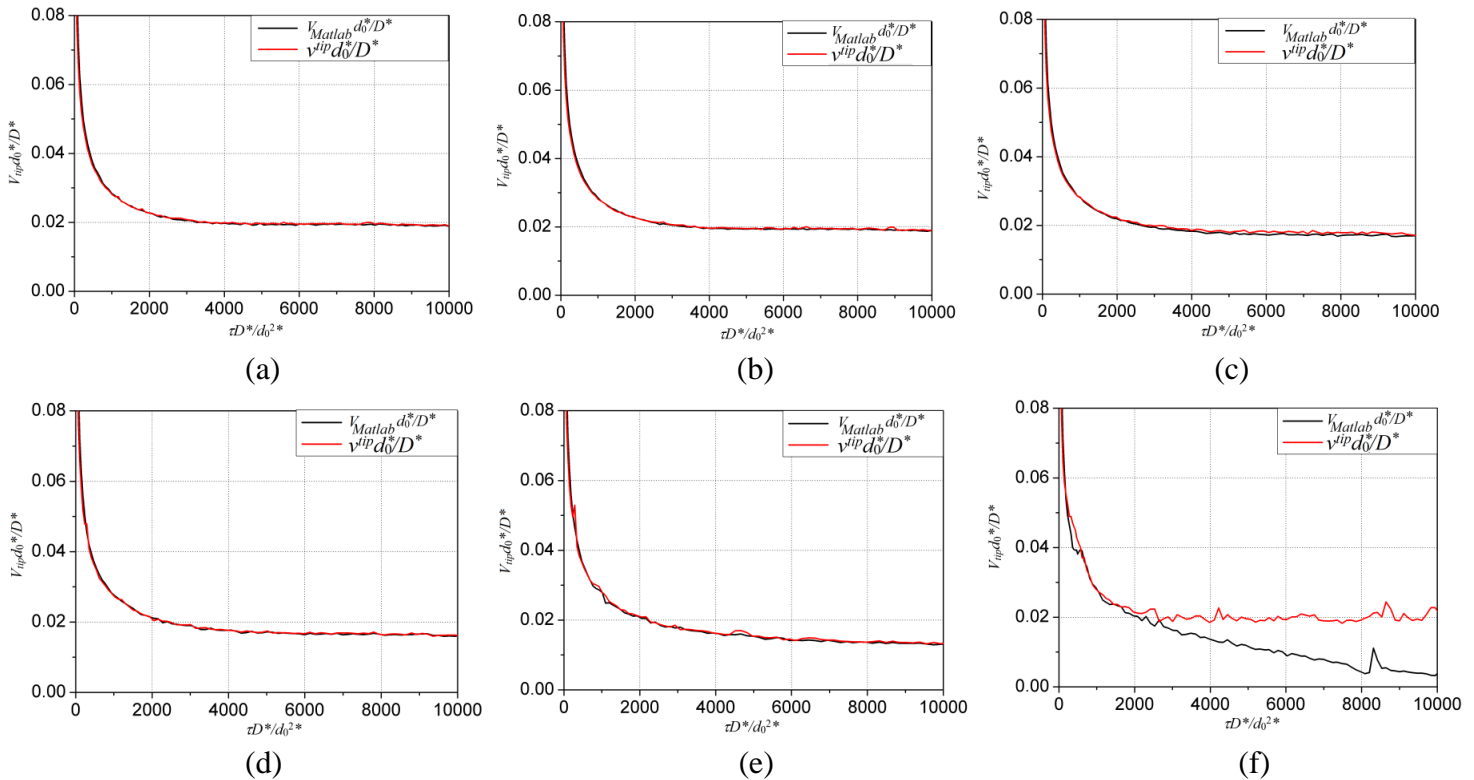


Figure 3.13 Tip velocity obtained for different  $N_2$  values, with  $e_{min} = 10^{-9}$  and  $\beta^* = 300$ : a)  $N_2 = 100,000$ , b)  $N_2 = 50,000$ , c)  $N_2 = 10,000$ , d)  $N_2 = 5,000$ , e)  $N_2 = 2,500$ , f)  $N_2 = 1,000$ .

Figure 3.13 shows that, when the number of elements decreases, the tip velocity decreases from the converged value of the velocity. The velocity profiles shown represent the tip velocity computed directly in the simulation as given by equation (2.63) (in red) compared to the tip velocity computed with a geometrical method, implemented in Matlab (in black), after finishing the simulation. When  $N_2 = 1\,000$ , the tip velocity (2.63) is above the converged value of the velocity and the other computed velocity is below it with a large difference. Below  $N_2 = 10\,000$  we lose the dendrite shape. The dendrite profiles are plotted in Figure 3.14 for these referred values of  $N_2$ , where we can observe that when we decrease  $N_2$ , dendrite shape deteriorates. Figure 3.14 shows also the variation of the number of elements computed to represent the interface ( $N_1$ ), the total number of elements to be used ( $NE$ ) and the real number of elements used in the simulation obtained after mesh adaptation ( $NE_{Real}$ ). In reality the number of elements used in the simulation is smaller than the computed and imposed one to the mesh adaptation. In fact, the constraint on a fixed number of elements is not always respected when the minimum error and the minimum mesh size given, combined with the adaptation on several fields, are also activated and too restrictive. We can see also that the number of elements decreases when decreasing  $N_2$ , from 100 000 to 1 000. At the latter, we do not have enough elements to represent the dendrite. In addition, the real number of elements used in the simulation approaches from the computed one when decreasing the number  $N_2$ .

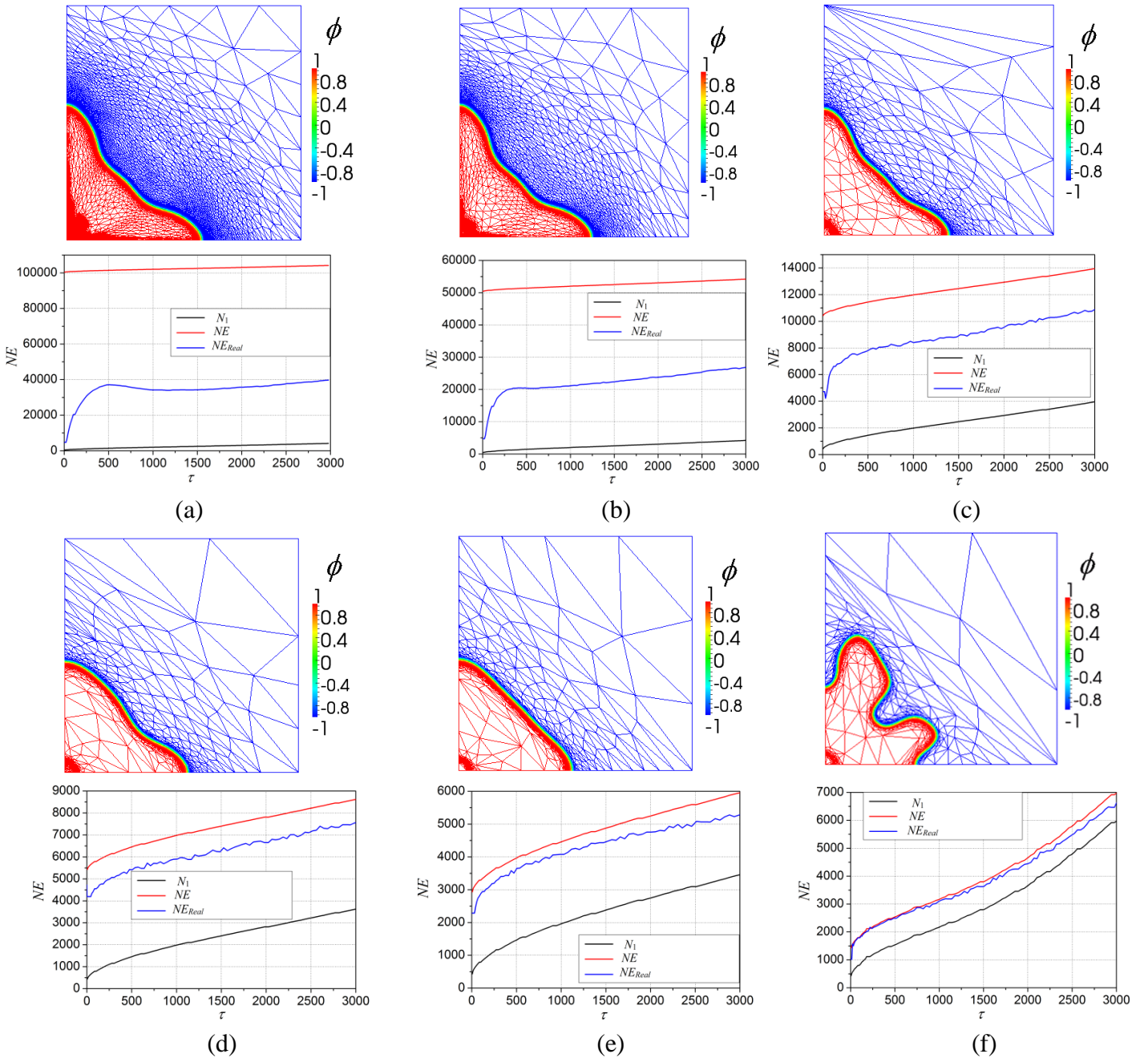


Figure 3.14 Dendrite profile drawn and variation of number of elements, for different values of  $N_2$  with  $e_{min} = 10^{-9}$  and  $\beta^r = 300$ , a)  $N_2 = 100\,000$ , b)  $N_2 = 50\,000$ , c)  $N_2 = 10\,000$ , d)  $N_2 = 5\,000$ , e)  $N_2 = 2\,500$ , f)  $N_2 = 1\,000$ .

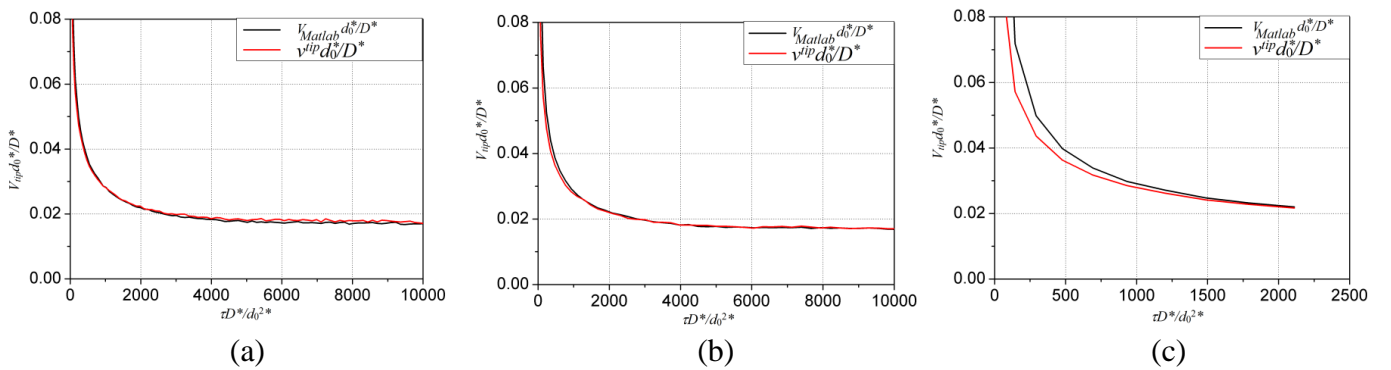


Figure 3.15 Tip velocity profile for different values of  $\beta^r$ , with  $N_2 = 10\,000$  and  $e_{min} = 10^{-9}$ : a)  $\beta^r = 300$ , b)  $\beta^r = 150$ , c)  $\beta^r = 100$ .

Figure 3.15 shows that the tip velocity decreases when decreasing  $\beta^*$ . While decreasing  $\beta^*$  the computed timestep, using equation (2.67), increases from 0.008 to 0.04, as shown in Figure 3.16. When a small value for  $\beta^*$  (as 100) is used, a large timestep arises, up to 0.1, which is large enough to break the dendritic growth and the simulation will stop.

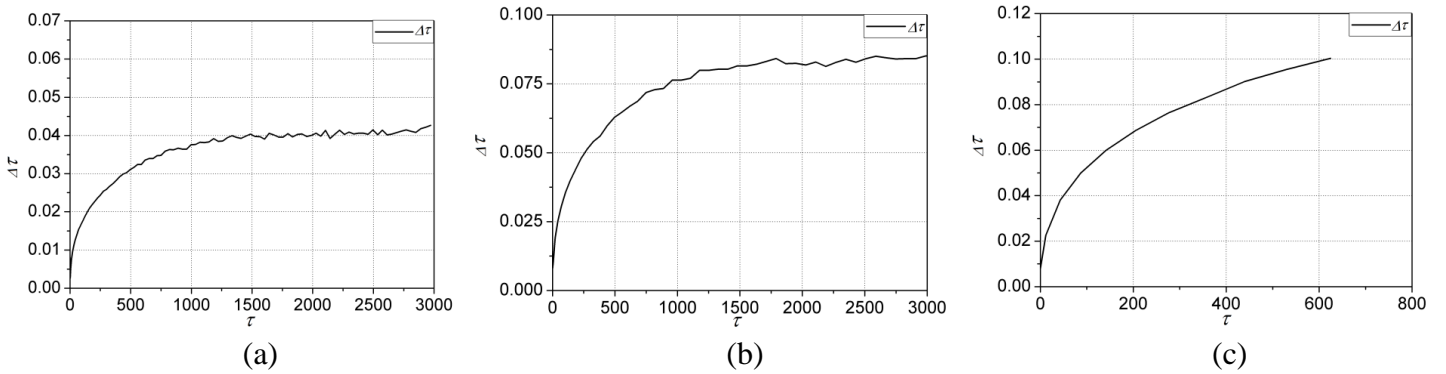


Figure 3.16 Time step evolution for different  $\beta^*$ , with  $N_2 = 10\,000$  and  $e_{min} = 10^{-9}$ : a)  $\beta^* = 300$ , b)  $\beta^* = 150$ , c)  $\beta^* = 100$ .

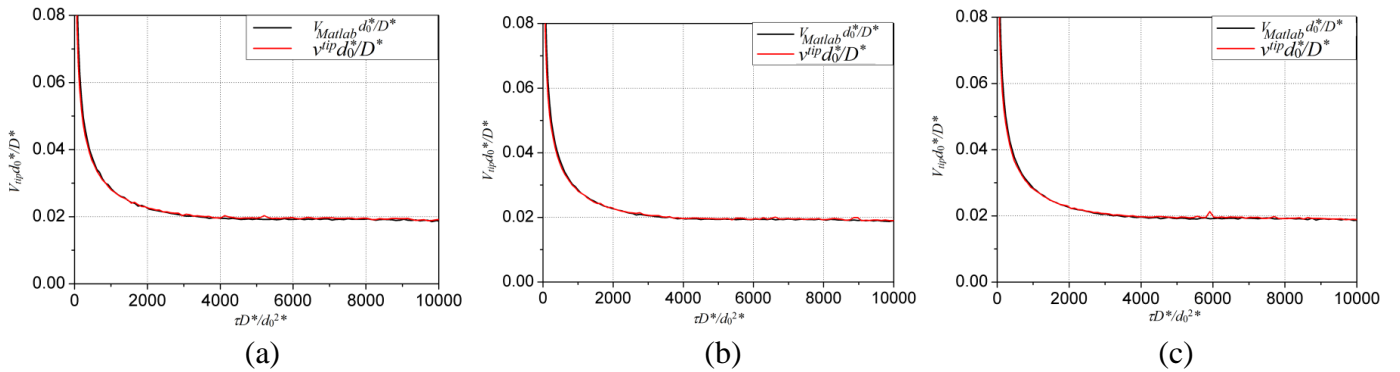


Figure 3.17 Evolution of the tip velocity for different values of  $e_{min}$ , with  $N_2 = 50\,000$  and  $\beta^* = 300$ : a)  $e_{min} = 10^{-6}$ , b)  $e_{min} = 10^{-9}$ , c)  $e_{min} = 10^{-11}$ .

Figure 3.17 shows that changing the value of  $e_{min}$  with the values given here does not affect the convergency toward the steady state value. In particular, one attains the analytical solution and the convergence speed is not altered, as well.

We can see also the influence of the use of the parallel computation by making the same solutal simulation using 8, 16 and 32 cores. When we add more cores, the simulation takes less time to be finished as in Figure 3.18. We finish the simulation for  $d_0^* = 0.277$  before the other simulation because  $D^*$  is bigger and thus the computational case in the red line will be smaller. But the two lines are decreasing while adding the number of cores used in the simulation. The graphs are shown at  $\tau = 3010$  for  $d_0^* = 0.544$  and  $\tau = 400$  for  $d_0^* = 0.277$  using  $N_2 = 10\,000$ .

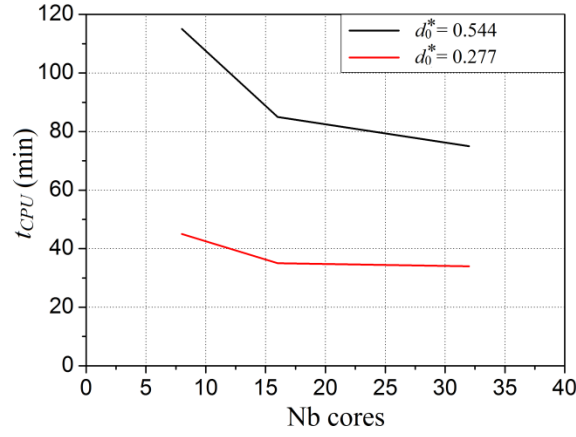


Figure 3.18 Computational time using 8, 16 and 32 cores when  $d_0^* = 0.544$  and  $d_0^* = 0.277$ .

The difference between the simulation using  $d_0^* = 0.277$  and  $d_0^* = 0.544$ , is due not only to the growth velocity but also to the number of elements used since we have a smaller number of elements for  $d_0^* = 0.277$ , as illustrated in Figure 3.19.

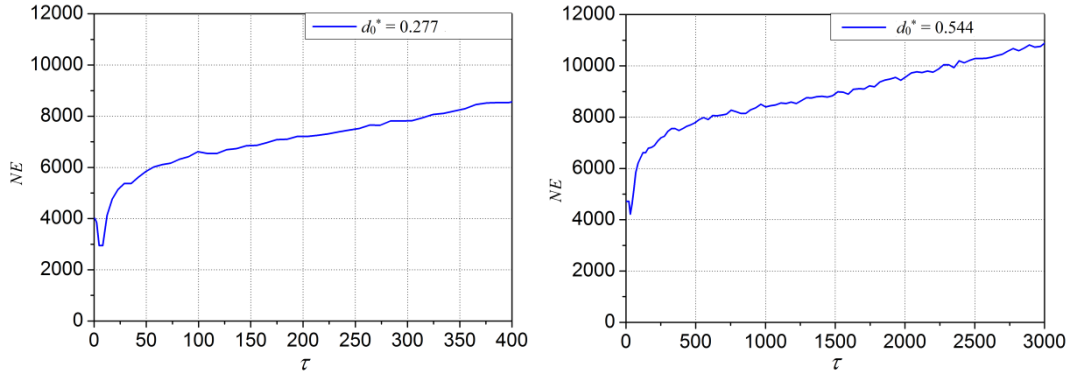


Figure 3.19 Variation of the number of elements with time using  $d_0^* = 0.544$  and  $d_0^* = 0.277$ .

### 3.4 Conclusion

In conclusion, there are two equations that need to be solved to simulate solutal dendritic growth: the phase-field equation and the mass conservation equation. They were here rewritten with dimensionless variables:

$$\begin{aligned} \tau(\mathbf{n}) \frac{\partial \phi}{\partial \tau} - \nabla \cdot (W^2(\mathbf{n}) \nabla \phi) &= [\phi - \lambda(\theta + Mc_\infty U)(1 - \phi^2)](1 - \phi^2) + \frac{\partial}{\partial x^*} \left( |\nabla \phi|^2 W(\mathbf{n}) \frac{\partial W(\mathbf{n})}{\partial (\partial_{x^*} \phi)} \right) \\ &+ \frac{\partial}{\partial y^*} \left( |\nabla \phi|^2 W(\mathbf{n}) \frac{\partial W(\mathbf{n})}{\partial (\partial_{y^*} \phi)} \right) + \frac{\partial}{\partial z^*} \left( |\nabla \phi|^2 W(\mathbf{n}) \frac{\partial W(\mathbf{n})}{\partial (\partial_{z^*} \phi)} \right) \end{aligned} \quad (3.63)$$

$$\begin{aligned} \frac{1}{2} (1 + k - (1 - k)\phi) \frac{\partial U}{\partial \tau} - \nabla \cdot \left( D^* \frac{1 - \phi}{2} \nabla U \right) &= \\ \nabla \cdot \left( \frac{W(\mathbf{n})}{2\sqrt{2}} (1 + (1 - k)U) \frac{\partial \phi}{\partial \tau} \frac{\nabla \phi}{|\nabla \phi|} \right) + \frac{1}{2} (1 + (1 - k)U) \cdot \frac{\partial \phi}{\partial \tau} \end{aligned} \quad (3.64)$$

With

$$U = \left[ \frac{2c/c_\infty}{1+k-(1-k)\phi} - 1 \right] \left( \frac{1}{1-k} \right) \quad (3.65)$$

$$\theta = \frac{T - T_M - mc_\infty}{L/c_p} \quad (3.66)$$

And

$$\phi = -\tanh\left(\frac{\eta}{W_0^* \sqrt{2}}\right) \quad (3.67)$$

We have validated its resolution in 1D by comparing the numerical results with analytical ones and by comparing them to other numerical resolutions in 2D. The solutal equation may now be fully coupled to heat transfer to study thermo-solutal dendritic growth, by combining the three problems presented before.

## Résumé

Dans ce chapitre, nous avons présenté les équations utilisées dans le modèle de champs de phase et leur développement pour la croissance dendritique solutale. Nous avons défini deux équations à résoudre : l'équation du champ de phase et l'équation de conservation de masse. La résolution numérique est présentée en montrant le maillage utilisée, qui minimise l'erreur sur  $\phi$  et  $U$ . Un cas 1D a été présenté pour valider les équations en 1D. A la fin, une croissance dendritique a été présentée en 2D avec une validation et une étude paramétrique (numérique).

## Chapter 4

### 4 Thermo-solutal model

---

|       |                                          |    |
|-------|------------------------------------------|----|
| 4.1   | Model equations .....                    | 83 |
| 4.2   | 1D thermo-solutal validation .....       | 84 |
| 4.3   | Thermo-solutal dendritic growth .....    | 88 |
| 4.3.1 | Mesh adaptation .....                    | 88 |
| 4.3.2 | 2D thermo-solutal dendritic growth ..... | 89 |
| 4.3.3 | 3D thermo-solutal dendritic growth ..... | 94 |
| 4.4   | Conclusions .....                        | 96 |

---

#### 4.1 Model equations

Phase-field energy and mass conservation equations are coupled and presented here for thermo-solutal dendritic growth simulations. The solved system of equations has been derived from the ones stated by [RAM2004]. Combining the solute and thermal cases, the standard set of sharp-interface equations consists in:

$$\frac{\partial c}{\partial t} = D^l \Delta c \quad (4.1)$$

$$\frac{\partial T}{\partial t} = \alpha \Delta T \quad (4.2)$$

$$c_i (1 - k) v_n = -D^l \nabla c_i \quad (4.3)$$

$$\rho L v_n = (\kappa^s \nabla T^s - \kappa^l \nabla T^l) \quad (4.4)$$

$$T_i = T_M + m c_i - \Gamma \kappa_r - v_n / \mu_\kappa \quad (4.5)$$

As previously, the following dimensionless variables are defined:

$$U = \left[ \frac{2c/c_\infty}{1 + k - (1 - k)\phi} - 1 \right] \left( \frac{1}{1 - k} \right) \quad (4.6)$$

$$\theta = \frac{T - T_M - mc_\infty}{L/c_p} \quad (4.7)$$

In terms of these variables, the free-boundary problem becomes:

$$\partial_\tau U = D^* \Delta U \quad (4.8)$$

$$\partial_\tau \theta = \alpha^* \Delta \theta \quad (4.9)$$

$$[1 + (1 - k)U_i] v_n = -D^* \nabla U^l \quad (4.10)$$

$$v_n = \alpha^* (\nabla \theta^s - \nabla \theta^l) \quad (4.11)$$

$$\theta_i + Mc_\infty U_i = -d_0 \kappa_r - \beta v_n \quad (4.12)$$

We define the free energy functional as,

$$F(\phi, T, c) = \int_{\Omega} \frac{W(\mathbf{n})^2}{2} |\nabla \phi|^2 + f_{AB}(\phi, T, c) \, dV = \int_{\Omega} F^{int} \, dV \quad (4.13)$$

In the same way as before, the variational derivatives of  $F$  must satisfy the following equations for equilibrium:

$$\frac{\delta F}{\delta c} = \frac{\partial F^{int}}{\partial c} - \nabla \cdot \frac{\partial F^{int}}{\partial \nabla c} = \mu_E = \text{constant} \quad (4.14)$$

$\mu_E$  is the chemical potential

$$\frac{\delta F}{\delta \phi} = \frac{\partial F^{int}}{\partial \phi} - \nabla \cdot \frac{\partial F^{int}}{\partial \nabla \phi} = 0 \quad (4.15)$$

We use the Allen-Cahn and Cahn-Hilliard framework [CAH1958],[CAH1979] to derive the equations:

$$\frac{\partial c}{\partial t} = \nabla \cdot \left( M_c \nabla \frac{\delta F}{\delta c} - \mathbf{j}_{at} \right) = \nabla \cdot \left( M_c \nabla \left( \frac{\partial F^{int}}{\partial c} - \nabla \cdot \frac{\partial F^{int}}{\partial \nabla c} \right) - \mathbf{j}_{at} \right) = \nabla \cdot (M_c \nabla \mu_E - \mathbf{j}_{at}) \quad (4.16)$$

$$\frac{\partial \phi}{\partial \tau} = -M_\phi \frac{\delta F}{\delta \phi} = -M_\phi \left( \frac{\partial F^{int}}{\partial \phi} - \nabla \cdot \frac{\partial F^{int}}{\partial \nabla \phi} \right) \quad (4.17)$$

$M_\phi$  and  $M_c$  are positive mobilities, parameters related, respectively, to the interface kinetic coefficient and to the solute diffusion coefficient. Adding together the energy and solute contributions yields to write  $f_{AB}(\phi, c, T)$  as follows:

$$f_{AB}(\phi, T, c) = g(\phi) + \frac{R_g T_M}{v_0} (c \ln c - c) + \bar{\varepsilon} c + \bar{g}(\phi) \frac{\Delta \varepsilon}{2} c \quad (4.18)$$

We deduce then the three equations to be solved [RAM2004].:

$$\begin{aligned} \alpha(\mathbf{n}) \frac{\partial \phi}{\partial \tau} - \nabla \cdot (W^2(\mathbf{n}) \nabla \phi) &= [\phi - \lambda(\theta + M_{c\infty} U) (1 - \phi^2)] (1 - \phi^2) + \frac{\partial}{\partial x^*} \left( |\nabla \phi|^2 W(\mathbf{n}) \frac{\partial W(\mathbf{n})}{\partial (\partial_{x^*} \phi)} \right) \\ &+ \frac{\partial}{\partial y^*} \left( |\nabla \phi|^2 W(\mathbf{n}) \frac{\partial W(\mathbf{n})}{\partial (\partial_{y^*} \phi)} \right) + \frac{\partial}{\partial z^*} \left( |\nabla \phi|^2 W(\mathbf{n}) \frac{\partial W(\mathbf{n})}{\partial (\partial_{z^*} \phi)} \right) \end{aligned} \quad (4.19)$$

$$\frac{\partial \theta}{\partial \tau} - \alpha^* \Delta \theta = -\frac{1}{2} \frac{\partial \phi}{\partial \tau} \quad (4.20)$$

$$\frac{1+k-(1-k)\phi}{2} \frac{\partial U}{\partial \tau} = \quad (4.21)$$

$$\nabla \cdot \left( D^* \frac{1-\phi}{2} \nabla U + \frac{W(\mathbf{n})}{2\sqrt{2}} [(1-k)U + 1] \frac{\partial \phi}{\partial \tau} \frac{\nabla \phi}{|\nabla \phi|} \right) + \frac{1}{2} (1 + (1-k)U) \frac{\partial \phi}{\partial \tau}$$

Notations used for each parameter were given in chapters 2 and 3.

As done for the pure thermal and solutal cases, validation of the model and its implementation will be done in the 1D and 2D cases.

## 4.2 1D thermo-solutal validation

Results obtained are compared with the analytical solutions in 1D presented in [RAM2004], corresponding to the planar front evolution problem. Solidification computation was performed using a 1D mesh with a mesh size  $\Delta x^* = 0.4$ , and by defining again initially the

function  $\phi = -\tanh\left(\frac{x^*}{W_0^* \sqrt{2}}\right)$  to represent the solid/liquid interface, as illustrated in Figure 4.1. The interface diffuses from an initial position  $x_0^*$ .

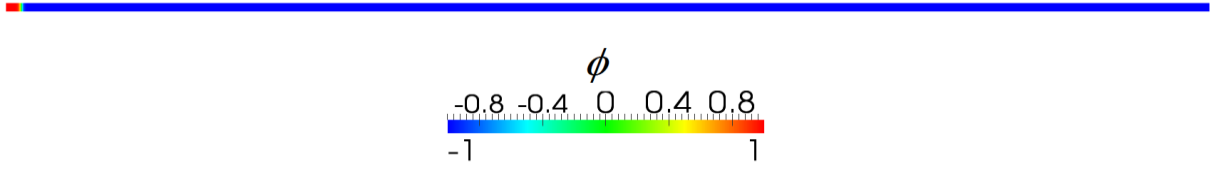


Figure 4.1 1D rectangular domain (below) and detail of the function  $\phi$  at the initial time  $\tau_0$ .

To obtain the analytical form for the steady-state energy and solute solutions in the adimensional case, the following equations are solved:

$$v_n^{st} \frac{\partial U}{\partial x^*} + D^* \frac{\partial^2 U}{\partial x^{*2}} = 0 \quad (4.22)$$

$$v_n^{st} \frac{\partial \theta}{\partial x^*} + \alpha^* \frac{\partial^2 \theta}{\partial x^{*2}} = 0 \quad (4.23)$$

with the interface conditions:

$$[1 + (1 - k) U_i] v_n^{st} = -D^* \partial_{x^*} U|_l \quad (4.24)$$

$$v_n^{st} = -\alpha^* \partial_{x^*} \theta|_l \quad (4.25)$$

$$\theta_i + Mc_\infty U_i = -\beta v_n^{st} \quad (4.26)$$

and the far-field boundary conditions:

$$\lim U(x^*) = 0 \text{ when } x^* \rightarrow +\infty \quad (4.27)$$

$$\lim \theta(x^*) = -\Delta \text{ when } x^* \rightarrow +\infty \quad (4.28)$$

Thus, the differential equation for  $U$  to be solved is,

$$D^* U'' + v_n^{st} U' = 0 \quad (4.29)$$

Its solution can be written as:

$$U = c_1 e^{ax^*} + c_2 e^{bx^*} \text{ with } a = 0 \text{ and } b = -v_n^{st}/D^* \quad (4.30)$$

Leading to  $U = c_1 + c_2 e^{\frac{-v_n^{st} x^*}{D^*}}$ . We use the boundary and the interface conditions to find the constant values  $c_1 = 0$  and  $c_2 = 1/k$ , which provide the analytical solution for the solute as:

$$U_{Anal} = \frac{1}{k} e^{\frac{-v_n^{st} x^*}{D^*}} \quad (4.31)$$

The differential equation for  $\theta$  evolution is:

$$\alpha^* \theta'' + v_n^{st} \theta' = 0 \quad (4.32)$$

And its solution is of the form:

$$\theta = c_1 e^{ax^*} + c_2 e^{bx^*} \text{ with } a = 0 \text{ and } b = -v_n^{st} / \alpha^* \quad (4.33)$$

which gives  $\theta = c_1 + c_2 e^{\frac{-v_n^{st} x^*}{\alpha^*}}$

As for the solute composition, boundary and interface values allow the determination of  $c_1$  and  $c_2$ , being  $c_1 = -\Delta$  and  $c_2 = 1$ .

The analytical solution for the adimensionalized temperature is:

$$\theta_{Anal} = e^{\frac{-v_n^{st} x^*}{\alpha^*}} - \Delta \quad (4.34)$$

Firstly, we start with diffusing the interface by solving the set of three equations (4.19), (4.20) and (4.21). The analytical solutions are defined as in equations (4.31) and (4.34), slightly changed since it is spatially located relatively to  $x_0^*$ :

$$\theta_{Anal} = \exp\left(\frac{v_n^{st} x_0^*}{D^*} - \frac{v_n^{st} x^*}{D^*}\right) - \Delta \quad (4.35)$$

$$U_{Anal} = \frac{1}{k} \exp\left(\frac{v_n^{st} x_0^*}{D^*} - \frac{v_n^{st} x^*}{D^*}\right) \quad (4.36)$$

The 1D rectangular domain is of dimension  $[-1600;1600]$ . The initial values and parameters considered are (mostly taken from [RAM2004]):  $\theta_0 = \theta_{Anal}$ ,  $U_0 = U_{Anal}$ ,  $NbNodes = 8000$ ,  $x_0^* = -1500$ ,  $\alpha^* = 2$ ,  $D^* = 2$ ,  $\beta = 1.5$ ,  $\Delta = 2.3$ ,  $Mc_\infty = 0.15$ ,  $k = 0.15$  and  $\Delta\tau = 0.008$ . Numerical resolution has been detailed in the previous chapters, and post-process includes computing the interface velocity given by  $v_n^{st} = \frac{\Delta - 1 - Mc_\infty/k}{\beta}$  (with  $\lambda = 1$ ) at the steady state.

This last decreases with time until stabilization, as illustrated in Figure 4.2. When the steady state velocity is reached, numerical and analytical profiles of temperature and composition around the interface can be compared.

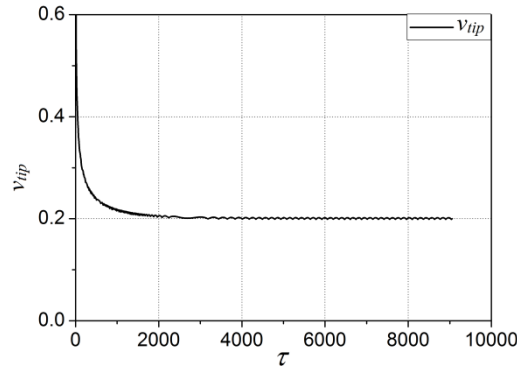


Figure 4.2 Computed interface velocity in 1D with  $\Delta = 2.3$ ,  $k = 0.15$ ,  $Mc_\infty = 0.15$  and  $\beta = 1.5$ . Steady state value is reached for  $\tau = 6000$  and is 0.2.

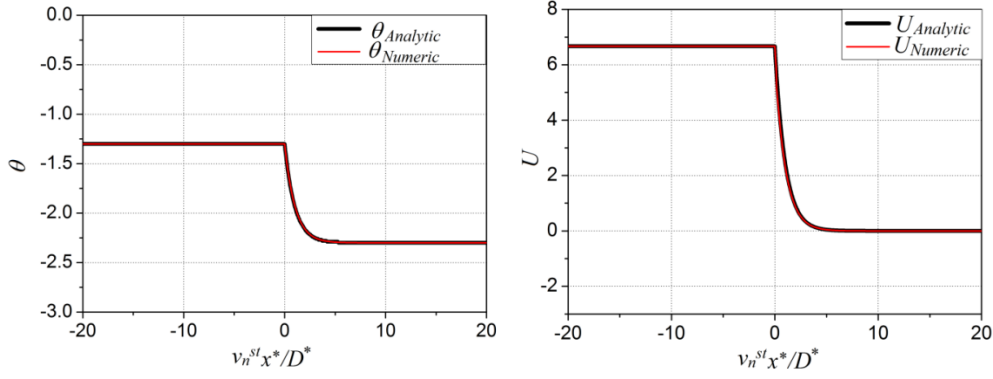


Figure 4.3 Comparison between analytical and numerical solutions for  $\theta$  and  $U$  at  $\tau = 6400$ , in the region around the interface,  $x^* \in [-200;200]$ .

Numerical and analytical profiles very well agree for the temperature and the solute composition, as shown in Figure 4.3, which well validate the model and its numerical implementation.

The dimensional composition value  $c$ , may be computed during post-process by:

$$c/c_\infty = \frac{1}{2} [1 + k - (1 - k)\phi] [(1 - k)U + 1] \quad (4.37)$$

As well as the liquid and solid compositions:

$$c_s/c_\infty = \frac{1}{2} [1 + k - (1 - k)] [(1 - k)U^S + 1] \quad (4.38)$$

$$c_l/c_\infty = \frac{1}{2} [1 + k + (1 - k)] [(1 - k)U^L + 1] \quad (4.39)$$

with  $U^S$  and  $U^L$  the values of the adimensional composition in the solid and liquid, respectively. Figure 4.4 illustrates the composition, interface and temperature around the interface at  $\tau = 2800$ . The liquid and solid compositions are both represented to well demonstrate that  $c_s = c_\infty$  and  $c_l = c_\infty \left[ 1 + \frac{1 - k}{k} \exp\left(\frac{v_n^{st} x_0^*}{D^*} - \frac{v_n^{st} x^*}{D^*}\right) \right]$ . Results clearly match the ones presented by [RAM2004].

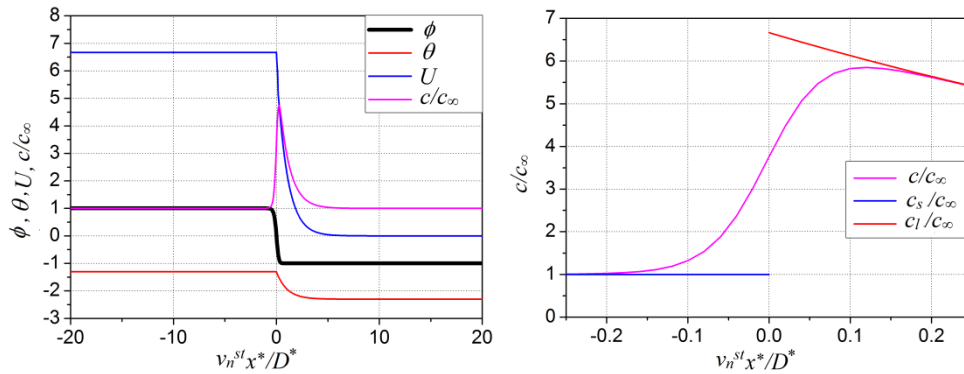


Figure 4.4 On the left,  $\phi$ ,  $\theta$  and  $U$  at  $\tau = 2800$  and, on the right, the dimensional compositions, both around the interface.

An important remark must be underlined: simulations performed start with the initial temperature and composition values identical to the analytical ones. During the transient phase, one observes a slight deviation from the theoretical composition profile, showing a bump (Figure 4.5.) that with time becomes stable, particularly when the steady-state growth velocity is reached. In this example, the analytical and numerical profiles do not exactly superpose. Some simulations with different parameters have been made and we have observed that this bump changes while changing the form of  $\tau(\mathbf{n})$  and  $\lambda$ , which may also lead to differences in the growth velocity. A deeper study of the influence of the initial parameters should be done to clearly enhance the influence of these two factors. In our opinion, simulations using larger domains will overcome this last problem, because stationary velocity has not been yet reached in the considered domain  $([-400;400])$ (small).

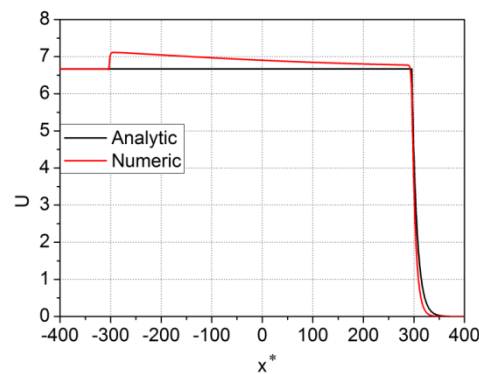


Figure 4.5 Non-dimensional composition profile at an instant of growth showing the deviation in a  $[-400;400]$  1D domain, plotted before steady-state is reached.

### 4.3 Thermo-solutal dendritic growth

#### 4.3.1 Mesh adaptation

The same method of metric construction is used to adapt the mesh using an error estimation and minimization procedure, but now on the vector  $\zeta = (\phi, \theta, U)$ . We have small meshes at the interface solid/liquid following the gradient of  $\phi$  and smaller meshes than the whole domain where we have composition and temperature gradient, as illustrated in Figure 4.6. The mesh captures thus the three diffusion profiles.

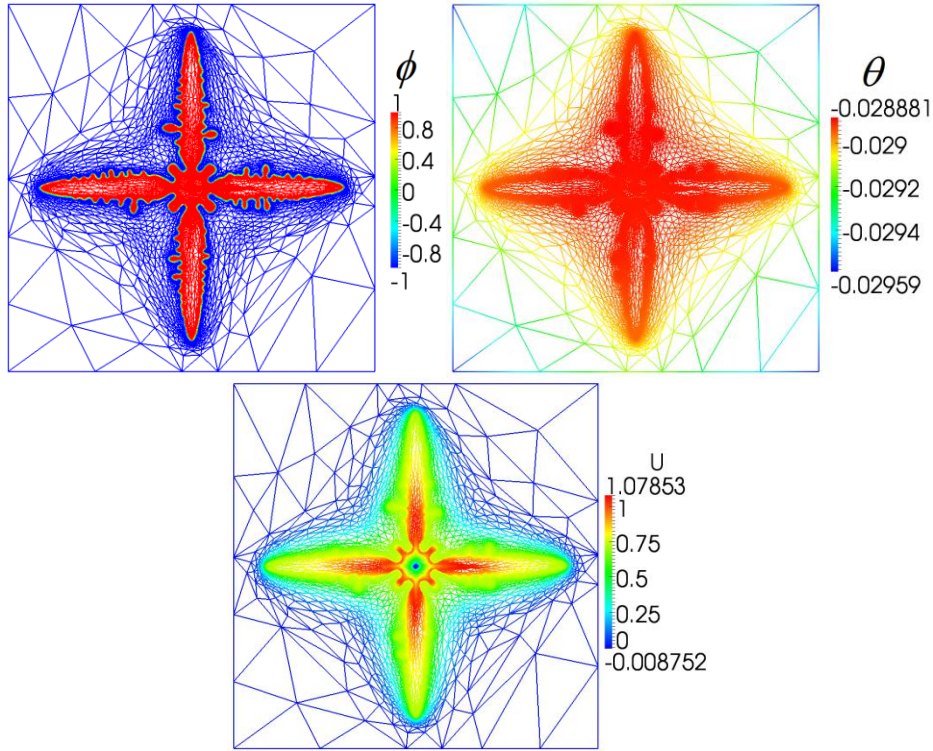


Figure 4.6 Thermo-solutal dendritic mesh, obtained by minimizing the error on  $\phi$ ,  $\theta$  and  $U$ .

We can see that the mesh is adapted following the solid/liquid interface, the temperature visualized outside the dendrite but also we can see that we have small meshes inside the dendrite because of the composition gradient, which did not happen for the pure thermal growth case.

### 4.3.2 2D thermo-solutal dendritic growth

An example of 2D thermo-solutal dendritic growth is now detailed to enhance each of the thermal and solute diffusion rates and show how mesh adaptation on the three parameters fits and improve the simulation. The set of equations solved during this simulation is composed of Equations (4.19), (4.20), (4.21) and Equations (4.19), (4.20), (4.21) and

$$\begin{aligned}
 U &= 0 && \text{on } \partial\Omega \\
 \theta &= -0.55 && \text{on } \partial\Omega \\
 \phi &= -1 && \text{on } \partial\Omega \\
 U(.,0) &= U_0 \\
 \theta(.,0) &= \theta_0 \\
 \phi(.,0) &= \phi_0
 \end{aligned} \tag{4.40}$$

Computation has been performed in a square domain of size  $[0;320] \times [0;320]$ , with:  $\theta_0 = -0.55$ ,  $e_{min} = 10^{-9}$ ,  $N_2 = 50\,000$ ,  $h_{min} = 0.4$ ,  $k = 0.15$ ,  $Mc_\infty = 0.5325$ ,  $U_0 = 0$ ,  $\Delta\tau = h_{min}/(300 \cdot v_{tip})$ ,  $D^* = 5$ ,  $\alpha^* = 250$  and starting from a nucleus of radius 1, the boundary conditions given above and by setting mesh adaptation parameters to take into account the solutions of  $(\phi, \theta, U)$ . An illustration of the results obtained after growth, is shown in Figure 4.7.

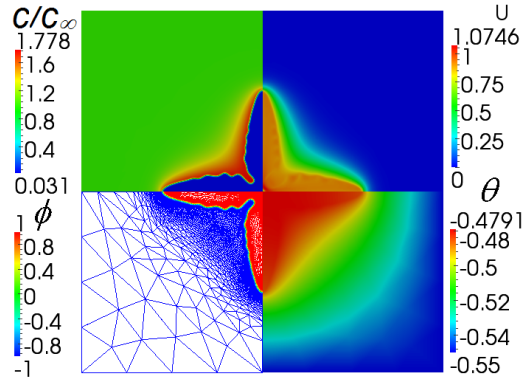


Figure 4.7 Thermo-solutal dendritic growth at  $\tau = 328.862$ , showing the difference between the thermal and solute diffusions and the adapted mesh. The parameters used are listed above.

Figure 4.7 shows that the temperature profile diffuses in a wider way than the composition one, since there is a ratio of 50 between the two diffusion coefficients, as also given by the Lewis number,  $Le = \alpha^*/D^*$ . Moreover, one observes that the mesh is well adapted following the three variables, as referred above: enriched around the interface and sizes varying with the gradient in the diffusion layer.

Figure 4.8 plots the variation of the solid and liquid compositions in the  $x$  direction for  $y = 0$ : constant in the solid since  $D^s = 0$ ; decreasing in an exponential way in the liquid, as expected.

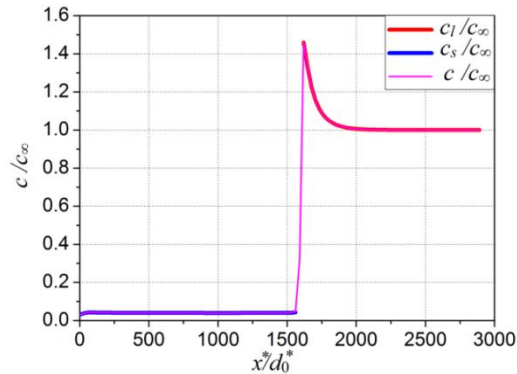


Figure 4.8 For 2D thermo-solutal dendritic growth, composition profiles at  $\tau = 328.862$  measured along the  $x$  direction for  $y = 0$ .

Results obtained may be compared with the ones from [RAM2004], where the authors have provided a 2D solution for thermo-solutal growth, computed with the phase-field method and by adding an anti-trapping term, using the finite difference method.

To study the convergence of our method, let us consider different square domains ( $[0;120] \times [0;120]$ ,  $[0;160] \times [0;160]$  and  $[0;240] \times [0;240]$ ), on which an initial seed of size  $65d_0^*$  is placed. Tip velocity evolution in the  $x$  direction is studied. The anisotropy function

considered is  $W(\mathbf{n}) = W_0^* (1 - 3\varepsilon_4) \left[ 1 + \frac{4\varepsilon_4}{1 - 3\varepsilon_4} \frac{(\partial_{x^*}\phi)^4 + (\partial_{y^*}\phi)^4}{|\nabla\phi|^4} \right]$ , with  $\varepsilon_4 = 0.02$ . The other

simulation parameters are:  $\theta_0 = -0.55$ ,  $U_0 = 0$ ,  $k = 0.15$ ,  $Mc_\infty = 0.5325$ ,  $\beta^* = 300$ ,  $\Delta\tau = h_{min}/(\beta^* \cdot v_{tip})$ . Figure 4.9 shows the variation of the tip velocity, the tip radius  $\rho_{tip}$  and  $\sigma^*$  (the tip selection parameter) where one observes that results are very close to the ones obtained in

[RAM2004]. The plots are shown for different  $\lambda$  as defined in chapter 1 as  $\lambda = a_1 W_0 / d_0$ , this parameter represents the variation of  $d_0$ .

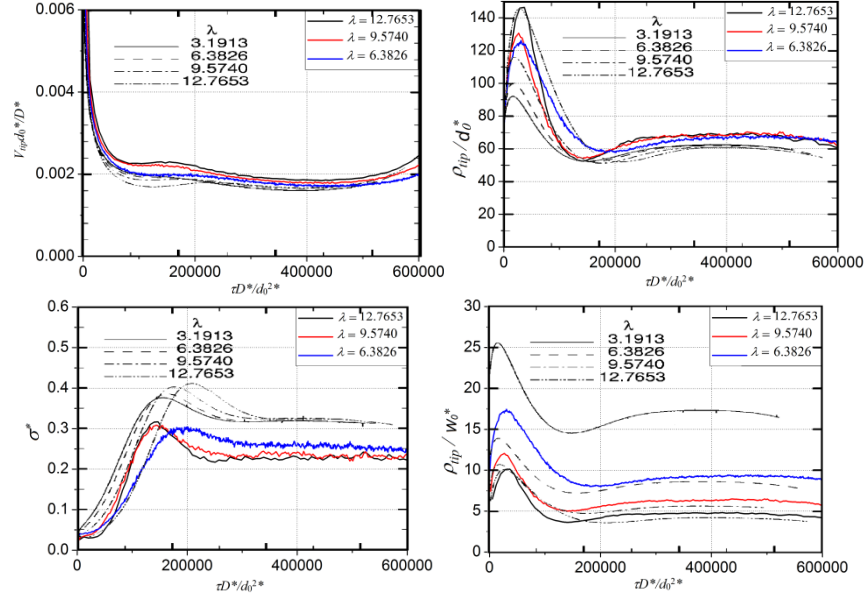


Figure 4.9 Temporal evolution of various growth parameters for two-dimensional dendritic solidification of a binary alloy in an undercooled melt, with coupled heat and solute diffusion ( $Le = 1$ ,  $Mc_\infty = 0.5325$ ,  $k = 0.15$ ,  $\varepsilon_4 = 0.02$  and  $\Delta = 0.55$ ) and for different  $\lambda = a_1 W_0 / d_0$ . The lines in each graph correspond to different  $\lambda$  (directly related with the interface width).

In these plots,  $\sigma^*$  is computed using the tip velocity, the solute diffusion, the capillarity and the tip radius,  $\rho_{tip}$ ,  $\sigma^* = \frac{2D^* d_0^*}{\rho_{tip} v_{tip}}$ . To compute the tip radius, a subset  $A = \{y^* / y^* > y_{max}^* - 3r_0\}$  has been taken, where  $y_{max}^*$  is the ordinate of the dendrite tip,  $r_0$  is the first estimation of the radius. The tip is approached with a parabola (P) of equation:

$$y^* = c_1 x^{*2} + c_2 x^* + c_3 \quad (4.41)$$

$c_1$ ,  $c_2$  and  $c_3$  are computed using the least squares method and used to obtain  $r_1 = \frac{(1 + c_2^2)^{3/2}}{2c_1}$ .

Finally,  $r_1$  allows to refine the subset A, to have a subset  $B = \{y^* / y^* > y_{max}^* - Const \cdot r_1\}$ , and so on.  $Const$  is initialized with 2 and decreases with iterations. This new subset is fitted with the parabola (P) to compute  $r_1$ . We refit while decreasing  $Const$  until  $\chi^2 < e$  and then  $\rho_{tip} = r_1$  is assumed.  $\chi$  is the sum of the squared residuals and  $\kappa_{tip}$  is the curvature. At the end:

$$\kappa_{tip} = \frac{y''^*}{(1 + y'^*{}^2)^{3/2}} = \frac{2c_1}{(1 + c_2^2)^{3/2}} \text{ for } x^* = 0 \text{ and } \rho_{tip} = \frac{1}{\kappa_{tip}} = \frac{(1 + c_2^2)^{3/2}}{2c_1} \quad (4.42)$$

Sensitivity of the results to the heat extraction (or the undercooling) has been studied. The problem to solve is the same as above, where we have included the heat extraction on the boundary as:

$$\alpha^* \nabla \theta = h_{ext}^* (\theta - \theta_{ext}) \quad \text{on } \partial\Omega \quad (4.43)$$

Let us consider a square domain of size  $[0;320] \times [0;320]$  with a different in-ital temperature  $\theta_0 = -0.5$  and  $\theta_{Nucl} = -0.55$ ,  $e_{min} = 10^{-9}$ ,  $N_2 = 50\,000$ ,  $h_{min} = 0.4$ ,  $k = 0.15$ ,  $Mc_\infty = 0.5325$ ,  $U_0 = 0$ ,  $\Delta\tau = h_{min}/(300 \cdot v_{tip})$ ,  $h_{ext}^* = 163.3 \cdot 10^{-4}$ ,  $\theta_{ext} = -2$ ,  $D^* = 5$ ,  $\alpha^* = 250$ . At the beginning of the computation, nucleation has not occurred, we have only liquid.

We observe that with the heat extraction, average temperature decreases. When the corner temperature is equal to the nucleus temperature, a nucleus of radius one appears in the domain, and solidification starts, maintaining the heat extraction.

Results obtained are shown in Figure 4.10 and Figure 4.11.

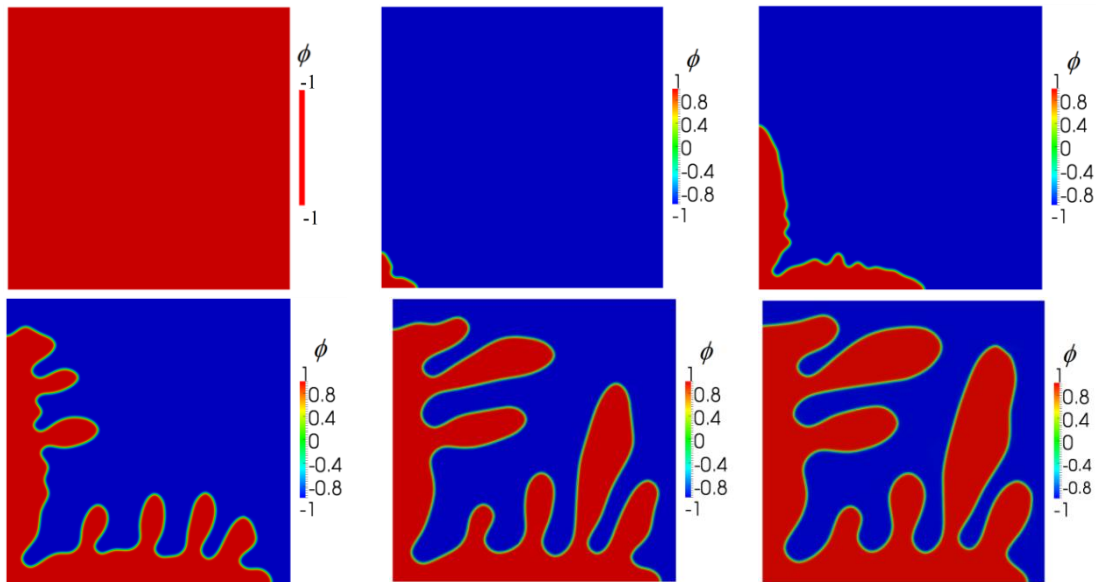


Figure 4.10 Thermo-solutal dendritic growth with heat extraction, plotted at  $\tau = 0, 80, 640.703, 975.205, 1\,677.21, 3\,137.88, 5\,197.26$ , for the conditions given in (4.40), showing the phase function distribution.

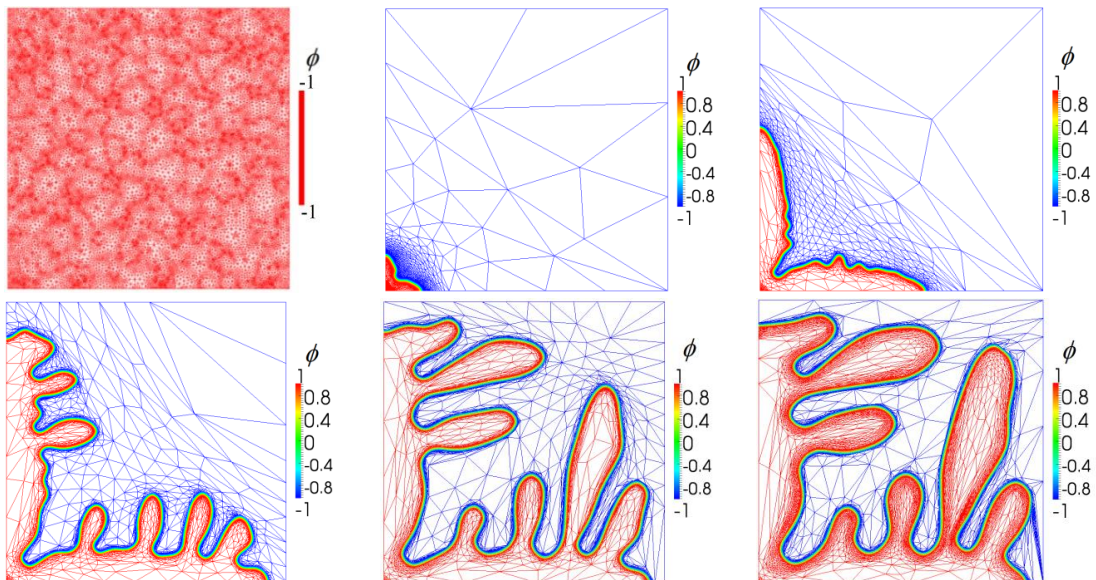


Figure 4.11 Thermo-solutal dendritic growth with heat extraction, plotted at  $\tau = 0, 80, 640.703, 975.205, 1\,677.21, 3\,137.88, 5\,197.26$ , showing the phase function distribution with the adapted mesh.

At the beginning, there is only liquid; after nucleation, the solid fraction begins to increase and the liquid fraction begins to decrease. The computed dendrite tip velocity decreases with time. Furthermore, one observes nucleation and the “recalescence” in the temperature evolution. Temperature decreases before nucleation, because we are extracting heat but when nucleation occurs the grain starts to solidify and temperature starts to increase with the phase change and the heated dendrite. During phase change, either the stationary growth velocity is reached or the border of the domain is attained. At this point, the primary tip stops its growth which implies again a decrease of the temperature, as seen in Figure 4.12. We can also see that with the formation of the nucleus the solid fraction,  $g^s$ , increases and the liquid fraction,  $g^l$ , decreases because the liquid zone is solidifying and transforming into solid. The fraction  $g^z$  of a phase  $z$  inside  $V$  is obtained through:

$$g^z = \frac{1}{V} \int_V \chi^z dV = \frac{V^z}{V} = \frac{\langle \xi^z \rangle}{\langle \xi^z \rangle^z} \quad (4.44)$$

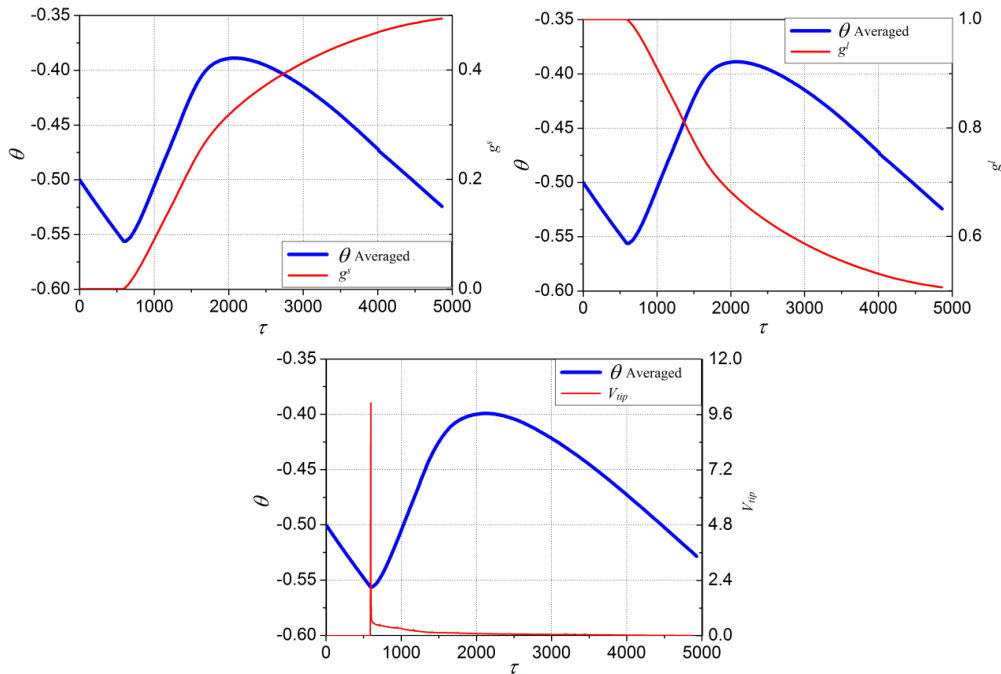


Figure 4.12 Thermo-solutal dendritic growth with heat extraction at  $\tau = 5\,197.26$ , showing the evolution of the averaged temperature and the solid fraction, liquid fraction and the dendrite tip velocity.

Supposing symmetry, simulations have been performed in 1/4 of the domain in 2D and 1/8 or 1/48 in 3D (even if this imposition is not a restrictive condition).

Growth starts using a radius small enough to have a real dendrite without splitting (i.e. primary dendrite splits from the border), as well as enough elements.  $N_2$  should be computed automatically to fix this problem. To enhance the main problem arising when these two points are not verified, Figure 4.13 provides two tested configurations in 2D, under the same physical conditions, but different domain sizes. One observes that, for a given nucleus radius ( $R_0 = 10$  with  $N_2 = 50\,000$ ), for a normalized domain of radius equal to 500, there is splitting of the primary arms, avoided by decreasing the initial nucleus radius to 1.5 or by using the whole domain. For a larger computational domain (with a radius equal to 1000), we should

have even smaller initial nucleus radius and increase the number of elements (in this case  $N_2 = 150\,000$ ).

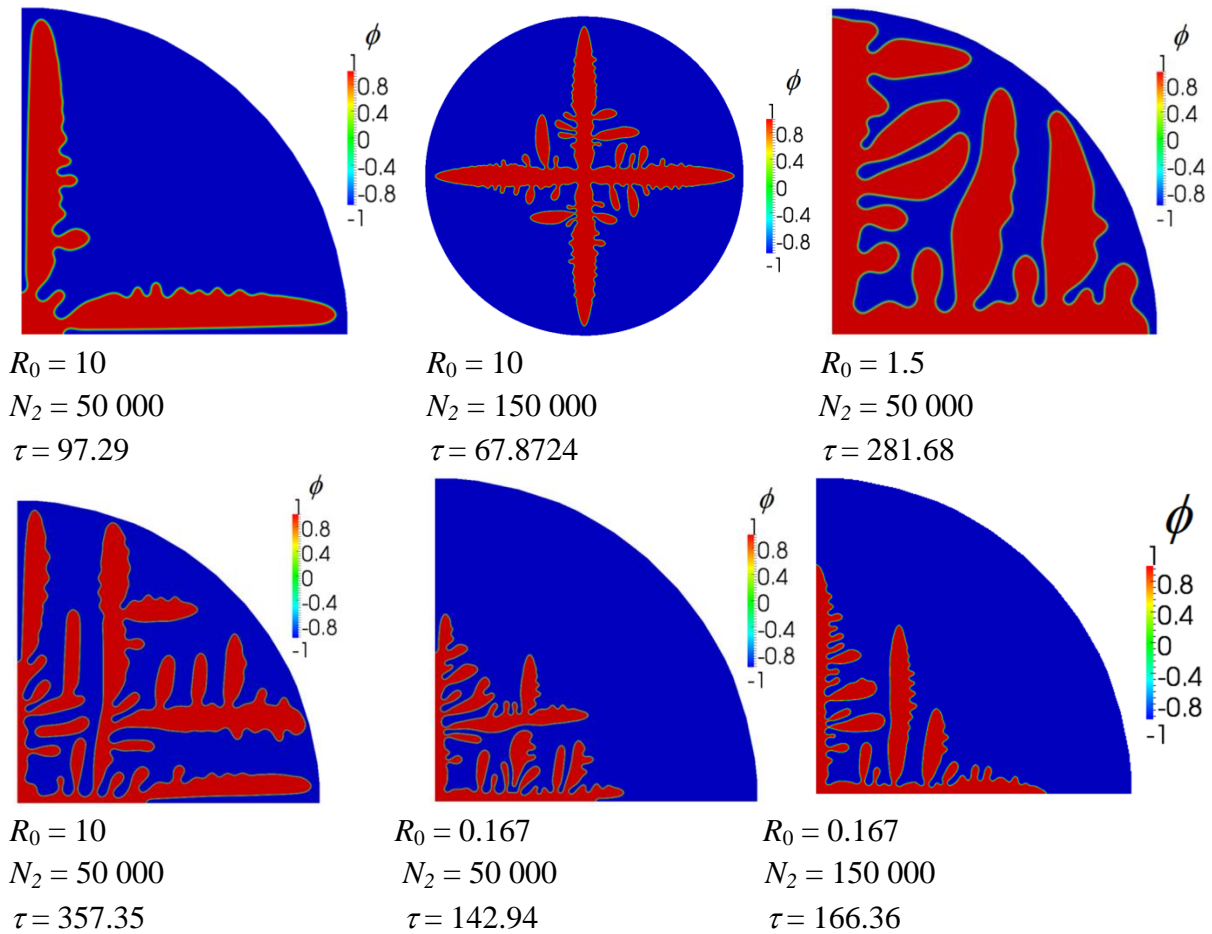


Figure 4.13 2D simulations showing the splitting and how to solve these numerical problems by reducing the initial radius and adding enough elements to do the simulations. The size of the computational domain is equal to 500 in the top row and 1000 in the bottom one.

### 4.3.3 3D thermo-solutal dendritic growth

3D simulations for dendritic growth have been performed. Figure 4.14 illustrates the thermo-solutal dendritic growth for a domain of size  $[0;1000] \times [0;1000] \times [0;1000]$ , with  $\theta_0 = -0.65$ ,  $e_{min} = 10^{-9}$ ,  $N_2 = 2\,000\,000$ ,  $h_{min} = 0.4$ ,  $\varepsilon_4 = 0.05$ ,  $D^* = 4$ ,  $\alpha^* = 40$ , an initial nucleus of radius 1, and remeshing following  $\phi$ ,  $\theta$ ,  $U$  solutions and  $\Delta\tau = h_{min}/(10 \cdot v_{tip})$ .

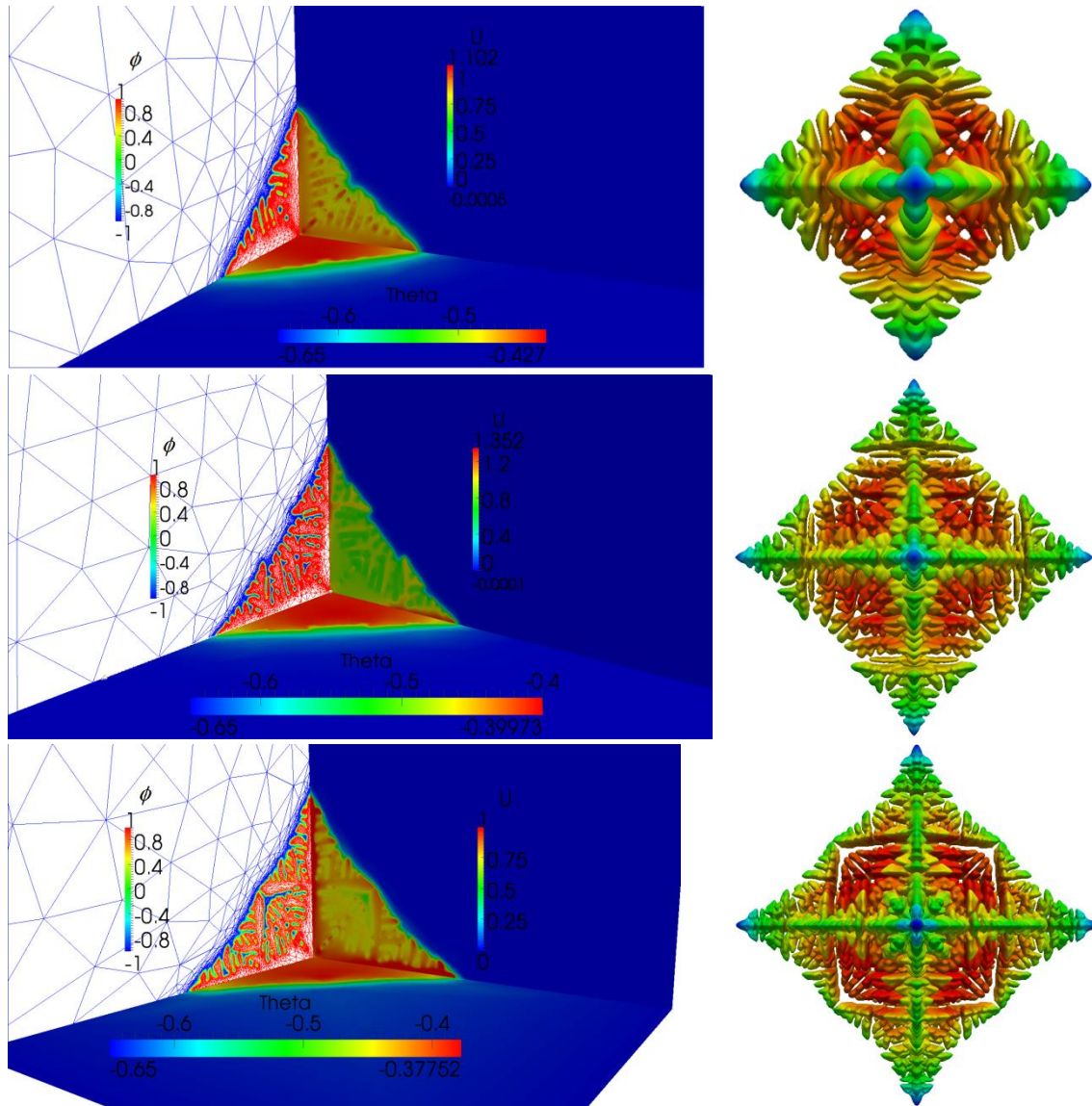


Figure 4.14 3D thermo-solutal dendritic growth at  $\tau = 164.976, 320.871, 416.195$ , showing cuts of the temperature and the composition profiles, as well as the mesh on the left, and the morphology development on the right.

Results are in agreement with previous 2D simulations (Figure 4.15). Numerical accuracy (different arm splitting), still depends on the numerical parameters taken. A strategy to impose this may be to further ameliorate adaptivity by establishing a relationship between the imposed (and wanted) equidistributed error and the number of elements.

Figure 4.15 shows two simulations (growth in the  $\langle 100 \rangle$  and  $\langle 111 \rangle$  directions), using  $1/48$  and  $1/8$  of the domain. In the cases using  $1/48$ , splitting rapidly occurs to finally loose the dendrite form. Same thing occurs for the  $1/8$  case but we will reach the splitting situation after. Thus, more studies should be done on supposing symmetry for the thermo-solutal case when the model will be applied for the physical parameters representing the Al-4.5wt%Cu droplet. Otherwise, it is better to do the simulation for the whole droplet and to ensure strictly the necessary number of elements.

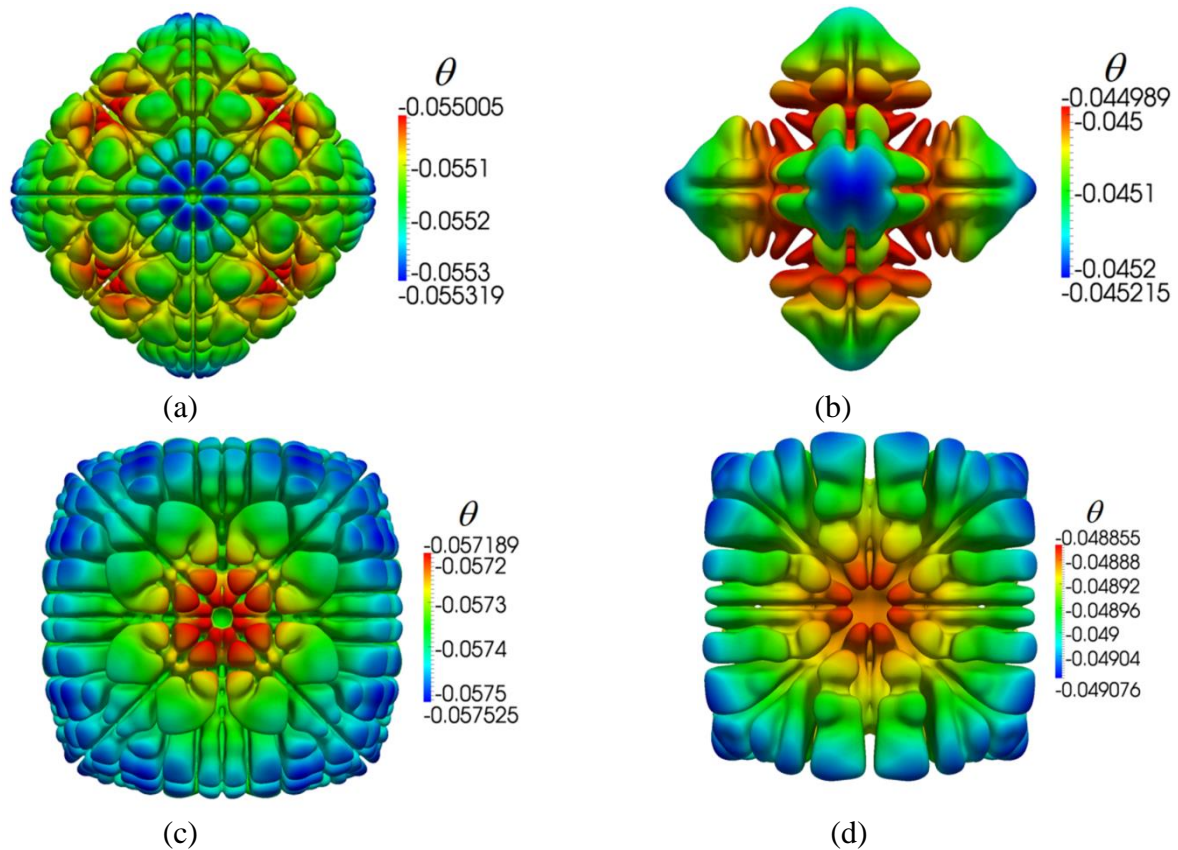
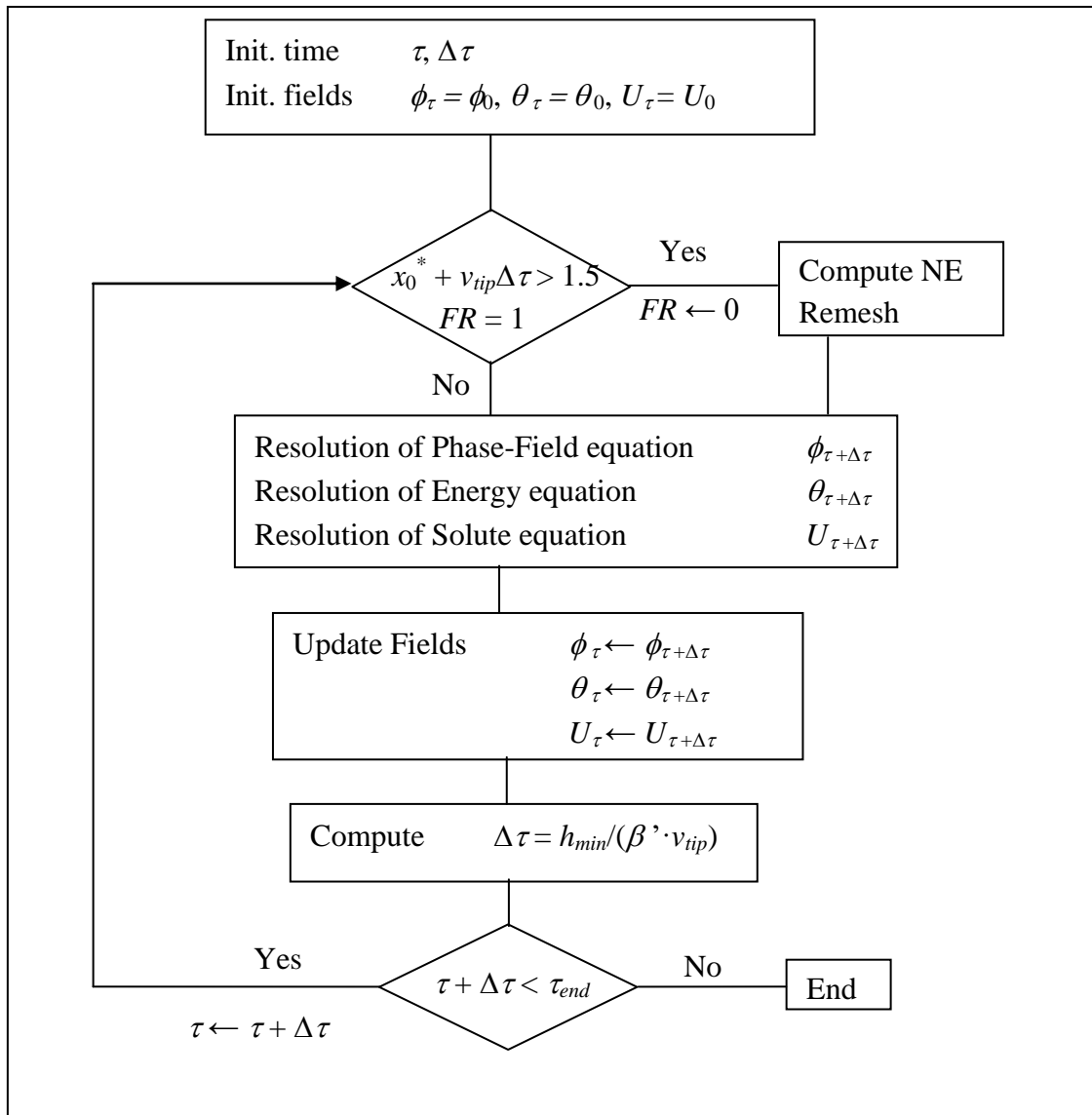


Figure 4.15 3D simulations showing the splitting with 1/48 and 1/8 of the domain, a) 1/48,  $\tau = 12.3$  and  $\varepsilon_4 = 0.02$ , b) 1/8,  $\tau = 11.9$  and  $\varepsilon_4 = -0.02$ , c) 1/48,  $\tau = 13.35$  and  $\varepsilon_4 = 0.02$ , d) 1/8,  $\tau = 14.09$  and  $\varepsilon_4 = -0.02$ .

#### 4.4 Conclusion

In conclusion, there are three equations that need to be solved to simulate thermo-solutal dendritic growth: the phase-field equation, the energy equation and the mass conservation equation. These equations are reformulated here with dimensionless variables. This model has been validated in 1D and 2D for different types of growth. We have seen that we can do 3D thermo-solutal growth but sensitivity studies to obtain the optimal parameters should be made on the parameters of the simulation. Solid and liquid fractions may be deduced, as well as the temperature profile, and one may study the nucleation and “recalescence” phenomena. Simulations in 3D for thermo-solutal growth to validate the model should be done in the future. Nevertheless, model can now be used to try to do simulations for physical growth of an Al-4.5wt%Cu alloy. In the next chapter, we will show the results for this alloy in 2D.

To conclude, the algorithm used to do a complete thermo-solutal dendritic growth is given below.



## Résumé

Dans ce chapitre nous avons présenté les équations du modèle thermo-solutale qui combine les trois mécanismes décrits auparavant. Nous avons fait des calculs en 1D et 2D pour valider les équations utilisées en comparant les résultats numériques avec des résultats analytiques ou considérés comme cas test. A la fin du chapitre, nous avons montré que nous pouvons faire des calculs 3D et extraire les profils de températures ou de compositions et les fractions solide et liquide, et des paramètres comme le rayon de la pointe et d'autres...



## Chapter 5

### 5 Physical simulations

---

|       |                                                              |     |
|-------|--------------------------------------------------------------|-----|
| 5.1   | Modeling of equiaxed solidification in alloys .....          | 100 |
| 5.1.1 | Phase-field model (PF) description .....                     | 101 |
| 5.1.2 | Mean-field model (MF) description .....                      | 104 |
| 5.2   | PF and MF simulations and methodologies for comparisons..... | 110 |
| 5.2.1 | Studied configurations.....                                  | 110 |
| 5.2.2 | Phase-field simulation .....                                 | 113 |
| 5.2.3 | Grain envelope extration .....                               | 121 |
| 5.2.4 | Computation of average and representative quantities.....    | 123 |
| 5.2.5 | Mean-field simulation .....                                  | 125 |
| 5.3   | Parametric study .....                                       | 130 |
| 5.3.1 | Microstructure parameter .....                               | 131 |
| 5.3.2 | Droplet radius .....                                         | 134 |
| 5.3.3 | Initial droplet velocity .....                               | 135 |
| 5.3.4 | Nucleation temperature .....                                 | 136 |
| 5.3.5 | External temperature .....                                   | 137 |
| 5.3.6 | Atomisation gas.....                                         | 138 |
| 5.3.7 | Timestep and initial radius .....                            | 139 |
| 5.4   | Conclusion.....                                              | 140 |

---

To model equiaxed solidification, several approaches have been considered in the literature, such as the previously described phase-field method [AST2009], [BOE2002], [FRI2009], [HEC2004], or others like the mean-field method [TOU2009], front tracking techniques (like the levelset one) [BAN1994], [NAK2006], [SAI1988], [UDA1999], or cellular automata [GAN1999], [RAP1993]. Other coarse-grained models have been developed at the mesoscale to predict the unsteady growth of dendritic grains, like the dendritic needle network model (DNN) [TOU2013] and their internal solid fraction [STE1999], [STE2005], [ZAL2013]. Between all these approaches, the mean-field method as developed by Tournet [TOU2009] has been applied to droplet solidification accounting for dendritic, peritectic and eutectic growth. Other applications of the latter include prediction of macrosegregation and microsegregation for columnar and equiaxed growth, like described in the thesis of Nguyen [NGU2015] and Leriche [LER2015] for heavy ingots solidification, as well as applications to multicomponent alloys

In this part, phase-field (PF) simulations with the present model are compared with mean-field (MF) computations using the developments presented in [TOU2009]. The test case considered is the simulation of a droplet of composition Al-4.5wt%Cu. To compare both

numerical simulations in a given configuration, we have supposed a cylindrical geometry in MF, whereas the geometry is a 2D disk for PF. There are several objectives when performing this comparison: firstly, it allows a more complete validation of our PF model; secondly, it helps improving the MF model through a better understanding of the approximations and the choice of various parameters. One other important motivation is the difference in the computation time between both implementations. We know that the phase-field model is yet not usable on very large domains, since typical systems require high performance computing capabilities available during long computation times to attain quantitative physical results. Looking at the domain of validity of each method will allow the choice of which is more pertinent, when considering the ratio accuracy/available computational power, as done by [NGU2015], [LER2015]. Typically, computations on the same configurations run on several days of CPU time using several processors using the phase-field approach, whereas mean-field one have a duration of a few seconds using one processor.

In the following, the PF model described previously is shortly summarized. Then, the MF model, as developed and implemented by Tourret [TOU2009], is presented. Results for both techniques on a given configuration are compared. Input data as the physical and numerical parameters needed to simulate solidification for the considered Al-Cu alloy are detailed, and outputs, like the topological and averaged quantities of certain variables, are given. For the latter, post-processing of phase-field results is necessary and described in the following. Finally, comparisons and a study on the sensitivity to model parameters are shown.

## 5.1 Modeling of equiaxed solidification in alloys

To perform direct simulations of Al-Cu samples, heat and mass balance equations are solved using the PF method. In parallel, by considering microscopic phenomena in macroscopic configurations, the MF model is applied. For both types of simulations, the following general assumptions were considered:

- (i) the chemical diffusion in the solid is neglected;
- (ii) a 2D disk (PF) envelope is assumed, representative of a transverse section of a cylindrical MF domain;
- (iii) the alloy is binary, i.e. a single chemical species is designated as the solute of the alloy;
- (iv) physical properties of the phases are constant. For example, density is assumed uniform, constant and equal in all the phases;
- (v) nucleation takes place and growth starts at the center of the domains;
- (vi) the computational domain is initially full of liquid, with uniform temperature, and heat is extracted from its boundary until a prescribed nucleation temperature is reached at the center of the domain;
- (vii) a closed system is supposed with respect to the mass balance, meaning that the global composition of the domain remains constant;
- (viii) the solidus and liquidus lines of the phase diagram are supposed linear;

(ix) diffusion takes place in the liquid, and a diffusion layer  $\delta$  is formed ahead of the growing envelope, which is computed with the PF model and be evaluated using an overall balance of solute with the MF model.

Furthermore, thermodynamic descriptions of the system were established with the CALPHAD method (for Calculation of Phase Diagrams). For that purpose, the THERMOCALC software has been used to extract constant physical properties used in the simulations.

### 5.1.1 Phase-field model (PF) description

The phase-field (PF) model has been extensively presented in the previous chapters. It consists in taking a function  $\phi$  to represent the distribution of the solid and liquid phases in the domain. A system of three equations is then solved: conservation of energy; conservation of the solute species; phase propagation to obtain the interface dynamics. To solve this system, a finite element method has been used.

As referred above,  $\phi$  is the function that describes the presence of the liquid and the solid phases in the computational domain  $\Omega$ , composed of the two subdomains, the solid,  $\Omega^s$ , and the liquid,  $\Omega^l$ , with  $\Omega^{s/l}$  their interface.  $\phi$  varies between  $-1$  and  $+1$  and may be defined as:

$$\phi = -\tanh\left(\frac{\eta}{W_0^* \sqrt{2}}\right) \quad (5.1)$$

In this expression,  $W_0^*$  is a non dimensional interface thickness ( $W_0^* = W/W_0$ ), where  $W_0$ , as previously introduced, measures a physical interface width.

The variable  $\eta$  used in this expression is the signed distance to the solid/liquid interface, given by

$$\eta = \begin{cases} d(x^*, \tau) & \text{if } x^* \in \Omega^s \\ 0 & \text{if } x \in \Omega^{s/l} \\ -d(x^*, \tau) & \text{if } x^* \in \Omega^l \end{cases} \quad (5.2)$$

where  $d(x^*, \tau)$  is the distance of  $x^*$  to the interface  $\Omega^{s/l}$ , at time  $\tau$ .

Let us consider the phase diagram of a dilute binary alloy. The system contains two components: the solvent (A) and the solute (B). Conservation equations may be written supposing a sharp interface, with the solid,  $s$ , growing in the liquid,  $l$ . Phase-field, energy, and solute equations are then coupled to give, at our scale, the thermo-solutal dendritic growth problem. Combining the solute and thermal cases, the standard set of sharp-interface equations consists in:

$$\frac{\partial c}{\partial t} = D^l \Delta c \quad (5.3)$$

$$\frac{\partial T}{\partial t} = \alpha \Delta T \quad (5.4)$$

$$c_i (1 - k) v_n = -D^l \nabla c_i \quad (5.5)$$

$$\rho L v_n = (\kappa^s \nabla T^s - \kappa^l \nabla T^l) \quad (5.6)$$

$$T_i = T_M + m c_i - \Gamma \kappa_r - v_n / \mu_\kappa \quad (5.7)$$

where all the variables were previously defined in chapters 2 to 4 and are given in the List of Variables. The dimensionless alloy solute composition  $U$  and temperature  $\theta$  are defined as:

$$U = \left[ \frac{2c/c_\infty}{1+k-(1-k)\phi} - 1 \right] \left( \frac{1}{1-k} \right) \quad (5.8)$$

$$\theta = \frac{T - T_M - mc_\infty}{L/c_p} \quad (5.9)$$

In terms of these variables, one may rewrite the free-boundary problem (5.3)-(5.7) as:

$$\partial_\tau U = D^* \Delta U \quad (5.10)$$

$$\partial_\tau \theta = \alpha^* \Delta \theta \quad (5.11)$$

$$[1 + (1-k)U_i] v_n = -D^* \nabla U^l \quad (5.12)$$

$$v_n = \alpha^* (\nabla \theta^s - \nabla \theta^l) \quad (5.13)$$

$$\theta_i + Mc_\infty U_i = -d_0 \kappa_r - \beta v_n \quad (5.14)$$

From the free energy functional and its derivation using the Cahn-Hilliard framework, we deduce the three equations to be solved as [RAM2004]:

$$\begin{aligned} \pi(\mathbf{n}) \frac{\partial \phi}{\partial \tau} - \nabla \cdot (W^2(\mathbf{n}) \nabla \phi) &= [\phi - \lambda(\theta + Mc_\infty U)(1 - \phi^2)](1 - \phi^2) + \frac{\partial}{\partial x^*} \left( |\nabla \phi|^2 W(\mathbf{n}) \frac{\partial W(\mathbf{n})}{\partial (\partial_{x^*} \phi)} \right) \\ &+ \frac{\partial}{\partial y^*} \left( |\nabla \phi|^2 W(\mathbf{n}) \frac{\partial W(\mathbf{n})}{\partial (\partial_{y^*} \phi)} \right) + \frac{\partial}{\partial z^*} \left( |\nabla \phi|^2 W(\mathbf{n}) \frac{\partial W(\mathbf{n})}{\partial (\partial_{z^*} \phi)} \right) \end{aligned} \quad (5.15)$$

$$\frac{\partial \theta}{\partial \tau} - \alpha^* \Delta \theta = -\frac{1}{2} \frac{\partial \phi}{\partial \tau} \quad (5.16)$$

$$\begin{aligned} \frac{1+k-(1-k)\phi}{2} \frac{\partial U}{\partial \tau} = \\ \nabla \cdot \left( D^* \frac{1-\phi}{2} \nabla U + \frac{W(\mathbf{n})}{2\sqrt{2}} [(1-k)U + 1] \frac{\partial \phi}{\partial \tau} \frac{\nabla \phi}{|\nabla \phi|} \right) + \frac{1}{2} (1 + (1-k)U) \frac{\partial \phi}{\partial \tau} \end{aligned} \quad (5.17)$$

$W(\mathbf{n})$  is a measure of the anisotropy in the surface energy, and may be defined as follows [KAR1998]:

$$W(\mathbf{n}) = W_0^* (1 - 3\varepsilon_4) \left[ 1 + \frac{4\varepsilon_4}{1 - 3\varepsilon_4} \frac{(\partial_{x^*} \phi)^4 + (\partial_{y^*} \phi)^4}{\nabla \phi^4} \right] \text{ in 2D} \quad (5.18)$$

or

$$W(\mathbf{n}) = W_0^* (1 - 3\varepsilon_4) \left[ 1 + \frac{4\varepsilon_4}{1 - 3\varepsilon_4} \frac{(\partial_{x^*} \phi)^4 + (\partial_{y^*} \phi)^4 + (\partial_{z^*} \phi)^4}{\nabla \phi^4} \right] \text{ in 3D} \quad (5.19)$$

where  $\varepsilon_4$  is the constant intensity of anisotropy that define how the secondary dendrite arms grow.

The dimensionless solute diffusivity  $D^*$  is written as:

$$D^* = \frac{D \tau_0}{W_0^2} \quad (5.20)$$

The dimensionless thermal diffusivity  $\alpha^*$  is given by:

$$\alpha^* = \frac{\alpha \tau_0}{W_0^2} \quad (5.21)$$

whereas the scaled magnitude of the liquidus slope is:

$$M = \frac{-m(1-k)}{L/c_p} \quad (5.22)$$

To perform simulations with non-dimensional coordinates, in space and in time, we define  $x^*$  as

$$x^* = x/W_0 \quad (5.23)$$

and  $\tau$  as a dimensionless time:

$$\tau = \frac{t}{\tau_0} \quad (5.24)$$

where  $\tau_0$  is the phase-field relaxation time, in [s].

The thermal capillarity length  $d_0$  [m] is given by:

$$d_0 = \frac{\Gamma}{\rho L / \rho c_p} = \frac{\gamma T_M \rho c_p}{\rho L^2} \quad (5.25)$$

where  $\gamma$  [J·m<sup>-2</sup>] is the excess free energy of the solid/liquid interface. The kinetic coefficient  $\beta$  [m<sup>-1</sup>s] is:

$$\beta = \frac{c_p}{\mu_k L} \quad (5.26)$$

This expression is related to the fact that one may redefine the coefficient  $\beta$  to include the variation of  $\theta$  across the interface using an asymptotic analysis [KAR1998]:

$$\beta = a_1 \left[ \frac{\tau_0}{\lambda W_0} - \frac{a_2 W_0}{\alpha} \right] \quad (5.27)$$

which vanishes when kinetic effects are eliminated. Langer [LAN1986] and then Caginalp [CAG1989] have derived:

$$d_0 = a_1 \frac{W_0}{\lambda} \quad (5.28)$$

In these expressions,  $\tau_0$  is the characteristic time of attachment of atoms at the interface (10<sup>-13</sup> s for metallic systems),  $a_1$  and  $a_2$  are positive constants of the order of the unity that depends on the details of the assumed form of the expression for the free energy. Karma and Rappel [KAR1998] deduced, from the asymptotic analysis, that  $a_1 = 0.8839$  and  $a_2 = 0.6267$ .  $\lambda$  is a dimensionless parameter that controls the strength of the coupling between the phase and diffusion fields. It is taken as  $\lambda = \frac{a_1 W_0}{d_0}$ .

Like detailed in the previous chapters, we have computed numerically  $\nabla W(\mathbf{n})$  and implemented the analytical form of  $\frac{\partial}{\partial x^*} \left( |\nabla \phi|^2 W(\mathbf{n}) \frac{\partial W(\mathbf{n})}{\partial (\partial_{x^*} \phi)} \right)$ ,  $\frac{\partial}{\partial y^*} \left( |\nabla \phi|^2 W(\mathbf{n}) \frac{\partial W(\mathbf{n})}{\partial (\partial_{y^*} \phi)} \right)$  and  $\frac{\partial}{\partial z^*} \left( |\nabla \phi|^2 W(\mathbf{n}) \frac{\partial W(\mathbf{n})}{\partial (\partial_{z^*} \phi)} \right)$ . The derivation forms are shown in Table 2.1.

### 5.1.2 Mean-field model (MF) description

To be able to take into account the microstructure scale (e.g. dendrite tip radius of the order of the micrometer), and phenomena at a larger scale (e.g. heat and mass transfer), which may go up to considering a whole metallurgical process or product (typically 0.01 to 1 meter), volume averaging or mean-field methods may be used. The physical quantities are averaged over an intermediate size between the process and the microstructure, and local conservation equations are replaced by equations on average quantities. When this representative domain is large enough so that fluctuations at the scale of the microstructure are averaged but not too large compared to macroscopic changes, the averaging domain is referred to as Representative Elementary Volume (REV).

In TOURET's work problem, the whole physical domain of the size of a metallic sample is considered. The growth of an equiaxed grain is based on a 1D spherical approximation whereas the growth in a columnar grain is approximated by a 1D cylindrical geometry. The domain size thus corresponds to the radius of a spherical droplet for the spacing between primary dendrites trunks. Microsegregation takes place throughout dendrite arms. A planar geometry for the secondary dendrite spacing  $\lambda_2$  is considered, which is the feature size of the microstructure. A one-dimensional configuration may then be obtained on a domain of dimension  $\lambda_2/2$ , as illustrated in Figure 5.1.

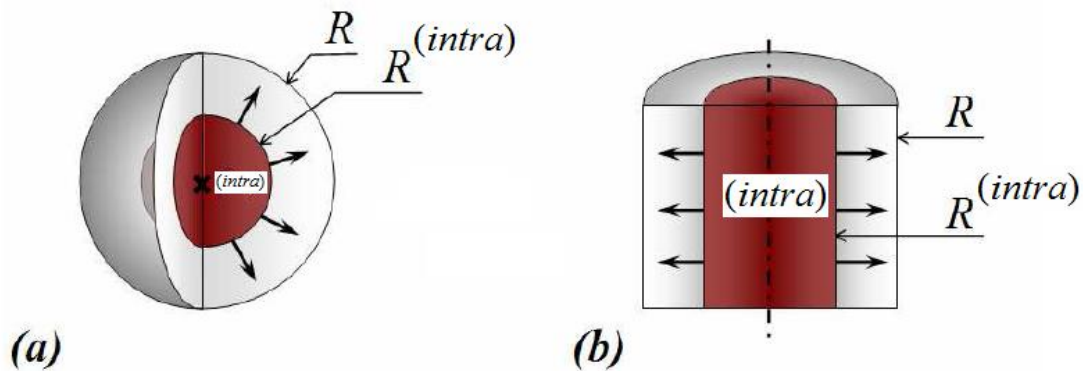


Figure 5.1 Growth of a zone (intra) of coordinates  $R^{(intra)}$  in a domain of dimension  $R$  and of symmetry (a) spherical, (b) cylindrical [TOU2009].

The general local equations of the total mass conservation and the solute mass conservation in each phase are:

$$\frac{\partial}{\partial t}(\rho) + \text{div}(\rho \mathbf{v}) = 0 \quad (5.29)$$

$$\frac{\partial}{\partial t}(\rho c) + \text{div}(\rho c \mathbf{v}) + \text{div}(\mathbf{j}) = \dot{Q} \quad (5.30)$$

Where  $\rho$  is the phase density,  $\mathbf{v}$  is the phase velocity,  $c$  is the phase composition expressed as a mass fraction of solute of the binary alloy,  $\mathbf{j}$  is the diffusion flux in the given phase.

In the following, assumptions considered are:

(i) the solid/liquid interface is supposed at the thermodynamic equilibrium;

- (ii) in metal alloys, thermal diffusion is very fast compared to chemical diffusion. The temperature of the system is assumed to be homogeneous;
- (iii) creation solution term  $\dot{Q}$  is neglected in the solute mass conservation equation.

To establish the equations of the problem to be solved, the following averages need to be defined:

- average value  $\langle \xi \rangle$  on the domain  $V$  of a quantity  $\xi$

$$\langle \xi \rangle = \frac{1}{V} \int_V \xi dV \quad (5.31)$$

- average value  $\langle \xi^z \rangle$  in the domain  $V$  of a quantity  $\xi$  in a phase  $z$ , being  $\chi^z$  a distribution function for phase  $z$  (0 outside  $z$  and 1 inside  $z$ );

$$\langle \xi^z \rangle = \frac{1}{V} \int_V \xi \chi^z dV \quad (5.32)$$

- intrinsic average value  $\langle \xi^z \rangle^z$  specific for each subdomain  $V^z$ , is:

$$\langle \xi^z \rangle^z = \frac{1}{V^z} \int_{V^z} \xi \chi^z dV \quad (5.33)$$

- volume fraction  $g^z$  of a phase  $z$  inside  $V$  is obtained through:

$$g^z = \frac{1}{V} \int_V \chi^z dV = \frac{V^z}{V} = \frac{\langle \xi^z \rangle}{\langle \xi^z \rangle^z} \quad (5.34)$$

Before introducing the derived system of equations, it is also necessary to define:

- $v^{z/w}$  as the average of the normal component of the velocity at the interface  $z/w$  between the phases  $z$  and  $w$ ;
- $c^{z/w}$  as the average of the composition of phase  $z$  at the interface  $z/w$ ;
- $S^{z/w}$  as the interface density, such that

$$S^{z/w} = S^{w/z} = A^{z/w} / V \quad (5.35)$$

with  $A^{z/w}$  the surface of the interface  $z/w$ .

The different combinations of zones used are shown in Figure 5.2. They consist of the solid ( $s$ ), the intradendritic ( $l$  (*intra*)) and the extradendritic liquid ( $l$  (*extra*)) phases. Thus the interface densities are  $S^{s/l(intra)} = S^{l(intra)/s}$  and  $S^{l(extra)/l(intra)} = S^{l(intra)/l(extra)}$ , given by:

$$S^{s/l(intra)} = S^{l(intra)/s} = A^{s/l(intra)} / V \quad (5.36)$$

$$S^{l(extra)/l(intra)} = S^{l(intra)/l(extra)} = A^{l(extra)/l(intra)} / V \quad (5.37)$$

- $l^{z/w}$  is the diffusion length (for composition) at the interface  $z/w$ , defined as

$$l^{z/w} = \frac{c^{z/w} - \langle c^z \rangle^z}{-\frac{\partial c^z}{\partial n^{z/w}}|_{z/w}} \quad (5.38)$$

where  $\mathbf{n}^{z/w}$  is the unit normal at the interface  $z/w$  directed from  $w$  to  $z$ . Different diffusion lengths are defined at the different interfaces  $s/l(intra)$ ,  $l(intra)/s$ ,  $l(intra)/l(extra)$ ,  $l(extra)/l(intra)$  through:

$$l^{l(intra)/s} = \frac{c^{l(intra)/s} - \langle c^{l(intra)} \rangle^{l(intra)}}{-\frac{\partial c^{l(intra)}}{\partial n^{l(intra)/s}} \Big|_{l(intra)/s}} \quad (5.39)$$

$$l^{s/l(intra)} = \frac{c^{s/l(intra)} - \langle c^s \rangle^s}{-\frac{\partial c^s}{\partial n^{s/l(intra)}} \Big|_{s/l(intra)}} \quad (5.40)$$

$$l^{l(extra)/l(intra)} = \frac{c^{l(extra)/l(intra)} - \langle c^{l(extra)} \rangle^{l(extra)}}{-\frac{\partial c^{l(extra)}}{\partial n^{l(extra)/l(intra)}} \Big|_{l(extra)/l(intra)}} = l^{l(intra)/l(extra)} \quad (5.41)$$

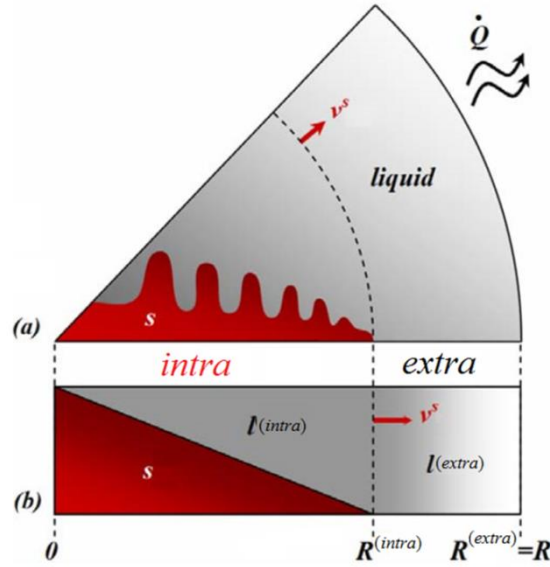


Figure 5.2 (a) Dendritic growth in a spherical geometry; (b) 1D schematic representation of the interface between  $s/l^{(intra)}$  and of the boundary between  $l^{(intra)}/l^{(extra)}$  zones [TOU2009].

Solid fraction ( $g^s$ ), total liquid ( $g^l$ ), made of intra liquid ( $g^{l(intra)}$ ) plus extra liquid ( $g^{l(extra)}$ ) fraction are computed by solving the total mass conservation equations. We can also determine the composition in the solid ( $c^s$ ), intra liquid ( $c^{l(intra)}$ ) and extra liquid ( $c^{l(extra)}$ ) through the resolution of the solute mass conservation equations.

As detailed in [TOU2009] and taking into account the assumptions described above, the total mass conservation equations, in the phases,  $s$ ,  $l(intra)$ ,  $l(extra)$  and at the interfaces  $s/l(intra)$ ,  $l(intra)/s$  and  $l(intra)/l(extra)$ ,  $l(extra)/l(intra)$  are given, respectively, by:

|                                                                   |        |
|-------------------------------------------------------------------|--------|
| $\frac{\partial g^s}{\partial t} = S^{s/l(intra)} v^{s/l(intra)}$ | (5.42) |
|-------------------------------------------------------------------|--------|

|                                                                                                                          |        |
|--------------------------------------------------------------------------------------------------------------------------|--------|
| $\frac{\partial g^{l(intra)}}{\partial t} = S^{l(intra)/s} v^{l(intra)/s} + S^{l(intra)/l(extra)} v^{l(intra)/l(extra)}$ | (5.43) |
|--------------------------------------------------------------------------------------------------------------------------|--------|

|                                                                                          |        |
|------------------------------------------------------------------------------------------|--------|
| $\frac{\partial g^{l(extra)}}{\partial t} = S^{l(extra)/l(intra)} v^{l(extra)/l(intra)}$ | (5.44) |
|------------------------------------------------------------------------------------------|--------|

|                                       |        |
|---------------------------------------|--------|
| $v^{s/l(intra)} + v^{l(intra)/s} = 0$ | (5.45) |
|---------------------------------------|--------|

|                                                     |        |
|-----------------------------------------------------|--------|
| $v^{l(extra)/l(intra)} + v^{l(intra)/l(extra)} = 0$ | (5.46) |
|-----------------------------------------------------|--------|

The solute mass conservation equations, in the phases,  $s$ ,  $l(intra)$ ,  $l(extra)$  and at the interface  $s/l(intra)$ ,  $l(intra)/s$ ,  $l(intra)/l(extra)$ ,  $l(extra)/l(intra)$  are also written as:

|                                                                                                                                                                                                                                                                                                                                                                                                                                |        |
|--------------------------------------------------------------------------------------------------------------------------------------------------------------------------------------------------------------------------------------------------------------------------------------------------------------------------------------------------------------------------------------------------------------------------------|--------|
| $g^s \frac{\partial}{\partial t} (\langle c^s \rangle^s) = \sum_{s/l(intra)} [S^{s/l(intra)} (c^{s/l(intra)} - \langle c^s \rangle^s) (v^{s/l(intra)})]$                                                                                                                                                                                                                                                                       | (5.47) |
| $g^{l(intra)} \frac{\partial}{\partial t} (\langle c^{l(intra)} \rangle^{l(intra)}) = \left[ S^{l(intra)/s} (c^{l(intra)/s} - \langle c^{l(intra)} \rangle^{l(intra)}) \left( v^{l(intra)/s} + \frac{D^l}{l^{l(intra)/s}} \right) \right]$ $+ \left[ S^{l(intra)/l(extra)} (c^{l(intra)/l(extra)} - \langle c^{l(intra)} \rangle^{l(intra)}) \left( v^{l(intra)/l(extra)} + \frac{D^l}{l^{l(intra)/l(extra)}} \right) \right]$ | (5.48) |
| $g^{l(extra)} \frac{\partial}{\partial t} (\langle c^{l(extra)} \rangle^{l(extra)}) =$ $\left[ S^{l(extra)/l(intra)} (c^{l(extra)/l(intra)} - \langle c^{l(extra)} \rangle^{l(extra)}) \left( v^{l(extra)/l(intra)} + \frac{D^l}{l^{l(extra)/l(intra)}} \right) \right]$                                                                                                                                                       | (5.49) |
| $(c^{s/l(intra)} - c^{l(intra)/s}) v^{s/l(intra)} + \frac{D^l}{l^{l(intra)/s}} (c^{l(intra)/s} - \langle c^{l(intra)} \rangle^{l(intra)}) = 0$                                                                                                                                                                                                                                                                                 | (5.50) |
| $(c^{l(extra)/l(intra)} - c^{l(intra)/l(extra)}) v^{l(extra)/l(intra)} + \frac{D^l}{l^{l(extra)/l(intra)}} (c^{l(extra)/l(intra)} - \langle c^{l(extra)} \rangle^{l(extra)})$ $+ \frac{D^l}{l^{l(intra)/l(extra)}} (c^{l(intra)/l(extra)} - \langle c^{l(intra)} \rangle^{l(intra)}) = 0$                                                                                                                                      | (5.51) |

In this approach, the total mass exchanges and the solute mass take place in the direction of structure growth, and throughout the microstructure scale. A planar geometry in a secondary dendrite spacing of  $\lambda_2$  is then considered, as already cited above and illustrated in Figure 5.3. All the geometrical factors defined above, such as the volume element area  $A$ , the interface densities ( $S^{z/w}$ ) and the diffusion length ( $l^{z/w}$ ), are expressed using  $\lambda_2$ .

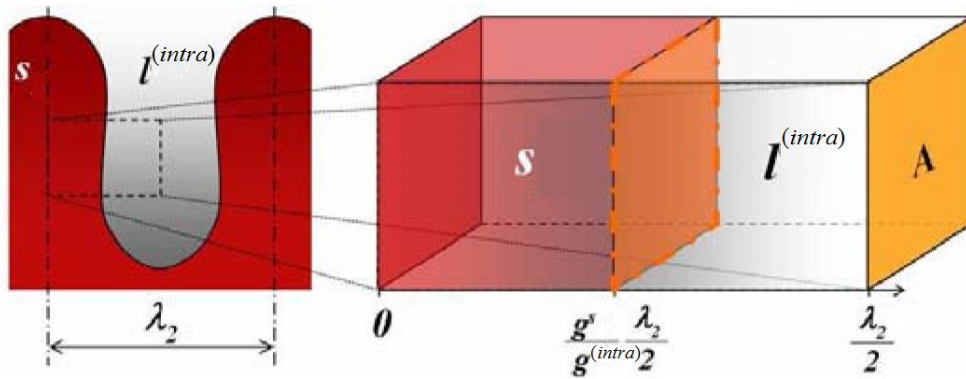


Figure 5.3 Secondary dendrite spacing in a dendritic area [TOU2009], real case and 1D representation.

In a volume element area  $A$  of side length  $\lambda_2/2$ , the ratio of area/volume based on the volume of the zone ( $intra$ ),  $V^{(intra)}$ , is:

$$A^{s/l(intra)}/V^{(intra)} = 2/\lambda_2 \quad (5.52)$$

The interface densities present in the balance equations are expressed based on the total volume of the domain,  $V$ . The interface densities are then given by:

$$S^{s/l(intra)} = \frac{V^{(intra)} A^{s/l(intra)}}{V} = g^{(intra)} \frac{2}{\lambda_2} \quad (5.53)$$

$$S^{l(extra)/l(intra)} = \frac{2R^{(intra)}}{R^2} \quad (5.54)$$

The diffusion length for the solid or intra dendritic liquid phases in zone (intra) depends also on  $\lambda_2$  as follows:

$$l^{l(intra)/s} = \frac{1}{3} \frac{g^{l(intra)}}{g^{(intra)}} \frac{\lambda_2}{2} \quad (5.55)$$

$$l^{s/l(intra)} = \frac{1}{3} \frac{g^s}{g^{(intra)}} \frac{\lambda_2}{2} \quad (5.56)$$

These expressions are deduced assuming a parabolic profile in the phases [TOU2009].

A sensitivity study on the value of  $\lambda_2$  is described in section 5.3, showing its influence on the growth pattern.

The diffusion length in  $l^{(intra)}$  and  $l^{(extra)}$ , at the interfaces  $l^{(intra)}/l^{(extra)}$ ,  $l^{(extra)}/l^{(intra)}$ , can be then written as follows [TOU2009]:

$$l^{l(intra)/l(extra)} = l^{l(extra)/l(intra)} = \frac{R^{(intra)}}{Pe^2 - Pe^{(intra)2}} \left[ \frac{Pe^2}{Pe^{(intra)}} Iv(Pe^{(intra)}) - Pe Iv(Pe) \exp(Pe - Pe^{(intra)}) + (1 + Pe) \exp(Pe - Pe^{(intra)}) - 1 - Pe^{(intra)} \right] \quad (5.57)$$

$Pe_i$  and  $Pe_e$  are Peclet numbers given by  $Pe^{(intra)} = R^{(intra)} v^{(intra)} / D^l$  and  $Pe = R v^{(intra)} / D^l$  with  $R_i$  and  $R_e$ , respectively, the interior and the exterior radius of the zone containing the considered liquid. Function  $Iv(Pe)$  in equation (5.57) is the 3D Ivantsov function  $Iv(P) = P \exp(P) E_1(P)$ . On the mushy dendritic growth zone (intra), the dendrite tip kinetic is imposed using the 2D Ivantsov approximation. Its equation is established in [KUR1986]:

$$v^{(intra)} = v_{tip}^{MF} = - \frac{D^l m_L c^{l/s} (1-k)}{\pi^2 \Gamma} [Iv_{2D}^{-1}(\Omega^{s/l})]^2 \quad (5.58)$$

with  $D^l$  the liquid chemical diffusion coefficient,  $m_L$  the slope of the liquidus line in the equilibrium diagram,  $c^{l/s}$  the compositions at the intragranular liquid boundary given by the equilibrium at the considered temperature and  $\Gamma$  the Gibbs-Thomson coefficient of the interface  $s/l$ .

The function  $Iv^{-1}$  is the inverse of the Ivantsov function, and the supersaturation  $\Omega^{s/l}$  is computed as:

$$\Omega^{s/l} = \frac{c^{l(intra)/s} - \langle c^{l(extra)} \rangle^{l(extra)}}{c^{l(intra)/s} - c^{s/l(intra)}} \quad (5.59)$$

where the average extragranular liquid composition  $l(extra)$ ,  $\langle c^{l(extra)} \rangle^{l(extra)}$ , is taken as the liquid composition far from the interface  $s/l(intra)$ . Note that for 2D growth,  $Iv_{2D}(x) = (\pi x)^{1/2} \exp(x) \operatorname{Erfc}(x^{1/2})$  is used.

To perform comparisons with the phase-field model, one computes the tip velocity, the phase fractions and the compositions in the different zones (solid (s), whole liquid (l), divided into intradendritic liquid ( $l(intra)$ ) and extradendritic liquid ( $l(extra)$ )), by solving the conservation

equations. Surface and the perimeter of the dendritic grain are also determined, by computing the grain radius.

The position  $R^{intra}$ , Figure 5.1, corresponds to the tip radius of the solid zone, which may be determined from the domain size and the solid fraction:

$$R^{intra} = R (g^s)^{1/2} \quad (5.60)$$

Finally, evolution of the temperature is obtained by solving the energy balance equation. Considering a heat exchange with the exterior domain and according to Fourier's law, the overall energy balance of the system, for a heat extraction coefficient,  $h_{ext}$ , is:

$$c_p \frac{dT}{dt} - \Delta H_f \frac{\partial g^s}{\partial t} = S_{ext} h_{ext} (T - T_{ext}) \quad (5.61)$$

where  $T$  is the system temperature,  $T_{ext}$  is the exterior temperature,  $S_{ext} = A_{ext}/V$  is the external interface density with  $A_{ext}$  the exchange surface of heat with the exterior and  $V$  the system volume,  $c_p$  and  $\Delta H_f$  are the heat capacity of the system and the solid fusion latent heat, respectively.

The external interface density  $S_{ext}$  is defined as follows:

$$S_{ext} = \frac{A_{ext}}{V} = \frac{2}{R} \quad (5.62)$$

The heat extraction coefficient has been computed as [TOU2009]:

$$h_{ext} = \frac{\kappa_f}{2R} \left( 2 \left( \frac{B}{\kappa_{ext}(m+1)} \frac{T^{m+1} - T_{ext}^{m+1}}{T - T_{ext}} \right) + (0.4 Re^{1/2} + 0.06 Re^{2/3}) Pr^{0.4} \frac{\mu_\infty^{0.25}}{\mu_p} \right) \quad (5.63)$$

In this equation,  $\kappa_f$  is the thermal conductivity of the atomization gas, evaluated at the system temperature.  $\kappa_{ext}$  is the thermal conductivity of the atomization gas outside,  $Re = 2R\rho_f v/\mu_f$  is the Reynolds number, where  $R$  is the droplet radius,  $\rho_f$  is the density of the atomizing gas,  $v$  is the velocity of the particle and  $\mu_f$  is the kinematic viscosity of the atomizing gas.  $Pr = \mu_f/\rho_f \alpha_f$  is the Prandtl number, where  $\alpha_f$  is the thermal diffusivity of gas.  $\mu_\infty$  is the kinematic viscosity of the atomizing gas away from the droplet,  $\mu_p$  is the kinematic viscosity of the atomizing gas at the surface. To compare with the phase-field model, where we use  $h_{ext}$  constant, we have taken the initial value given by eq(5.63). This is reasonable, as  $h_{ext}$  does not vary much during the solidification time computed. The same has been done for other physical parameters, such as the solute diffusion.

The overall equations for the mean-field model were implemented in C++ and coupled to the TQ version 7.0 of THERMOCALC software (version S) by [TOU2009]. Nevertheless, no coupling with THERMOCALC and constant properties of the phase diagram and phases have been assumed in this work.

## 5.2 PF and MF simulations and methodologies for comparisons

In this section, a review of the computations is performed (including the used material and numerical parameters) and comparisons between phase-field and mean-field simulations are detailed.

### 5.2.1 Studied configurations

As referred before, we consider a binary Al-Cu alloy and a 2D approximation, meaning that the physical studied domain corresponds to the transverse section of a cylinder. Different configurations are presented in Table 5.1 for the 2D standard case (STD 2D), the 3D standard case (STD 3D) and 2D cases changing different parameters. In the following, details on the material and numerical parameters chosen are given, in particular for phase-field simulations.

#### Material parameters

Physical parameters of the alloy are hereafter given and converted to the non-dimensional ones used in the PF simulation. For that, let us consider the Al-Cu phase diagram, shown in Figure 5.4 (obtained with Thermo-Calc [BOG2013]), linearized with a constant liquidus slope  $m$  and a segregation coefficient  $k$  (i.e. solidus slope  $m/k$ ) and illustrated through the red dashed lines. The melting temperature  $T_M$ , the liquidus temperature  $T_L = T_M + mc_\infty$ , the liquidus slope  $m$  and the segregation coefficient  $k$  are also indicated in Figure 5.4.

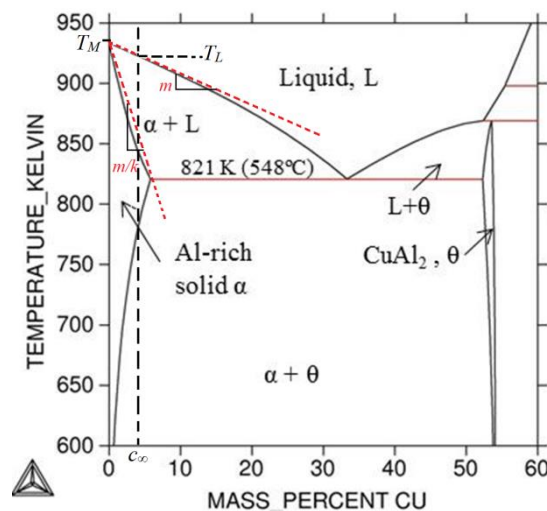


Figure 5.4 Phase diagram of the Al-Cu system, calculated with Thermo-Calc [BOG2013].

Parameter values extracted and used are listed in Table 5.1. Latent heat,  $\rho L$ , heat capacity  $\rho c_p$ , heat diffusion coefficient  $\alpha^l$ , solute diffusion  $D^l$ , and Gibbs-Thomson coefficient  $\Gamma$  are provided in [GAN2008] and [HER2006]. Temperatures can be deduced from the phase diagram for different concentrations of Cu. Capillary length is calculated from  $\Gamma$ ,  $\rho c_p$  and  $\rho L$  as  $d_0 = \frac{\rho c_p \Gamma}{\rho L}$ . The liquidus temperature  $T_L$  is read according to the above phase diagram by choosing the nominal composition  $c_\infty = 4.5$  wt% Cu. Diffusion  $D^s$  of Cu in the Al solid has

been neglected. Nucleation supercooling,  $\Delta T_{Nucl}$ , is the difference of temperature between the melting temperature of the alloy (or the liquidus) and the temperature at which the nucleus will appear. The anisotropy coefficient  $\varepsilon_4$  defines the intensity of dendrite anisotropy, i.e. how much dendrite arms will grow in different directions. Its value is of the order of few % for pure Al, and here its value is 0.02.

### Numerical parameters

A minimal mesh size,  $h_{min}$ , has been chosen to represent both the  $s/l$  interface and the gradients of the composition and the temperature. As described previously, the interface thickness is normalized as  $W_0^* = W_0 / W_0 = 1$  and the normalized time is  $\tau_0^* = t / \tau_0$ . The numerical domain  $R^*$  and the nucleus radius  $R_0^*$  are dimensionless and computed by dividing the original ones by the characteristic thickness  $W_0$  as  $R^* = R / W_0$  and  $R_0^* = R_0 / W_0$ , as done in the previous chapters. The non-dimensional diffusion coefficients were computed as:

$$\alpha^{l*} = \frac{\alpha^l \tau_0}{W_0^2} \quad \text{and} \quad D^{l*} = \frac{D^l \tau_0}{W_0^2}$$

The non-dimensional temperatures (initial  $\theta_0$ , nucleation  $\theta_{Nucl}$  and external  $\theta_{ext}$ ) were determined through Gibbs-Thomson equation, which depends on the melting temperature, the liquidus slope, the latent heat and the heat capacity, such that

$$\theta = \frac{T - T_M - mc_\infty}{L/c_p}$$

As referred previously, the heat transfer coefficient is supposed constant in phase-field simulations, using the first value obtained from the mean-field model (which varies, as will be explained later), given by:

$$h_{ext}^* = h_{ext} \tau_0 / (W_0 \rho c_p)$$

For a given value of  $W_0$  and knowing  $d_0$  and  $\lambda$ , one may determine the needed  $\tau_0$  as follows:

$$\tau_0 = \frac{\lambda W_0^2 a_2}{D^l}$$

Table 5.1 shows the physical and numerical parameters used to compare phase-field and mean-field results, corresponding to the reference simulations in 2D (column “STD 2D”) and 3D (column “STD 3D”). The additional column “2D” details the variation of the parameters that will be considered after for the sensibility analysis, detailed in section 5.3. They include varying the supercooling for nucleation  $\Delta T_{Nucl}$ , the heat transfer coefficient  $h_{ext}$ , the external temperature  $T_{ext}$  and the domain radius  $R_D$ .

| Parameter                                                                                 | Symbol          | STD 2D                | 2D                                              | STD 3D                 | Unit                           |
|-------------------------------------------------------------------------------------------|-----------------|-----------------------|-------------------------------------------------|------------------------|--------------------------------|
| <i>Material physical parameters</i>                                                       |                 |                       |                                                 |                        |                                |
| Nominal composition of Cu                                                                 | $c_\infty$      | 4.5                   | 4.5                                             | 4.5                    | wt%                            |
| Latent heat                                                                               | $\rho L$        | $9.5 \cdot 10^8$      | $9.5 \cdot 10^8$                                | $9.5 \cdot 10^8$       | $\text{Jm}^{-3}$               |
| Heat capacity                                                                             | $\rho c_p$      | $3 \cdot 10^6$        | $3 \cdot 10^6$                                  | $3 \cdot 10^6$         | $\text{Jm}^{-3} \text{K}^{-1}$ |
| Gibbs-Thomson coefficient                                                                 | $\Gamma$        | $2.41 \cdot 10^{-7}$  | $2.41 \cdot 10^{-7}$                            | $2.41 \cdot 10^{-7}$   | Km                             |
| Diffusion of Cu in the Al liquid                                                          | $D^l$           | $4.37 \cdot 10^{-9}$  | $4.37 \cdot 10^{-9}$                            | $4.37 \cdot 10^{-9}$   | $\text{m}^2 \text{s}^{-1}$     |
| Diffusion of Cu in the Al solid                                                           | $D^s$           | 0.0                   | 0.0                                             | 0.0                    | $\text{m}^2 \text{s}^{-1}$     |
| Thermal diffusivity                                                                       | $\alpha^l$      | $33.33 \cdot 10^{-6}$ | $33.33 \cdot 10^{-6}$                           | $33.33 \cdot 10^{-6}$  | $\text{m}^2 \text{s}^{-1}$     |
| Melting temperature                                                                       | $T_M$           | 933.6                 | 933.6                                           | 933.6                  | K                              |
| Liquidus temperature                                                                      | $T_L$           | 918.435               | 918.435                                         | 918.435                | K                              |
| Liquidus slope                                                                            | $m$             | -3.37                 | -3.37                                           | -3.37                  | $\text{Kwt}\%^{-1}$            |
| Segregation coefficient                                                                   | $k$             | 0.17                  | 0.17                                            | 0.17                   | $\text{wt}\% \text{wt}\%^{-1}$ |
| Supercooling for nucleation                                                               | $\Delta_{Nucl}$ | 5.0                   | <b>[5.0,50.0]</b>                               | 5.0                    | K                              |
| Capillarity length                                                                        | $d_0$           | $0.761 \cdot 10^{-9}$ | $0.761 \cdot 10^{-9}$                           | $0.761 \cdot 10^{-9}$  | m                              |
| Surface energy                                                                            | $\gamma$        | 0.245                 | 0.245                                           | 0.245                  | $\text{Jm}^{-2}$               |
| Anisotropy coefficient                                                                    | $\varepsilon_4$ | 0.02                  | 0.02                                            | 0.02                   | -                              |
| <i>Initial and boundary conditions, geometry</i>                                          |                 |                       |                                                 |                        |                                |
| Initial temperature                                                                       | $T_0$           | 933                   | 933                                             | 933                    | K                              |
| Heat transfer coefficient                                                                 | $h_{ext}$       | 1561.86               | <b>709-5706</b>                                 | 1561.86                | $\text{Wm}^{-2}\text{K}^{-1}$  |
| External temperature                                                                      | $T_{ext}$       | 293                   | <b>293-613</b>                                  | 293                    | K                              |
| Domain radius                                                                             | $R_D$           | $50 \cdot 10^{-6}$    | <b>[25·10<sup>-6</sup>,150·10<sup>-6</sup>]</b> | $25 \cdot 10^{-6}$     | m                              |
| Nucleus radius                                                                            | $R_0$           | $0.001 \cdot 10^{-6}$ | $0.0167 \cdot 10^{-6}$                          | $0.0167 \cdot 10^{-6}$ | m                              |
| Interface thickness                                                                       | $W_0$           | $10^{-7}$             | $10^{-7}$                                       | $10^{-7}$              | m                              |
| Time step                                                                                 | $\tau_0$        | $16.65 \cdot 10^{-5}$ | $16.65 \cdot 10^{-5}$                           | $16.65 \cdot 10^{-5}$  | S                              |
| Dimensionless parameter                                                                   | $\lambda$       | 116.15                | 116.15                                          | 116.15                 | -                              |
| Secondary arm spacing (computed from PF)                                                  | $\lambda_2$     | $2 \cdot 10^{-6}$     | <b>2·10<sup>-6</sup>-12·10<sup>-6</sup></b>     | $2 \cdot 10^{-6}$      | m                              |
| <i>Model numerical parameters : including above defined but after adimensionalization</i> |                 |                       |                                                 |                        |                                |
| Mesh size                                                                                 | $h_{min}$       | 0.4                   | 0.4                                             | 0.4                    | -                              |
| Interface thickness                                                                       | $W_0^*$         | 1                     | 1                                               | 1                      | -                              |
| Time unit                                                                                 | $\tau_0^*$      | 1                     | 1                                               | 1                      | -                              |
| Domain radius                                                                             | $R_D^*$         | 500                   | <b>[250,1 500]</b>                              | 250                    | -                              |
| Nucleus radius                                                                            | $R_0^*$         | 0.01                  | 0.167                                           | 0.167                  | -                              |
| Nominal composition of Cu                                                                 | $Mc_\infty$     | 0.0397                | 0.0397                                          | 0.0397                 | -                              |
| Numerical Heat transfer coefficient                                                       | $h_{ext}^*$     | 0.479                 | <b>[0.393,3.166]</b>                            | 0.866                  | -                              |
| Numerical initial temperature                                                             | $\theta_0$      | 0                     | 0                                               | 0                      | -                              |
| Numerical nucleus temperature                                                             | $\theta_{Nucl}$ | -0.0157               | <b>[-0.0157, - 0.1579]</b>                      | -0.0157                | -                              |
| Numerical outside temperature                                                             | $\theta_{ext}$  | -1.975                | <b>[-1.975,- 0.694]</b>                         | -1.975                 | -                              |
| Numerical thermal diffusivity                                                             | $\alpha^{l*}$   | 554 944.5             | 554 944.5                                       | 554 944.5              | -                              |
| Numerical solute diffusivity                                                              | $D^{l*}$        | 72.7605               | 72.7605                                         | 72.7605                | -                              |

Table 5.1 Parameters for solidification simulations of an Al-4.5 wt% Cu system. STD 2D represents a standard case in 2D, STD 3D is the equivalent in 3D, while 2D gives the range of variation of the different parameters that has been considered for the results' sensitivity studies.

## 5.2.2 Phase-field simulation

As detailed in the previous chapters, phase-field simulations involve the resolution of a system of equations on the phase function, temperature and alloy composition using an adaptive finite element method. The dendrite is represented by an implicit function  $\phi$  such that  $\phi = 1$  in the solid,  $\phi = -1$  in the liquid and  $\phi = 0$  at the solid-liquid interface. The developed methodology is mainly based on three steps: phase function  $\phi$  is computed, the non-dimensional temperature  $\theta$  and the non-dimensional composition  $U$  are built; an *a posteriori* error is estimated using the gradients of these variables; from the error, a metric field is constructed and given to the mesher, interfaced with CimLib. The constraints imposed to this procedure are: the minimal mesh size; the number of elements, varying during growth (given by equation (2.69), chapter 2); the remeshing frequency, computed from the maximum growth velocity (as established in equation ((2.63))).

To compare the results obtained by the phase-field solver with the mean-field one, average values will be computed. Hence, the analysis performed hereafter includes:

- the maximum, minimal and average temperatures, where the different slopes of the average temperature plot as a function time are used to detail the different dendrite arm growth and the heat extraction;
- the maximum value of the growth velocity, to show the different variation of the position of this maximum value during the process, which will change according to the variation of the temperature at different instants;
- the radius and the angle of the point of the plane that has the maximum values of temperature and velocity. This point is found to be the dendrite tip before the solid reaches the boundary.

Let us consider first a simulation performed using the reference parameters of the alloy, as defined in Table 5.1 (Column STD 2D). Supposing symmetry, the computation was performed on  $\frac{1}{4}$  of the domain of radius  $R = 50 \mu\text{m}$ , with an initial homogeneous temperature  $T_0 = 933 \text{ K}$  and a nucleation undercooling  $\Delta T_{Nucl} = 5 \text{ K}$ . A heat exchange with the exterior domain is applied, according to the Fourier's law. We recall that the energy balance of the system used with the heat extraction coefficient,  $h_{ext}$ , is,  $c_p \frac{dT}{dt} - \Delta H_f \frac{\partial g^s}{\partial t} = \frac{A_{ext}}{V} h_{ext} (T - T_{ext})$  where  $T$  is the temperature at the boundary of the domain. Figure 5.5 shows the dendritic morphologies obtained at six different instants of our computation, but also the temperature, and the solid and liquid compositions. In these illustrations, the obtained anisotropic mesh is represented on the top-right, with small-sized elements at the interface, variable sizes in the diffusion layers and very large ones where no gradients are present. At the bottom-right, temperature solution was drawn. Its scaling has been adjusted at each time step to better illustrate its distribution in the computational domain. One observes that temperature is higher inside the dendrite than outside and that the boundary of the domain is cooler, since heat is being extracted. The maximum temperature attained at step  $t_3$  is  $907.677 \text{ K}$  (3K above the one shown at  $t_1$ ), after which this maximum value decreases. On the top-left, the solid composition distribution is shown, where the values of the scale take into account the variation of the composition inside

the dendrite during the whole process. Since the chemical diffusion in the solid is supposed zero, solid solute distribution is directly linked to the local temperature (and curvature) of the interface. Thus, it is firstly high in the dendrite's core and decreases during growth as temperature increases due to recalescence. On the bottom-left, the liquid composition is also given, the scale being the same in all the images. During the first stage of solidification, solute rejection by the liquid is localized close to the solid/liquid interface. Temporal evolution of the liquid composition in the interdendritic liquid follows the same trend as the solid: high value when low temperature occurs, and lower values at high temperatures.

In Figure 5.5, the position of the point where the value of the growth velocity is maximum (black cross) is shown, as well as the position of the point where the temperature value is also maximum (black circle).

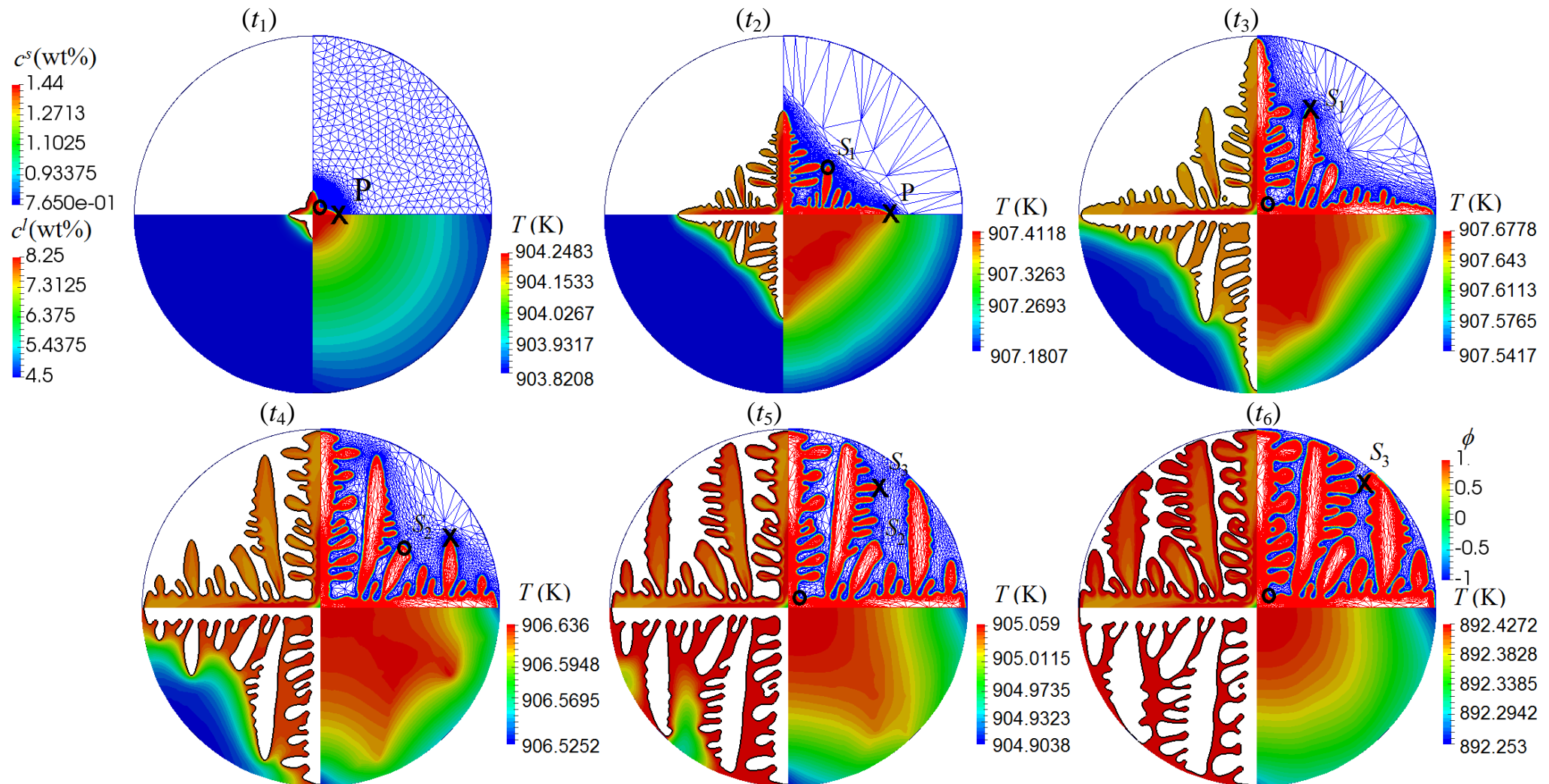


Figure 5.5 2D dendrite growth simulation, using the parameters defined in Table 5.1 (Column STD 2D), images taken at different instants of the computation ( $t_1 = 0.004$  s,  $t_2 = 0.007529$  s,  $t_3 = 0.01403$  s,  $t_4 = 0.01958$  s,  $t_5 = 0.02504$  s,  $t_6 = 0.039025$  s). On the top left, solid composition is shown, on the bottom left, the liquid composition, on the top right, the solid phase field distribution and on the bottom right, the temperature. The black cross shows the position where the growth velocity is maximum, the black circle shows the position where the temperature maximum.

Since the heat capacity is supposed constant and equal for all phases, the average temperature in the domain may be computed as

$$T_{Averaged} = \frac{\int_{\Omega} T dV}{\int_{\Omega} dV} \quad (5.64)$$

To show the difference in the evolution of the maximum, minimum and averaged temperatures, we have determined  $T_{Min} = \min(T)$  and  $T_{Max} = \max(T)$  at each time step, variables shown in Figure 5.6(a), where we see that the temporal evolutions of the maximum and minimum temperature are practically superimposed. One observes that temperature, initially equal to  $T_0$ , starts by decreasing, since heat is being extracted from the domain until the nucleation temperature ( $T_M - \Delta T_{Nucl}$ ) is reached (before  $t_1$ ). A nucleus was created with a small radius ( $R_0 = 0.001 \cdot 10^{-6}$  m), formed at the center of the domain (i.e., for the radius  $\rho = 0$ ).

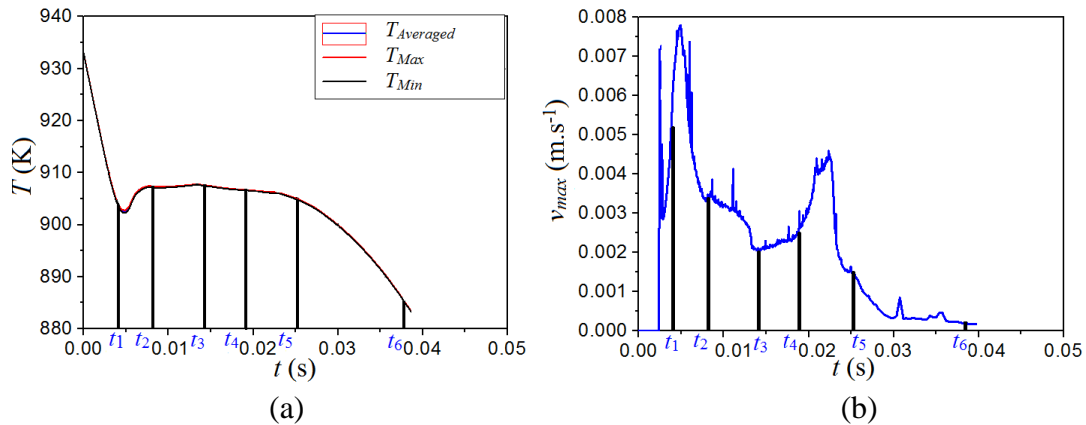


Figure 5.6 (a) Average, minimum and maximum temperature evolution, (b) maximum velocity evolution,  $v_{max}$ .

At the beginning, the maximum velocity occurs at the tip of a primary dendrite arm, as shown by the black cross at the two first instants of Figure 5.5, meaning that the first part of the curve in Figure 5.6(b), after nucleation, provides a very good estimation of the tip velocity. During growth, the temperature increases due to the phase change and at  $t_3$ , a secondary arm,  $S_1$ , appears as growing faster than the primary ones. The latter being stopped at the boundary of the domain. This can also be put into evidence through the temperature plot, where the sign of the slope of the curve changes and the maximum velocity increases. At  $t_3$ , the temperature also starts to decrease and primary dendrite arms have reached the boundary of the domain and continue growing, but at a low velocity. At  $t_4$ , one other secondary arm,  $S_2$ , has the fastest growth inducing more energy release and a change of the slope on the decreasing temperature curve. Then,  $S_2$  touches the computational domain border and its growth stops, but the temperature still continues to decrease due to heat extraction, until the instant  $t_6$ , when growth

becomes very slow and homogeneous between the different arms since there is a small quantity of liquid.

Figure 5.6(b) represents the evolution of the maximum velocity, which varies in relation with the temperature evolution. It increases when the nucleus is created (before  $t_1$ ), but after recalescence ( $t_2$ ) it decreases. When there is growth of a secondary dendritic arm ( $t_3$ ), it increases again and when all arms touch the boundary ( $t_5$ ), temperature and maximum velocity decrease.

Figure 5.7 illustrates the evolution of the polar coordinates of the points having the maximum temperature and velocity (the black circle and cross drawn in Figure 5.5), but also the minimum temperature. To extract the different positions of the maximum value for the growth velocity or the minimum and maximum temperature, we have computed the growth velocity (or temperature) at each mesh node and extracted its maximum or minimum value, as well as the corresponding coordinates. From these latter, the radius  $\rho$  the angle between the  $x$ - or  $y$ -coordinates and the position ( $\theta = \arccos(x/\rho)$  or  $\theta = \arcsin(y/\rho)$ ) may be determined. Polar coordinates of the point with maximum temperature and maximum velocity are presented in a  $\frac{1}{4}$  of a circle, respectively, in Figure 5.7 (c) and (f). This representation allows a clearer visualization of the motion of these points in the computational domain.

For the other figures, the different instants used for analysis are also underlined:  $t_1$  is the time after the nucleus is created,  $t_2$  the one considered for the growing nucleus; at  $t_3$ , the dendrite approaches from the boundary and the temperature starts decreasing at  $t_4$ ; at  $t_5$ , the second arm grows fast so the energy released slows down the heat extraction; at  $t_6$ , the second arm reaches the boundary and the temperature continues to decrease.

Figure 5.7 (a) represents the temporal evolution of the first polar coordinate, being plotted in red the polar coordinate of minimum temperature value and in blue the one of maximum value. One observes that the value of  $\rho$  is  $50 \mu\text{m}$  for the minimum temperature, i.e., it belongs to a point always placed on the boundary of the computational domain. For the maximum temperature, the first polar coordinate changes during the simulation. From  $t_1$  to almost  $t_2$ , it increases when the temperature increases, showing that the position is getting away from the center of the domain. Note that, during this period, the position of the max velocity is mainly on the primary tip along the horizontal ( $\theta = 0^\circ$ ) as shown in Figure 5.7 (e). After recalescence, at  $t_3$ , the first polar coordinate decreases up until when the maximum temperature reaches a plateau around  $t_4$ . Finally, the first polar coordinate increases and is located on the growing secondary arm,  $S_2$ , and at  $t_6$ , it has decreased.

Maximum velocity begins at zero (before nucleation). When the nucleus is created and starts to grow, maximum velocity decreases from the one obtained just after nucleation and when the second arm releases energy, maximum velocity increases until the second arm touches the boundary to again decrease. At the beginning of the growth, the maximum velocity is situated on the dendrite tip in the two directions ( $x$  and  $y$ ), as seen in Figure 5.7 (f); when the dendrite reaches the boundary, the maximum velocity is now on secondary arms growing faster, in particular those located near the dendrite tip.

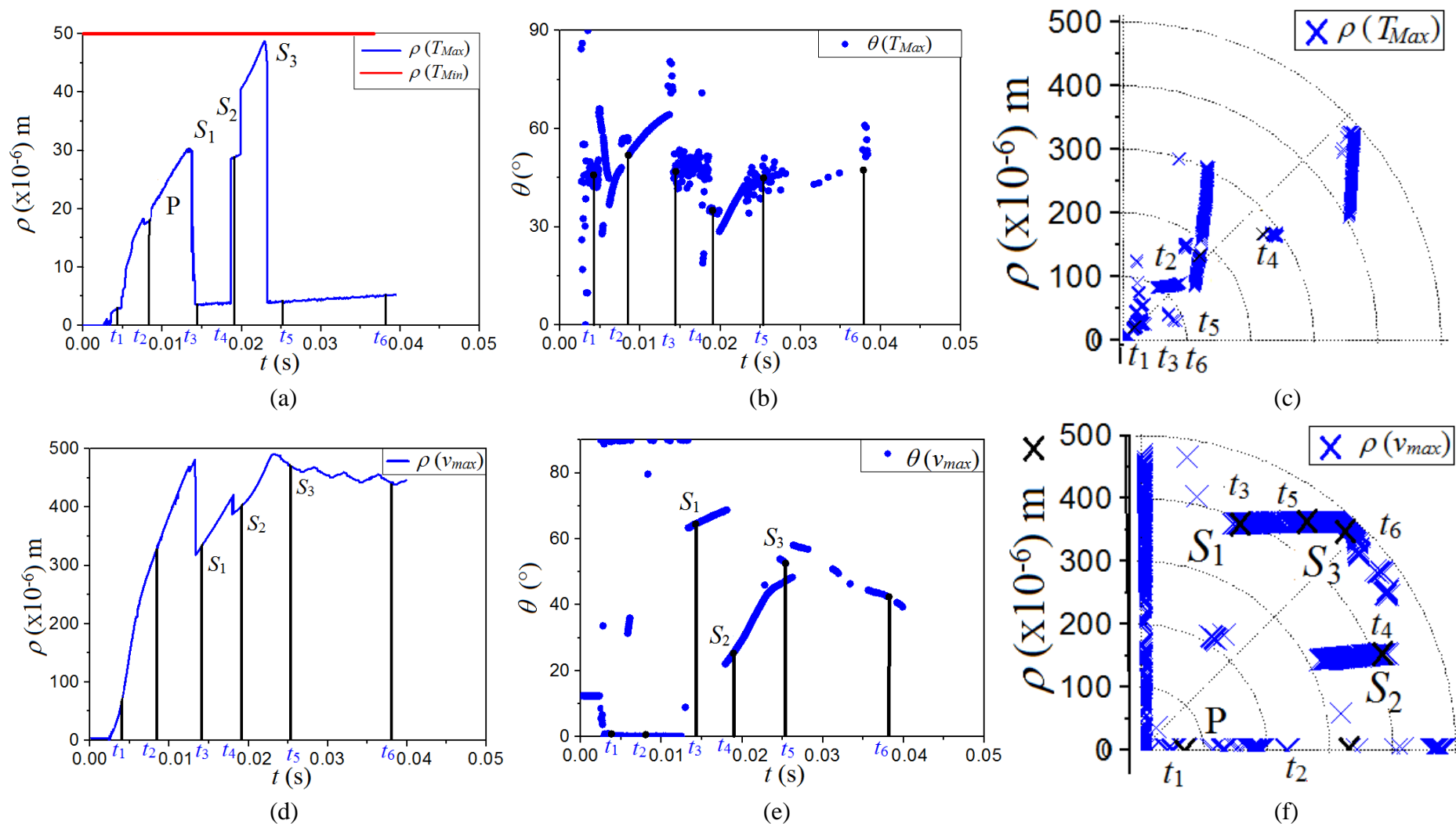


Figure 5.7 Position of the point where the temperature or the velocity is maximum, (a,d) first polar coordinates, (b,e) second polar coordinates, (c,f) location in the droplet domain.

Figure 5.8 presents the distribution of the dimensional temperature and composition for the reference case (2D STD), at  $t_2 = 0.007529$ s. The computational domain and a zoom of the growing dendrite tip are given in Figure 5.8 (a) and (b), respectively. Figure 5.8 (c) represents the variation of the composition and temperature along principal growth directions  $x$ -axis (#1),  $y$ -axis (#2). One may observe that the dimensional temperature and composition at the dendrite tip have smaller values than inside the dendrite. For a planar front, the lowest interface temperature should correspond to the largest composition, but since the Gibbs-Thomson establishes a relation which also depends on the curvature ( $T_i = T_M + m c_i - \Gamma \kappa_r$ , with  $\beta = 0$ ), this is not the case. We conclude that the composition at the tip (from #1) is smaller than the composition at the interface (from #2), from this conclusion we know that we have at the tip the maximum velocity because we have the minimum solute rejected and then we can extract the grain envelope from the position of the dendrite tip.

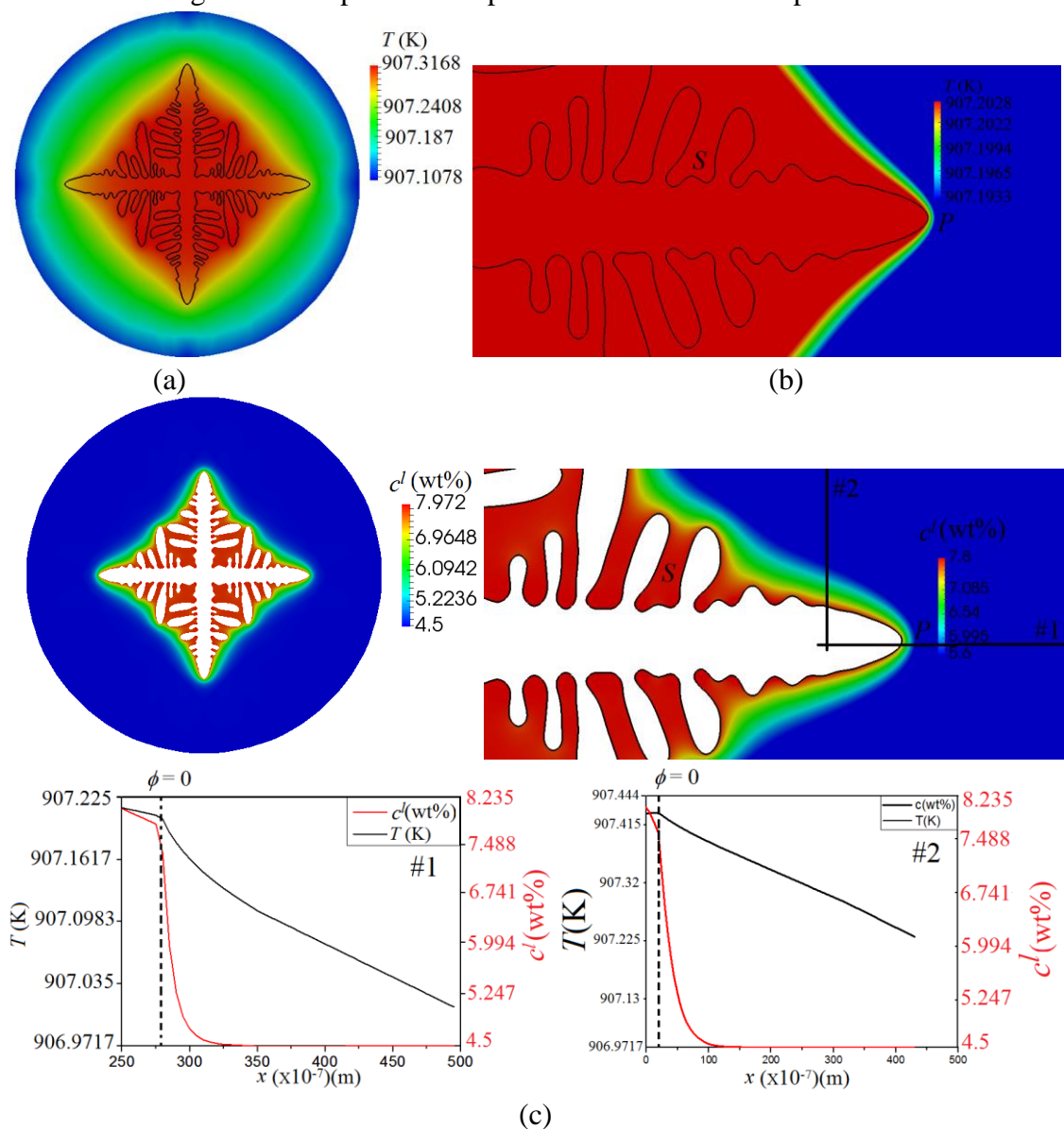


Figure 5.8 Spatial distributions of temperature and composition, with a profile of both variables in the liquid along the center of the primary dendrite arm growing in the  $x$ -direction and  $y$ -direction, all plotted at  $t_2 = 0.007529$  s. The vertical dashed line represents the position of the  $s/l$  interface at this instant.

We notice also that the temperature and the composition start to decrease outside the dendrite, with a larger diffusion layer for temperature because the heat diffusivity is larger than the solute one. Composition decreases thus more abruptly in the liquid, just after the dendrite tip, up until reaching  $c_\infty$ .

Results may also be commented by comparing temperature and composition obtained with the ones theoretically predicted by the phase diagram (Figure 5.9). Firstly, temperature and composition have been extracted using Paraview by selecting a mesh node located at the dendrite tip (**P**) and one placed near a secondary arm next to the interface (**S**) at several time. These extractions, named *Tip (Manual)* and *Interface not Tip (Manual)* have been done manually from the results file and at each 1000 iterations. Temperature at the tip has been also extracted automatically while the simulation is running by identifying the location with highest velocity, named in the following as *Tip (MTC)*.

By plotting the occurred interfacial paths in the phase diagram, computed results show that the composition at the dendrite tip is smaller than inside the dendrite (Figure 5.9 (a)), as well as the temperature, as already observed in Figure 5.8. For a temperature of 908.935, one has  $c_i = 6.76$  at the dendrite tip (**P**) and  $c_i = 6.92$  at the interface (**S**), far from the dendrite tip. The blue line represents the temperature computed at the dendrite tip manually while post-processing the results, and in black the temperature is computed directly (*Tip (MTC)*) for each iteration in the simulation, respectively. The black and blue lines are coincident, which validate our method for tip's representation and the computation of its temperature directly from the simulation, by defining the envelopes and the dendrite thickness as follows. The red line shows the temperature at the interface, point (**S**), extracted manually by a post-processing procedure. This curve is slightly different from the other, showing that the temperature at the interface is higher than at the dendrite tip.

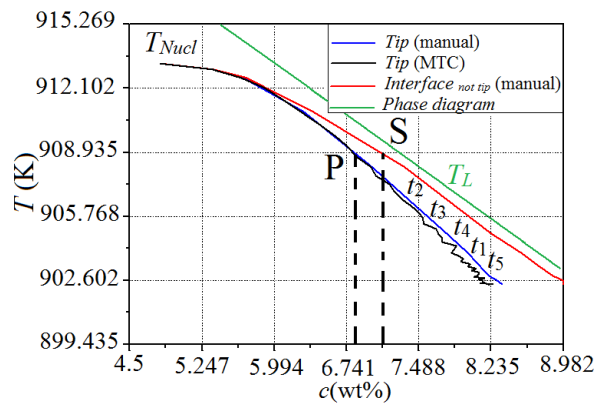


Figure 5.9 Dimensional temperature at the tip computed manually (blue) and automatically (black), and on the interface behind the tip (red), liquidus temperature line (green). P and S position are illustrated in Figure 5.8.

The green lines represent the liquidus temperature obtained from the phase diagram for this Al-4.5wt%Cu droplet. The liquid computed temperature at the interface (**S**) and on the dendrite tip (**P**) have the same variation as the phase diagram liquidus temperature, with a small offset that is shown in Figure 5.9(a).

### 5.2.3 Grain envelope extraction

For the purpose of comparing Phase-Field (PF) and Mean-Field (MF) simulations, the part of the domain which represents the envelope of the grain must be determined from PF results. For that, the non-dimensional composition in the liquid is used (Figure 5.10). Knowing that  $\phi = 0$  represents the interface, one considers,

$$U_l = \begin{cases} U & \text{for } \phi < 0 \text{ (Liquid)} \\ 0 & \text{for } \phi \geq 0 \text{ (Solid)} \end{cases} \quad (5.65)$$

We choose to extract the point where  $v_{max}$  occurs. Once this point is extracted, one gets its composition, designated  $U_{vmax}$ . Then, all the points that have this value of the composition are identified and an isosurface of  $U_{vmax}$  is built (Figure 5.10(d)). This iso-surface is drawn to represent the grain envelope.

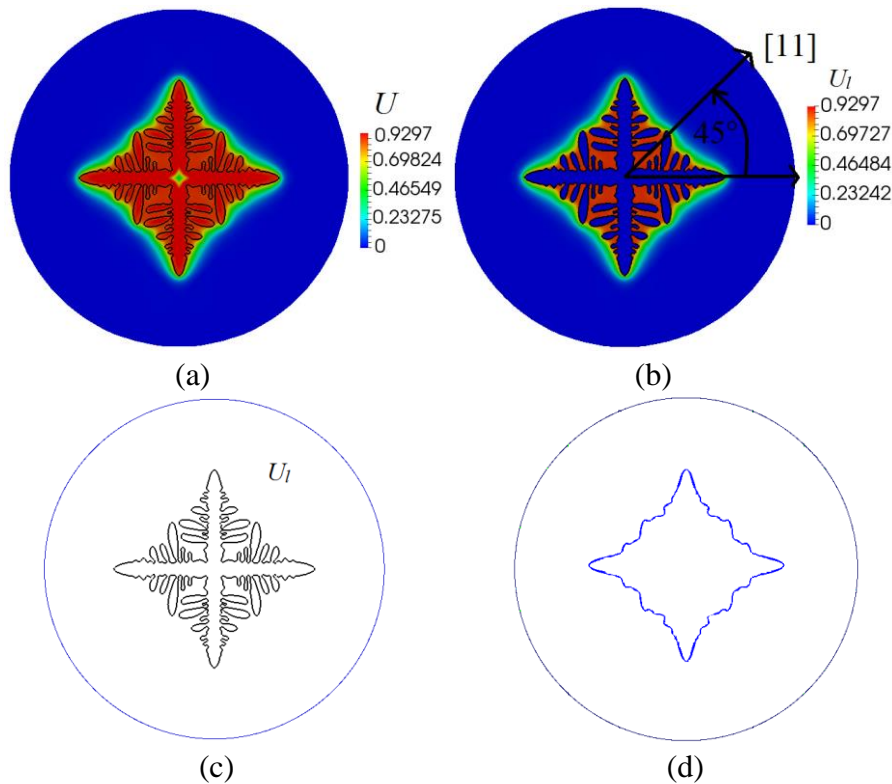


Figure 5.10 a) Distribution of the non-dimensional composition  $U$  at  $t = 0.007529$  s for a simulation under the conditions STD2D (Table 5.1), b) Distribution of the non-dimensional composition in the liquid  $U_l$  at  $t = 0.007529$  s extracted from  $U$ , c) profile of the dendrite contour  $\phi = 0$ , d) grain envelope extracted from the isovalue  $U_{vmax} = 0.7731$ .

In fact, the methodology to extract  $U_{vmax}$  provides two contours. This is illustrated in Figure 5.11(a), by drawing the profile of  $U_l$  along the  $x$ -direction (blue line) defined in Figure 5.10(b).  $U_{vmax}$  value cuts the profile at two different positions on the top of the curve. Consequently, we have two contours as seen in Figure 5.11(b): one for the grain envelope itself, as shown in Figure 5.12(b), and one other superposed with the dendrite interface, as illustrated in Figure 5.12 (a). The reason is linked to the decrease of the  $U_l$  field when entering the solid phase as illustrated in the vicinity of the dendrite tip where the two contours are

superposed. One may then also easily compute the surface occupied by intragranular liquid, by subtracting the surface of the solid dendrite defined with  $\phi = 0$ , from the surface of the grain defined by the two contours provided by our extraction method. We can see also from Figure 5.11(a) from the black line, drawn in the [11] direction, that  $U_{vmax}$  cuts the curve four times. These four cuts represent the dendrite and the envelope contour for this direction. The different cuts can be seen in Figure 5.10(b) when the black line in the [11] direction cuts the dendrite and the envelope. While making the difference between the two directions ( $0^\circ$  and  $45^\circ$ ), we can conclude that the best way is the use of  $U_{vmax}$  as an index to extract the envelope.

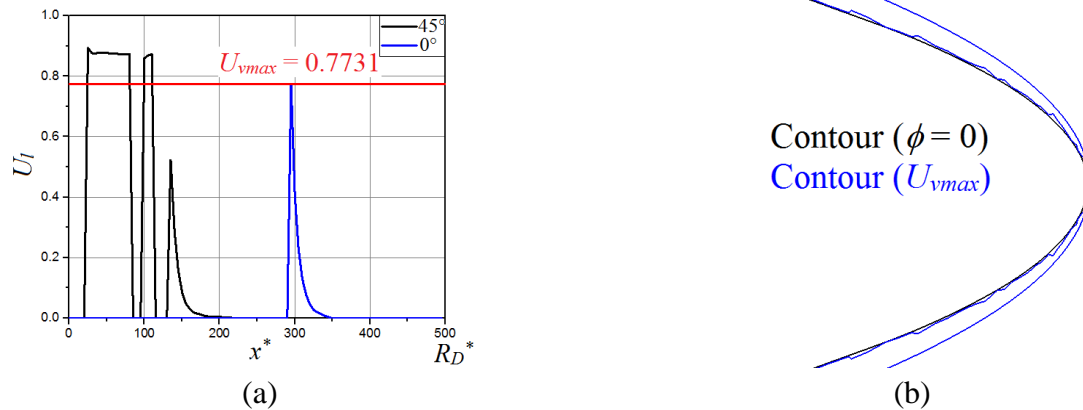


Figure 5.11 a) Composition profile in the liquid,  $U_l$ , plotted along a  $45^\circ$  angle direction with the  $x$ -axis from the cylindrical domain center (black line) and for the  $x$ -direction at  $0^\circ$  (blue line), at  $t = 0.007529$  s, b) grain boundary close to the dendrite tip at  $t_2 = 0.007529$  s.

Figure 5.12 shows the  $s/l$  interface contours and the grain envelope ones, corresponding to the two isosurfaces obtained from  $U_{vmax}$ : (a) gives the dendrite contour for  $\phi = 0$  and b) illustrates the grain contour that contains solid plus intragranular liquid.

|                    |                     |
|--------------------|---------------------|
| $t_1 = 0.004$ s    | $U_{vmax} = 0.9326$ |
| $t_2 = 0.007529$ s | $U_{vmax} = 0.7731$ |
| $t_3 = 0.01403$ s  | $U_{vmax} = 0.785$  |
| $t_4 = 0.01958$ s  | $U_{vmax} = 0.8391$ |
| $t_5 = 0.02504$ s  | $U_{vmax} = 0.9984$ |

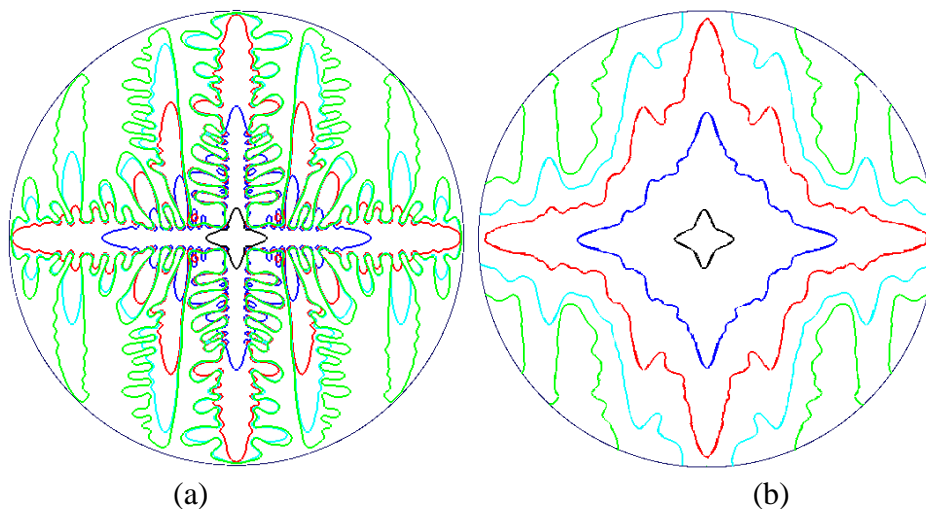


Figure 5.12 Contour at different instants of a)  $s/l$  interface, b) grain envelope.

### 5.2.4 Computation of average and representative quantities

To compute average values of the different fields, it is necessary to establish the mathematical criteria of extraction of the existing zones. A point belongs to: the solid zone ( $s$ ),  $\Omega^s$  when  $\phi > 0$ ; the liquid zone ( $l$ ),  $\Omega^l$  when  $\phi < 0$ ; the extragranular liquid zone (extra),  $\Omega^{extra}$  when  $\phi < 0$  and  $U_l < U_{vmax}$ ; the intragranular liquid zone (intra),  $\Omega^{intra}$  when  $\phi < 0$  and  $U_l > U_{vmax}$ ; the solid (liquid) zone at the interface when  $\phi > 0$  for  $\partial\Omega^s$  ( $\phi < 0$  for  $\partial\Omega^l$ ) and inside the thickness  $W_0$  computed with a Dirac function.

In summary:

$$\begin{aligned}\Omega^s &= \{x \in \Omega, \phi(x) > 0\}, \quad \Omega^l = \{x \in \Omega, \phi(x) < 0\}, \\ \Omega^{extra} &= \{x \in \Omega, U_l(x) < U_{vmax}\}, \\ \Omega^{intra} &= \{x \in \Omega, U_l(x) > U_{vmax}\}, \\ \partial\Omega^s &= \{x \in \Omega, \phi(x) > 0 \text{ and } \phi(x) < 0.99\}, \\ \partial\Omega^l &= \{x \in \Omega, \phi(x) < 0 \text{ and } \phi(x) > -0.99\}, \\ \partial\Omega^{intra} &= \{x \in \Omega, U_l(x) > U_{vmax} \text{ and } U_l(x) > U_{vmax} - 0.01\}\end{aligned}$$

To obtain average values, it is important to define a Heaviside function per zone:

$$\chi^Z = \begin{cases} 0 & \text{outside zone } \Omega^Z \\ 1 & \text{inside zone } \Omega^Z \end{cases} \quad (5.66)$$

This function may be applied to the solid and liquid phases and smoothed using the phase-field variable to determine the phase fraction. Thus,  $\chi^l$  and  $\chi^s$  can be explicitly determined as:

$$\chi^l = \frac{1 - \phi}{2} \quad \text{and} \quad \chi^s = \frac{1 + \phi}{2}$$

According to the equations (5.31), (5.34), one has thus:

- the total liquid fraction,  $g_l$  and the total solid fraction,  $g_s$ 

$$g_l = \int_{\Omega} \chi^l dV / \int_{\Omega} dV \quad g_s = \int_{\Omega} \chi^s dV / \int_{\Omega} dV$$
- three integrals are defined to simplify the notations
$$A^{l(intra)} = \int_{\Omega} \chi^l \chi^{intra} dV \quad A^{l(extra)} = \int_{\Omega} \chi^l \chi^{extra} dV \quad A = \int_{\Omega} dV$$
- the liquid fraction in the extragranular zone,  $g_l^{extra}$  and in the intragranular zone,  $g_l^{intra}$ 

$$g_l^{l(extra)} = A^{l(extra)} / A \quad g_l^{l(intra)} = A^{l(intra)} / A$$
- the total fraction of the intragranular zone,  $g^{intra}$ 

$$g^{intra} = \int_{\Omega} \chi^{intra} dV / \int_{\Omega} dV$$
- the average liquid composition,  $\langle c^l \rangle^l$ , and the average solid composition,  $\langle c^s \rangle^s$ , with  $c/c_{\infty} = \frac{1}{2}[1 + k - (1 - k)\phi][(1 - k)U + 1]$ 

$$\langle c^l \rangle^l = \int_{\Omega} \frac{2c}{[1+k-(1-k)\phi]} \chi^l dV / \int_{\Omega} \chi^l dV \quad \langle c^s \rangle^s = \int_{\Omega} \frac{2ck}{[1+k-(1-k)\phi]} \chi^s dV / \int_{\Omega} \chi^s dV$$
- the average liquid composition in the extragranular zone,  $\langle c^{l(extra)} \rangle^{l(extra)}$  and in the intragranular zone,  $\langle c^{l(intra)} \rangle^{l(intra)}$

$$\begin{aligned} \langle c^{l(extra)} \rangle^{l(extra)} &= \int_{\Omega} \frac{2c}{[1+k-(1-k)\phi]} \chi^l \chi^{extra} dV / A^{l(extra)} \\ \langle c^{l(intra)} \rangle^{l(intra)} &= \int_{\Omega} \frac{2c}{[1+k-(1-k)\phi]} \chi^l \chi^{intra} dV / A^{l(intra)} \end{aligned}$$

- the average solid composition at the interface,  $\langle c^{s/l} \rangle^{s/l}$  and the average liquid composition at the interface,  $\langle c^{l/s} \rangle^{l/s}$

$$\begin{aligned} \langle c^{s/l} \rangle^{s/l} &= \int_{\Omega} \frac{2ck}{[1+k-(1-k)\phi]} \chi^s \chi^{interface} dV / \int_{\Omega} \chi^s \chi^{interface} dV \\ \langle c^{l/s} \rangle^{l/s} &= \int_{\Omega} \frac{2c}{[1+k-(1-k)\phi]} \chi^l \chi^{interface} dV / \int_{\Omega} \chi^l \chi^{interface} dV \end{aligned}$$

Figure 5.13 (a) shows the solid ( $s$ , white) dendrite, and liquid ( $l$ , red) zones, where the latter is divided in the ( $extra$ ) and ( $intra$ ) zones in Figure 5.13 (b), representing the extragranular liquid (outside the grain envelope, red) and the intragranular liquid (inside the grain envelope, blue). The grain envelope contains thus the solid and the intragranular liquid. On the right, Figure 5.13 (c), the ( $s/interface$ ) and ( $l/interface$ ) zones are plotted, providing the solid and the liquid at the interface.

To compute an average grain radius for comparison with an equivalent cylindrical system, one may use one of the following formulas:

$$\begin{aligned} R_{Sgrain} \text{ (computed from the surface)} \quad R_{Sgrain} &= \sqrt{\frac{A_{solid} + A_{intra}}{\pi}} \\ R_{Pgrain} \text{ (computed from perimeter): } R_{Pgrain} &= \sqrt{\frac{P_{intra}}{2\pi}} \end{aligned}$$

The solid surface and the intra surface used in the computation of  $R_{Sgrain}$  equation are defined as:

$$A_{solid} = \int_{\Omega} \chi^S dV, \quad A_{intra} = \int_{\Omega} \chi^{intra} dV, \quad A_{extra} = \int_{\Omega} \chi^{extra} dV$$

The intra perimeter used in the computation of  $R_{Pgrain}$  equations is defined as:

$$P_{intra} = \int_{\partial\Omega^{intra}} \chi^{intra} dV - P_{solid}$$

Others values used later are:

$$P_{solid} = \int_{\partial\Omega^s} \chi^S dV$$

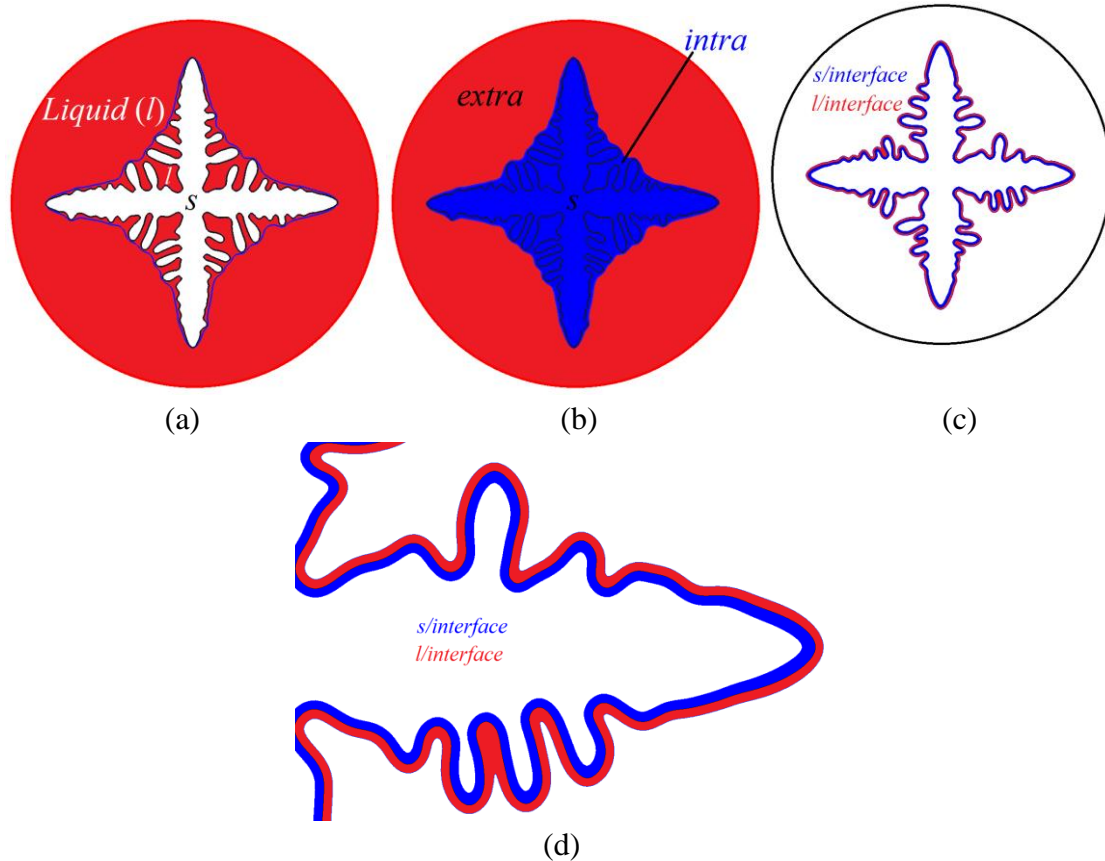


Figure 5.13 Representation of the different zones, a) solid ( $s$ , white), liquid ( $l$ , red), b) intragranular (*intra*, blue), extragranular (*extra*, red), c) solid at the interface ( $s/interface$ , blue,  $s/l$ ), liquid at the interface ( $l/interface$ , red,  $l/s$ ), d) zoom of c)

### 5.2.5 Mean-field simulation

Results obtained with the MF and the PF models may now be compared. The Argon atomization environment is first considered, corresponding to  $h_{ext} = 863.253 \text{ W m}^{-2} \text{ K}^{-1}$  in Table 5.1 (case STD 2D).

Figure 5.14 gives the overall surface of the solid (black line), intragranular liquid (green line) and extragranular liquid (blue line), for phase-field simulations. Since the grain perimeter decreases after the dendrite touches the boundary, we chose to compute the grain radius from the grain surface. The latter is obtained by adding the surface of the solid to the intragranular liquid surface.

The solid perimeter and the grain perimeter increase while solidification proceeds and the dendrite is growing. The solid perimeter is bigger than the grain perimeter because inside the grain there are several dendrite arms. The solid surface also increases with solidification and the surface of the extra liquid decreases because the liquid is being transformed into solid. The intracellular liquid also increases slowly due to the formation of the dendritic solid phase. At the end of the solidification, the intracellular surface falls toward zero because all the liquid is solidified.

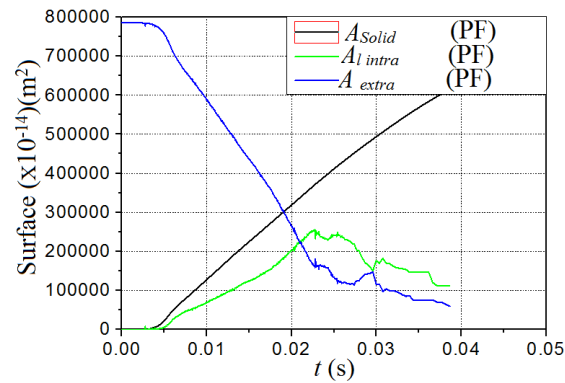


Figure 5.14 Surface of the solid, intragranular zone and extragranular zone.

As input to the MF model, a length scale for diffusion in the solid is required. It is approximated by the secondary dendrite arm spacing, evaluated by  $\lambda_2 = 2 \cdot 10^{-6}$  m. Average temperature, tip velocity and grain radius evolutions are compared in Figure 5.15. Temperature and velocity are in good agreement for the two models and the grain radius is also very close, when it is computed using the grain surface. The grain radius computed in the PF method (in blue) using the grain perimeter does not provide a good value to compare with the MF model used, because the perimeter decreases when the dendrite comes into contact with the boundary due to our method of extracting the grain envelope.

The cooling plot presents a quick decrease of the temperature in the liquid zone due to heat extraction, the recalescence, and then a slow cooling which corresponds to the formation and evolution of the solid phase with the latent heat release.

One observes that, at the recalescence point, the temperature decreases quicker in mean-field results than for phase field ones. This induces a late increase for the velocity tip, as seen in Figure 5.15(a). Generally, temperature presents always lower values in mean-field simulations, providing also lower tip velocities.

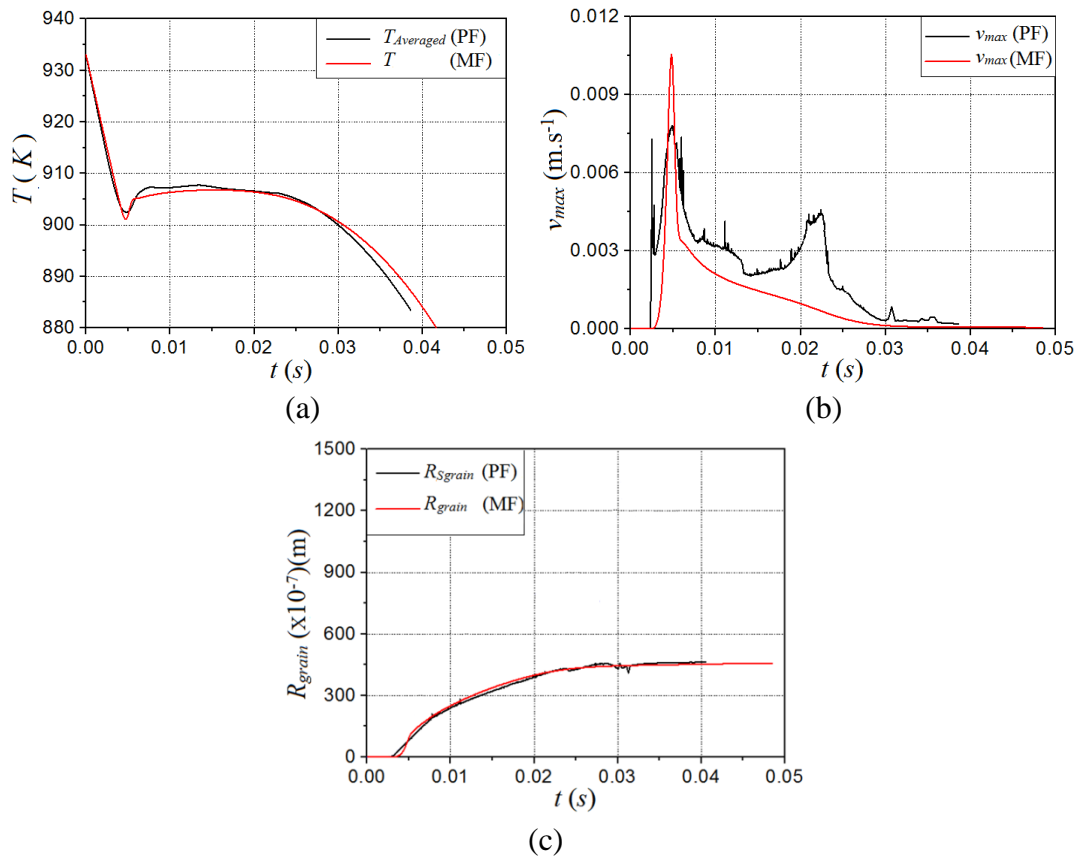


Figure 5.15 Comparison between PF and MF for 2D growth: a) average temperature evolution, b) tip velocity evolution, c) grain radius evolution (with a value extracted from the grain surface  $S_{grain}$ , in the phase-field case).

Evolution of the average solid and liquid fractions and of the composition may also be drawn. Figure 5.16 and Figure 5.17 show a comparison between MF and PF results for these variables, in the different zones. Solid (black) and liquid (red) average fractions superpose quite well. The intragranular (green) and extragranular (blue) liquid fractions follow the same tendency using the two models with small differences. The same happens for the intragranular (purple) fraction, which is equal to the intragranular liquid fraction added to the solid average fraction, included also in the intragranular zone.

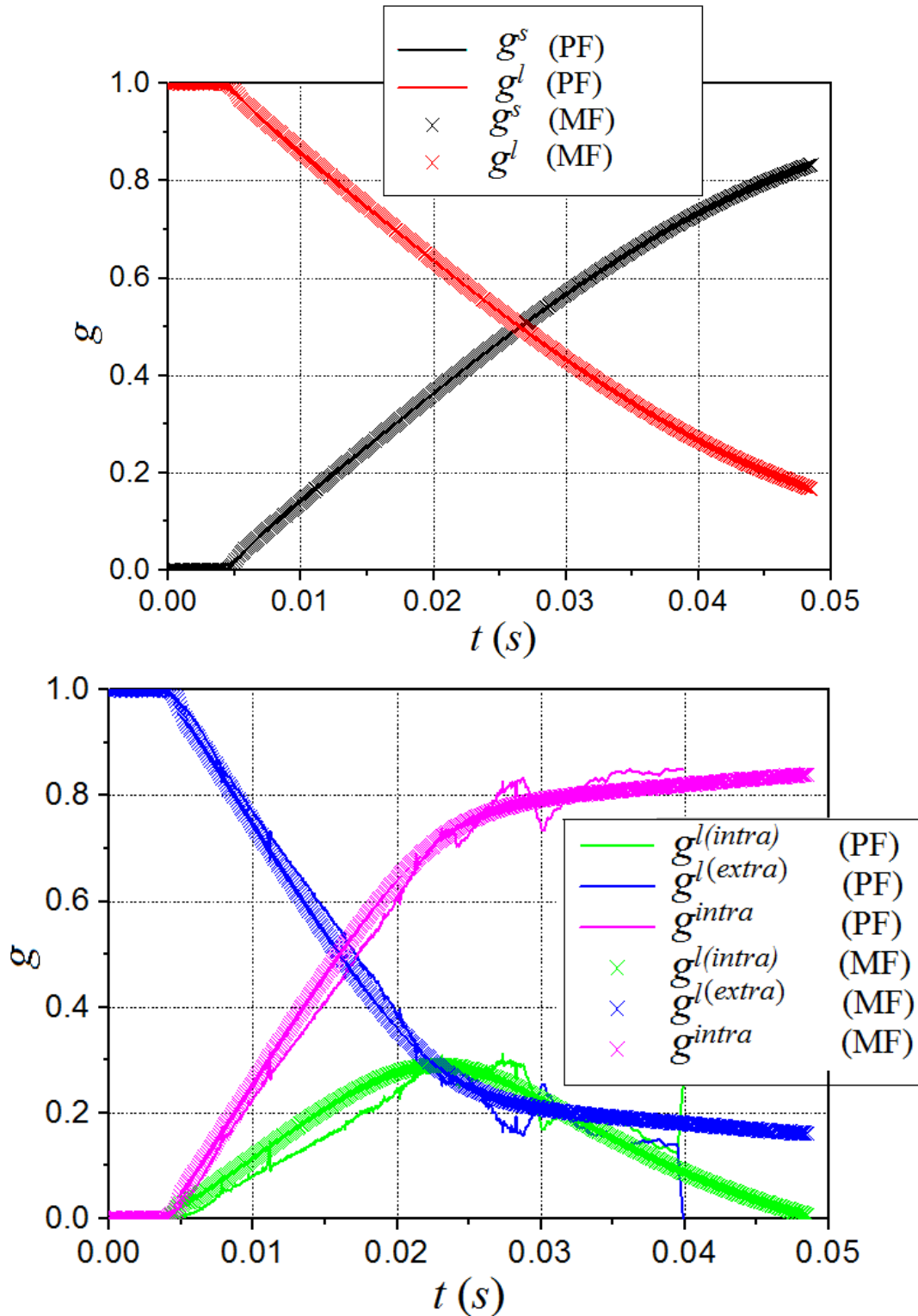


Figure 5.16 Solid and liquid fractions in the different zones of the computational domain, comparison between phase-field (PF) and mean-field (MF) models.

For the composition, a similar evolution exists for the liquid and solid average values. For the solid (black) composition at the interface, its evolution is also similar. For the liquid (red) composition, the intragranular (green), extragranular (blue) and interface zones (purple, light blue) show the same evolution with a small offset variation.

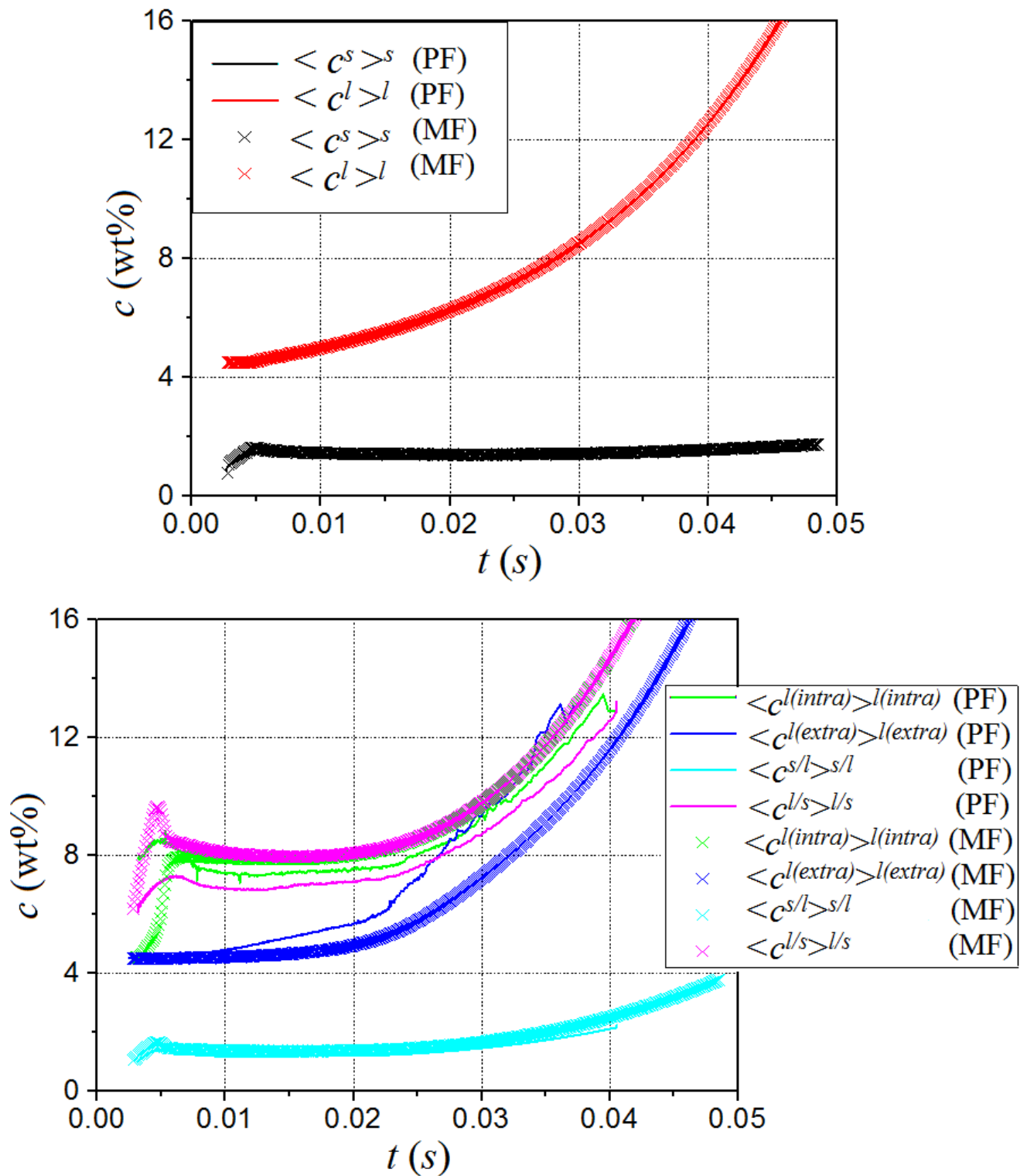


Figure 5.17 Solid and liquid compositions in the different zones, comparison between phase-field (PF) and mean-field (MF) models.

During the formation of solid grains, the solute rejected from the solid to the liquid is accumulated between dendrite arm and at the grain boundary. When the process advances, the solutal gradient progressively increases around growing grain surfaces, leading to a higher

solute flux in the liquid. The concentration difference in the liquid phase over the one at the interface is referred to the solutal undercooling.

Gradually, as the extragranular liquid disappears in favor of intragranular liquid and solid, the average composition of intragranular liquid grows fastly before the recalescence phenomenon Figure 5.15 (a), shown by a small bump beginning at  $t = 0.005$  s in Figure 5.17. The formation of solid causes the solute enrichment of the intragranular liquid. This solute is also partly rejected into the extragranular liquid. As long as there is sufficient extragranular liquid, enrichment due to growth influences very little the composition of the extragranular liquid. When it is in a smaller amount after around 0.025, it is enriched brutally with solute and compositions of extragranular liquid increase together as the temperature decreases, following the interfacial composition.

The dendritic solid zone increases with the intragranular liquid (Figure 5.16) which has a higher composition as that of the extragranular liquid, but less than the composition of the interface  $l/s$  (Figure 5.17). We can see that the composition of the extragranular liquid using the PF model is higher than using the MF model, this comparison is due to the same explanation in Figure 5.9. At the same time  $t$  if we want to obtain the same temperature for the PF and MF models, we should have the extragranular liquid composition higher for the PF model to verify the equation ( $T_i = T_M + m c_i - \Gamma \kappa_r$ ), depending on the curvature but in the MF model we don't have the curvature so the composition for the extragranular liquid should be smaller to verify the same temperature.

Initially, the system temperature decrease causes the increase of the intragranular liquid composition and a stagnated extragranular liquid composition, and growth in the solid zone (black curve in Figure 5.16(a)), showed by the blue line in Figure 5.16 (b), with no variation at the beginning while the green curve increases rapidly. At the same time, the formation of solid generates recalescence and the composition of the interface  $l/s$  decreases. Thus, the local minimum temperature before recalescence corresponds to the maximum of chemical oversaturation and maximum growth rate. When the mean composition of the extragranular liquid tends towards that of the equilibrium  $l/s$ , the supersaturation term in front of the dendrite tends towards a zero value. The solid zone will then stop to grow (in fact, it continues to grow but with a much lower speed).

### 5.3 Parametric study

In the case of equiaxed crystals that are surrounded by an undercooled melt, rejection of solute takes place in all directions on the growth of the solid-liquid interface with eventually lead to a solute accumulation outside the grains. Solid grains can grow with more or less dendritic shape, corresponding to different solidification kinetics at the solid-liquid interface. The formed structures and the grain morphology depend on many factors such as phase change conditions, composition, thermodynamic properties of phase transformations, impacts of phase convection, etc... To complete the previous analysis, sensitivity of the results to different parameters has been performed and is presented in the following.

The reference computation (STD2D) uses a chosen initial droplet velocity, a droplet radius  $R = 50 \cdot 10^{-6}$  m, a supercooling for nucleation  $\Delta T_{Nucleation} = 5$  K, an external temperature  $T_{ext} = 293$  K, and is atomized in Argon. In each of the following comparisons, we have changed one of these parameters, and one additional sensitivity study (to the secondary arm spacing,  $\lambda_2$ , necessary in mean-field computations) has been done.

### 5.3.1 Microstructure parameter

The secondary arm spacing,  $\lambda_2$ , depends on the droplet radius and on the atomization gas and has been given by [BED2015] as follows for argon environment:

$$\lambda_2 [\mu\text{m}] = 4.50 + 0.015 \times 2R_{droplet} [\mu\text{m}] \quad (5.67)$$

This expression has been deduced from experiments on this droplets of the same alloy and gives us a value of  $6 \cdot 10^{-6}$  m for a droplet radius equal to  $50 \cdot 10^{-6}$  m. It has been observed that, for phase-field simulations, the computed  $\lambda_2$  presents the average value of  $3.69 \cdot 10^{-6}$  m, as illustrated in Figure 5.18. It is also clear that  $\lambda_2$  increases during growth, so it would be more pertinent to vary  $\lambda_2$  in mean-field simulations, improving the way comparisons are made between both approaches.

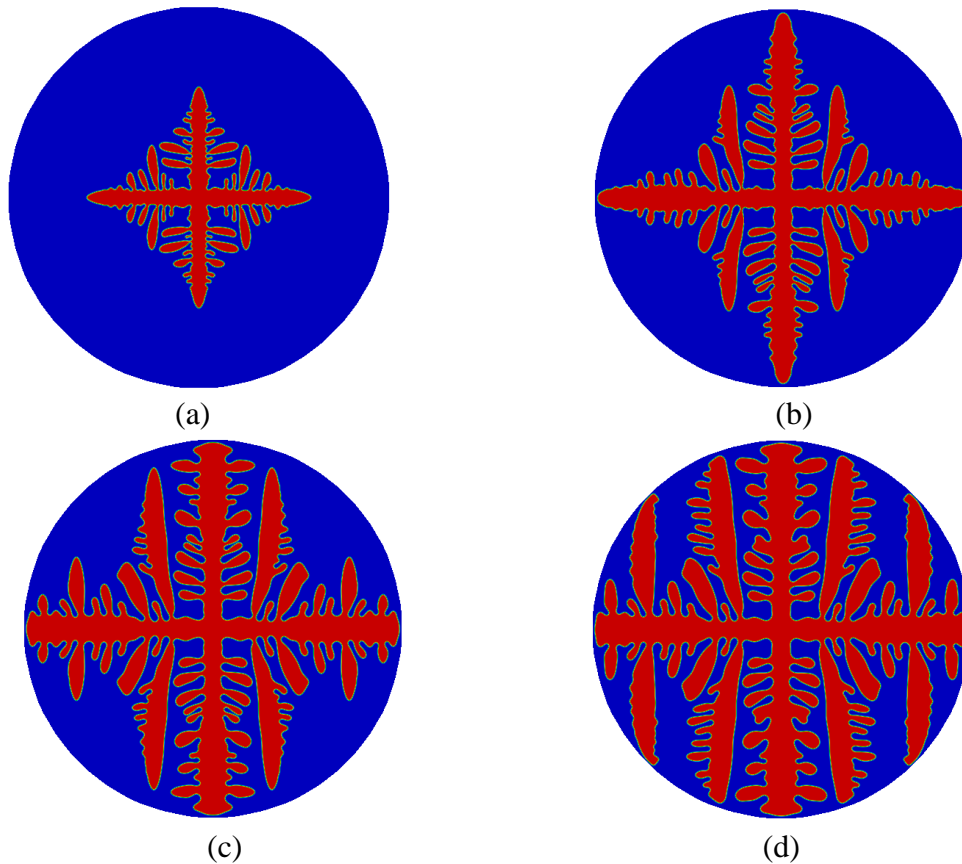


Figure 5.18 Dendritic growth in 2D for Al-4.5%wt Cu at a)  $t_2 = 0.007529$  s,  $\lambda_2 = 2.5015 \cdot 10^{-6}$  m, b)  $t_3 = 0.01403$  s,  $\lambda_2 = 3.3976 \cdot 10^{-6}$  m, c)  $t_4 = 0.019581$  s,  $\lambda_2 = 4.4 \cdot 10^{-6}$  m, d)  $t_5 = 0.025044$  s,  $\lambda_2 = 4.47625 \cdot 10^{-6}$  m

To check on the sensitivity of the mean-field results to  $\lambda_2$ , different values have been considered (Figure 5.19). When decreasing its value, mean-field temperature, grain radius and maximum growth velocity are closer to phase-field ones. For these two variables (radius and velocity), one observes that mean-field  $\lambda_2$  based on the phase-field average value provides closer results to this later, as expected. In particular, mean-field and phase-field results are very close when  $\lambda_2$  decreases.

Figure 5.19 shows also the temporal evolution of the average temperature for these simulations, with very close results for all plots. The secondary dendrite spacing  $\lambda_2$  depends on both the alloy and the cooling conditions. Most simple models unfortunately assume an *a priori* knowledge of the total solidification time, with a constant  $\lambda_2$ . However, the  $\lambda_2$  value should also vary with the cooling rate.

Solidification kinetics should be faster for a larger  $\lambda_2$ , even if the drawn temperature plot has been relatively little affected by the change of  $\lambda_2$ . The most important effect of  $\lambda_2$  variation is observed with the recalescence phenomenon. Firstly, the primary solidification phase is rather fast. It is clear that a relatively small change in the characteristic size of the microstructure may have a sizeable influence on the evolution at this stage, especially on kinetic reactions at the solid state. It means that when  $\lambda_2$  is high the solutal interaction (amount of solute rejected outside the envelope) is weaker, so the dendritic kinetic is faster. The result for the PF model show that: i- the model takes into account the solutal interaction, ii- the effect is saturated for small values of  $\lambda_2$  since the curves are coincident for  $\lambda_2 = 2$  and  $4 \mu\text{m}$ .

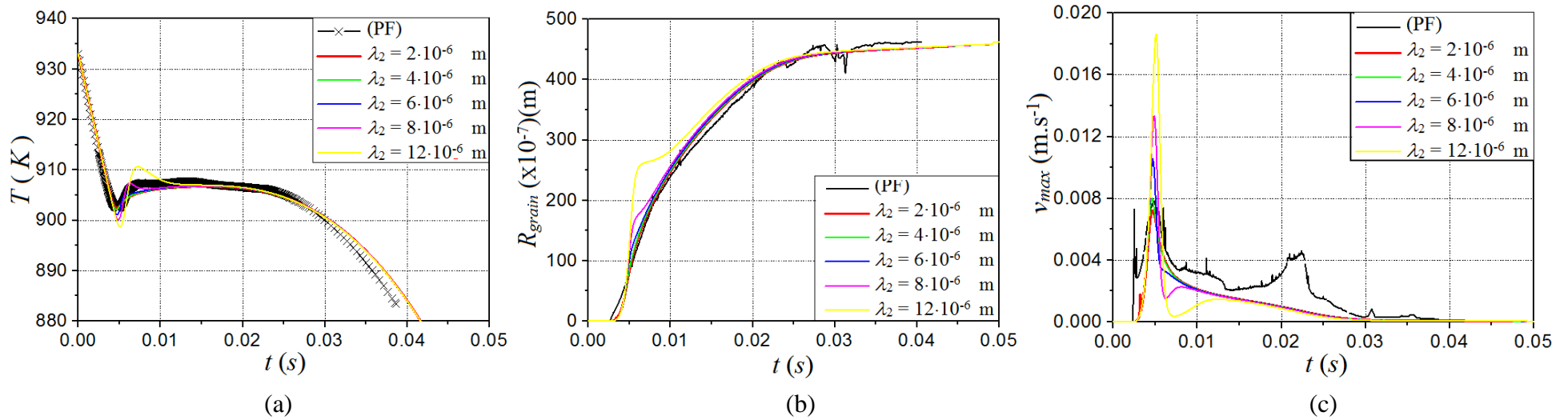


Figure 5.19 Comparison between mean-field simulations using different values of  $\lambda_2$  and 2D phase-field simulations, a) average temperature evolution, b) grain radius evolution, c) maximum dendrite velocity.

### 5.3.2 Droplet radius

One other sensitivity study consists in varying the radius of the droplet (or of the computational domain). In fact, decreasing the radius will instantly increase the heat extraction term, as shown in Figure 5.20, since the exchange coefficient with the outer environment,  $h_{ext}$ , depends directly on the size of the droplet: a smaller drop has greater heat exchange coefficient.

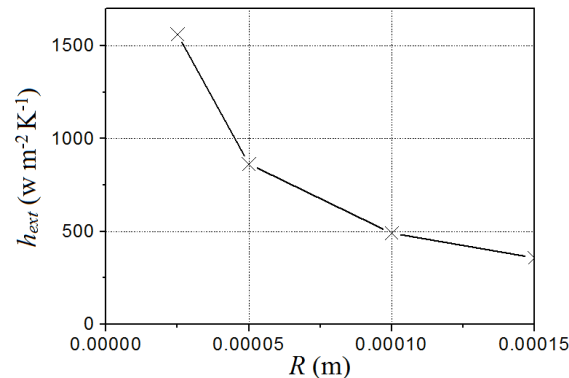


Figure 5.20 Heat extraction coefficient variation with the radius of the domain, computed with the mean-field method.

Figure 5.21 shows the evolution of the average temperature and phase fractions for different radii, where one observes that the growth velocity will be effectively higher in smaller domains. Cooling conditions depend strongly on the size of the atomized particle. The ratio between the heat exchange surface and the volume to be cooled evolves with  $1/R$ . Hence a smaller droplet will cool faster and its microstructure will be finer.

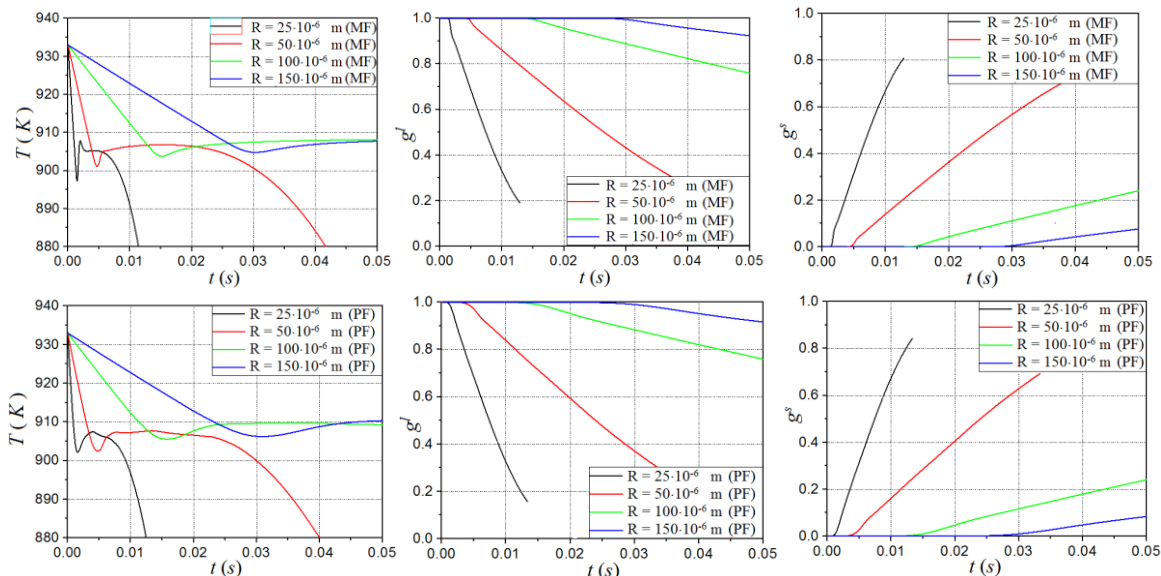


Figure 5.21 Average temperature and phase fractions evolutions for different droplet radius.

On the top the mean-field results and at the bottom the phase-field ones.

The solidification time of a drop of  $50.10^{-6}$  m radius is about 0.04 s, while it was 0.01 s for the simulation with a radius of  $25.10^{-6}$  m. Thus, the value of  $g_l$  and  $g_s$  are reduced, and the

solidification time decreases. For the small droplet, rapid cooling produces a high supercooling.

### 5.3.3 Initial droplet velocity

When the initial droplet velocity increases, the heat extraction term also becomes more important, as shown in Figure 5.22. The  $h_{ext}$  coefficient increases with the Reynolds number of the flow, proportional to the speed of the falling droplet, also because of the area ratio (frictional forces) on volume (mass) which generates a higher speed for the larger particles.

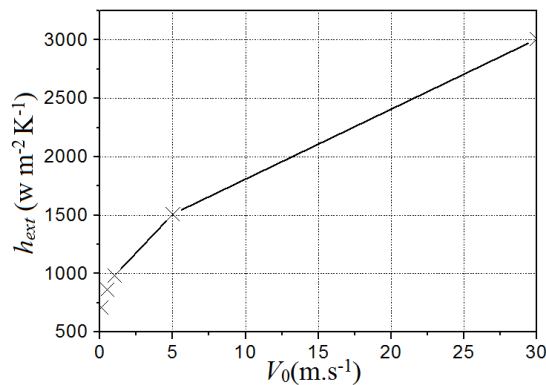


Figure 5.22 Heat extraction coefficient variation with the initial droplet velocity.

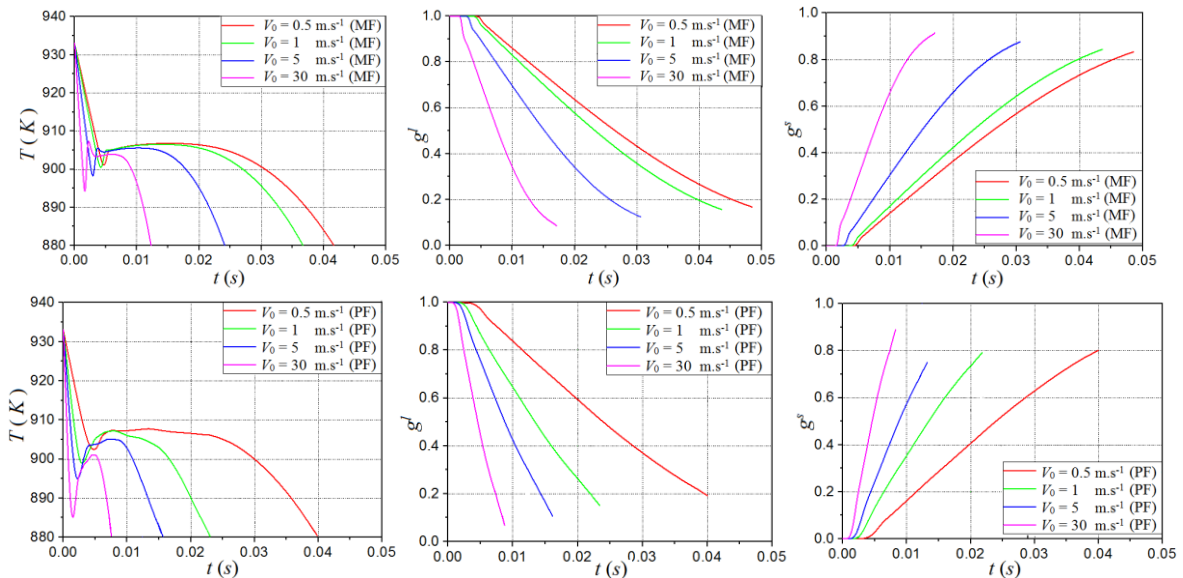


Figure 5.23 Temperature evolution for different droplet initial velocities: at the top, the mean-field results and, at the bottom, the phase-field ones.

The velocity of the droplet influences indirectly phase-field simulations by changing the value of  $h_{ext}$ . When the velocity is higher,  $h_{ext}$  is larger and the solidification is faster, as seen in Figure 5.23. Figure 5.23 shows that the average temperature will decrease in a faster way using a larger initial velocity droplet whereas the growth velocity will increase, as expected. The high cooling rate generates growth surfusions before the recalescence. At  $t = 0.009$  s, the droplet with a higher initial velocity has less liquid and a larger solid fraction.

### 5.3.4 Nucleation temperature

Temperature evolution is sensitive to the nucleus temperature  $T_{Nucl}$ , as illustrated in Figure 5.24. The nucleation undercooling temperature  $\Delta_{Nucl}$  is the difference between the initial temperature  $T_0$  and the nucleation temperature (chosen temperature when the nucleus will appear). In fact, the average temperature decreases to reach the nucleation point, which is smaller when we have a larger nucleation temperature, to increase after and then decrease again. It coincides at the end when the dendrite reaches the border of the domain.

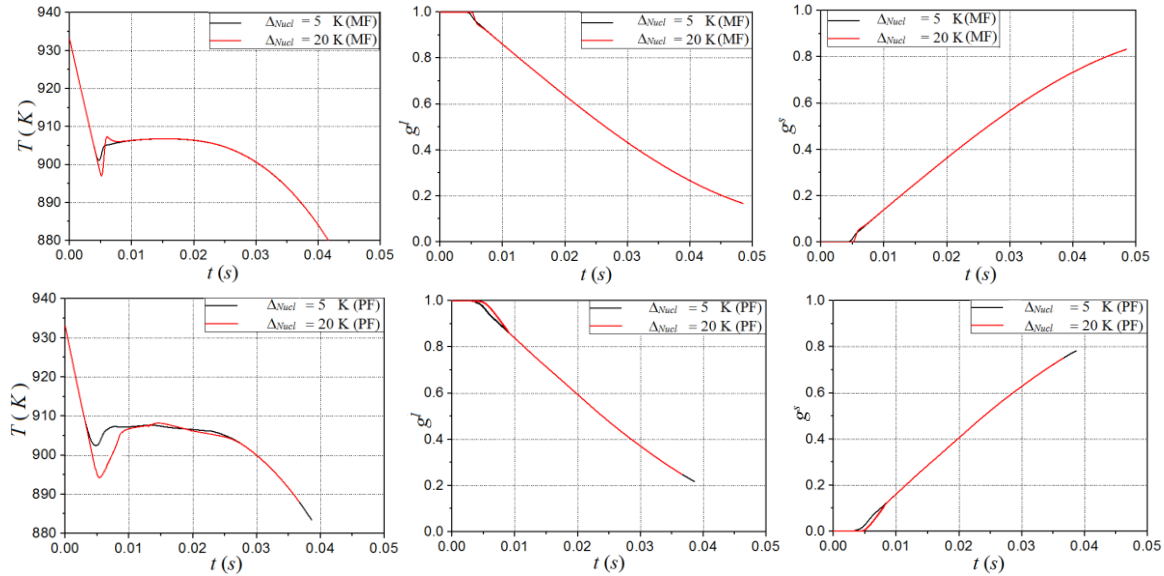


Figure 5.24 Average temperature and phase fraction evolution for different nucleation temperatures, at the top the mean-field results and at the bottom the phase-field ones.

For the simulation with  $\Delta_{Nucl} = 20$  K, the larger and faster recalescence reduces the temperature to the one given by  $\Delta_{Nucl} = 5$  K. On phase fraction curves, the appearance of the solid phase is delayed because the nucleus will appear after some time for  $\Delta_{Nucl} = 20$  K reaching the temperature of its creation and appearance of the solid. But except for that delay, the end of the simulation looks the same as for zero supercooling. Imposing a primary germination supercooling has relatively little influence on the solidification in the mean-field and phase-field models.

Without imposing a nucleation supercooling  $\Delta_{Nucl}$ , the growth supercooling is large enough due to cooling kinetics of the system (fast). Imposing a nucleation lower than the "natural" one, supercooling growth of the system has a negligible influence on the solidification.

When we increase the nucleation temperature we delay the appearance of the solid phase and an additional solidification takes place with a larger heat release, which slows down the cooling of the system.

The growth kinetic is directly used in the equations for the PF model, but for the MF model the velocity is computed as seen in equation (5.58) depending on the variation of the composition at the  $s/l$  interface ( $c^{s/l}$ ) that depends also on the temperature as follows  $m_L c^{l/s} = \Delta_{Nucl} + \Gamma \kappa_r$ , so when we have  $\Delta_{Nucl}$  higher we have a bigger  $c^{l/s}$  and then a faster velocity that corresponds to a higher  $\lambda_2$  for the case of  $\Delta_{Nucl} = 20$  K. For the highest value of the velocity so

the highest value for  $\lambda_2$  we have the smallest value for the enthalpy  $\Delta H_f$  in the liquid, this can be deduced from the equations (5.53) and (5.61).

At the beginning, the solid fraction formed is smaller for a large  $\Delta_{Nucl}$ , whereas the liquid phase fraction is slightly higher. After the recalescence phenomenon, these fractions are the same for the different nucleation temperatures.

### 5.3.5 External temperature

When the external temperature increases, the heat extraction term will also increase, as shown in Figure 5.25. For the phase-field model, a constant external temperature has been considered.

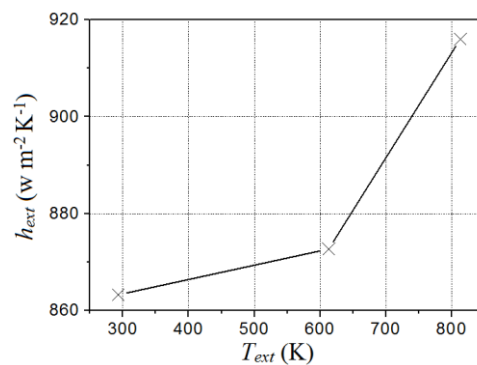


Figure 5.25 Heat extraction coefficient variation with the external temperature.

If we compare to previous results, we have a smaller  $h_{ext}$  when the droplet is larger and the cooling rate is lower. In this example, when we increase the external temperature, we are forcing the system to cool slowly. This is identical to large droplet case.

Figure 5.26 shows that the temperature decreases faster with a lower external temperature and, subsequently, the growth velocity increases. We notice that the temperature evolution also evolves more rapidly before recalescence in the mean-field model than in the phase-field model.

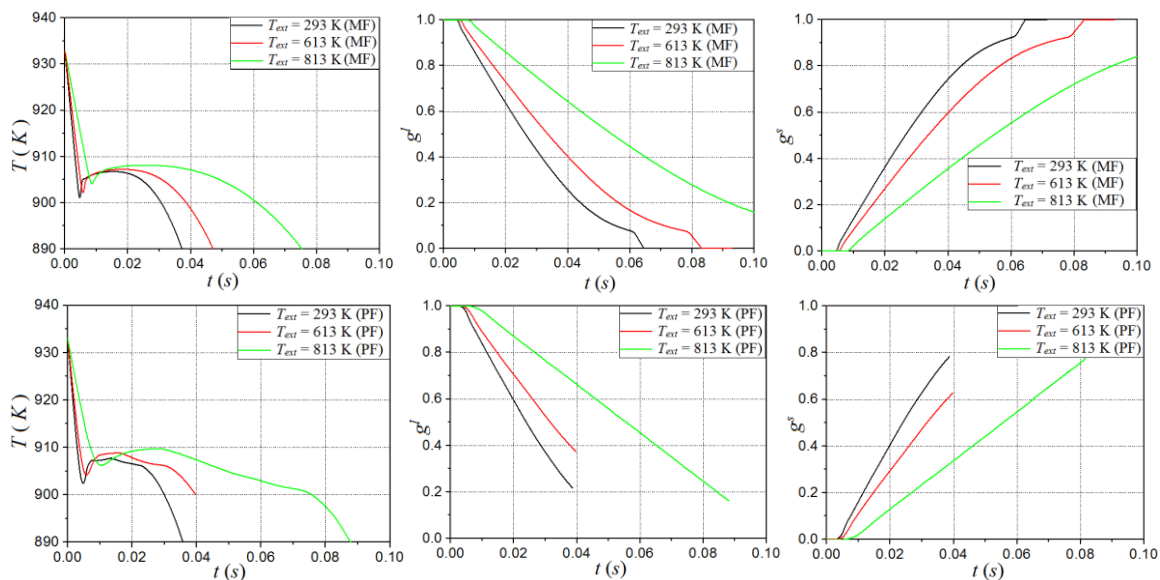


Figure 5.26 Average temperature and phase fraction evolutions for different droplet external temperatures: at the top, the mean-field results and, at the bottom, the phase-field ones.

The solid/liquid fraction increases/decreases faster for small external temperatures. In this case, the temporal evolution of the boundary conditions has a relatively small influence on the results.

### 5.3.6 Atomisation gas

The heat extraction coefficient is larger using Helium than using Argon, as seen in Figure 5.27, since Helium presents a higher thermal conductivity than the one of Argon refer to eq.(5.63).

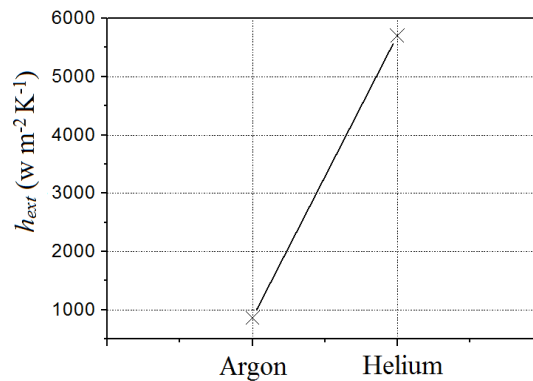


Figure 5.27 Heat extraction coefficient variation with the atomization gas.

Figure 5.28 shows that the average temperature decreases faster for droplets atomized in Helium, generating a larger growth velocity. For all the cases, the average temperature and phase fractions show the same tendency. The solid fraction increases because the dendrite is created and is growing, and the liquid fraction is decreasing because it is solidifying, as expected.

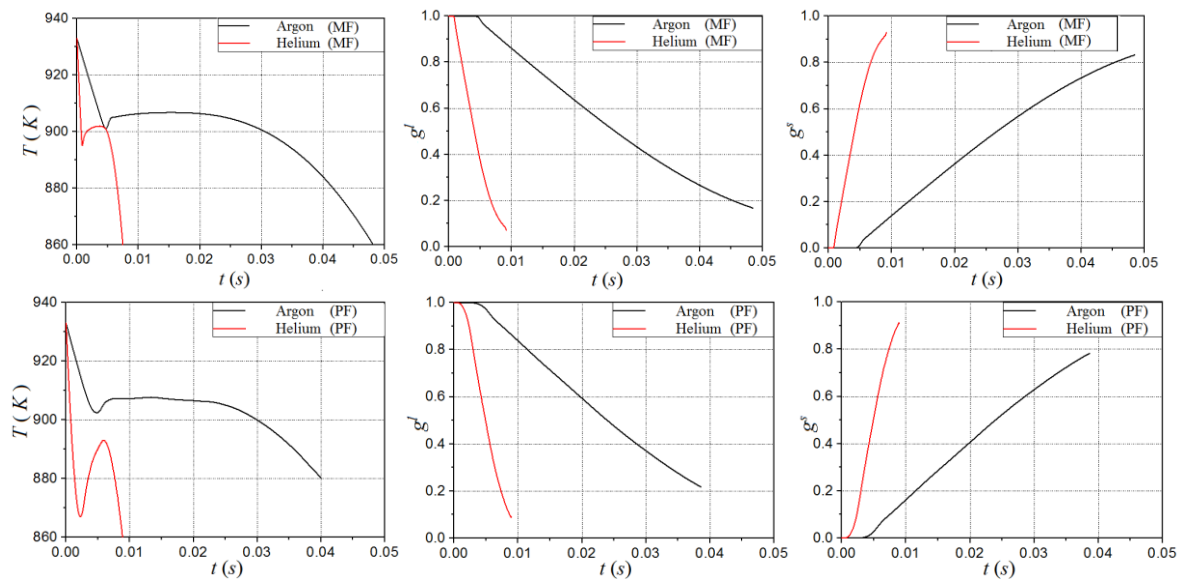


Figure 5.28 Average temperature and phase fraction evolution for different atomization gas (Helium, Argon): at the top, the mean-field results and, at the bottom, the phase-field ones.

### 5.3.7 Timestep and initial radius

A sensitivity study of the timestep value for both models has been done, but also for the initial radius for the phase-field method, as shown in Figure 5.29.

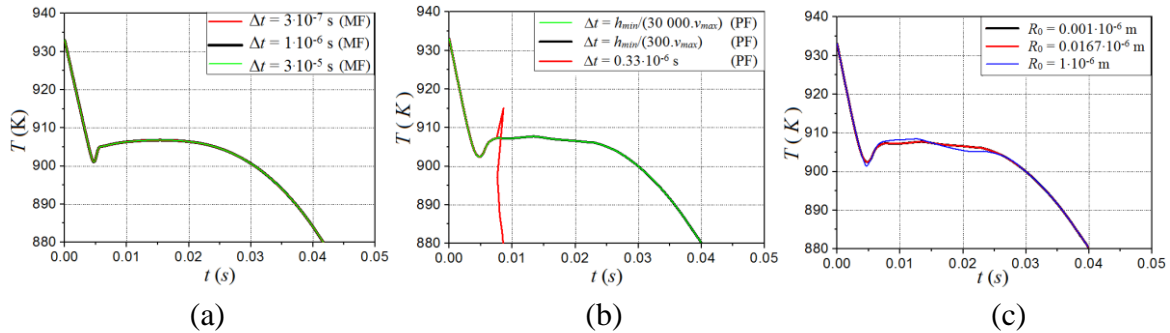


Figure 5.29 Average temperature evolution for different parameters such as the timestep, a) mean-field model, b) phase-field model, c) the initial nucleus radius for the PF model.

In mean-field results, one observes that the temperature evolution does not depend on the timestep in the range of values studied. For phase-field computations, the values of the timestep vary from  $3 \cdot 10^{-7}$  s to  $3.549 \cdot 10^{-3}$  s for  $\beta' = 300$  and from  $3 \cdot 10^{-9}$  s to  $3.549 \cdot 10^{-5}$  s for  $\beta' = 30\,000$  (since we use a single  $\beta'$  value throughout simulation). For very large timesteps, simulation diverges, as seen in Figure 5.29 (b) and we lose the dendrite morphologies. The initial radius of the nucleus influences the growth; it should be chosen small enough to have a convergent evolution and morphology, as shown in Figure 5.30. For a larger initial radius, dendrite grows but some particular features may appear like splitting or even numerical problems, which influence the temperature evolution and distribution.

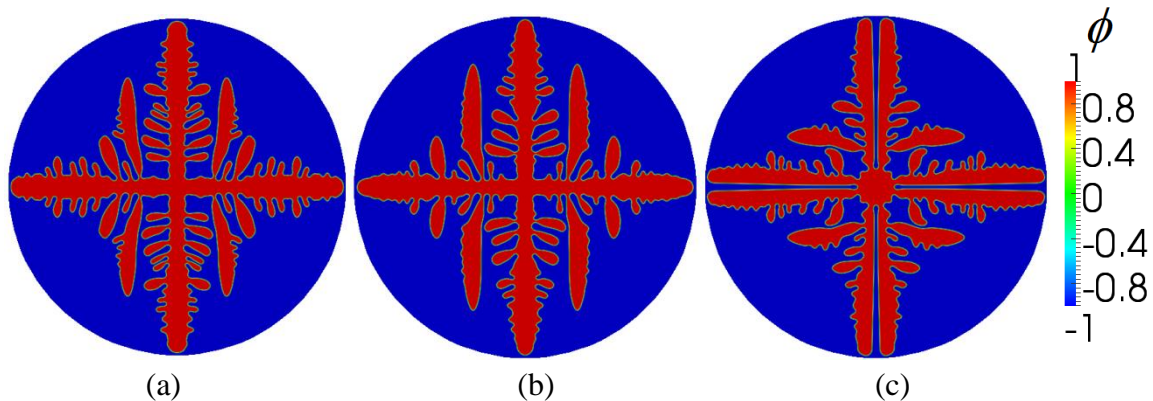


Figure 5.30 Different morphologies obtained for different values of  $R_0$  and plotted at  $t = 0.01517$  s: a)  $R_0 = 0.001 \cdot 10^{-6}$  m, b)  $R_0 = 0.0167 \cdot 10^{-6}$  m, c)  $R_0 = 1 \cdot 10^{-6}$  m.

The developed phase-field model has been also applied to the solidification of an Al-Cu droplet in 3D, for which the physical parameters are defined in Table 5.1, and using the non-dimensional parameterization of these parameters for the simulation for the standard case (STD 3D). Simulation has been performed considering the whole droplet geometry (no symmetry conditions).

Simulation could not be finished, but one has a beginning of qualitative comparison between both models. Time to achieve the phase-field computation is of several months. This problem may be solved, by improving the mesh adaptation to provide a better result using  $1/48$  or  $1/8$  of the domain and by adapting the mesh based on  $\phi$  and  $\theta$ . Indeed, when trying to verify the composition gradient a very small mesh size arises inside the dendrite.

## 5.4 Conclusion

Advanced solidification models are able to account for the effect of convection on solute gradients in a small layer near the solid-liquid interface as well as for complex shapes of interfacial structures that are associated to instability conditions and curvatures of interfaces. In this situation, the present thesis was proposed which aims at modeling solidification of equiaxed grains in the finite element context. We adapted and implemented the phase field model into the FE framework using anisotropic meshing.

Through our work, three main tasks accomplished can be summarized:

- Implementation of the growth model. The growth model consists in solving a set of three equations established to describe the thermo-solutal kinetics of a solid-liquid interface which is controlled by solute diffusion at the microscopic scale. The numerical implementation was effectuated to locally solve the system at each node of the discretized domain.
- Integration of an automatic anisotropic adaptive mesh and an automatically adapted timestep.
- Comparison with a macroscopic mean-field model for droplet solidification in 2D.

The model developed in our work is innovative mainly due to its numerical methodologies. But the physical approach is not new, since our work is strongly based on the assumptions introduced by Karma and Rappel [KAR1998] and enriched by Ramirez et al. [RAM2004] and Coupez et al. [COU2011]. The model is valid but its wide implementation to the industrial process is still unthinkable.

Using the phase field model, we are able to represent variation of the temperature curve that explains the solidification process accompanied with recalescence phenomenon, result of heat and mass exchange between the phases. Morphological representation of the dendrite can be shown with its different primary and secondary arms.

Using the mean-field model, we can compare the same simulation configuration as for the phase-field model without the detailed representation of the morphological form, but we can continue the simulation procedure to show the growth of a eutectic structure and peritectic solidification [TOU2009], modeled as new zones growing from the center of the domain. The MF simulation takes a few seconds or minutes to finish an entire solidification path.

We do not have exactly the same evolution for PF and MF models, but a good qualitative agreement is demonstrated in 2D. Behavior of the average fields is the same and varies in the

same direction. It is a first relevant application of our PF model, which may be further analysed. Mesh dependency and simulations time should be improved in the following works, to be able to perform accurate 3D comparisons.

Domain size influences the cooling rate of the system, and therefore the size of the microstructure. If the cooling rate is high enough, a competition can be held between the kinetics of cooling and kinetic transformations. Additionally, faster cooling implies greater growth supercoolings, and therefore growth structures of the compositions can be different.

Replacing limit atomisation conditions by a constant factor of heat exchange ( $h_{ext}$  constant) impacts quite a few the results.

The solid nucleation undercoolings have little influence on the primary structure in our PF simulations. A supercooling germination changes the cooling curve temperature profile. Thereby the growth kinetics influence final phase fractions in a significant manner way.

There is a competition between the diffusion kinetics (dependent on the alloy properties) and the kinetics of cooling (depending on the size of the particle), taking into account the particularities of the phase diagram and supercooling growth. This first analysis was performed with approximate parameters (diffusion coefficients, nucleation supercoolings, etc.). The mean-field model developed can address combinations of microscopic phenomena occurring during solidification of alloys and measure the relative influence of the different kinetics.

In conclusion, taking into account the nucleation supercoolings of solid phases may be important, if certain other conditions, such as cooling rate, do not themselves impose a supercooling of growth. It would be useful to find a way to evaluate these supercoolings, which in the case of atomization are very difficult to measure.

Solving the equations of boundary conditions is easy enough numerically and consumes relatively little time calculation. These boundary conditions, although quite simple (no radiative transfer, for example), allow for a quick and easy evaluation of heat exchange and its evolution over time depending on the size of the particles and gas atomizing, which justifies its use.

The differences between PF and MF models are listed here:

| <b>The present Phase-field model</b>                                                                                                                                                    |                                                                                            |
|-----------------------------------------------------------------------------------------------------------------------------------------------------------------------------------------|--------------------------------------------------------------------------------------------|
| <b>Advantages:</b>                                                                                                                                                                      | <b>Limitations:</b>                                                                        |
| - Resolution of three diffusion equations using the finite element method.                                                                                                              | - Does not represent eutectic and peritectic growth.                                       |
| - Use of automatic anisotropic mesh adaptation.                                                                                                                                         | - Physico-chemical properties for comparison with experimental characterizations.          |
| - Representative variation of the temperature curve that explain the solidification process accompanied with recalescence.                                                              | - Densities of the phases constant and equal (no shrinkage phenomenon).                    |
| - Can represent the real variation of the temperature while solving temperature equation.                                                                                               | - Long computation time for small simulation domains in comparison with macroscopic model. |
| - Morphological representation                                                                                                                                                          | - Incapability to do 3D physical simulation of Al-4.5wt% Cu alloy.                         |
| - Quantitative results for dendrite tip kinetics, which can be compared with literature results considered as reference results.                                                        |                                                                                            |
| - Qualitative comparison with macroscopic mean-field.                                                                                                                                   |                                                                                            |
| - Possibility for further develop the model to account for fluid flow and multicomponent alloys, coupling with the CALPHAD approach, multi solid phase, demonstrated in the literature. |                                                                                            |

| <b>The present mean-field model</b>                                                                                                                                                          |                                                                                                                                                     |
|----------------------------------------------------------------------------------------------------------------------------------------------------------------------------------------------|-----------------------------------------------------------------------------------------------------------------------------------------------------|
| <b>Advantges:</b>                                                                                                                                                                            | <b>Limitations:</b>                                                                                                                                 |
| - The model can be implemented in macroscopic heat and mass solver for applications to casting.                                                                                              | - The solidification of the particle is simulated under a uniform temperature.                                                                      |
| - Bringing new results without using heavy numerical calculations. This type of model is still relevant and still has a relatively high margin evolution.                                    | - The growth kinetics for dendritic growth is approximated by a steady regime using the Ivantsov solution and a constant selection parameters.      |
| - Computational ressources required are relatively low compared to PF modeling.                                                                                                              | - There are several unknown parameters to pretend give precise quantitative estimates of final fractions (e.g. $\lambda_2$ ).                       |
| - Extensions were demonstrated in the literature such as coupling with phase transportation, multicomponent alloys, multi solid pahse transformations,... Coupling with the CALPHAD approach | - The model does not consider changes in morphology of the structure that take place during the solidification, thus approximating diffusion length |

## Résumé

Dans ce chapitre, nous décrivons le phénomène de croissance dendritique dans une goutte exploitant les distributions de température et composition, ainsi qu'en étudiant les températures minimale, maximale et la vitesse de croissance maximale. Nous avons comparé l'évolution de ces températures, des fractions solide et liquide, et des compositions résultantes du calcul avec le modèle de champ de phase et des calculs avec un modèle de champs moyen, avec un très bon accord qualitative. Finalement une étude paramétrique a été réalisée pour évaluer la sensibilité de certains paramètres sur le calcul en champs de phase, mais aussi pour améliorer les simulations par champ moyen.



## Chapter 6

### 6 Conclusions and perspectives

---

|       |                              |     |
|-------|------------------------------|-----|
| 6.1   | Conclusions .....            | 145 |
| 6.2   | Perspectives .....           | 146 |
| 6.2.1 | 3D PF simulations .....      | 146 |
| 6.2.2 | Kinetic anisotropy .....     | 147 |
| 6.2.3 | Growth with fluid flow ..... | 147 |

---

#### 6.1 Conclusions

We recall that the three main goals stated in the introduction of this work were:

- The simulation of dendritic growth using a mesh adaptation technique based on an error estimator as well as using parallel computation.
- The simulation of thermo-solutal dendritic growth.
- The validation of the model with dedicated numerical tests.
- The simulation of the solidification of an Al-Cu droplet with  $\langle 100 \rangle$  growth directions and the comparison with a macroscopic mean-field (MF) model.

We have constructed a model based on the phase-field (PF) approach using mesh adaptation based on an error estimator and parallel computation to simulate dendritic solidification, with non-solutal diffusion in the solid and equal thermal diffusivities. This model is used with non-dimensional parameters computed from physical ones. It can be used for thermal growth, for solutal growth and for thermo-solutal growth. This model is validated in 1D and 2D. We can apply this model to represent the solidification of Al-Cu droplets.

The use of the model can reduce the computational time (comparing with isotropic cases) and the memory used for the simulation. It can represent the solidification microstructure. While benefiting from symmetries. Dendrites can grow with different directions without changing its form because the mesh adapts to represent the solid/liquid interface. One disadvantage of the model is the computation of  $N_2$  for adjustment of the number of element. It should be computed automatically while changing the parameters and the symmetry problems for thermo-solutal growth.

We have differences between PF and MF models. Phase-field model consists of the resolution of three diffusion equations using the finite element methods and automatic anisotropic mesh adaptation which induce a gain in the memory and computation time. The variation of the temperature curve that explains the solidification process accompanied with recalescence phenomenon can be studied into details and linked to the development of each dendrite branch. Morphological representation can be shown. Quantitative results can be compared with

literature results considered as reference results. Quantitative comparison with macroscopic mean-field simulation is also possible. Less unknown and less numerical approximations are needed to do the simulation with PF. A long computation time is needed to end the simulations in comparison with MF macroscopic model because of the complexity in the resolution of the system of equations. Mean-field model can represent the eutectic and peritectic growth as well as multicomponent alloys while the present PF model can not. Lot examples of the present limitations with the PF model exist in the literature. The MF model can be coupled with simulation of macrosegregation for heavy ingots inducing the transport of equiaxed grain during solidification. MF model is thus relevant for coupling with large scale and still has a relatively high potential for improvement. It yet asks for different morphological approximations, and so far does not consider non stationary dendritic growth.

In conclusion, we can use now the PF model to simulate solidification of droplets and compare with MF simulations. Experimental results may also be compared with numerical ones, but are not as common to produce. PF simulations could thus be seen as an alternative to experimental results to help improving MF models.

## 6.2 Perspectives

After this work, we can do simulations of thermal or thermo-solutal dendritic growth adding kinetic anisotropy and fluid flow. The purpose could be to simulate the growth in atomized Al-Cu droplets. We can try to explore how the dendrite growth direction can change as observed by Bedel et al. [BED2015]. To make comparison with experiments using a low supercooling or a greater number is also a possible extension to 3D, is still to be demonstrated with the present model.

### 6.2.1 3D PF simulations

We have seen in chapter 4 that we can do simulations (not physical ones) in 3D using the PF model. When we need to do a computation using the real physical parameters (for Al-4.5wt% Cu) that we obtain from experiments, we will have a high number of Lewis (higher than 10 used in chapter 4), around 7000. Because of this big difference in solute and temperature diffusions we could not continue the simulations.

The developed phase-field model has been applied to the solidification of an Al-Cu droplet in 3D, for which the physical parameters are defined in Table 5.1, and using the non-dimensional parameterization of these parameters for the simulation for the standard case (STD 3D). Simulation has been performed considering the whole droplet geometry (no symmetry conditions).

Simulation has not been finished, but one has a beginning of qualitative comparison between both models. Time to achieve the computation is of several months. This problem may be solved, by improving the mesh adaptation to provide well computation using 1/48 or 1/8 of the domain and may be try to adapt this mesh based on  $\phi$  and  $\theta$  only because when trying to verify the composition gradient many small elements will appear inside the dendrite and we will need

a lot of time to finish the simulation. Results obtained, until now, give us an idea of the similarity between the two models.

### 6.2.2 Kinetic anisotropy

We have seen in the experiments [bedel et al] that we have  $\langle 111 \rangle$  growth directions for the aluminum copper alloy. If we use  $\varepsilon_4 < 0$  in the PF model we will have this growth direction. But physically  $\varepsilon_4$  is always positive. So to have growth along the  $\langle 111 \rangle$  direction we can propose to use kinetic anisotropy as described in Dantzig paper communications [DAN2014]. This communication gives us a kinetic anisotropy and a capillary anisotropy as follows:

$$a_s(\mathbf{n}) = 1 + \varepsilon_1(Q - 3/5) + \varepsilon_2(3Q + 66S - 17/7) \quad (6.1)$$

$$a_k(\mathbf{n}) = 1 + \varepsilon_1^k(Q - 3/5) + \varepsilon_2^k(3Q + 66S - 17/7) \quad (6.2)$$

Then we have the  $\langle 100 \rangle$  dendrite or the  $\langle 111 \rangle$  dendrite by changing the values of  $\varepsilon_1^k$ :

Taking  $\varepsilon_1 > 0$  and  $\varepsilon_1^k = 0 \Rightarrow \langle 100 \rangle$  dendrite

Taking  $\varepsilon_1 > 0$  and  $\varepsilon_1^k < 0 \Rightarrow \langle 100 \rangle$  dendrite at low velocity

$\langle 111 \rangle$  dendrite at high velocity

This way could be considered for trying to give a better explanation of the formation of  $\langle 111 \rangle$  growth directions.

### 6.2.3 Growth with fluid flow

We can propose to extend the PF model for dendritic growth with fluid flow following the method used by [LU2005], [TON1998a], [YAM2013] where the solid is not moving.

Taking the formulation in [LU2005] we write the phase-field equation as:

$$\begin{aligned} \alpha(\mathbf{n}) \frac{\partial \phi}{\partial \tau} - \nabla \cdot (W^2(\mathbf{n}) \nabla \phi) &= [\phi - \lambda \theta (1 - \phi^2)](1 - \phi^2) + \frac{\partial}{\partial x^*} \left( |\nabla \phi|^2 W(\mathbf{n}) \frac{\partial W(\mathbf{n})}{\partial \partial_{x^*} \phi} \right) \\ &+ \frac{\partial}{\partial y^*} \left( |\nabla \phi|^2 W(\mathbf{n}) \frac{\partial W(\mathbf{n})}{\partial \partial_{y^*} \phi} \right) \end{aligned} \quad (6.3)$$

And the energy conservation equation as:

$$\frac{\partial \theta}{\partial \tau} - \alpha^* \Delta \theta + V_{Conv} \cdot \nabla \theta = \frac{\partial \phi}{\partial \tau} \quad (6.4)$$

To compute the convection velocity of the fluid,  $V_{Conv}$ , we have these equations to solve [LU2005]:

$$\nabla \cdot [(1 - \phi) V_{Conv}] = 0 \quad (6.5)$$

$$\begin{aligned} \frac{\partial [(1 - \phi) V_{Conv}]}{\partial \tau} + (1 - \phi) V_{Conv} \cdot \nabla V_{Conv} &= \\ - (1 - \phi) V_{Conv} \frac{\nabla p}{\rho} + \nu \nabla^2 [(1 - \phi) V_{Conv}] \cdot \nabla V_{Conv} &- \frac{2 \nu h \phi^2 (1 - \phi) V_{Conv}}{W_0^2} \end{aligned} \quad (6.6)$$

Where  $p$  is the pressure,  $\rho$  is the density,  $h = 2.757$  (asymptotic analyses),  $\nu$  is the kinetic viscosity in the melt. We have the Prandtl number  $Pr = \nu / \alpha^*$ .

The main physical problems that we would like to study with fluid flow are:

- The influence of fluid flow on tip kinetics for non stationary growth conditions;
- The role of the flow on the selection of growth directions;
- the effect of the flow on the upstream growing dendrite tip velocity and radius of curvature can be investigated as a function of the imposed flow velocity, undercooling, crystalline anisotropy and Prandtl number;
- To determine the mechanical behavior of solidifying structure;

## Appendix A Energy conservation equation

We will show the derivation of the energy conservation equation according to Rappaz-Bellet-Deville [RAP2003].

The first law of thermodynamics tells us that the variation of total energy of a domain under consideration is due to mechanical power of the external forces,  $P_{mech}$ , and the caloric power applied,  $P_{cal}$ . The total energy is composed of the kinetic energy,  $E_k$ , and the internal energy,  $E_i$ .

$$\frac{dE_k}{dt} + \frac{dE_i}{dt} = P_{mech} + P_{cal} \quad (A1)$$

Where the time derivatives are total derivatives. The mechanical power is applied to the system by volume forces and contact forces on the surface  $\partial\Omega$  of the domain:

$$P_{mech} = \int_{\Omega} \mathbf{F}_v \cdot \mathbf{v} \, dV + \int_{\partial\Omega} \mathbf{T} \cdot \mathbf{v} \, dS \quad (A2)$$

$\mathbf{T}$  is the stress vector ( $\mathbf{T} = \boldsymbol{\sigma} \cdot \mathbf{n}$ ,  $\boldsymbol{\sigma}$  is the stress tensor and  $\mathbf{n}$  is the outgoing unit normal of the domain) and  $\mathbf{F}_v$  is the volumetric force and  $\mathbf{v}$  is the velocity

The caloric power into a system is also composed of two parts. The volume contribution  $\dot{Q}_T$  can be due to the chemical reactions, radioactive decay or the Joule effect. Heat flux  $-\mathbf{j}_T \cdot \mathbf{n}$  can enter the domain by radiation, convection, or conduction. The minus sign is present because a flux in (i.e.,  $\mathbf{j}_T$  in the opposite sense of the outward normal  $\mathbf{n}$  of the domain) increases the internal energy

$$P_{cal} = \int_{\Omega} \dot{Q}_T \, dV - \int_{\partial\Omega} \mathbf{j}_T \cdot \mathbf{n} \, dS = \int_{\Omega} (\dot{Q}_T - \text{div} \mathbf{j}_T) \, dV \quad (A3)$$

Taking the kinetic power:

$$\frac{dE_k}{dt} = \frac{d}{dt} \int_{\Omega} \frac{1}{2} \rho \mathbf{v}^2 \, dV = \int_{\Omega} \rho \frac{d}{dt} \left[ \frac{\mathbf{v}^2}{2} \right] \, dV \quad (A4)$$

The internal energy balance becomes:

$$\frac{dE_i}{dt} = - \int_{\Omega} \rho \frac{d}{dt} \left[ \frac{\mathbf{v}^2}{2} \right] \, dV + \int_{\Omega} \mathbf{F}_v \cdot \mathbf{v} \, dV + \int_{\partial\Omega} \mathbf{T} \cdot \mathbf{v} \, dS + \int_{\Omega} (\dot{Q}_T - \text{div} \mathbf{j}_T) \, dV \quad (A5)$$

The sum of the first three terms on the right hand side of the equation is the deformation power integrated over the volume of the domain.

$$E_i = \int_{\Omega} \rho e_i \, dV \quad (A6)$$

Where  $e_i$  is the mass specific internal energy, the total derivative of this equation with respect to time is:

$$\frac{dE_i}{dt} = \int_{\Omega} \frac{\partial(\rho e_i)}{\partial t} + \text{div}(\rho e_i \mathbf{v}) \, dV \quad (A7)$$

Taking all the contributions, the local internal energy balance becomes:

$$\frac{\partial(\rho e_i)}{\partial t} + \text{div}(\rho e_i \mathbf{v}) = \boldsymbol{\sigma} : \dot{\boldsymbol{\varepsilon}} + \dot{Q}_T - \text{div} \mathbf{j}_T \quad (\text{A8})$$

$\dot{\boldsymbol{\varepsilon}}$  is the strain tensor. Taking into account the conservation mass (stationary case or steady state or incompressible material).

$$\rho \frac{\partial(e_i)}{\partial t} + \rho \mathbf{v} \cdot \mathbf{grad}(e_i) = \rho \frac{de_i}{dt} = \boldsymbol{\sigma} : \dot{\boldsymbol{\varepsilon}} + \dot{Q}_T - \text{div} \mathbf{j}_T \quad (\text{A9})$$

Using the enthalpy per unit mass,  $H$ , given by:

$$H = e_i + \frac{p}{\rho} \quad (\text{A10})$$

Where  $p$  is the pressure. The equation can be written:

$$\frac{\partial(\rho H)}{\partial t} + \text{div}(\rho H \mathbf{v}) = \left[ \frac{\partial(p)}{\partial t} + \text{div}(p \mathbf{v}) \right] + \boldsymbol{\sigma} : \dot{\boldsymbol{\varepsilon}} + \dot{Q}_T - \text{div} \mathbf{j}_T \quad (\text{A11})$$

The variation of enthalpy can be caused by four different kinds of contributions on the right hand side of the equation. The first two correspond to the total derivatives of the pressure and thus to enthalpy variation due to local compression and decompression. For example following a volume element containing gas that does not exchange heat with the exterior (local adiabatic condition), it is well known that the increase in the enthalpy due to strain. As for the last two terms, they have the same signification as for the conservation of solute.  $\dot{Q}_T$  is a volumetric enthalpy production term (for example by the Joule effect or chemical reaction) and  $\mathbf{j}_T$  corresponds to heat diffusion.

When mechanical contributions (compression, strain) to the energy balance can be ignored, we find the heat balance in analogous form as the equation of conservation of solute:

$$\frac{\partial(\rho H)}{\partial t} + \text{div}(\rho H \mathbf{v}) + \text{div} \mathbf{j}_T = \dot{Q}_T \quad (\text{A12})$$

$H$  en [ $\text{J} \cdot \text{kg}^{-1}$ ],  $\mathbf{j}_T$  en [ $\text{w} \cdot \text{m}^{-2}$ ],  $\dot{Q}_T$  en [ $\text{w} \cdot \text{m}^{-3}$ ]

### Constitutive equation for energy

Besides the temperature and velocity fields, the heat conservation equation contains three other variables that must be described with constitutive equations. They are: the heat flux,  $\mathbf{j}_T$ , the volume specific enthalpy,  $\rho H$ , and the source term,  $\dot{Q}_T$ . The diffusive heat flux,  $\mathbf{j}_T$ , is given by an equation similar to Fick's first law (Fourier's law):

$$\mathbf{j}_T(\mathbf{x}, t) = - \kappa \mathbf{grad} T(\mathbf{x}, t) \quad (\text{A13})$$

$\kappa$  is the thermal conductivity of the material. Note that the equation (A12) takes into account the heat transfer by advection with the term  $\text{div}(\rho H \mathbf{v})$ , but not the exchanges by radiation if the material is transparent or semi-transparent.

Considering the pressure constant, which is a good approximation for condensed matter, the specific enthalpy of a phase,  $H$ , is given by:

$$H(\mathbf{x}, t) = \int_0^{T(\mathbf{x}, t)} c_p(T) dT \quad (\text{A14})$$

Where  $c_p(T)$  is the specific heat at constant pressure of the material. The specific heat can be a function of the temperature, but not explicitly on position or time. The source term for heat  $\dot{Q}_T$ , can have various origins. In the case of chemical reactions, the heat source term becomes a sum over all the chemical species.

We don't have volumetric enthalpy production term (an external energy source like a radioactive metal or by the Joule effect or chemical reaction). The equation to solve for one phase is:

$$\frac{\partial(\rho^\alpha H^\alpha)}{\partial t} + \text{div}(\rho^\alpha H^\alpha \mathbf{v}^\alpha) - \text{div}(\kappa^\alpha \mathbf{grad} T^\alpha) = 0 \quad (\text{A15})$$

$$\frac{\partial(\rho^\beta H^\beta)}{\partial t} + \text{div}(\rho^\beta H^\beta \mathbf{v}^\beta) - \text{div}(\kappa^\beta \mathbf{grad} T^\beta) = 0 \quad (\text{A16})$$

The definition of the average values is:

$$\langle \rho H \rangle = \langle (\rho H)^\alpha \rangle + \langle (\rho H)^\beta \rangle = f_\alpha \langle \rho H \rangle^\alpha + f_\beta \langle \rho H \rangle^\beta = \frac{1}{\Delta V} \int \rho H dV \quad (\text{A17})$$

$$\langle \rho H \mathbf{v} \rangle = \langle (\rho H \mathbf{v})^\alpha \rangle + \langle (\rho H \mathbf{v})^\beta \rangle = f_\alpha \langle \rho H \mathbf{v} \rangle^\alpha + f_\beta \langle \rho H \mathbf{v} \rangle^\beta = \frac{1}{\Delta V} \int \rho H \mathbf{v} dV \quad (\text{A18})$$

$$\begin{aligned} \langle \kappa \mathbf{grad} T \rangle &= \langle (\kappa \mathbf{grad} T)^\alpha \rangle + \langle (\kappa \mathbf{grad} T)^\beta \rangle = f_\alpha \langle \kappa \mathbf{grad} T \rangle^\alpha + f_\beta \langle \kappa \mathbf{grad} T \rangle^\beta \\ &= \frac{1}{\Delta V} \int \kappa \mathbf{grad} T dV \end{aligned} \quad (\text{A19})$$

The averging of the two phases  $\alpha$  and  $\beta$  leads to add the terms of these two equations and obtain:

$$\begin{aligned} \left\langle \frac{\partial(\rho^\alpha H^\alpha)}{\partial t} + \text{div}(\rho^\alpha H^\alpha \mathbf{v}^\alpha) - \text{div}(\kappa^\alpha \mathbf{grad} T^\alpha) + \frac{\partial(\rho^\beta H^\beta)}{\partial t} + \text{div}(\rho^\beta H^\beta \mathbf{v}^\beta) - \text{div}(\kappa^\beta \mathbf{grad} T^\beta) \right\rangle \\ = 0 \end{aligned} \quad (\text{A20})$$

Then

$$\begin{aligned} \left\langle \frac{\partial(\rho^\alpha H^\alpha)}{\partial t} \right\rangle + \langle \text{div}(\rho^\alpha H^\alpha \mathbf{v}^\alpha) \rangle - \langle \text{div}(\kappa^\alpha \mathbf{grad} T^\alpha) \rangle + \\ \left\langle \frac{\partial(\rho^\beta H^\beta)}{\partial t} \right\rangle + \langle \text{div}(\rho^\beta H^\beta \mathbf{v}^\beta) \rangle - \langle \text{div}(\kappa^\beta \mathbf{grad} T^\beta) \rangle = 0 \end{aligned} \quad (\text{A21})$$

From the average of the temporal derivatives we have

$$\left\langle \frac{\partial(\rho^\alpha H^\alpha)}{\partial t} \right\rangle = \frac{\partial \langle (\rho^\alpha H^\alpha) \rangle}{\partial t} - \langle \rho^\alpha H^\alpha v_n^{\alpha/\beta} \rangle \quad (\text{A22})$$

$$\left\langle \frac{\partial(\rho^\beta H^\beta)}{\partial t} \right\rangle = \frac{\partial \langle (\rho^\beta H^\beta) \rangle}{\partial t} + \langle \rho^\beta H^\beta v_n^{\alpha/\beta} \rangle \quad (\text{A23})$$

From the average of the spatial derivatives we have

$$\langle \text{div}(\rho^\alpha H^\alpha \mathbf{v}^\alpha) \rangle = \text{div} \langle (\rho^\alpha H^\alpha \mathbf{v}^\alpha) \rangle + \langle \rho^\alpha H^\alpha \mathbf{v}^\alpha \rangle \quad (\text{A24})$$

$$\langle \text{div}(\rho^\beta H^\beta \mathbf{v}^\beta) \rangle = \text{div} \langle (\rho^\beta H^\beta \mathbf{v}^\beta) \rangle - \langle \rho^\beta H^\beta \mathbf{v}^\beta \rangle \quad (\text{A25})$$

And

$$\langle \text{div}(\kappa^\alpha \mathbf{grad} T^\alpha) \rangle = \text{div} \langle (\kappa^\alpha \mathbf{grad} T^\alpha) \rangle + \langle \kappa^\alpha \mathbf{grad} T^\alpha \rangle \quad (\text{A26})$$

$$\langle \text{div}(\kappa^\beta \mathbf{grad} T^\beta) \rangle = \text{div} \langle (\kappa^\beta \mathbf{grad} T^\beta) \rangle - \langle \kappa^\beta \mathbf{grad} T^\beta \rangle \quad (\text{A27})$$

We replace on the original equation, we obtain:

$$\begin{aligned} & \frac{\partial \langle (\rho^\alpha H^\alpha) \rangle}{\partial t} - \langle \rho^\alpha H^\alpha v_n^{\alpha/\beta} \rangle + \text{div} \langle (\rho^\alpha H^\alpha \mathbf{v}^\alpha) \rangle + \langle \rho^\alpha H^\alpha \mathbf{v}^\alpha \rangle - \text{div} \langle (\kappa^\alpha \mathbf{grad} T^\alpha) \rangle - \langle \kappa^\alpha \mathbf{grad} T^\alpha \rangle + \\ & \frac{\partial \langle (\rho^\beta H^\beta) \rangle}{\partial t} + \langle \rho^\beta H^\beta v_n^{\alpha/\beta} \rangle + \text{div} \langle (\rho^\beta H^\beta \mathbf{v}^\beta) \rangle - \langle \rho^\beta H^\beta \mathbf{v}^\beta \rangle - \text{div} \langle (\kappa^\beta \mathbf{grad} T^\beta) \rangle + \langle \kappa^\beta \mathbf{grad} T^\beta \rangle = 0 \end{aligned} \quad (\text{A28})$$

Developing we obtain:

$$\begin{aligned} & \left[ \frac{\partial \langle (\rho^\alpha H^\alpha) \rangle}{\partial t} + \frac{\partial \langle (\rho^\beta H^\beta) \rangle}{\partial t} \right] - [\langle \rho^\alpha H^\alpha v_n^{\alpha/\beta} \rangle - \langle \rho^\beta H^\beta v_n^{\alpha/\beta} \rangle] + [\text{div} \langle (\rho^\alpha H^\alpha \mathbf{v}^\alpha) \rangle + \text{div} \langle (\rho^\beta H^\beta \mathbf{v}^\beta) \rangle] \\ & + [\langle \rho^\alpha H^\alpha \mathbf{v}^\alpha \rangle - \langle \rho^\beta H^\beta \mathbf{v}^\beta \rangle] - [\text{div} \langle (\kappa^\alpha \mathbf{grad} T^\alpha) \rangle + \text{div} \langle (\kappa^\beta \mathbf{grad} T^\beta) \rangle] \\ & - [\langle \kappa^\alpha \mathbf{grad} T^\alpha \rangle - \langle \kappa^\beta \mathbf{grad} T^\beta \rangle] = 0 \end{aligned} \quad (\text{A29})$$

Then

$$\begin{aligned} & \frac{\partial \langle \rho H \rangle}{\partial t} + \text{div} \langle \rho H \mathbf{v} \rangle - \text{div} \langle (\kappa \mathbf{grad} T) \rangle + \\ & \langle (\rho^\beta H^\beta - \rho^\alpha H^\alpha) v_n^{\alpha/\beta} + \rho^\alpha H^\alpha \mathbf{v}^\alpha - \rho^\beta H^\beta \mathbf{v}^\beta + \kappa^\beta \mathbf{grad} T^\beta - \kappa^\alpha \mathbf{grad} T^\alpha \rangle = 0 \end{aligned} \quad (\text{A30})$$

We know that from the general conservation equation [reference, p.214 -215]

$$\langle (\rho^\beta H^\beta - \rho^\alpha H^\alpha) v_n^{\alpha/\beta} + \rho^\alpha H^\alpha \mathbf{v}^\alpha - \rho^\beta H^\beta \mathbf{v}^\beta + \kappa^\beta \mathbf{grad} T^\beta - \kappa^\alpha \mathbf{grad} T^\alpha \rangle = 0 \quad (\text{A31})$$

And the average heat conservation equation takes the form:

$$\frac{\partial \langle \rho H \rangle}{\partial t} + \text{div} \langle \rho H \mathbf{v} \rangle - \text{div} \langle \kappa \mathbf{grad} T \rangle = 0 \quad (\text{A32})$$

The local temperature (in the sense of  $\Delta V$ ) in the two phases being the same (equilibrium condition) we obtain:

$$\langle \kappa \mathbf{grad} T \rangle = \langle \kappa \rangle \mathbf{grad} T \text{ with } \langle \kappa \rangle = \langle \kappa^\alpha \rangle + \langle \kappa^\beta \rangle = f_\alpha \langle \kappa \rangle^\alpha + f_\beta \langle \kappa \rangle^\beta \quad (\text{A33})$$

Where  $\langle \kappa \rangle$  is none other than the thermal conductivity averaged over the phases.

The average volumetric enthalpy,  $\langle \rho H \rangle$  can be expressed in terms of the specific heats of each of the phases and the latent heat of the transformation  $(\rho L)^{\alpha/\beta}$ .

$$\langle \rho H \rangle = f_\alpha \int_0^T (\rho c_p)^\alpha + f_\beta \left[ \int_0^T (\rho c_p)^\beta + (\rho L)^{\alpha/\beta} \right] \quad (\text{A34})$$

We define the average specific heat per unit of volume,  $\langle \rho c_p \rangle$  by:

$$\int_0^T \langle \rho c_p \rangle = f_\alpha \int_0^T (\rho c_p)^\alpha + f_\beta \int_0^T (\rho c_p)^\beta \quad (\text{A35})$$

And assuming that it doesn't depend explicitly on time and knowing that  $f_\beta + f_\alpha = 1$ , the temporal variation of the average volumetric enthalpy becomes:

$$\frac{\partial \langle \rho H \rangle}{\partial t} = \langle \rho c_p \rangle \frac{\partial T}{\partial t} - (\rho L)^{\alpha/\beta} \frac{\partial f_\alpha}{\partial t} \quad (\text{A36})$$

Two contributions appear: the first is related to a variation if the average specific heat over the two phases, while the second can be assimilated with a source term for heat, related to the evolution of the latent heat release during the transformation  $\beta \rightarrow \alpha$ .

The average heat equation can then be written as follows:

$$\langle \rho c_p \rangle \frac{\partial T}{\partial t} - (\rho L)^{\alpha/\beta} \frac{\partial f_\alpha}{\partial t} + \text{div} \langle \rho H \mathbf{v} \rangle - \text{div} (\langle \kappa \rangle \mathbf{grad} T) = 0 \quad (\text{A37})$$

The source term introduced by a phase transformation is a volumetric source term:  $(\rho L)^{\alpha/\beta} \frac{df_\alpha}{dt}$

Where  $f^\alpha$  is the volume fraction of the phase  $\alpha$ . (computed using  $\phi$ , where  $\phi$  is a function that varies between  $-1$  and  $1$  as defined in chapter 2). For the static case  $\mathbf{v} = 0$ . Then the conservation equation becomes:

$$\langle \rho c_p \rangle \frac{\partial T}{\partial t} - \text{div} (\langle \kappa \rangle \mathbf{grad} T) = (\rho L)^{\alpha/\beta} \frac{\partial f_\alpha}{\partial t} \quad (\text{A38})$$

From the thesis of Damien Tourret p.32 [TOU2009], we note that:

$$\text{We know that } f_\beta + f_\alpha = 1 \Rightarrow f_\beta = 1 - f_\alpha \Rightarrow \frac{\partial f_\beta}{\partial t} = - \frac{\partial f_\alpha}{\partial t}$$

We replace and we take  $f_\alpha = -\phi/2$ . The conservation equation becomes:

$$\langle \rho c_p \rangle \frac{\partial T}{\partial t} - \text{div} (\langle \kappa \rangle \mathbf{grad} T) = - \frac{1}{2} (\rho L)^{\alpha/\beta} \frac{\partial \phi}{\partial t} \quad (\text{A39})$$

We represent  $\alpha$  the thermal diffusivity defined as  $\alpha = \frac{\kappa}{\rho c_p}$ . So the energy conservation equation used becomes:

$$\frac{\partial T}{\partial t} - \text{div} (\langle \alpha \rangle \mathbf{grad} T) = - \frac{1}{2} \frac{(\rho L)^{\alpha/\beta}}{\langle \rho c_p \rangle} \frac{\partial \phi}{\partial t} \quad (\text{A40})$$

In our case we will consider that the diffusivity is equal in the solid and the liquid so  $\langle \alpha \rangle = \alpha^s = \alpha^l = \text{cte}$ , and the heat capacity are the same  $\langle \rho c_p \rangle = \rho c_p^s = \rho c_p^l = \text{cte}$ , and the equation becomes:

$$\frac{\partial T}{\partial t} - \alpha \Delta T = - \frac{1}{2} \frac{(\rho L)^{\alpha/\beta}}{\rho c_p} \frac{\partial \phi}{\partial t} \quad (\text{A41})$$

To do the simulation using the phase-field model for dendritic growth, we will take the dimensionless temperature  $\theta$  as defined before. The equation to solve becomes:

$$\frac{\partial \theta}{\partial \tau} - \alpha^* \Delta \theta = - \frac{1}{2} \frac{\partial \phi}{\partial \tau} \quad (\text{A42})$$



## Appendix B Analytical solution for corner test

### Computing analytical solution for the temperature [RAT1971]

Equation to represent the analytical temperature variation with the condition  $-1$  and initial temperature  $\theta_0$ :

$$\theta(x^*; y^*) = -1 + (1 + \theta_0) \operatorname{erf} \left[ \frac{x}{\sqrt{4\alpha t}} \right] \operatorname{erf} \left[ \frac{y}{\sqrt{4\alpha t}} \right] + V \left( \left( \frac{x}{\sqrt{4\alpha t}} \right); \left( \frac{y}{\sqrt{4\alpha t}} \right) \right) = \quad (\text{B1})$$

$$\theta(x^*; y^*) = -1 + (1 + \theta_0) \operatorname{erf}(x^*) \operatorname{erf}(y^*) + V(x^*; y^*)$$

Here  $x^* = \frac{x}{\sqrt{4\alpha t}}$ ,  $y^* = \frac{y}{\sqrt{4\alpha t}}$  and  $\theta_0$  the dimensionless initial temperature =  $\frac{\kappa^l [T_0 - T_F]}{\kappa^s [T_F - T_W]}$

With

$$V(x^*; y^*) =$$

$$\frac{\beta}{2\pi} \int_0^1 \int_{x_0}^{\Lambda} \left[ f(\eta) - \eta \frac{df(\eta)}{d\eta} \right] \times [K(\eta, \tau; x^*) K(f(\eta), \tau; y^*) + K(f(\eta), \tau; x^*) K(\eta, \tau; y^*)] \times d\eta \frac{d\tau}{1 - \tau}$$

$$+ \frac{\beta\lambda}{4\sqrt{\pi}} \int_0^1 [K(\lambda, \tau; y^*) E(\tau, \Lambda; x^*) + K(\lambda, \tau; x^*) E(\tau, \Lambda; y^*)] \frac{d\tau}{\sqrt{\tau(1 - \tau)}} \quad (\text{B2})$$

$f(\eta)$  is the interface position in  $x^*, y^*$  domain.

With

$$K(\eta, \tau; x^*) = \exp \left[ \frac{-(x^* - \sqrt{\tau}\eta)^2}{(1 - \tau)} \right] - \exp \left[ \frac{-(x^* + \sqrt{\tau}\eta)^2}{(1 - \tau)} \right] \quad (\text{B3})$$

And

$$E(\tau, \Lambda; x^*) = \operatorname{erf} \left[ \frac{(x^* - \Lambda\sqrt{\tau})}{\sqrt{(1 - \tau)}} \right] + \operatorname{erf} \left[ \frac{(x^* + \Lambda\sqrt{\tau})}{\sqrt{(1 - \tau)}} \right] \quad (\text{B4})$$

We compute  $V$  using a numerical integration, so  $V$  becomes:

$$V(x^*; y^*) = \frac{\beta}{2\pi} \sum_{i=1}^{40} \sum_{j=1}^{40} w'_i \tilde{w}'_j \left[ f(\eta_j) - \eta_j \frac{df(\eta_j)}{d\eta} \right] \times [K(\eta_j, \tau_i; x^*) K(f(\eta_j), \tau_i; y^*) + K(f(\eta_j), \tau_i; x^*) K(\eta_j, \tau_i; y^*)] (1 - \tau_i)^{-1}$$

$$+ \frac{\beta\lambda}{4\sqrt{\pi}} \sum_{i=1}^{40} w'_i [K(\lambda, \tau_i; y^*) E(\tau_i, \Lambda; x^*) + K(\lambda, \tau_i; x^*) E(\tau_i, \Lambda; y^*)] \frac{1}{\sqrt{\tau_i(1 - \tau_i)}} \quad (\text{B5})$$

With

$$w'_{i=1} = \left( \frac{0.9 - 0}{2} \right) w_i = 0.45 w_i \quad i = 1, 2, \dots, 20$$

$$w'_{41-i} = \left( \frac{1 - 0.9}{2} \right) w_i = 0.05 w_i \quad i = 1, 2, \dots, 20$$

$$\tilde{w}'_i = \left( \frac{x_1^* - x_0^*}{2} \right) w_i \quad i = 1, 2, \dots, 20$$

$$w_{41-i} \tilde{w}'_i = \left( \frac{\Lambda - x_1^*}{2} \right) w_i \quad i = 1, 2, \dots, 20$$

$$\tau_i = \left(\frac{0.9 - 0}{2}\right) \xi_i + \left(\frac{0.9 + 0}{2}\right) = 0.45 \xi_i + 0.45 \quad i = 1, 2, \dots, 20$$

$$\tau_{41-i} = \left(\frac{1 - 0.9}{2}\right) \xi_i + \left(\frac{1 + 0.9}{2}\right) = 0.05 \xi_i + 0.05 \quad i = 1, 2, \dots, 20$$

$$\eta_i = \left(\frac{x_1^* - x_0^*}{2}\right) \xi_i + \left(\frac{x_1^* + x_0^*}{2}\right) \quad i = 1, 2, \dots, 20$$

$$\eta_{41-i} = \left(\frac{\Lambda - x_1^*}{2}\right) \xi_i + \left(\frac{\Lambda + x_1^*}{2}\right) \quad i = 1, 2, \dots, 20$$

The value of  $w_i$  and  $\xi_i$  are given in this table:

| $\pm \xi_i$ | $w_i$     |
|-------------|-----------|
| 0.0765265   | 0.1527534 |
| 0.2277859   | 0.1491730 |
| 0.3737061   | 0.1420961 |
| 0.5108670   | 0.1316886 |
| 0.6360537   | 0.1181945 |
| 0.7463319   | 0.1019301 |
| 0.8391170   | 0.0832767 |
| 0.9122344   | 0.0626720 |
| 0.9639719   | 0.0406014 |
| 0.9931286   | 0.0176140 |

We take  $w = [0.1527534 \ 0.1527534 \ 0.1491730 \ 0.1491730 \ \dots]$ ;

$\xi = [-0.0765265 \ 0.0765265 \ -0.2277859 \ 0.2277859 \ \dots]$ ;

### Computing analytical solution for the interface

Equation to draw the analytical liquid/solid interface:

$$f(x^*) = \left[ \lambda^m + \frac{C}{x^{*m} - \lambda^m} \right]^{\frac{1}{m}} \tag{B6}$$

C is a constant in super hyperbola and  $\lambda$  is computed from :

$$\frac{\exp(-\lambda^2)}{\operatorname{erf} \lambda} - \frac{\theta_0 \exp(-\lambda^2)}{\operatorname{erfc} \lambda} = \sqrt{\pi} \beta \lambda \tag{B7}$$

### Computation of $x_0^*$ and $x_1^*$ :

$x_0^*$  et  $x_1^*$  are computed as:

$$f(x_0^*) = x_0^* \tag{B8}$$

And

$$f(x_1^*) = (x_0^* + \lambda)/2 \tag{B9}$$

And

$$-1 + (1 + \theta_0) \operatorname{erf}(x^*) \operatorname{erf}(y^*) + \tag{B10}$$

$$\begin{aligned} & \frac{\beta}{2\pi} \int_0^1 \int_{x_0^*}^{\Lambda} \left[ f(\eta) - \eta \frac{df(\eta)}{d\eta} \right] \times [K(\eta, \tau; x^*) K(f(\eta), \tau; y^*) + K(f(\eta), \tau; x^*) K(\eta, \tau; y^*)] \times d\eta \frac{d\tau}{1-\tau} \\ & + \frac{\beta\lambda}{4\sqrt{\pi}} \int_0^1 [K(\lambda, \tau; y^*) E(\tau, \Lambda; x^*) + K(\lambda, \tau; x^*) E(\tau, \Lambda; y^*)] \frac{d\tau}{\sqrt{\tau(1-\tau)}} = 0 \end{aligned}$$

We write the equation above twice once with  $x^* = x_0^*$  and once with  $x^* = x_1^*$ . We obtain two equations with two unknowns. Then we replace the integral with the quadrature formulas and we have now a system of two nonlinear equations to solve. These equations can be solved using a trial and error procedure on a digital computer (ex. Matlab : fsolve).

To eliminate the infinite limit in equation of V, we divide the interval  $(x_0^*, \infty)$  into two intervals  $(x_0^*, \Lambda)$  and  $(\Lambda, \infty)$  and selecting  $\Lambda$  such as  $\eta \geq \Lambda, f(\eta) \approx 1$  and  $\frac{df(\eta)}{d\eta} \approx 0$ .

So we write this equation twice once with  $x^* = x_0^*$  and once with  $x^* = x_1^*$ .

$$\begin{aligned} & -1 + (1 + \theta_0) \operatorname{erf}(x^*) \operatorname{erf}(y^*) + \\ & \frac{\beta}{2\pi} \int_0^1 \int_{x_0^*}^{\Lambda} \lambda \times [K(\eta, \tau; x^*) K(\lambda, \tau; y^*) + K(\lambda, \tau; x^*) K(\eta, \tau; y^*)] \times d\eta \frac{d\tau}{1-\tau} \\ & + \frac{\beta\lambda}{4\sqrt{\pi}} \int_0^1 [K(\lambda, \tau; y^*) E(\tau, \Lambda; x^*) + K(\lambda, \tau; x^*) E(\tau, \Lambda; y^*)] \frac{d\tau}{\sqrt{\tau(1-\tau)}} = 0 \end{aligned} \tag{B11}$$

We obtain the values of  $x_0^*$  and  $x_1^*$  then  $C$  and  $m$  are computed solving these two equations:

$$C = (x_0^{*m} - \lambda^m)^2 \tag{B12}$$

$$(x_0^{*m} - \lambda^m)^2 = (x_1^{*m} - \lambda^m) \left[ \left( \frac{x_0^* + \lambda^m}{2} \right)^m - \lambda^m \right] \tag{B13}$$



## Appendix C 1D analytical solution

We present here how to obtain the analytical solution for the non-stationary velocity.

To obtain the analytical solution we will solve the equation  $D^* \partial^2 c / \partial x^{*2} = \partial c / \partial \tau$ .

To do that we consider that the solution depends on  $x^*$  and  $\tau$  as:

$$c(x^*, \tau) = f\left(\frac{x^*}{\sqrt{D^* \tau}}\right) = f(F) \quad (C1)$$

We replace this form in the equation and we obtain:

$$\frac{D^*}{D^* \tau} f''(F) = \frac{-x^* D^*}{2\sqrt{D^{*3} \tau^3}} f'(F) \quad (C2)$$

Then we have  $\frac{f''}{f'} = \frac{-x^* D^* \tau}{2D^* \tau \sqrt{D^* \tau}} = \frac{-F}{2}$ .

Integrating the equation we obtain:

$$\ln(f') = \frac{-F^2}{4} \Rightarrow f' = K_1 \exp\left(\frac{-F^2}{4}\right) \quad (C3)$$

Then  $c(x^*, \tau) = f(F) = K_1 \operatorname{Erfc}\left(\frac{F}{2}\right) + K_2$

If  $x^* \rightarrow +\infty \Rightarrow c(+\infty, \tau) = K_2 = c_\infty$

If  $x^* = R = x_{0t}^* \Rightarrow c(R, \tau) = K_1 \operatorname{Erfc}\left(\frac{R}{2\sqrt{D^* \tau}}\right) + c_\infty = c_{l/s}$  so  $K_1 = (c_{l/s} - c_\infty) \frac{1}{\operatorname{Erfc}\left(\frac{R}{2\sqrt{D^* \tau}}\right)}$

Whis  $v \neq \text{cte}$  it can be defined as  $v = \frac{\lambda_c \sqrt{D^*}}{2\sqrt{\tau}}$  with  $x_{0t}^* = R = \lambda_c \sqrt{D^* \tau}$   $\lambda_c$  is a constant.

$$vR = \frac{\lambda_c \sqrt{D^*}}{2\sqrt{\tau}} \lambda_c \sqrt{D^* \tau} = \frac{\lambda_c^2}{2D^*}$$

We have the unique solution [AAR1970]:

$$c(x^*, \tau) = c_\infty + (c_{l/s} - c_\infty) \frac{\operatorname{Erfc}\left(\frac{x^* - x_0^*}{2\sqrt{D^* \tau}}\right)}{\operatorname{Erfc}\left(\frac{\lambda_c}{2}\right)} \quad (C4)$$

and  $\lambda_c$  must verify:

$$\Omega_c = \frac{c_\infty - c_{l/s}}{c_s - c_{l/s}} = \frac{\sqrt{\pi}}{2} \lambda_c \exp\left(\frac{\lambda_c^2}{4}\right) \operatorname{Erfc}\left(\frac{\lambda_c}{2}\right) \quad (C5)$$

$\lambda_c$  satisfy this equation because of the mass conservation at the interface:

$$D^* \frac{\partial c}{\partial x^*} \Big|_{x^*=R} = (c_s - c_\infty) \frac{dR}{d\tau}$$

So  $D^* (c_{l/s} - c_\infty) \frac{1}{2\sqrt{D^* \tau}} \frac{2 \exp\left(-\frac{R^2}{4D^* \tau}\right)}{\sqrt{\pi}} \frac{1}{\operatorname{Erfc}(\lambda_c/2)} = (c_s - c_{l/s}) \frac{\lambda_c}{2} \sqrt{\frac{D^*}{\tau}}$

We can use another form for the composition without introducing the time:

$$c(x^*, \tau) = c_\infty + (c_{l/s} - c_\infty) \frac{\operatorname{Erfc}\left(\frac{\lambda_c (x^* - x_0^*)}{2 (x_{0t}^* - x_0^*)}\right)}{\operatorname{Erfc}\left(\frac{\lambda_c}{2}\right)} \quad (\text{C6})$$

To obtain the analytical solution, we compute  $\lambda_c$  from equation (C5) and we use it in equation (C6).

## References

- [AAR1970] H.B. Aaron, D. Fainstein, G.R. Kotler, «Diffusion-Limited phase transformations: A comparison and critical evaluation of the mathematical approximations», *J. of Appl. Phys.*, vol. 11, pp. 4404-4410, 1970.
- [ABE1997] T. Abel, E. Brener and H. Muller-Krumbhaar, «Three-dimensional growth morphologies in diffusion-controlled channel growth», *Phys. Rev. E*, vol.55, pp.7789, 1997.
- [ABR2004] M.D. Abramoff, P.J. Magalhães and S.J. Ram, «Image processing with imageJ», *Biophotonics Int.*, vol. 11, pp.36-42, 2004.
- [ALM1999] R. Almgren, «Second-order phase field asymptotics for unequal conductivities», *SIAM J. Appl. Math.*, vol.59, pp.2086-2107, 1999.
- [AST2009] M. Asta, C. Beckermann, A. Karma, W. Kurz and M. Rappaz, «Solidification microstructures and solid-state parallels: recent developments, future directions», *Acta Materialia*, vol.57, pp.941-971, 2009.
- [BAL2015] S. Balay, S. Abhyankar, M.F. Adams, J. Brown, P. Brune, K. Buschelman, L. Dalcin, V. Eijkhout, W.D. Gropp, D. Kaushik, M.G. Knepley, L.C. McInnes, K. Rupp, B.F. Smith, S. Zampini, and H. Zhang. PETSc Web page. <http://www.mcs.anl.gov/petsc>, 2015.
- [BAN1994] C. Bandle, A. Brillard, G. Dziuk, A. Schmidt , «Course on mean curvature flow», 1994.
- [BEC2002] C. Beckermann, «Modelling of macrosegregation: Applications and future needs», *Int Mater Rev*, vol.47, pp.243-261, 2002.
- [BED2015] M. Bedel, G. Reinhart, Ch.-A. Gandin, A-A. Bogno, H. Nguyen-Thi, and H. Henein, «Evolution of the dendritic morphology with the solidification velocity in rapidly solidified Al-4.5wt%Cu droplets», *IOP Conf. Ser. Mater. Sci. Eng.*, vol.84, 2015.
- [BEL2003] L. Beltran-Sanchez and D. Stefanescu, «Growth of solutal dendrites:A cellular automaton model and its quantitative capabilities», *Metallurgical and Materials Transactions A*, vol.34, pp.367-382, 2003.
- [BEL2004] L. Beltran-Sanchez and D. Stefanescu, «A quantitative dendrite growth model and analysis of stability concepts», *Metallurgical and Materials Transactions A*, vol.35, pp.2471-2485, 2004.
- [BEN1984a] E. Ben-Jacob, N. Golenfeld, B.G. Kotliar, «Pattern selection in dendrite Solidification», *J. Phys Rev Lett*, vol. 53, pp.2110-2113, 1984.
- [BEN1984b] E. Ben-Jacob, N. Golenfeld, J.S. Langer, «Boundary-layer model of pattern formation in solidification», *J. Phys Rev A*, vol. 29, pp.330-340, 1984.
- [BEN1993] M. Ben Amar, and E. Brener, «Theory of pattern selection in three-dimensional nonaxisymmetric dendritic growth», *Phys. Rev. Lett.*, vol.71, vol.589, 1993.
- [BOE2002] W. Boettinger, J. Warren, C. Beckermann and A. Karma, «Phase-field simulation of solidification», *Annual Review on Material Research*, vol.32, pp.163-194, 2002.
- [BOG2013] A-A. Bogno, P. Delshad Khatibi, H. Henein and Ch-A. Gandin, «Quantification of primary dendritic and secondary eutectic undercoolings of rapidly solidified Al-Cu droplets», *Materials science and technology*, vol.2, pp.1153-116, 2013.
- [BOU1989] Ph. Bouissou, B. Perrin, P. Tabeling, «Influence of an external flow on dendritic crystal growth», *Physical Review A*, vol.40, pp.509, 1989.
- [BRA1997] R. J. Braun and M. T. Murray, «Adaptive phase-field computations of dendritic crystal growth», *J. Cryst. Growth*, vol.174, pp.41, 1997.

- [CAG1989] G. Caginalp, «Stefan and Hele-Shaw type models as asymptotic limits of the phase-field equations», *Physical Review A*, vol.39, pp.5887-5896, 1989.
- [CAH1958] J. W. Cahn and J. E. Hilliard, «Free energy of a nonuniform system. I. Interfacial free energy», *The Journal of Chemical Physics*, vol.28, pp.258-267, 1958.
- [CAH1979] S.M. Allen, J. W. Cahn, «A microscopic theory for antiphase boundary motion and its application to antiphase domain coarsening », *Acta Metallurgica*, vol.27, pp.1085-1095, 1979.
- [CAR2012] T. Carozzani, *PHD thesis MinesParisTech*, 2012.
- [CHA1987] S.K. Chan, H.H. Reimer, M. Kahlweit, «On the growth of  $\text{NH}_4\text{Cl}$  dendrites at very low supersaturation», *Journal of Crystal Growth*, vol.43, pp.229-234, 1978.
- [CHO1988] M.A. Chopra, M.E. Glicksman, N.B. Singh, «Dendritic solidification in binary alloys», *Metallurgical Transactions A*, vol.19, pp.3087-3096, 1988.
- [CHO2012] A. Choudhury, K. Reuther, E. Wesner, A. August, B. Nestler, M. Rettenmayr, «Comparison of phase-field and cellular automaton models for dendritic solidification in Al-Cu alloy», *Computational Materials Science*, vol.55, pp.263-268, 2012.
- [COL1985] J. B. Collins and H. Levine, «Diffuse interface model of diffusion-limited crystal growth», *Phys. Rev. B*, vol.31, pp.6119, 1985.
- [COU2000a] T. Coupez, «Generation et Adaptation de maillage par optimisation locale », *Revue europeenne des elements finis*, vol. 9(4), pp. 403-423, 2000.
- [COU2000b] T. Coupez, H. Dignonnet, and R. Ducloux., « Parallel meshing and remeshing.» *Applied Mathematical Modelling*, vol. 25, pp.153–175, 2000.
- [COU2011] T. Coupez, «Metric construction by length distribution tensor and edge based error for anisotropic adaptive meshing », *Journal of Computational Physics*, vol. 230, pp.2391-2405, 2011.
- [COU2014] T. Coupez, L. Silva and E. Hachem, «Implicit boundary and adaptive anisotropic meshing», *Tetrahedron IV, SEMA SIMAI Springer Series*, 2014.
- [DIG2001] H. Dignonnet, «Repartitionnement dynamique, mailleur parallèle et leurs applications à la simulation numérique en mise en forme des matériaux», *PHD Thesis, ENSMP*, 2001.
- [DIG2003] H.Dignonnet, T. Coupez, «Object-oriented programming for "fast and easy" development of parallel applications in forming processes simulation», *2nd MIT Conference on Computational Fluid and Solid Mechanics*, pp.1922-1924, 2003
- [DIG2007] H. Dignonnet, L. Silva, T. Coupez, «Cimlib: A fully parallel application for numerical simulations based on components assembly», *AIP Conference Proceedings*, vol. 908, pp.269, 2007.
- [DAN2014] J.A. Dantzig, *Communication notes*, 2014.
- [DIL1997] U. Dilthey, V. Pavlik and T. Reichel, *Mathematical Modelling of Weld Phenomena 3 ed Cerjak H and Bhadeshia H* (London: The Institute of Materials), pp.85-105, 1997.
- [DIN1997] Y. Ding, *PhD Thesis, University of Alberta, Canada* (1997).
- [DOU1988] A. Dougherty, J.P. Gollub, «Steady-state dendritic growth of  $\text{NH}_4\text{Br}$  from solution», *Physical Review A*, vol.38, pp.3043-3053, 1988.
- [EIK2010] J. Eiken, «A phase-field model for technical alloy solidification», *PHD thesis, Foundry institute Germany*, 2010.
- [ELD1994] K.R. Elder, F. Drolet, J.M. Kosterlitz, and M. Grant, «Stochastic eutectic growth», *Phys. Rev. Lett.*, vol.72, pp.677, 1994.

- [ELL2004] N. Ellendt, R. Schmidt, J. Knabe, H. Henein, V. Uhlenwinkel, «Spray deposition using impulse atomization technique», *Materials Science and Engineering A*, vol.383, pp.107-113, 2004.
- [FED2012] Federation M P I 2012 (S.I.: Metal Powder Industry).
- [FRI2009] S. Fries, B. Boettinger, J. Eiken and I. Steinbach, «Upgrading CALPHAD to microstructure simulation: the phase-field method», *International Journal of Materials Research*, vol.100, pp.128-134, 2009.
- [GAL2010] M. Gallerneault, Novelis Inc., private communications, April 2010.
- [GAN1999] Ch.-A. Gandin, J.L. Desbailles, M. Rappaz and P. Thevoz, «A three-dimensional cellular automaton-finite element model for the prediction of solidification grain structures», *Metallurgical and Materials Transactions A*, vol.30, pp.3153-3165, 1999.
- [GAN2008] Ch.-A. Gandin, S. Mosbah, Th. Volkman, D.M. Herlach, «Experimental and numerical modeling of equiaxed solidification in metallic alloys», *Acta Materialia*, vol.56, pp.3023, 2008.
- [GLI1988] M.E. Glicksman, N.B. Singh, M. Chopra, «measurement of the diffusion coefficient of acetone in succinonitrile at its melting point», *Journal of Crystal Growth*, vol.92, pp.543, 1988.
- [HAC2009] E. Hachem «Stabilized finite element method for heat transfer and turbulent flows inside industrial furnace», *PHD thesis*, Mines Paristech, 2009.
- [HEC2004] U. Hecht, L. Granasy, T. Pusztai, B. Boettinger, M. Apel, V. Witusiewicz, L. Ratke, J. De Wilde, L. Froyen, D. Camel, B. Drevet, G. Faivre, S. Fries, B. Legendre and S. Rex, «Multiphase solidification in multicomponent alloys», *Material Science and Engineering R*, vol.46, pp.1-49, 2004.
- [HEN1999] S. Henry, *Ph.D. thesis*, EPFL, Lausanne, 1999.
- [HEN2010] H. Henein, V. Buchoud, R.-R. Schmidt, C. Watt, D. Malahof, Ch.-A. Gandin, G. Lesoult and V. Uhlenwinkel, «Droplet solidification of Impulse Atomised Al-0.61 and 1.9 wt% Fe», *Canadian Metallurgical Quarterly*, vol.49, pp 275-292, 2010.
- [HER2006] R. Heringer, Ch.-A. Gandin, G. Lesoult, H. Henein, «Atomized droplet solidification as an equiaxed growth models», *Acta Materialia*, vol.54, pp.4427-4440, 2006.
- [HER2007] D. M . Herlach, R. Lengsdorf, P. Galenko, Ch.-A. Gandin, S. Mosbah, A. Garcia-Escorial, H. Henein, final report of the European Space Agency project NEQUISOL II, September 2007.
- [HOU2008] H. Hou, Y-H. Zhao, X-f. Niu, «3D anisotropy simulation of dendrites growth with phase field method», *trans. Nonferrous Met. Soc. China*, vol. 18, pp.223-228, 2008.
- [IHL1994] T. Ihle, and H. Muller-Krumbhaar, «Fractal and compact growth morphologies in phase transition with diffusion transport», *Phys. Rev. E*, vol.49, pp.2972, 1994.
- [KAH1970] M. Kahlweit, «On the dendritic growth of NH<sub>4</sub>Cl crystals from aqueous solutions», *Journal of Crystal Growth*, vol.6, pp.125-129, 1970.
- [KAR1994] A. Karma, «Phase-field model of eutectic growth», *Phys. Rev. E*, vol.49, pp.2245, 1994.
- [KAR1996] A. Karma, W.J. Rappel, «Phase field model for computationally efficient modelling of solidification with arbitrary interface kinetics», *Phys. Rev. E*, vol.53, pp.3017-3020, 1996.
- [KAR1998] A. Karma, and W.J. Rappel, «Quantitative phase-field modeling of dendritic growth in two and three dimensions», *Phys. Rev.E*, vol.57, pp.4323, 1998.

- [KAR2001] A. Karma, «Phase-Field Formulation for Quantitative Modeling of Alloy Solidification», *Physical Review Letters*, vol.87,115701, 2001.
- [KIM1999] S.-G. Kim, W. T. Kim, and T. Suzuki, «Phase-field model for binary alloys», *Phys. Rev. E*, vol.60, pp.7186, 1999.
- [KRA2009] M. Krane, D. Johnson, S. Raghavan, «The development of a cellular automaton finite volume model for dendritic growth», *Applied Mathematical Modelling*, vol.33, pp.2234-47, 2009.
- [KUR1986] W. Kurz, B. Giovanola, R. Trivedi, «Theory of microstructural development during rapid solidification», *Acta Metall. Mater.*, vol.34, pp.823-830, 1986.
- [KUR1998] W. Kurz, D.J. Fisher, «Fundamentals of solidification», *Trans tech publications*, 1998.
- [LAN1986] J. S. Langer, «Models of pattern formation in first order phase transitions», *Directions in Condensed Matter*, vol.1, pp.165-186, 1986.
- [LER2015] N. Leriche, «Etude de la Transition Colonnaire-Equiaxe dans les lingots et en coulée continue d'acier et influence du mouvement des grains », *PHD thesis*, Institut Jean Lamour Nancy, 2015.
- [LO2001] T.S. Lo, A. Karma, and M. Plapp, «Phase-field modeling of microstructural pattern formation during directional solidification of peritectic alloys without morphological instability», *Phys. Rev. E*, vol.63, 031504, 2001.
- [LU2005] Y. Lu, C. Beckermann and J.C. Ramirez, «Three dimensional phase-field simulations of the effect of convection on free dendritic growth», *Journal of crystal growth* 280, pp.320-334, 2005.
- [LUD2004] O. Ludwig, «Etude expérimentale et modélisation du comportement rhéologique d'alliages d'Al-Cu en cours de solidification dans le cadre de la fissuration à chaud en coulée continue», *PHD Thesis Institut National Polytechnique de Grenoble*, 2004.
- [MCF2000] G. B. McFadden, A. A. Wheeler, and D. M. Anderson, «The interface asymptotics for an energy/entropy approach to phase-field models with unequal conductivities», *Physica D*, vol.144, pp.154, 2000.
- [MEC2010] F. Mechighel, «Modélisation de la convection au cours des changements de phase liquide-solide : Effet d'un champ magnétique», *PHD Thesis Université de Limoges*, 2010.
- [MES2009] Y. Mesri, H. Dignonnet, T. Coupez, «Advanced parallel computing in material forming with CIMLib», *European Journal of Computational Mechanics*, 18:7-8, pp.669-694, 2009.
- [MOS2010] S. Mosbah, M. Bellet, Ch.-A. Gandin, «Experimental and numerical modeling of segregation in metallic alloys», *Metallurgical and Materials Transactions A*, vol. 41, pp.651-669, 2010.
- [MUL1964] W.W. Mullions, R.F. Sekerka, «The stability of planar interface during solidification», *J. App Phys*, vol. 35, pp.444-451, 1964.
- [NAK2006] M. Nakagawa, Y. Natsume and K. Ohsasa, «Dendrite growth model using front tracking technique with new growth algorithm», *ISIJ International*, vol.46, pp.909-913, 2006.
- [NAR2007] J. Narski, M. Picasso, «Adapative finite elements with high aspect ratio for dendritic growth of a binary alloy including fluid flow induced by shrinkage», *Comput. Method Appl. Mech. Engrg.*, vol.196, pp. 3562-3576, 2007.

- [NAS1999] L. Nastac, «Numerical modeling of solidification morphologies and segregation patterns in cast dendritic alloys», *Acta Materialia*, vol.47, pp.4253-4262, 1999.
- [NGU2012] H. Nguyen-Thi, L. Salvo, R.H. Mathiesen, L. Arnberg, B. Billia, M. Suery and G. Reinhart, «On the interest of synchrotron X-ray imaging for the study of solidification in metallic alloy», *Comptes Rendus Phys.*, vol.13, pp.237-45, 2012.
- [NGU2015] T.T.M. Nguyen, «Multiscale finite element modeling of macrosegregation and grain transport », *PHD thesis*, Mines Paristech, 2015.
- [PLA2000a] M. Plapp and A. Karma, «Multiscale random-walk algorithm for simulating interfacial pattern formation», *Phys. Rev. Lett.*, vol.84, pp.1740, 2000.
- [PLA2000b] M. Plapp, A. Karma, «Multiscale Finite-Difference-Diffusion-Monte-Carlo Method for Simulating Dendritic Solidification», *journal of computational physics*, vol.165, pp.592-619, 2000.
- [PRA2006] A. Prasad, PhD Thesis, University of Alberta, Canada, 2006.
- [PRA2009] A. Prasad, S. Mosbah, H. Henein, Ch.-A. Gandin, «A solidification model for atomization», *ISIJ International*, vol.49, pp.992, 2009.
- [PRO1998] N. Provatas, N. Goldenfeld, and J. Dantzig, «Efficient computation of dendritic microstructures using adaptive mesh refinement», *Phys. Rev. Lett.*, vol.80, pp.3308, 1998.
- [PRO1999] N. Provatas, N. Goldenfeld, J. Danzig, «Adaptive Mesh Refinement Computation of Solidification Microstructures Using Dynamic Data Structures», *Journal of Computational Physics*, vol.148, pp.265-290, 1999.
- [RAM2004] J.C. Ramirez , C. Beckermann, A. Karma and H-J. Diepers, «Phase field modeling of binary alloy solidification with coupled heat and solute diffusion», *Physical review E*, vol.69, 2004.
- [RAM2005] J.C. Ramirez , C. Beckermann, «Examination of binary alloy free dendritic growth theories with a phase-field model», *Acta Materialia*, vol.53, pp. 1721-1736, 2005.
- [RAP1993] M. Rappaz and Ch-A. Gandin, «Probabilistic modeling of microstructure formation in solidification processes», *Acta Metallurgica et Materialia*, vol.41, pp.345-360, 1993.
- [RAP2003] M. Rappaz, M. Bellet, M. Deville, «Numerical Modeling in Materials Science and Engineering», *Springer-Verlag Berlin Heidelberg*, 2003.
- [RAT1971] K.A. Rathjen, L.M. Jiji, « Heat conduction with melting or freezing in a corner », *Journal of heat transfer*, pp.101, 1971.
- [ROY2005] J. Røyset and N. Ryum, «Scandium in aluminum alloys», *International Materials Reviews*, vol.50, pp.19, 2005.
- [SAI1988] Y. Saito, G. Goldbeck-Wood and H. Muller-Krumbhaar, «Numerical simulation of dendritic growth», *Physical Review A*, vol.38, pp.2148, 1988.
- [SCH1996] A. Schmidt, «Computations of three-dimensional dendrites with finite elements», *J. Comput. Phys.*, vol.125, pp.293, 1996.
- [STE1999] I. Steinbach, C. Beckermann, B. Kauerauf, Q. Li, J. Guo, «Three dimensional modeling of equiaxed dendritic growth on a mesoscopic scale», *Acta Mater*, vol.47, pp.971-982, 1999.
- [STE2005] I. Steinbach, H-J. Diepers, C. Beckermann, «Transient growth and interaction of equiaxed dendrites», *J Cryst Growth*, vol.275, pp.624-638, 2005.
- [TAN2006] L. Tan, N. Zabaras, «A level set simulation of dendritic solidification with combined features of front-tracking and fixed-domain methods», *Journal of computational Physics*, vol. 211, pp.36-63, 2006.

- [TON1998a] R. Tonhardt, G. Amberg, «Phase-field simulation of dendritic growth in shear flow», *Journal of crystal growth*, vol.194, pp.406-425, 1998.
- [TON1998b] X. Tong, C. Beckermann, and A. Karma, «in Modeling of Casting», *Welding and Advanced Solidification Conference VIII*, ed. B. G. Thomas and C. Beckermann. TMS, Warrendale, PA, pp.613, 1998.
- [TOU2009] D. Tournet «Modélisation de cinétiques de transformations multiples dans les alliages métalliques», *PHD thesis*, Mines Paristech, 2009.
- [TOU2011a] D. Tournet, Ch-A. Gandin, T. Volkman, D. Herlach, «Multiplenon-equilibrium phase transformations: modeling versus electro-magnetic levitation experiment», *Acta Mater*, vol.59, pp.4665-4677, 2011.
- [TOU2011b] D. Tournet, G. Reinhart, Ch-A. Gandin G.N. Iles, U. Dahlborg, M. Calvo-Dahlborg, et al., «Gas atomization of Al-Ni powders: solidification modeling and neutron diffraction analysis», *Acta Mater*, vol.59, pp.6658-6669, 2011.
- [TOU2013] D. Tournet, A. Karma, «Multisclae dendritic needle network model of alloy solidification», *Acta Mater*, vol.61, pp.6474-6491, 2013.
- [UDA1999] H. Udaykumar, R. Mittal and W. Shyy, «Computation of solid-liquid fronts in the sharp interface limit on fixed grids», *Journal of Computational Physics*, vol.153, pp.535-574, 1999.
- [WHE1992] A. A. Wheeler, W. J. Boettinger, and G. B. McFadden, «Phase-field model for isothermal phase transitions in binary alloys», *Phys. Rev. A*, vol.45, pp.7424, 1992.
- [WHE1996] A.A. Wheeler, G.B. McFadden, and W.J. Boettinger, «Phase-fieldmodel for solidification of a eutectic alloy», *Proc. R. Soc. Lond. A*, vol.452-525, pp.495, 1996.
- [WIS2002] J.B. Wiskel, H. Henein, E. Maire, «Solidification study of aluminum alloys using impulse atomization: Part I - Heat transfer analysis of an atomized droplet», *can. Metall. Quart.*, vol.41, pp.97-110, 2002.
- [XIE2013] Y. Xie, H.B. Dong, J.A. Dantzig, «Using the interface Peclet number to select the maximum simulation interface width in phase-field solidification modelling», *computational materials science*, vol.70, pp.71-76, 2013.
- [YAM2013] M. Yamaguchi and C. Beckermann, «Simulation of solid deformation during solidification : Shearing and compression of polycrystalline structures», *Acta Materialia* 61, pp.2268-2280, 2013.
- [YIN2011] H. Yin, S. Felicelli, L. Wang, «Simulation of a dendritic microstructure with the lattice Boltzmann and cellular automaton methods», *Acta Materialia*, vol.59, pp.3124-3136, 2011.
- [YOS2006] H. Yoshioka, Y. Tada, K. Kunimine, T. Furuichi, Y. Hayashi, «Heat transfer and solidification processes of alloy melt with undercooling: II. Solidification model», *Acta Materialia*, vol. 54, pp.765–771, 2006.
- [ZAB2006] N. Zabaras, B. Ganapathysubramanian, L. Tan, «Modelling dendritic solidification with melt convection using the extended finite element method», *Journal of Computational Physics*, vol.218, pp.200-227, 2006.
- [ZAL2013] M. Zaloznik, A. Kumar, H. Combeau, M. Bedel, P. Jarry, E. Waz, «The coupling of macrosegregation with grain nucleation, growth and motion in DC Cast aluminum alloy ingots», *Essential reading in light metals*, vol.3, pp.848-853, 2013.

- [ZAR2009] J-F. Zaragoci, «Modeling dendritic microstructure by a Level-Set method», *Ecole Nationale Supérieure des Mines de Paris*, Internship, 2008.
- [ZHU2001] M. Zhu, C. Hong, «A Modified Cellular Automaton Model for the Simulation of Dendritic Growth in Solidification of Alloys», *ISIJ International*, vol.41, pp.436-445, 2001.
- [ZHU2007] M. Zhu, C. Hong, D. Stefanescu, Y. Chang, «Computational Modeling of Microstructure Evolution in Solidification of Aluminum Alloys», *Metallurgical and Materials Transactions B*, vol.38, pp.517-524, 2007.

## Résumé

La croissance dendritique est calculée en utilisant un modèle champ de phase avec adaptation automatique anisotrope et non structurées d'un maillage éléments finis. Les inconnues sont la fonction champ de phase, une température adimensionnelle et une composition adimensionnelle, tel que proposé par [KAR1998] et [RAM2004].

Une interpolation linéaire d'éléments finis est utilisée pour les trois variables, après des techniques de stabilisation de discrétisation qui assurent la convergence vers une solution correcte non-oscillante. Afin d'effectuer des calculs quantitatifs de la croissance dendritique sur un grand domaine, deux ingrédients numériques supplémentaires sont nécessaires: un maillage adaptatif anisotrope et non structuré [COU2011], [COU2014] et un calcul parallèle [DIG2001], mis à disposition de la plateforme numérique utilisée (CimLib) basée sur des développements C++. L'adaptation du maillage se trouve à réduire considérablement le nombre de degrés de liberté. Les résultats des simulations en champ de phase pour les dendrites pour une solidification d'un matériau pur et d'un alliage binaire en deux et trois dimensions sont présentés et comparés à des travaux de référence. Une discussion sur les détails de l'algorithme et le temps CPU sont présentés et une comparaison avec un modèle macroscopique sont faite.

## Mots Clés

Solidification, dendrite, champ de phase, éléments finis, calcul parallèle, adaptation maillage.

## Abstract

Dendritic growth is computed using a phase-field model with automatic adaptation of an anisotropic and unstructured finite element mesh. Unknowns are the phase-field function, a dimensionless temperature and a dimensionless composition, as proposed by [KAR1998] and [RAM2004].

Linear finite element interpolation is used for all variables, after discretization stabilization techniques that ensure convergence towards a correct non-oscillating solution. In order to perform quantitative computations of dendritic growth on a large domain, two additional numerical ingredients are necessary: automatic anisotropic unstructured adaptive meshing [COU2011], [COU2014] and parallel implementations [DIG2001], both made available with the numerical platform used (CimLib) based on C++ developments. Mesh adaptation is found to greatly reduce the number of degrees of freedom. Results of phase-field simulations for dendritic solidification of a pure material and a binary alloy in two and three dimensions are shown and compared with reference work. Discussion on algorithm details and the CPU time are outlined and a comparison with a macroscopic model are made.

## Keywords

Solidification, dendrite, phase-field, finite element, parallel computation, mesh adaptation.